Quantum Dot-basierte FRET Systeme zur Templat-vermittelten Detektion von RNA

Dissertation

zur Erlangung des akademischen Grades

doctor rerum naturalium

(Dr. rer. nat.)

im Fach Chemie

eingereicht an der

Mathematisch-Naturwissenschaftlichen Fakultät

der Humboldt-Universität zu Berlin

von

M.Sc. Oleksandr Zavoiura

Präsidentin der Humboldt-Universität zu Berlin

Prof. Dr.-Ing. Dr. Sabine Kunst

Dekan der Mathematisch-Naturwissenschaftlichen Fakultät

Prof. Dr. Elmar Kulke

Gutachter:

1. Prof. Dr. Oliver Seitz

2. Prof. Dr. Ilko Bald

3. Prof. Dr. Kannan Balasubramanian

Tag der mündlichen Prüfung: 21.11.2018

Die vorlegende Arbeit wurde im Arbeitskreis von Prof. Dr. Oliver Seitz am Institut für Chemie der Humboldt-Universität zu Berlin und im Fachbereich Biophotonik der BAM bei Dr. Ute Resch-Genger von Oktober 2014 bis Juli 2018 angefertigt.

Kurzzusammenfassung

Die Detektion von Nukleinsäuren ist eine der am häufigsten verwendeten Methoden zur Erkennung von viralen und bakteriellen Spezies in biologischen Proben. Oligonukleotid-vermittelte Reaktionen (OVR), die die Zielsequenz als Katalysator der chemischen Reaktion zwischen reaktiven Sonden verwenden, bieten gegenüber den enzymatischen Methoden viele Vorteile, wie z.B. Simplizität und Kosteneffizienz. Normalerweise besitzt das Produkt der OVR deutliche fluoreszierende Eigenschaften, die durch Fluoreszenzspektroskopie gemessen werden können. Die Haupteinschränkung solcher Systeme ist die nur moderate Helligkeit (Produkt der Quantenausbeute und des Extinktionskoeffizienten) von organischen Farbstoffen, die meistens zur Markierung von reaktiven Sonden genutzt werden. Dies limitiert das Auslesen des optischen Signals bei geringen Konzentrationen der Sonden. Um dieses Problem zu lösen, sind Fluorophore mit höherer Helligkeit erforderlich.

Die vorliegende Arbeit beschreibt die Entwicklung einer Methode zur Detektion von RNA durch Templat-vermittelten Transfer des Fluorophors auf den Quantum Dot (QD). Das System besteht aus zwei reaktiven Peptide Nucleic Acid (PNA)-basierten Antisense-Sonden. Die Label Akzeptor PNA (LAPNA) Sonde ist auf dem QD immobilisiert und enthält eine Cysteineinheit am N-terminus. Die Label Donor PNA (LDPNA) Sonde trägt eine Cy5-Einheit, die als Thioester gebunden ist. Durch die benachbarte Hybridisierung der Sonden am RNA-Templat nimmt die effektive Molarität der reaktiven Gruppen zu, und führt somit durch das Prinzip von *Native Chemical Ligation* zum Transfer des Cy5 auf den QD. Dies resultiert in Förster−Resonanzenergietransfer (FRET) zwischen dem QD und den Cy5-Molekülen, der durch die Löschung der Emission des QDs sowie die Verstärkung der Fluoreszenz des Cy5 beobachtet werden kann. Die Verwendung von sehr hellen QDs als FRET-Donor ermöglicht die Umsetzung von Sonden bei geringen Konzentrationen (im Bereich von pikomolar) und bewirkt eine erhöhte Sensitivität von Templat-vermittelten Detektion von RNA.

Ein kupferfreies Azid-Alkin-Cycloaddition-basiertes Verfahren zur Immobilisierung der LAPNA-Sonde auf dem QD wurde entwickelt. Dies ermöglicht die bioorthogonale Kopplung von LAPNA unter milden Bedingungen und erlaubt es, den Beladungsgrad des QDs einzustellen. Die Dichte von PNA hat einen starken Einfluß auf die Kinetik sowie die Affinität der Bindung zu RNA. Nukleinbase- und Aminosäurebestandteile der PNA−Sonden wurden optimiert, um sowohl eine hohe Affinität zur RNA als auch gute Wasserlöslichkeit zu erreichen. Das Hinzufügen von Glutamateinheiten zu beiden Sonden erhöht ihre Hydrophilie und die unspezifischen Wechselwirkungen zwischen den PNA nehmen ab. Das optimierte System ermöglicht die Erkennung von RNA mit Nachweisgrenzen im Bereich von weniger pikomolar und das Verfahren kann in Mikrotiterplatte durchgeführt werden.

Abstract

Detection of nucleic acids is one of the most reliable methods for the identification of bacterial and viral species in biological samples. Oligonucleotide-templated reactions (OTRs) that exploit an RNA or DNA target to catalyze a chemical reaction hold great promise for the development of enzyme-free and low-cost detection schemes. Commonly, these strategies rely on organic dyes and are designed so that the product of OTR exhibits distinct fluorogenic properties. The main constraint of such schemes is the moderate brightness of organic fluorophores, which limits the read-out when the probes are used at low concentrations. To tackle this obstacle, significantly brighter fluorophores are needed.

This work describes the development of an RNA detection scheme that relies on target-templated fluorophore transfer onto a semiconductor quantum dot (QD). The approach uses two reactive peptide nucleic acid (PNA) antisense probes. Label acceptor peptide nucleic acid (LAPNA) probe is immobilized on a QD and bears a cysteine at the N-terminus; label donor peptide nucleic acid (LDPNA) probe is equipped with a Cy5 dye, attached as a thioester. The adjacent annealing of these recognition elements following binding to target RNA triggers the transfer of Cy5 onto a QD in a native chemical ligation manner. This leads to a detectable fluorescence signal brought about by FRET from QD to the Cy5. The use of unprecedentedly bright QDs that can act as FRET donors for several Cy5 functionalities allows application of probes at very low concentrations (pM range) and achieves enhanced sensitivity of target-templated RNA detection.

For this purpose, a two-step strain-promoted azide-alkyne cycloaddition (SPAAC) strategy for the immobilization of LAPNA on a QD was designed. Such approach permitted bioorthogonal attachment of LAPNA to the QD using mild conditions and fine-tuning of the PNA labeling density on a nanoparticle. The PNA load was found to have a profound effect on the kinetics and affinity of binding with the target, with high PNA content being advantageous.

To achieve high affinity for the target, as well as good water solubility, the optimization of nucleobase and amino acid composition of both PNA probes was performed. It has been established that incorporation of glutamic acid residues into both PNA probes was vital for the suppression of nonspecific interactions (NSI) between the LDPNA and LAPNA. In addition, a study of the impact of various surfactants on the degree of NSI between the PNA probes was performed. This allowed to substantially improve the sensitivity of the approach and to simplify the assay conditions. The method enabled RNA detection in the low pM range using a conventional microtiter plate reader.

Table of contents

1 Introduction

Nucleic acids are common biomarkers in clinical diagnostics. Sensitive and selective detection of DNA or RNA can enable the identification of a broad spectrum of bacterial and viral diseases.[1] Today, polymerase chain reaction (PCR)-based methods are considered a "gold standard" in the field of RNA and DNA diagnostics.[2-3] PCR uses enzyme-induced replication of the target DNA prior to analysis, thereby enabling the detection of extremely low target concentrations. Detection of RNA is achieved via reverse-transcription PCR (RT-PCR).[4] In this instance, target RNA is reversely transcribed into its complementary DNA prior to PCR. The PCR-amplified product is typically detected by using fluorogenic DNA binders and it can be performed in real time.[5] While exceptionally sensitive, PCR has drawbacks. Firstly, the method is susceptible to cross-contamination by nucleic acids, which may lead to false-positive results.[6-7] Secondly, PCR is sensitive to trace amounts of chemicals and detergents, thus requiring trained personnel and well-equipped laboratory to perform the detection. Therefore, an alternative strategy that would provide simple, sensitive, and cost-efficient approach for nucleic acid diagnostics and could be implemented in point-of-care testing (POCT) or at least with minimal laboratory equipment, is highly desirable.

Bypassing enzymatic amplification could significantly simplify the detection of RNA, provided that alternative approaches exhibit equally high sensitivity. A possible way to address this challenge is the application of oligonucleotide-templated reactions (OTR). OTRs occur between two reactive nucleic acid-based antisense probes following their hybridization with an RNA target.[8-9] The adjacent annealing of such probes enhances their effective molarity, thereby facilitating the chemical reaction and yielding a product with distinctive fluorescent features. This utilizes the nucleic acid target both as a catalyst of chemical reaction, and to amplify the signal − an advantage that conventional non-reactive hybridization probes lack. The course of an OTR can be conveniently monitored via Förster resonance energy transfer (FRET), exploiting two dyes with overlapping emission and absorbance spectra.[10]

The majority of current FRET-based OTR detection schemes relies on the use of organic dyes as fluorescent labels. This demands relatively high concentrations of probes for signal generation due to the moderate brightness of these fluorophores, compared to brighter nanoparticles, such as QDs.[11-12] Despite successful efforts made to accelerate the kinetics of OTRs,[13-15] and thus to boost the catalytic activity of the nucleic acid target, the need to keep the concentrations of probes in high nM range effectively constrains the achievable limits of detection (LODs). Conceptually, decreasing the concentrations of probes by several orders of magnitude must result in a proportional decrease in a LOD, provided the probes exhibit sufficient affinity for the target and the appropriate read-out

strategy is used. Adjusting the probes' affinity is very straightforward and can be accomplished by using longer oligonucleotides. However, the read-out strategy that would allow to detect the fluorescent signal at low nM or pM probe concentrations using standard laboratory equipment is a nontrivial challenge, which must be addressed using fluorophores with advanced spectroscopic features. The use of semiconductor QD as a FRET donor in conjunction with the emissive FRET acceptor in an OTR detection scheme could present a possible solution to the described problem. Using reactive oligonucleotides labeled with these fluorophores could allow use of very low concentrations of probes while still maintaining the effective optical read-out, brought about by the exceptionally bright QDs. Provided that the OTR functions effectively on the surface of a nanoparticle, such strategy could be envisioned to perform superiorly to the current organic dye-based OTRs.

2 Fundamentals

2.1 Hybridization Probes for the Detection of Nucleic Acids

To identify the DNA or RNA of interest a range of synthetically produced hybridization probes can be used. These are designed so that the probe exhibits clearly distinguishable properties between the unbound state and upon hybridization with the nucleic acid target (NAT). A convenient approach is the use of fluorescently-labeled oligonucleotides that alter their emissive properties following the formation of a double strand through Watson-Crick interactions with the target sequence. These include molecular beacons (MBs), forced intercalation (FIT) probes, Taqman probes, nanoflares, catalytic beacons, and many others.[16]

Two representative examples are molecular beacons (MB) and forced intercalation (FIT) probes. MBs, first introduced by Tyagi et al.,[17] contain an oligonucleotide sequence that is designed to bind both the nucleic acid of interest in a specific manner, and also intramolecularly to its own stem region. When not bound to the NAT, base-pairing between two short complementary regions leads to the formation of a hairpin structure (*Scheme 2.1*a). The 5' and 3' of the MBs are labeled with a fluorophore and a quencher that are positioned very close to each other in the absence of a target sequence. The presence of the NAT leads to formation of a new double strand and concomitant breakage of the stem structure, thereby effectively separating the fluorophore and the quencher. The breakage of the hairpin results in the enhanced emission of the fluorophore under light illumination and signals the presence of the NAT. Alternatively, a pair of fluorescent labels that form a FRET pair can be used for the labeling of the 5' and 3' of a hairpin, thereby enabling a ratiometric read-out, as illustrated in *Scheme 2.1*a`.[18]

While many MBs are labeled with organic dyes, other materials, e.g., semiconductor QDs,[19] gold nanoparticles (AuNPs),[20] AuNPs-containing silicon nanowires,[21] carbon nanotubes,[22] can be used as platforms for the design of MBs as well. Due to their versatility and simplicity, MBs have found broad utility in clinical diagnostics,[23] e.g., for the detection of amplicons in real time PCR.[24] The sensitivity of MB-based strategies can be enhanced by using catalytic beacons that involve the use of DNAzymes or multicomponent nucleic acid enzymes.[16]

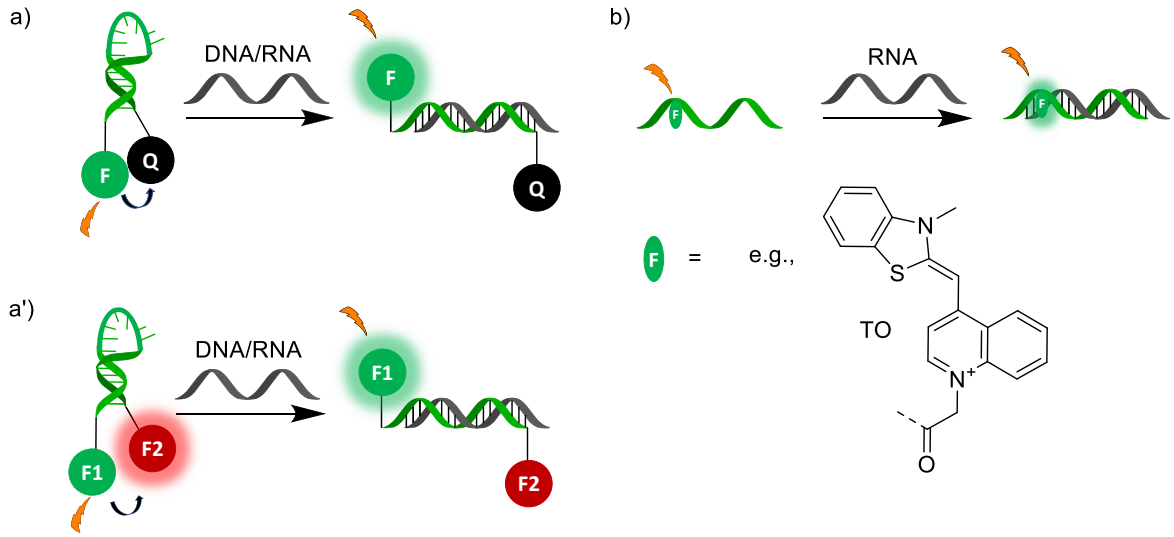

Scheme 2.1. Nucleic acid detection using molecular beacons (MBs) that contain a fluorophore and a non-emissive quencher (a) or a FRET pair of two fluorogenic dyes (a`). Concept of RNA detection using forced intercalation (FIT) probes (b). TO = thiazole orange.

FIT probes contain environmentally-sensitive fluorescent dyes, which are linked as nucleobase surrogates. The brightness of emission is strongly enhanced upon hybridization with the nucleic acid target (*Scheme 2.1*b).[25] The nucleobase surrogates are typically dyes of thiazole orange family. In the absence of target sequence, the FIT probe exists in a single strand and the quantum yield (QY) of the dye is very low due to the unperturbed rotation around the central methine bridge that leads to a conical intersection and rapidly depletes the excited state. Following the formation of a double strand with the nucleic acid target, this rotation is restricted, thereby strongly increasing the fluorescence of the dye and providing the means to identify the presence of a target sequence. FIT probes have proven to be a powerful tool for wash-free RNA imaging owing to the simplicity of the procedure, high signal-to-noise ratios, and the potential of multiplexed imaging via the use of base surrogates with spectrally resolved emission bands.[26-29]

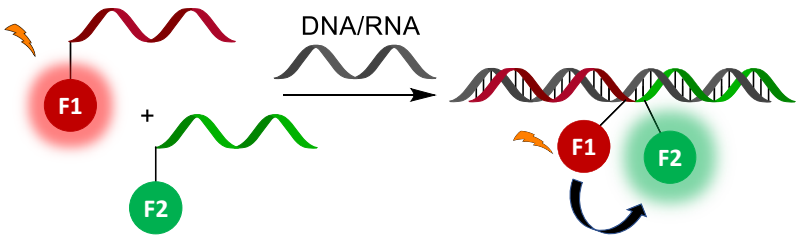

Scheme 2.2. Nucleic acid detection using adjacent hybridization probes labeled with organic dyes. The dyes F1 and F2 are FRET donor and FRET acceptor respectively.

Following an alternative approach, a pair of hybridization probes that bind adjacently to the NAT can be used instead of one long probe (*Scheme 2.2*). This design provides a high specificity owing to the higher destabilizing effect of single base mismatches on the shorter probes compared to longer ones. To achieve a read-out, the probes can be labeled with the dyes that form a FRET pair.[30] In the absence of NAT, the two FRET probes exist as single strands and the dyes are spatially separated.

However, in the presence of a NAT, the dyes are brought in proximity thereby allowing for FRET; the efficiency of which can be monitored by measuring the quenching of FRET donor. While the FRET acceptor does not have to be emissive, the use of a fluorogenic acceptor allows for ratiometric measurements, and, thereby, signaling that is independent of probe concentration.

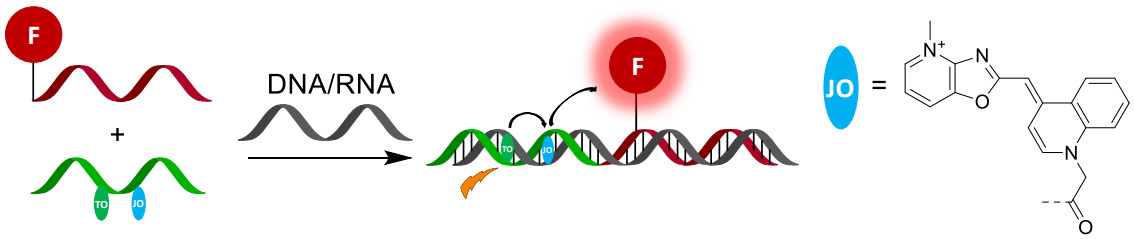

Scheme 2.3. Nucleic acid detection using adjacent hybridization probes based on the combination of a dually labeled FIT probe as FRET donor and near infrared dye as FRET acceptor. F = NIR664. TO = thiazole orange.

Recently, a pair of probes that consisted of a dually labeled FIT probe that acted as FRET donor and a second hybridization probe labeled with a conventional emissive FRET acceptor has been developed (*Scheme 2.3*). The system combined the benefits of FIT probes and FRET-based energy transfer, thereby effectively minimizing the spectral cross-talk between the emission bands of the luminophores. This advanced strategy was successfully utilized for RNA imaging in cells.[31]

2.2 Oligonucleotide-Templated Reactions for Nucleic Acid Detection

OTRs are reactions that are accelerated by an oligonucleotide template (ONT). The OTRs are designed so that the two reactive oligonucleotides are aligned by the ONT. This brings two functional groups in proximity. The ONT-triggered enhancement of the effective molarity induces the chemical reaction. Since the first report on the template-directed synthesis by Naylor and Gilham,[32] substantial progress has been made in a pursuit of faster and more efficient OTR strategies.[8, 33-36] These advancements allowed to transform the OTRs into a fascinating and unique group of methods for nucleic acid detection. The OTRs are developed so that the product has clearly distinguishable (in most cases fluorogenic) features. Such design allows to monitor the course of OTR in real time using fluorometric methods. Importantly, one template can catalyze multiple reactions, thereby providing a signal enhancement even when the template is present at very low concentration. In contrast to polymerase chain reaction (PCR) schemes that enzymatically multiply the NAT prior to its detection with hybridization probes, OTRs are responsible for both the amplification and detection steps, i.e., the chemical reaction leading to the turnover in nucleic acid template (amplification) results in the formation of a fluorogenic product, which is subsequently detected.

Broadly speaking, OTR-based detection schemes can be divided into three groups: ligation reactions, inter-conversion reactions, and cleavage reactions. The reactions in the former group are designed to join two reactive oligonucleotides via a covalent linkage. This results in a formation of a longer oligonucleotide, which has a higher affinity for the target than each of the reactive probes, thereby hampering the catalytical activity of a nucleic acid template. To circumvent this obstacle, various approaches have been developed that rely on the inter-conversion or cleavage reactions. These result in the formation of products with similar affinity for the target as the reactants. OTRs are designed so that both reactive groups are orthogonal toward naturally occurring functional groups, and the reaction has a negligible rate in the absence of a nucleic acid template at the required concentrations of probes, i.e., the concentration at which the binding affinity for the target is optimal.

The chemistries that have been successfully used for template-directed ligations include native chemical ligation,[37] selenocystine-selenoester ligation,[38] phosphorothioate-based ligation,[39-41] electrophilic phosphorothioester-based ligation,[42] tetrazine-based ligation,[43-44] and others (*Scheme 2.4*). These techniques have been used for RNA imaging in bacterial cells [40], human cells[41, 44], and cell lysates.[38] However, product inhibition of turnover in template remains a major challenge, despite the successful attempts to alleviate it by the introduction of destabilizing linker at the ligation site.[37, 45-46]

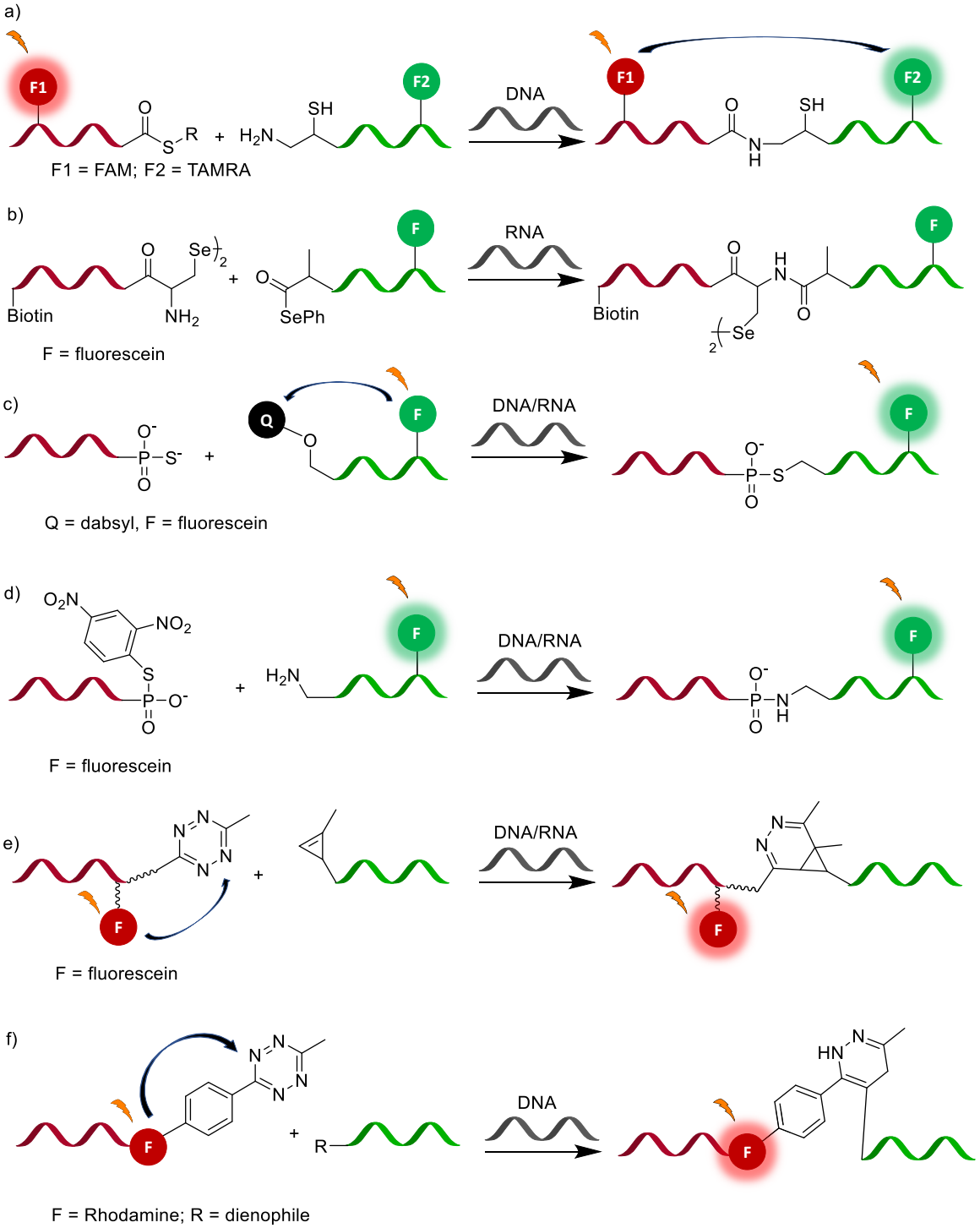

Scheme 2.4. Examples of ligation-based oligonucleotide-templated reactions (OTRs). a) Native chemical ligation between the thioester and iso-cysteine[37]; b) selenocystine-selenoester ligation[38]; c) phosporothioate-based ligation[39-40]; d) electrophilic prosphorothioester-based ligation[42]; e) tetrazine-based ligation reported by Seckute et al.[44] and f) tetrazine-based ligation reported by Werther et al.[43]

Transfer-based OTR relocates a functional unit such as a quencher[15, 47-48] or a fluorophore[49] from one reactive probe to another (*Scheme 2.5*a and a`).

In cleavage reactions, the quencher may be cleaved using phosphine-induced azide reduction. The so-called QSTAR approach (quenched Staudinger triggered α-azidoether release) involves the fragmentation of azidoethers (*Scheme 2.5*b) which release a fluorescence quencher.[46, 50] A similar strategy that relies on Ru(II)-catalyzed photoreduction and concomitant uncaging of a fluorophore was reported by the Winssinnger group.[51] This approach involves the conversion of the fluorophore into its fluorescent state from a non-fluorescent precursor by the chemical alteration of its molecular structure, namely by the reduction of an azido group (*Scheme 2.5*c). The variation of the latter approach has been shown to provide exceptionally high turnover in template numbers (>4000)[13] and it is one of the most efficient OTR strategies reported to date.

Another interesting example of fluorophore uncaging has been recently reported by Devaraj et al.[52] This concept relies on the uncaging of a vinyl ether-modified fluorophore by a tetrazine. Impressively, this strategy could be applied to a symmetric Cy7 dye (*Scheme 2.5*d) that exhibits emission in the near infrared region making it a very promising label for the use in biological media such as cells and tissues.

While many OTRs result in the formation of a covalent bond, unconventional multicomponent systems have also been developed. For example, Prusty et al. have shown that two phosphine-functionalized probes can be joined together through the coordination to the *in situ*-formed Pd.[53] The as-formed Pd complex was used to catalyze the conversion of a non-fluorescent form of a BODIPY-derivative into a fluorescent one, thereby allowing for the optical read-out.

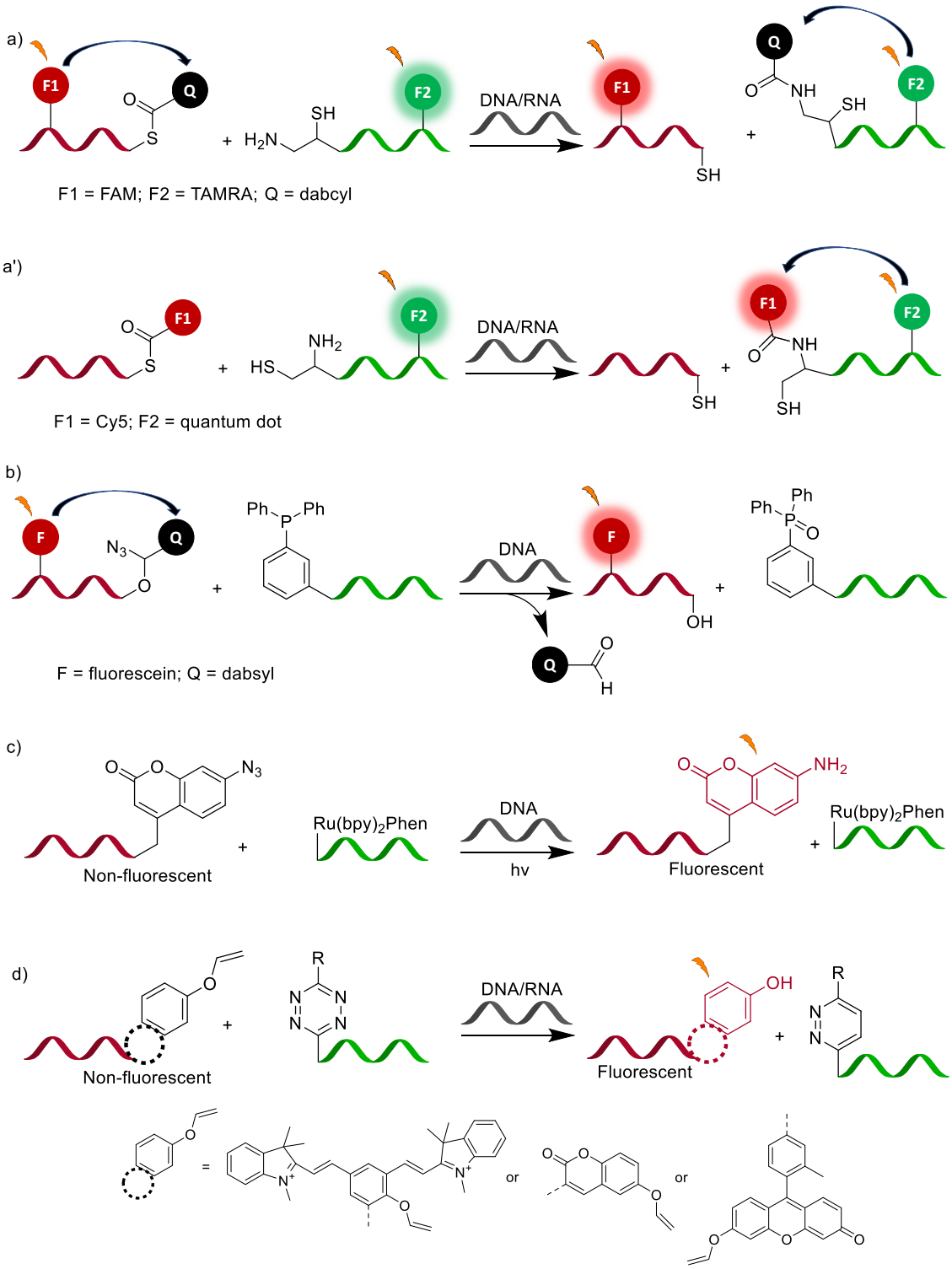

Scheme 2.5 Schematic presentation of different approaches used for transfer- and cleavage-based OTR detection schemes. a) and a`) native chemical ligation-based transfer reactions[47, 49]; b) quenched Staudinger triggered α-azidoether release (Q-STAR) probes[50]; c) Ru(II)-catalyzed photoreduction[51]; d) tetrazine-based uncaging of vinyl ether-modified dyes[52].

2.3 Quantum Dots. Properties & Bioanalytical Applications

2.3.1 Quantum dot materials

Quantum dots (QDs) are nanocrystals that typically consist of II-IV (CdSe, CdS, CdTe, ZnS, ZnSe) or III-V (InP, InAs) type semiconductors. These materials exhibit unique optical properties that are induced by the so-called quantum confinement effect, first described by Rossetti et al.[54] for CdS crystallites. This term refers to an increase in bandgap energy (E_{bg}) once the nanocrystal dimensions fall below the size of the exciton Bohr radius. The latter value is specific for every semiconductor material. The increase in the bandgap between the valence and conduction energy states is inversely proportional to QD size, with smaller particles having a larger bandgap energy and thus blue-shifted absorption and luminescence spectra. Such size-dependent features allow to fine-tune the spectroscopic properties of QD materials by changing the size of a nanoparticle.[12]

Since the pioneer works by Steigerwald et al.[55] aimed at the synthesis of colloidally stable semiconductor nanoparticles, significant efforts have been dedicated to the improvement of the synthetic routes to produce high quality monodisperse QDs with controlled composition.[56-61] The advancements made during the last thirty years led to the commercialization of QDs and today a variety of semiconductor nanoparticles are available on the market.

Generally, colloidal QDs can be divided into two groups: core-only and core-shell nanoparticles (*Scheme 2.6*). The core-only nanoparticles consist of a semiconductor material, e.g., CdTe or PbS, and a stabilization layer that contains organic ligands with high affinity for the QD surface atoms and controls QD dispersibility. The main drawback of such materials is the exposure of the inorganic core to the environment that can translate into diminished photoluminescence QY, can alter the spectroscopic features of the QDs and limit their long-term stability.[62] To circumvent these obstacles, core-shell QDs were developed using sophisticated inorganic shells that passivate the surface defects and shield the QD core.[63] These core-shell QDs are composed of a core semiconductor that functions as an emitter and a shell that typically consists of a semiconductor with a larger band-gap energy.[64] Such a design, that still requires stabilizing organic surface ligands, improves the QY of most QDs through the passivation of the trap states on the core surface,[58] and enhances the stability of the core material by physically shielding it from the microenvironment.

Typically, the synthesis of QDs involves the pyrolysis of metalorganic precursors using the so-called “hot injection” method and is carried out in hydrophobic coordinating solvents, e.g., trioctylphosphine (TOP), trioctylphosphine oxide (TOPO).[57, 65] The resulting nanoparticles often contain TOP/TOPO ligands that bind the surface atoms of semiconductor material with high affinity and colloidally stabilize the nanoparticles in nonpolar environment through the long alkyl chains.

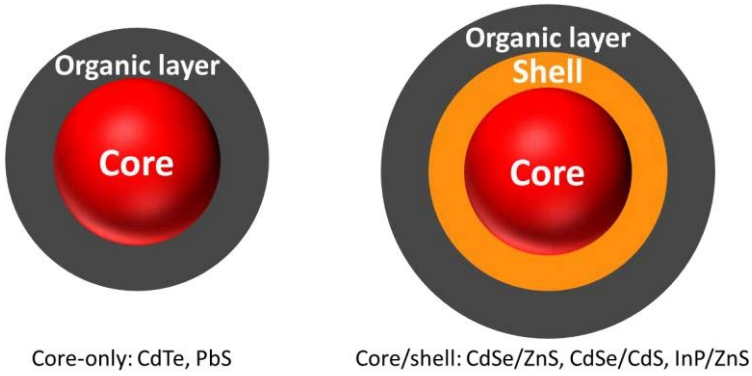

Scheme 2.6. Schematic presentation of core-only and core-shell quantum dots, and the most commonly used constituent materials. Organic layer designates the outer shell that consists of organic ligands with high affinity for the surface atoms of QD or a polymeric shell wrapped around the surface-coordinated ligands. More details on the structure of inorganic ligands are provided in the following schemes.

To make the QDs useful for bioanalytical applications they must be rendered water soluble. The strategies for the preparation of hydrophilic QDs from hydrophobic ones can be divided into two groups: i) ligand exchange with hydrophilic, bifunctional ligands and ii) encapsulation of native QDs with a polymer shell. The former strategy is based on the replacement of native ligands with a new ligand, or a combination of several ligands that contain an anchoring group that exhibits high affinity for surface ions and a hydrophilic moiety which ensures water solubility and provides the means for subsequent bioconjugation.

QDs prepared by phase transfer exhibit two major drawbacks: i) dependence of colloidal stability on the dissociation rate of the respective ligand, and ii) diminished QY after phase transfer.[11, 66] To avoid the stripping down of the original QD ligand cap, a variety of amphiphilic polymers has been developed that encapsulate the hydrophobic QDs thereby preserving the native ligand coating and maintaining the high QY of as-synthesized QDs. Examples of these two groups of stabilization layers are provided in the next section.

2.3.2 Quantum dot surface chemistry

Monothiol ligands of various classes have been successfully used to prepare water-soluble QDs (*Scheme 2.7*a) [67-69]. Such approach was not only used to transfer the QDs for subsequent conjugation with biomolecules, but also for direct attachment of the thiol-terminated DNA strands onto the surface of a nanoparticle as was shown by Mitchell et al. (*Scheme 2.7*a).[69] Several groups have developed bidentate dihydrolipoic acid-based ligands that exhibit a stronger, compared to mono-dentate ligands, affinity for the metal ions on the QD surface (*Scheme 2.7*b).[70-71] It has been shown that not only thiol ligands, but also imidazole-based ligands can be successfully used for the immobilization of biomolecules on the CdSeS/ZnS core-shell QDs, as was reported by Petryayeva et al. (*Scheme 2.7*c).[72]

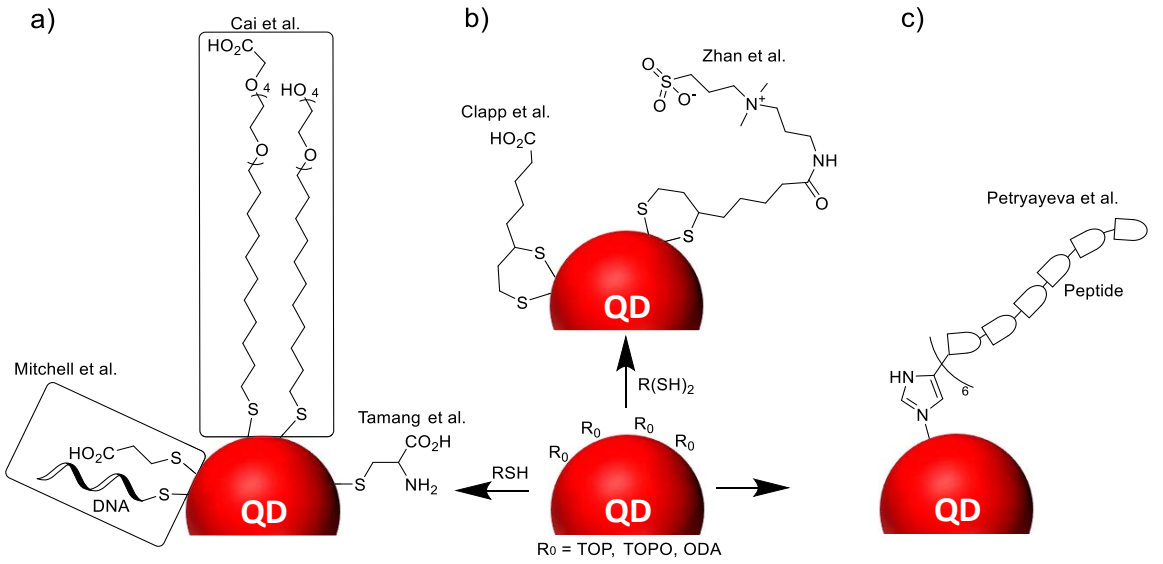

Scheme 2.7. Examples of phase transfer of nonpolar QDs into water by using monothiol ligands (a) [67-69], dithiol ligands (b) [70-71], and hexa-histidine tags (c) [72].

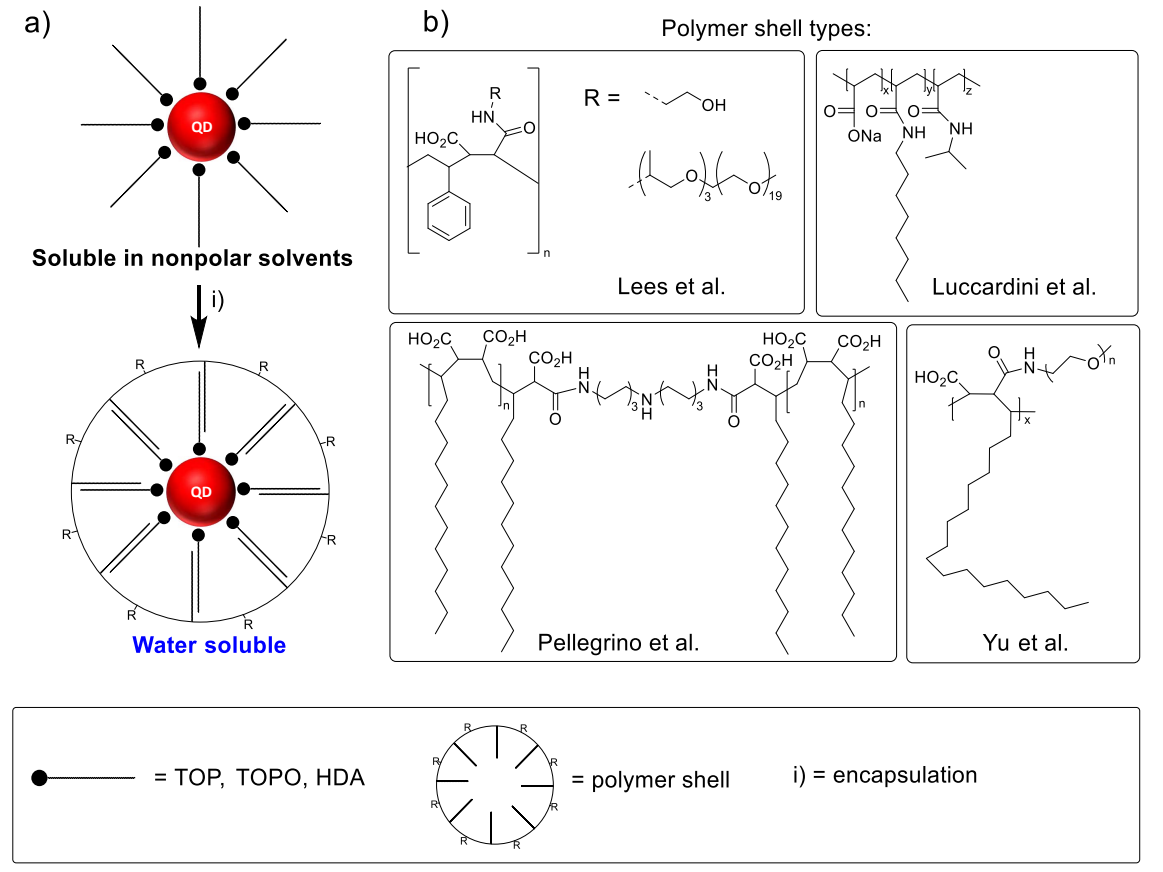

Scheme 2.8. a) Schematic presentation of QD encapsulation using amphiphilic polymers. b) Different classes of polymers used for QD encapsulation.[73-76] TOP = trioctylphosphine, TOPO = trioctylphosphine oxide, HDA = hexadecyl amine.

Amphiphilic polymers used for QD encapsulation contain a hydrophobic part that interdigitates the alkyl chains of the original ligands and a hydrophilic part that renders the resulting conjugate water soluble. As illustrated in *Scheme 2.8* a hydrophobic block may consist of a phenyl moiety[73] or long alkyl chains[74-76] which nonspecifically intercalate the native organic shell. The hydrophilic moiety

is composed of an ionizable group that confers water solubility (often a carboxylic group) and serves as a handle for subsequent bioconjugation. In addition, the hydrophilic segment may contain polyethylene glycol chains that have been shown to reduce the degree of nonspecific binding to biomolecules.[73, 77]

2.3.3 Quantum dots in nucleic acid detection

The advantageous optical properties of QDs such as narrow and highly symmetric emission band, very broad absorption spectrum, and high molar extinction coefficient and QY make them very useful FRET donors. Moreover, QDs can act as carriers for several FRET acceptors, thereby driving very efficient energy transfer. Some examples of "sandwich" assays for the detection of nucleic acids that exploit QDs are illustrated in *Scheme 2.9*.

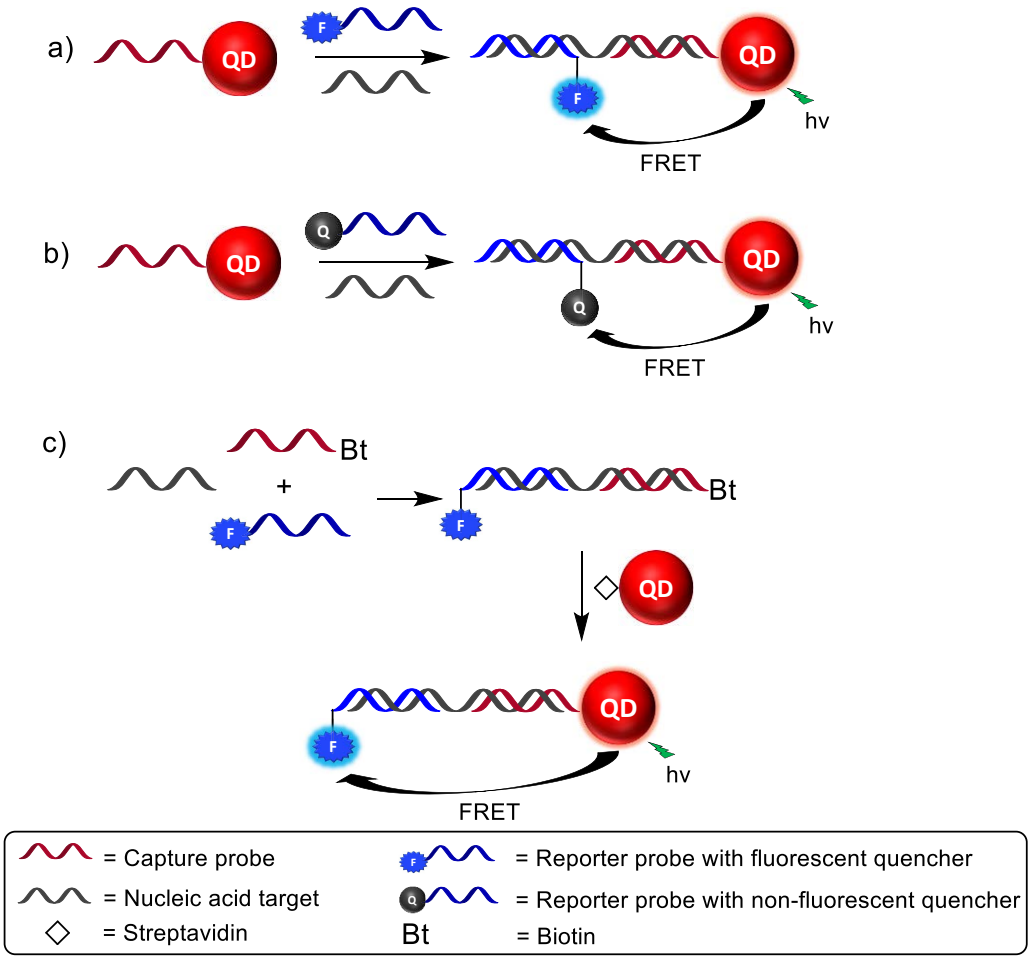

Scheme 2.9. Different QD-based "sandwich" FRET schemes for the detection of nucleic acids. a, b) Formation of a ternary complex between the probes and target on the nanoparticle surface using fluorescent (a) and non-fluorescent (b) FRET acceptor. c) Solution-based hybridization with subsequent capture of the complex using streptavidin-functionalized QDs.

For the detection schemes that involve the formation of a ternary complex on the QD surface (*Scheme 2.9*a and b) the probes are designed to adjacently anneal with the DNA or RNA target, with the capture probe immobilized on a QD and the reporter probe functionalized with the dye, the

absorption band of which overlaps with the emission of the QD. Both fluorescent[78-79] and non-fluorescent[80] dyes can be used as FRET acceptor. The use of the former, however, enables two-channel detection, which makes the optical read-out more robust. Alternatively, the hybridization can be performed in solution and the ternary complex subsequently separated using streptavidin-functionalized QDs and biotin-functionalized capture strand (*Scheme 2.9*c).[81-83] The latter approach has been employed for the ultrasensitive detection of DNA using confocal fluorescence spectroscopy with an impressive LOD of 4.8 fM.[81]

2.4 Synthesis and Properties of Peptide Nucleic Acids (PNA)

2.4.1 Properties of PNA

PNA is an artificial nucleic acid that consists of a peptide-like backbone which carries nucleobases attached through methylene carbonyl linkers (*Scheme 2.10*). Since the first publication on the PNA by Nielsen et al.,[84] this class of molecules has attracted great interest in the field of biotechnology, particularly in the area of nucleic acid detection, since it has several important advantages over conventional DNA-based probe .[85-86] Firstly, PNA binds DNA and RNA with very high affinity and specificity, higher than DNA itself. Another advantage of PNA is its enzymatic stability since it is neither a nucleic acid nor a peptide, despite what its name might suggest, which confers resistance to both nucleases and proteases, and allows it to apply PNA-based probes in biological media. Finally, PNA exhibits high chemical stability to acids and bases and can be synthesized using standard solid phase chemistry protocols used for the synthesis of peptides.[85-88] The major drawback of this class of oligonucleotides is the significant hydrophobicity, especially of long and purine-rich probes, which may lead to poor water solubility.

PNA has found broad utility in various areas of biotechnology, and has been used for the production of forced-intercalation probes,[29, 89] as reactive probes for OTR,[13, 35, 38, 47, 90] for the preparation of electrochemical devices,[91-92] as carriers for drugs, for the purification of nucleic acids, for the construction of microarrays, for information tagging, and in many other applications.[86, 93]

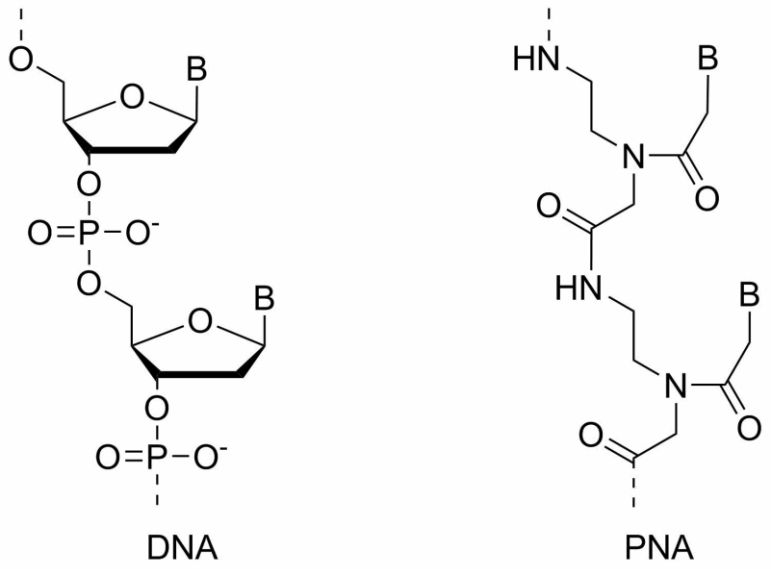

Scheme 2.10. Schematic presentation of DNA and PNA structural motifs. B = nucleobase.

2.4.2 Synthesis of PNA

Synthesis of PNA and PNA-peptide conjugates is performed similarly to the solid phase synthesis of peptides using the two main methods: the Boc/Bzl or Fmoc/tBu strategy.[84, 94-95] The latter approach allows milder conditions and is typically used for automated peptide synthesis, for example using the protocol illustrated in *Scheme 2.11*. Such synthesis is carried out on solid support. In the example illustrated in *Scheme 2.11*, a resin with an Fmoc-protected amino group is used for synthesis. Alternatively, the growing PNA chain may be anchored by means of hydroxyl groups.

The first step involves the *deprotection* of an Fmoc-protected amino group upon treatment with a base, e.g., piperidine, in organic solvent, e.g., DMF (deprotection step). The released fluorene adduct can be monitored photometrically.

The next step involves the *coupling* of the monomeric unit which proceeds via the formation of an amide bond between the activated carboxyl group of amino acid (AA) or PNA monomer and a deprotected N-terminus of the resin. The AA monomers used for the Fmoc-SPPS contain an Fmoc-protected α-amino group and a base-resistant side chain protecting group. To convert the carboxylic acid into an active ester, a mixture of a coupling agent (e.g., PyBOP, HCTU), a base (e.g., DIPEA, NMM) and an additive (e.g., HOBt, Oxyma) is used. Milder bases, such as 2,4,6-collidine, are recommended for the couplings of racemization-prone AAs such as cysteine.[96]

Fmoc-protected PNA monomers are coupled similarly to AAs, yet additives are not required since PNA is achiral and racemization is not of concern. Exocyclic amino groups of PNA nucleobases are protected using the base-resistant benzhydryloxycarbonyl (Bhoc) moiety, which can be removed during the cleavage of the resulting product from the solid support (*Scheme 2.11*).

The *capping* step can be effectively accomplished by using acetic anhydride in the presence of a base. This step ensures that any unreacted amino groups are acetylated, thereby preventing the formation of deletion sequences during the following steps. These three steps (deprotection-coupling-capping) constitute the synthetic cycle during the synthesis of PNA-peptide conjugates and are iterated up until the last coupling step.

The *cleavage* of the resulting product from the resin and the deprotection of acid-labile side-chain protecting groups are carried out using trifluoroacetic acid (TFA) in the presence of scavengers, e.g., triisopropylsilane (TIS), water, m-cresol, 1,2-ethanedithiol (EDT), thiophenol. The use of scavengers prevents the side reactions between the nucleophilic groups of the deprotected product and carbo-cationic species released during the deprotection of the side chains.

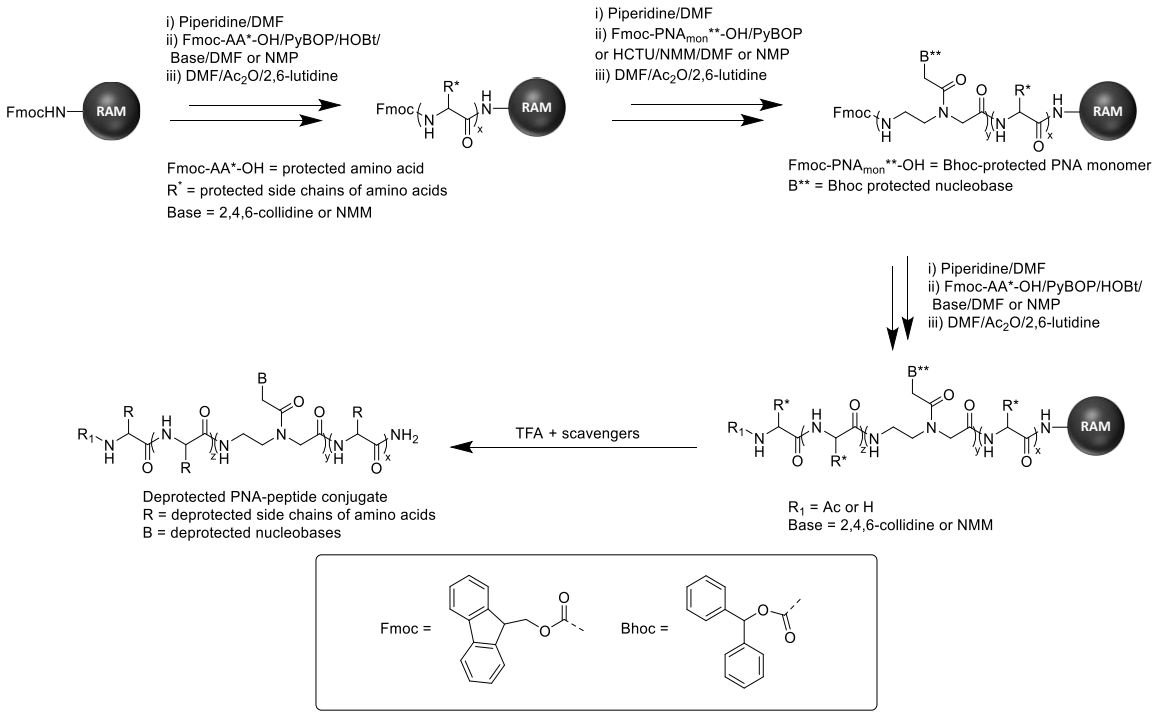

Scheme 2.11. Schematic depiction of the solid phase synthesis of PNA-peptide conjugates according to an Fmoc-strategy. The choice of scavengers during the total cleavage/deprotection step depends on the amino acid composition of the respective PNA-peptide conjugate. Some of the commonly used scavengers are: TIS, water, m-cresol, EDT, thiophenol. For simplicity the side chains of amino acid fragments are designated as R (or R^* in a protected form). RAM = Rink Amide Resin.

As is shown in *Scheme 2.11*, AA units can be incorporated at the C-terminus or at the N-terminus during the assembly of the PNA. The incorporation of AA allows to introduce functional groups that can enhance the water solubility of the resulting PNA molecule, e.g., via the introduction of lysine, or aspartic and glutamic acid.[97] In addition, the functional groups of natural or unnatural AAs can be used for the labelling with various organic dyes[10, 38, 48, 98-99] directly on the solid phase or post-synthesis in solution.

3 Research Objectives

The primary objective of this work was the development and optimization of QD-based FRET systems for enzyme-free target-templated detection of RNA. This system was envisioned to provide high sensitivity of RNA detection by combining the high brightness (a product of molar extinction coefficient and QY) of QDs with exceptional binding affinity exhibited by peptide nucleic acid-based probes. Previously, the Seitz group introduced a variety of FRET-based OTRs that exploit a nucleic acid target to catalyze a chemical reaction between the two functionalized hybridization probes yielding a fluorogenic product.[10, 15, 37, 47-48] Until recently, these schemes relied on the use of organic dyes as fluorescent labels, thereby requiring high concentrations of probes to generate a sufficiently high optical signal. In a pursuit to overcome this limitation, Michaelis et al.[100] have shown that OTRs can also be performed using bright QDs as a FRET donor. The sensitivity of the approach was, however, moderate, which was attributed to the slow hybridization kinetics. In addition, the use of streptavidin-biotin for the immobilization of the label acceptor probes on the QD restricted the responsivity of the system by imposing additional distance between the dipoles of the QD and FRET acceptor.

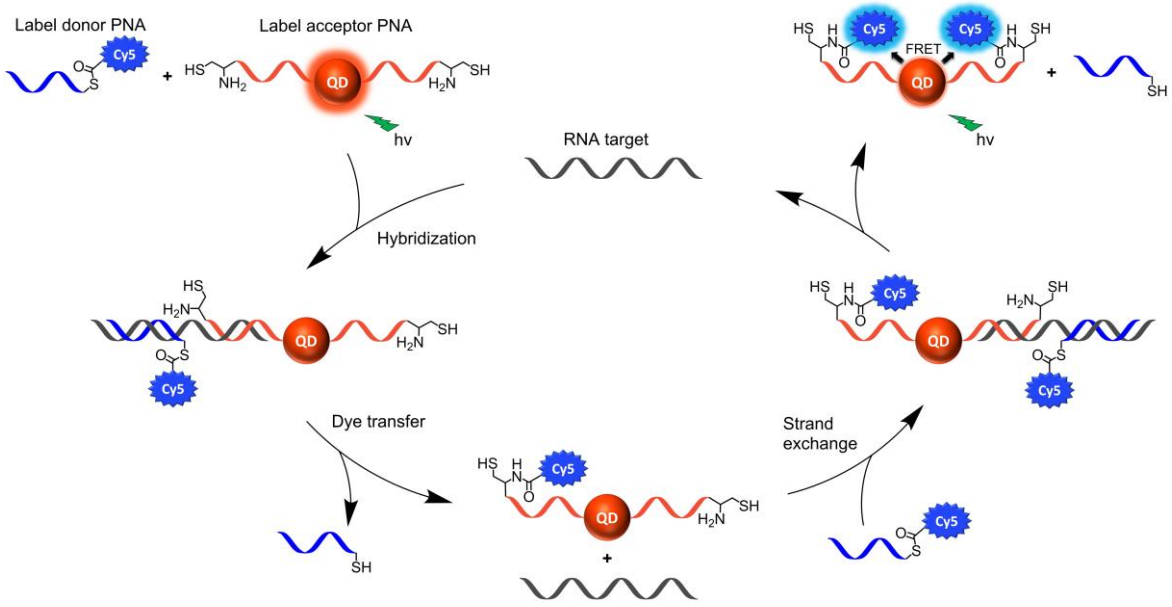

Scheme 3.1. Schematic presentation of QD-based FRET system for target-catalyzed RNA detection. Adopted with permission from[101]. Copyright 2018 American Chemical Society.

To design a sensitive QD-based OTR system, several issues had to be addressed. Firstly, synthesis of QD-PNA conjugates with small diameters was essential to reduce the distance separating the QD donor and a FRET acceptor, thereby improving the efficiency of FRET. To that end, nanoparticles with small diameters and a conjugation chemistry that relies on the use of small building blocks were required. This was expected to provide the means to drive efficient FRET and to fine-tune the

number of label acceptor probes on the QD. Secondly, the design of label acceptor and label donor PNA with high affinity for the RNA target and good solubility in common buffers, was needed. Both these features are strongly dependent on the length and base composition of the probe, thus making the careful design of LD and LAPNA mandatory. As a target sequence a highly conservative fragment within 3' UTR of the dengue viral genome was chosen.[102]

The optimized system was expected to provide two main advantages over existing OTR schemes. Firstly, owing to the high brightness of the QDs, it should be possible to maintain considerably lower, compared to organic dye-based systems, concentrations of probes. This can be expected to result in lower LODs, provided that the affinity of recognition elements is sufficiently high and target-catalyzed amplification is potent. Secondly, since QDs allow to substantially decrease the quantities of both reactive hybridization probes to generate the optical signal, the overall cost of the assay can be decreased.

4 Results & Discussion

4.1 Selection of FRET Donor and FRET Acceptor

4.1.1 Selection of QD material

The choice of bright and colloidally stable QD is of essence for the development of an efficient FRET scheme. The QD brightness determines the photon output it can produce, thereby having a direct impact on the read-out sensitivity of the assay. Additionally, the QDs need to maintain high colloidal stability and resistance to degradation to ensure the robustness of the detection scheme under assay-relevant conditions. Finally, the use of relatively small nanoparticles is beneficial to ensure efficient FRET to an organic dye. The latter requirement stems from the widely accepted notion that Förster dipole-dipole formalism applies to the FRET pairs in which QD acts as a FRET donor with QD being treated as a point dipole with the exciton wavefunction positioned around the center of the nanocrystal.[103-105] Therefore, the distance between the dipoles of a QD and an organic FRET acceptor must be calculated from the center of a nanoparticle.

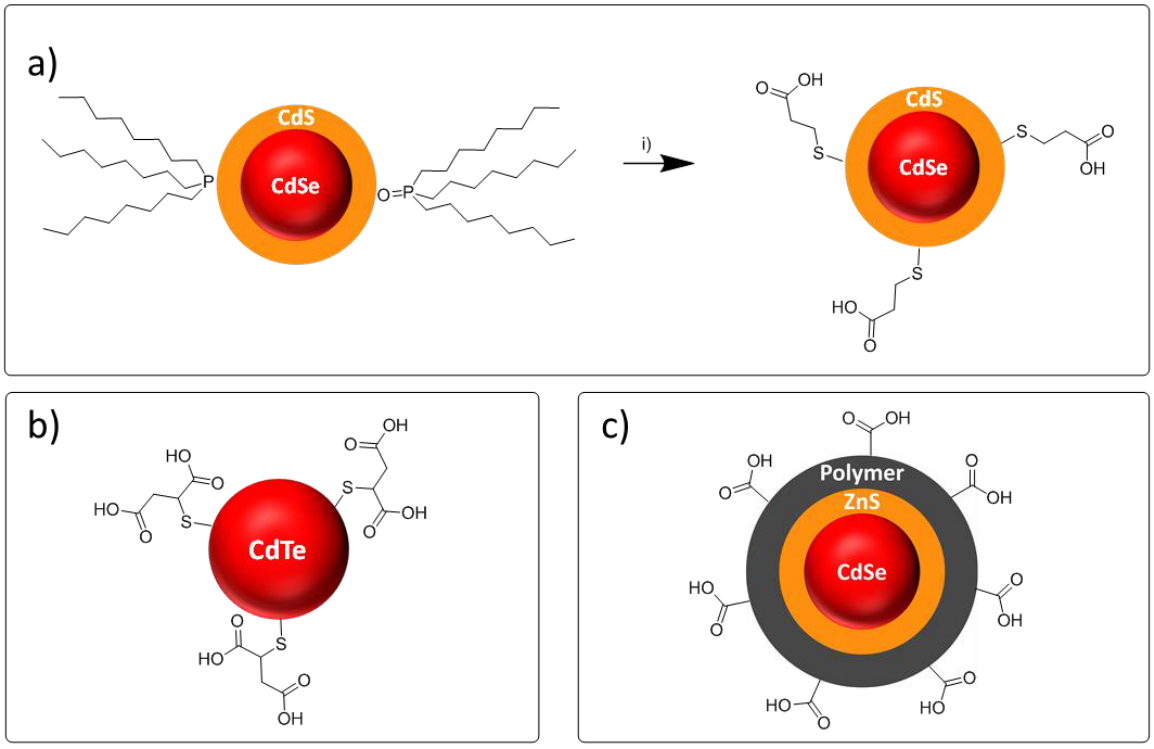

Scheme 4.1. Schematic presentation of three QD classes considered for the role of FRET donor. a) Phase transfer of TOP/TOPO passivated core/shell CdSe/CdS QDs into water via EDA-mediated phase transfer i) 1. EDA, $CHCl_3$, 2. MPA, H_2O. b) Commercial (core-only) CdTe QDs with mercaptosuccinic acid (MSA) surface ligands (CdTe-MSA). c) Commercial (core/shell) CdSe/ZnS QDs encapsulated in amphiphilic polymer (ITK605).

To select the optimal QD, three types of nanoparticles were evaluated: core/shell CdSe/CdS with a mercaptopropionic acid (MPA) cap obtained via transfer from an organic solvent using a literature-based protocol (*Scheme 4.1*a); commercial core-only CdTe QDs with mercaptosuccinic acid (MSA)

cap (*Scheme 4.1*b); and commercial core/shell CdSe/ZnS QDs encapsulated by an amphiphilic polymer (*Scheme 4.1*c). All these particles contained carboxylic acid surface groups that conferred the water solubility and provided the handle for bioconjugation.

Transfer of hydrophobic QDs into water via ligand exchange

The transfer of hydrophobic CdSe/CdS QDs into water through an ethylenediamine (EDA)-mediated phase transfer was performed based on the procedure described by Dai et al.,[106] adopted for CdSe/CdS QDs. The ligand exchange (*Figure 4.1*a) leads to a blue shift in the absorbance and emission of the original QDs (*Figure 4.1*b and c), which was attributed to the etching of a nanoparticle surface. Depending on the amount of MPA used for ligand exchange, the QY of the QDs drops to 22 - 34 % of the original QY of the QDs in hexane (*Figure 4.1*d). The QY is higher for increased MPA-to-QD ratios, in contrast to the results reported by Dai et al.,[106] who found such high excess of MPA to have a negative effect on the QY of the final nanoparticle. While stable in aqueous solution directly after transfer, the obtained conjugates exhibited low colloidal stability after the removal of excess ligand by precipitation with iso-propanol, which was evident by the rapid precipitation of the nanoparticles. This rendered them unsuitable for the intended bioconjugation. The colloidal instability of the obtained CdSe/CdS-MPA QDs combined with their poor QYs led me to exclude them from further studies and to focus on the commercial water soluble QDs instead.

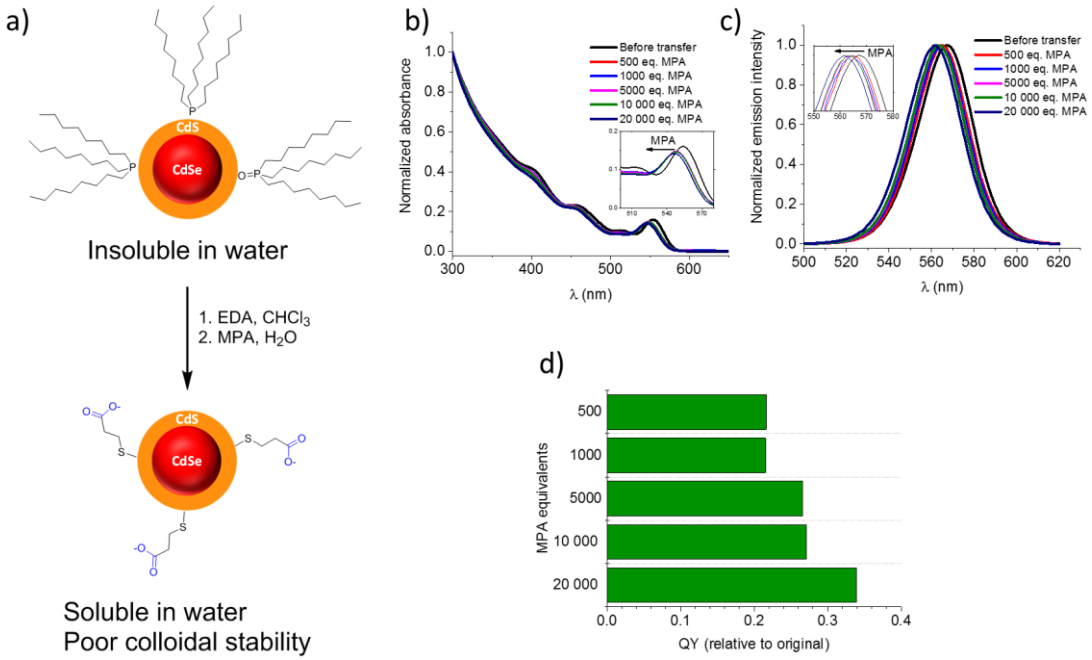

Figure 4.1. a) Schematic presentation of ethylenediamine (EDA)-mediated ligand exchange. Normalized absorption (b) and emission (c) spectra of QDs in hexane before phase transfer and after EDA-mediated phase transfer into water using different amounts of mercaptopropionic acid (MPA) for ligand exchange. d) Relative quantum yield of QDs transferred into water as a function of MPA excess used for the procedure.

Assessment of water soluble QDs as potential FRET donors

Two commercial water soluble QDs, namely, core-only CdTe QDs passivated with mercaptosuccinic acid (MSA) (CdTe-MSA) (PlasmaChem GmbH) and core/shell CdSe/ZnS QDs encapsulated by a polymer coating (ITK605) (ThermoFischer Scientific, product Qdot® 605 ITK™ carboxyl) were evaluated in terms of their spectroscopic features, applicability for FRET applications, and colloidal stability. The absorption and emission spectra of CdTe-MSA and ITK605 are presented in *Figure 4.2*. From the spectroscopic point of view, ITK605 is a better luminophore, since it exhibits a higher QY and molar extinction coefficient (*Figure 4.2* and *Table 4.1*) in comparison to CdTe-MSA. The brightness of ITK605 is 59 times higher than that of CdTe-MSA. In practical terms it means that one ITK605 nanocrystal can produce the same photon output as 59 CdTe-MSA nanocrystals, provided the excitation is performed under the same conditions at 435 nm. Moreover, the emission band of ITK605 is narrower and more symmetric compare to CdTe-MSA thereby minimizing the possibility of spectral cross-talk with FRET acceptor. The exceptional brightness of an ITK605 results from the presence of a ZnS shell and outer polymer coating, which protect the emissive core from the changes in microenvironment.

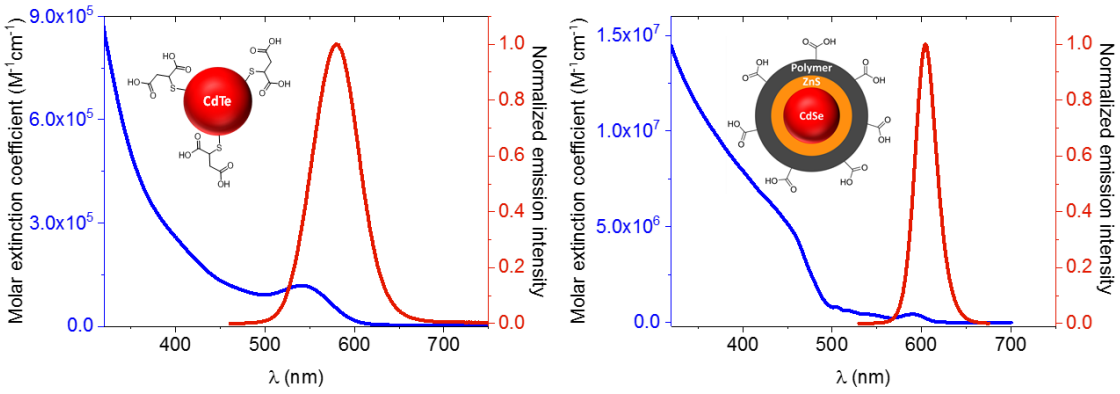

Figure 4.2 Absorbance and emission spectra of CdTe-MSA (left) and ITK605 (right). Absorbance spectra are presented as molar extinction coefficients to illustrate the difference in absorptivity between the two QD materials.

These inherent advantages of ITK605, however, come at the price of a larger overall diameter (*Table 4.1*), compared to core-only QDs. This feature can have a direct impact on the FRET efficiency between the QD and a FRET acceptor due to the increased distance between the dipoles of FRET partners. In this respect, the CdTe-MSA QDs are more advantageous.

Table 4.1 Comparison of spectroscopic features of CdTe-MSA and ITK605. λ_{em} designates the wavelength at the emission maximum, QY = quantum yield; B = $\varepsilon_{435} \cdot$ QY; FWHM = full width at half maximum of the emission band.

QD	ε_{435}, $M^{-1}cm^{-1}$	λ_{em}, nm	QY	B, $M^{-1}cm^{-1}$	FWHM, nm	$r_{core\ or\ core/shell}$, Å
CdTe-MSA	$1.61 \cdot 10^5$	579	0.50	$8.1 \cdot 10^4$	61	16
ITK605	$6.05 \cdot 10^6$	604	0.80	$4.8 \cdot 10^6$	28	53

To quantitively assess the compatibility of both QDs with the chosen FRET acceptor, Cy5, the Förster radii (R_0) of two FRET pairs were calculated. R_0 expressed in Å were calculated according to equation 1 (eq. 1)[107]:

$$R_o = 0.211(\kappa^2 \cdot n^{-4} \cdot QY_D \cdot J(\lambda))^{1/6} \quad \text{(eq. 1)}$$

Here, κ^2 is an orientation factor for randomly oriented transition dipoles, commonly assumed to be 2/3, n is the refractive index of water (1.33), QY_D the quantum yield of FRET donor, and $J(\lambda)$ the overlap integral between the donor´s emission and the acceptor´s absorption band, expressed in $M^{-1}cm^{-1}nm^4$, respectively. The overlap integral was calculated according to equation 2 (eq. 2).

$$J(\lambda) = \int_0^\infty F_D(\lambda)\, \varepsilon_A(\lambda)\lambda^4 d\lambda \quad \text{(eq. 2)}$$

Here, $F_D(\lambda)$ is the total emission intensity of the FRET donor normalized to unity, $\varepsilon_A(\lambda)$ is the wavelength-dependent molar extinction coefficient of FRET acceptor expressed in $M^{-1}cm^{-1}$, and λ is the wavelength in nm, respectively. The spectral overlap and calculated Förster parameters are presented in *Figure 4.3* and *Table 4.2*. Both FRET pairs exhibit a high spectral overlap and a large R_0, thereby emphasizing the benefits of such luminophores in the context of FRET-based detection system, with ITK605 providing the highest R_0 of 75 Å.

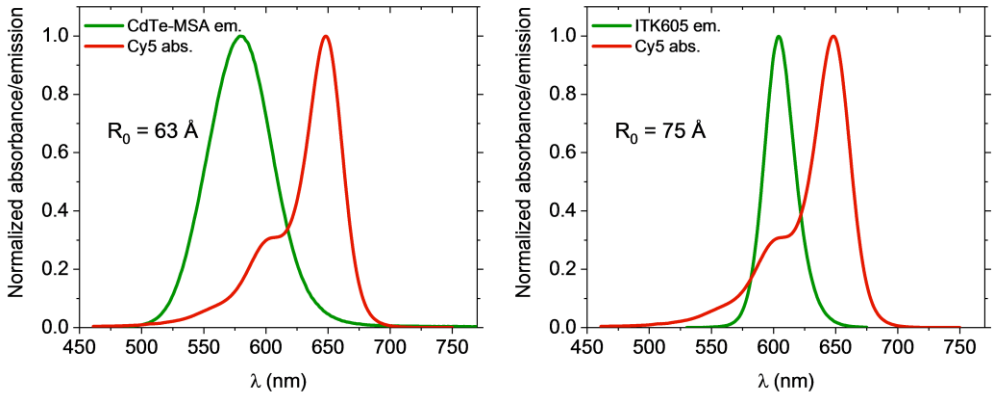

Figure 4.3. Spectral overlap between the emission bands of CdTe-MSA (left) and ITK605 (right) with the absorption spectrum of Cy5 dye (trisulfo-Cy5-azide, Jena Bioscience). R_0 is Förster radius.

Preliminary experiments with CdTe-MSA revealed that the stability of its conjugates is very limited at low nM concentrations (*Figure 9.16*) – a phenomenon that attributed to the dissociation of thiol ligands from the nanoparticle surface upon dilution. Combined with the brightness considerations discussed above, this observation led to the exclusion of CdTe-MSA from further studies. Thus, all subsequent experiments were performed using polymer-coated QDs. From this point on, the terms "ITK605" and "QD" are used interchangeably in the context of QD-based OTR.

Table 4.2 Overlap integrals and Förster radii for CdTe-MSA and ITK605 FRET donors in combination with Cy5 FRET acceptor. Jena Bioscience Cy5-azide was used as FRET acceptor for these calculations (Cy5).

FRET donor	FRET acceptor	$J(\lambda)$, $M^{-1}cm^{-1}nm^4$	R_0, Å
CdTe-MSA	Cy5	$6.33 \cdot 10^{15}$	63
ITK605	Cy5	$1.13 \cdot 10^{16}$	75

4.1.2 Selection of FRET acceptor

FRET efficiency strongly depends on the spectral overlap between the QD emission and the FRET acceptor absorption, as well as on the molar extinction coefficient of the latter. Additionally, it would be strongly beneficial to use a FRET acceptor with a high QY to enable the sensitive monitoring of energy transfer not only via the quenching of the QD photoluminescence but also through the sensitized emission of the FRET acceptor. Finally, the ideal dye must be highly water soluble to compensate for the inherent hydrophobicity of the PNA probes and prevent their aggregation. Three near-infrared NIR cyanine dyes were considered for the role of a FRET acceptor. Two symmetric dyes (Cy5(**4**) and **7**) (*Scheme 4.2*) were synthesized and compared to the commercially available asymmetric tri-sulfo Cy5 (FEWCy5). While asymmetric cyanine dyes have been used for the labeling of reactive oligonucleotides in the past,[108] symmetric dyes are less commonly utilized for the labeling of reactive oligonucleotides and PNA in particular. All dyes were designed to exhibit significant spectral overlap with the emission of the QD. Moreover, the fluorophores were equipped with either two or three sulfonate groups that were expected to render them sufficiently water soluble and therefore to alleviate the hydrophobicity of LDPNA following their bioconjugation.

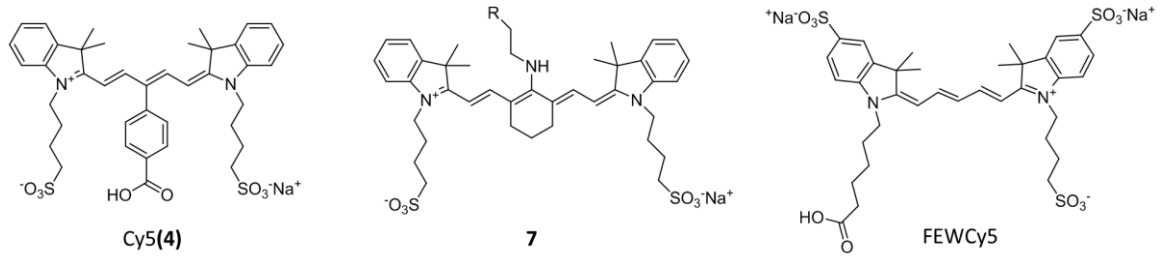

Scheme 4.2. Chemical structures of cyanine dyes considered for the role of FRET acceptor. Left: symmetric disulfo-Cy5 (Cy5(**4**)); middle: symmetric disulfo-Cy7 (**7**) R = Boc-NH-$((CH_2)_2$-O$)_2$-; right: asymmetric trisulfo-Cy5 (FEWCy5).

Synthesis and spectroscopic features of symmetric disulfo-Cy5

The decision to synthesize a symmetric Cy5 dye was driven by two goals. Firstly, it was expected that the synthesis based on just one indolium quaternary salt (**1**) (*Figure 4.4*) instead of two, as required to produce an asymmetric cyanine dye, would simplify the synthetic strategy. Secondly, provided that such symmetric dye withstands the conditions used for the cleavage of PNA from the solid phase, it could prove to be a cost-efficient alternative to the conventional NIR dyes used for PNA labeling. Synthesis of **1** was performed according to the reported procedure[109] with some modifications. Thus, 2,3,3-trimethylindolenine was alkylated with 1,4-butane sultone in the absence of solvent and purified by simple re-crystallization. Synthesis of the azatrimethine unit (**2**) was accomplished according to a modified procedure reported by Nanjunda et al.[110] Subsequently the polymethine condensation was performed to afford the Cy5 dye carrying a bromo substituent in the *meso*-position of the methine bridge (**3**). As a last step, Suzuki coupling was carried out to incorporate the carboxyl moiety into the dye molecule (Cy5(**4**)). Initial attempts to perform Suzuki coupling according to the procedure reported by Wycisk et al.[111] were unsuccessful and required optimization. The reaction was found to be efficient in the presence of Na_2CO_3, while only minimal conversion could be achieved in its absence, in contrast to the previous reports.[111]

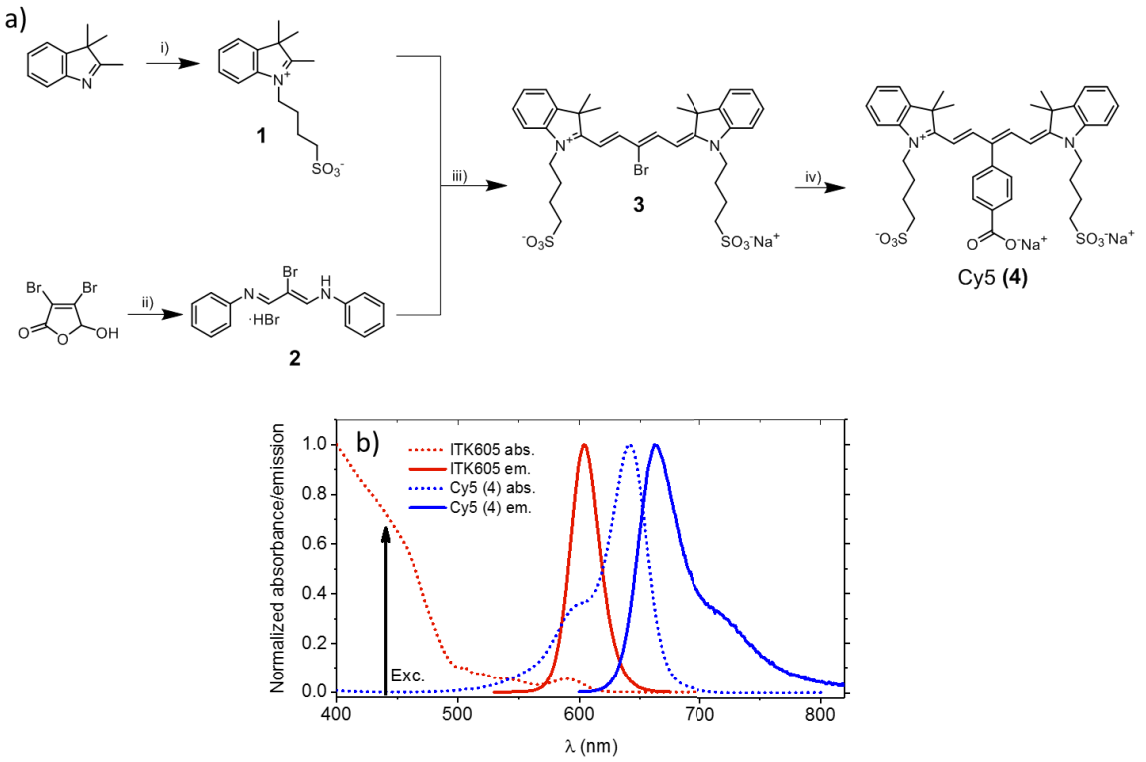

Figure 4.4. a) Synthesis of Cy5(**4**) i) 1,4-butane sultone, 39 %; ii) $PhNH_2$, EtOH, 29 %; iii) NaOAc, EtOH, 43 %; iv) 4-carboxyphenylboronic acid, $Pd(dppf)Cl_2$, Na_2CO_3, DMF/H_2O, 28 %. b) Juxtaposition of absorbance and emission bands of ITK605 and Cy5(**4**). The arrow indicates the wavelength at which the absorption of Cy5 is minimal, while the absorption of the QD is strong, thereby preventing the direct excitation of the acceptor in a FRET format.

While all synthetic procedures were successfully optimized and executed, the yields of reactions depicted in *Figure 4.4* were low or moderate. The reason for such results in the case of compounds **1** and **2** was the purification via re-crystallization since the products of reactions were not completely precipitated using the selected solvent mixtures and were partly retained in the liquid phase and discarded along with impurities. This decreased the overall reaction yields. Yet, the approach allowed for simple and fast purification that produced sufficient quantities of very pure compounds. The yields of 43 % and 28 % during the synthesis of **3** and Cy5(**4**), respectively, were caused by the incomplete conversion of starting materials and the formation of side products. The latter process was likely due to the accelerated degradation of cyanine dyes at elevated temperatures used for the synthesis.

As can be seen in *Figure 4.4*b, the absorption of Cy5(**4**) overlaps with the emission of ITK605 to a significant extent, while the spectral cross-talk between the respective emission bands is low. Additionally, the excitation of QD can be performed at a wavelength where Cy5 absorbs only negligibly, thereby excluding the direct excitation of the FRET acceptor. Furthermore, the dye was stable to the treatment with TFA – an important requirement for the envisioned conjugation to PNA on the solid phase.

Synthesis and spectroscopic features of symmetric disullfo-Cy7 (7)

The synthesis of symmetric cyanine dyes not only allows to simplify the procedure of dye fabrication but also to adjust the spectroscopic features of the dye by e.g., changing the substitution pattern in the *meso*-position of the polymethine bridge. It has been shown that the substitution of the *meso*-chlorine atom in the heptamethine chain of Cy7 dye with an amino group significantly alters the spectroscopic features of Cy7, resulting in blue-shifted absorbance and high Stokers shift due to the donation of nitrogen lone pair to the polymethine system.[112-113] The synthesis of a chloro-substituted methine bridge (**5**) was accomplished starting with cyclohexanone using the Vilsmeier-Haack reaction similar to the reported procedures.[114] Next, the condensation with **1** was performed to afford a *meso*-Cl-substituted Cy7 (**6**) based on the protocol optimized for the synthesis of compound **3**. Finally, the substitution of the chlorine atom was accomplished by using a bifunctional ethylene glycol-based linker affording compound **7**. The synthesis and spectroscopic features of the obtained dye are presented in *Figure 4.5*. The moderate yields of the reactions depicted in *Figure 4.5* were caused by the phenomena, which were similar to the once observed during the synthesis of Cy5(**4**).

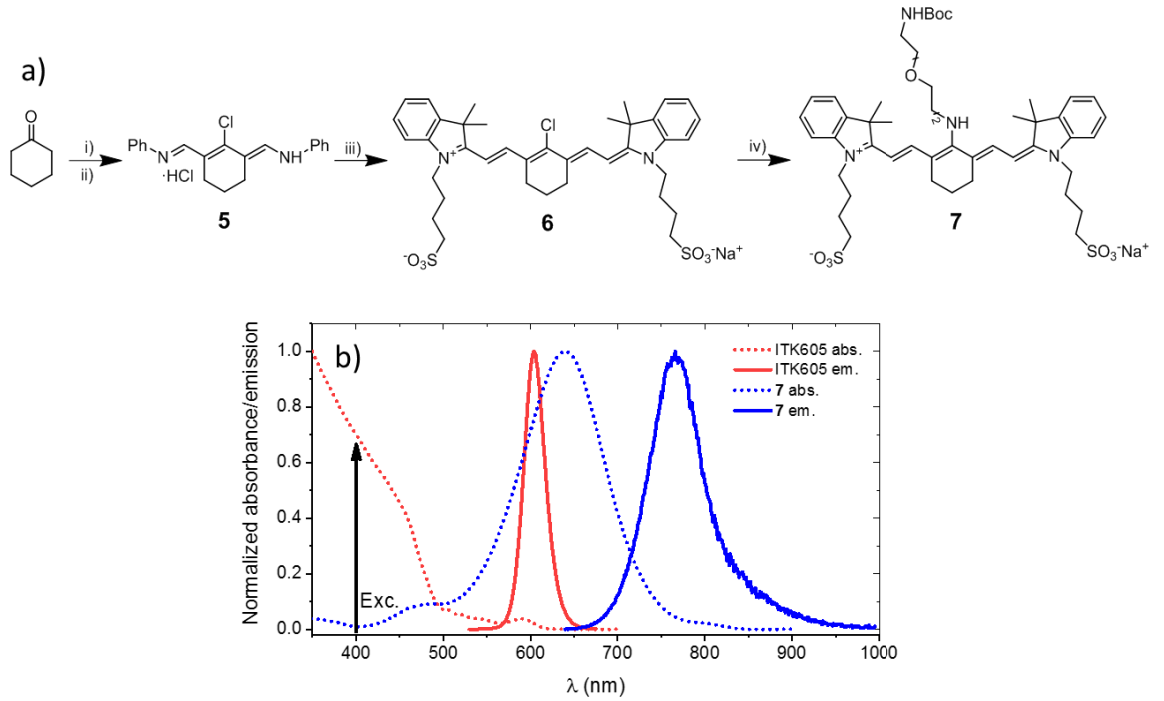

Figure 4.5 a) Synthesis of symmetric disulfo-Cy7 (compound **7**). i) $POCl_3$, DMF; ii) $PhNH_2$, EtOH, H_2O/HCl, 24%; iii) **1**, NaOAc, EtOH, 23 %; iv) Boc-DOOA, DIPEA, DMF.* b) Juxtaposition of absorbance and emission bands of ITK605 and **7**. The arrow indicates the wavelength at which the absorption of Cy7 is minimal, while the absorption of the QD is strong. *The reaction yield was not estimated due to the rapid degradation of the dye. DOOA = 3,6-dioxa-8-octaneamine.

The spectroscopic features of **7** are typical of those of a charge transfer dye with a broad, absorption band and high Stokes shift, thereby offering a very high degree of spectral overlap with ITK605, while providing almost no spectral cross-talk between the emission bands of the luminophores. The Dye **7** was, however, very susceptible to oxidation by air. In fact, the degradation was so rapid that it started to occur during the purification with reverse phase chromatography. Additionally, the dye is extremely unstable to treatment with TFA even in the presence of scavengers (thioanisole and water), thereby limiting its use for the solid phase synthesis of PNA probes. Due to these severe drawbacks, dye **7** was excluded from further studies.

Spectroscopic features of asymmetric trisulfo-Cy5

Commercially available Cy5 (FEWCy5) (*Figure 4.6*) was compared with the synthesized symmetric Cy5(**4**) in terms of spectroscopic features (*Table 4.3*). The spectral positions of absorption and emission bands of the two dyes are similar, with Cy5(**4**) having slightly blue-shifted bands, most likely due to the aromatic substituent in the polymethine chain. The molar absorption coefficient of FEWCy5 is higher than that of Cy5(**4**). This translates into an increased overlap integral and Förster radius for the ITK605-FEWCy5 FRET pair. However, in the presence of multiple dyes on the surface of a QD, this difference is expected to play only a minor role.

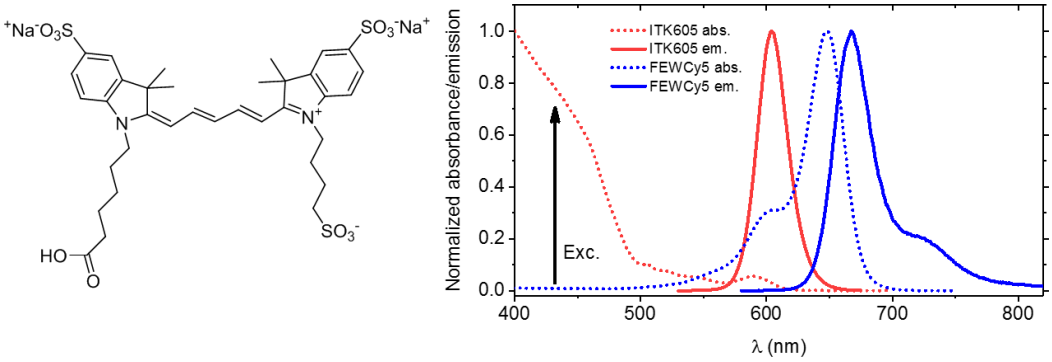

Figure 4.6. Chemical structure of FEWCy5 (left) and juxtaposition of absorption and emission bands of ITK605 and FEWCy5 (right). The arrow indicates the wavelength at which the absorption of Cy5 is minimal, while the absorption of the QD is strong.

The QY of FEWCy5 is substantially higher than that of Cy5(**4**). However, the QYs of these dyes could be affected by bioconjugation, which has been shown to impact the QYs of cyanine dyes in a biomolecule-specific manner.[115-116] Therefore, the dyes were conjugated to the LAPNA and their spectroscopic features were examined. In addition, the hydrophobicity of the respective conjugates was compared to identify the least hydrophobic candidate.

Table 4.3 Comparison of the spectroscopic properties of Cy5(**4**) and FEWCy5 and their compatibility for FRET applications with ITK605 as FRET donor.

Dye	λ_{abs}*	λ_{em}*	ε, $M^{-1}cm^{-1}$**	QY***	J(λ), $M^{-1}cm^{-1}nm^4$****	R_0, Å****
Cy5(4)	642	662	101 000	0.09	$5.81 \cdot 10^{15}$	67
FEWCy5	648	667	251 000	0.32	$1.14 \cdot 10^{16}$	75

*maxima of absorption and emission bands are shown; **molar absorption coefficient at the maximum of the absorption band; ***QYs in phosphate buffer were measured relatively using the dye Oxazine1 (QY = 0.15 in ethanol[117]) as a reference; ****overlap integral and Förster radius with ITK605 as FRET donor.

Synthesis and properties of PNA conjugates of FEWCy5 and Cy5(4)

To evaluate the hydrophobicity and fluorescence features of the PNA conjugates with Cy5(**4**) and FEWCy5, both dyes were conjugated to the LAPNA probe on a solid phase to synthetically produce the product of OTR (*Scheme 4.3*). Dye Cy5(**4**) was either conjugated via a Gly junction (Cy5(**4**)-Gly-PNAa) or via a short diethylene glycol-based linker and a Gly unit (Cy5(**4**)-AEEA-Gly-PNAa). The incorporation of AEEA into the PNA conjugate was expected to improve the solubility and decrease potential aggregation of the PNA probes. FEWCy5 was coupled to the LAPNA via a Gly junction only (FEWCy5-Gly-PNAa).

As a first indication of the different hydrophobicity of the three PNA-Cy5 conjugates, the differences in retention time during RP-UPLC was used (*Figure 4.7*a). The shortest retention time was observed for FEWCy5-Gly-PNAa, indicating its least hydrophobic nature, compared to the other two conjugates. Contrary to the original hypothesis, the incorporation of the diethylene glycol linker did

not have a substantial effect on the retention time of the Cy5(**4**)-labeled PNAa. Additionally, all Cy5-labeled PNAa conjugates aggregated in solution significantly stronger than the respective free dyes, which was evident by the formation of H-type dimers revealed by their absorption spectra (*Figure 9.17*).

Next, the QYs of the conjugates were measured to assess the impact of bioconjugation on the spectroscopic features of these Cy5 dyes. As shown in *Figure 4.7*b, the QYs of PNA conjugates are higher than those of the free dyes, with FEWCy5-Gly-PNAa exhibiting the greatest QY of 36 %.

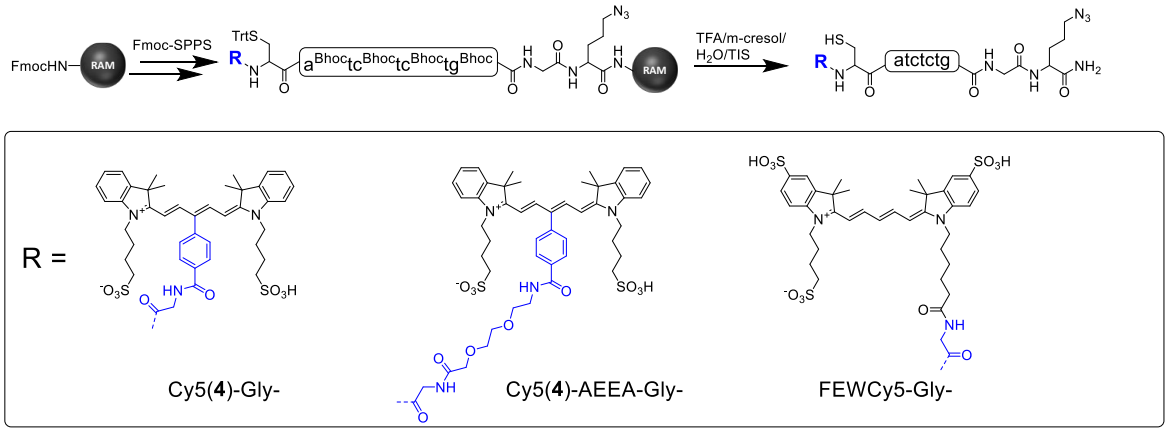

Scheme 4.3. Schematic presentation of SPPS synthesis (top) and chemical structures (bottom) of PNAa labeled with either Cy5(**4**) or FEWCy5. These conjugates are synthetically produced products of envisioned OTR and were prepared to assess the spectroscopic properties and hydrophilicity of PNA-conjugated dyes.

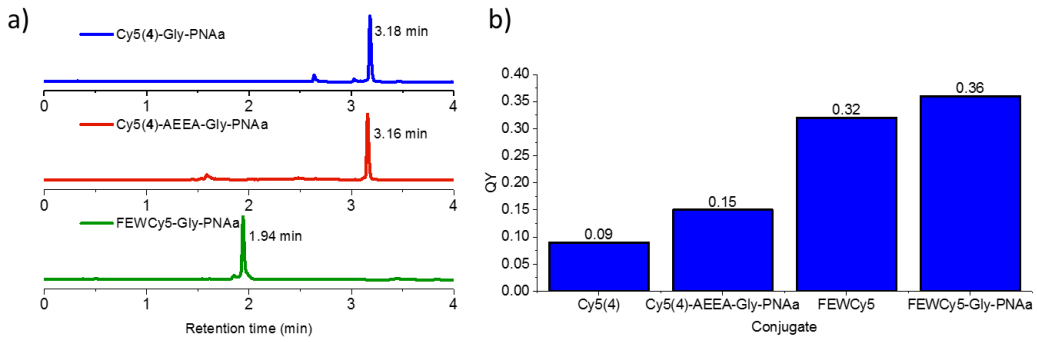

Figure 4.7 Retention times of three different PNAa-Cy5 conjugates (a) and quantum yields of the Cy5 dyes and their conjugates (b). *Cy5(**4**)-Gly-PNAa exhibited strong aggregation in solution at the concentrations required for precise measurements of optical density (Figure 9.17a), therefore its QY was not measured.

Despite the advantages of Cy5(**4**), such as simple synthesis, stability to TFA, and moderate brightness, the obtained results clearly indicate that the use of FEWCy5 as FRET acceptor is more beneficial from both the spectroscopic point of view and the considerations of hydrophilicity. Therefore, FEWCy5 was subsequently used for the synthesis of LDPNA probes and QD-based OTR. In the following, the FEWCy5 is referred to as Cy5 and it will be used for the synthesis of all LDPNA probes in the subsequent sections.

4.2 Synthesis of PNA Probes and their Conjugation to Fluorescent Labels

4.2.1 Synthesis of label acceptor PNA (LAPNA) and its immobilization on a QD

Immobilization of a cysteine-containing LAPNA on a QD had to be performed in a biorthogonal fashion to keep the nucleophilic functional groups of the LAPNA intact. Azide-alkyne cycloaddition was envisioned to be a suitable method for this purpose. It was decided to incorporate the azido functionality at the C-terminus of a PNA oligomer during its assembly on the solid support, since azides withstand the conditions used for Fmoc-based SPPS. This provided the means to synthesize the PNA acceptor probe in a straightforward manner without the need for post modifications.

It has been reported that immobilization of DNA probes on the gold[118] and iron oxide[119] nanoparticles can be accomplished using Cu(I)-catalyzed cycloaddition that exploits linear alkynes. However, the copper(I) catalyst has been shown to irreversibly quench the emission of semiconductor QDs,[120] making this strategy impractical for the bioconjugation of the QDs. In contrast to linear alkynes, strained cyclooctynes (COs) react with azides in the absence of catalyst under mild conditions due to their ring strain, thereby eliminating the need to use Cu(I) species, which are damaging for QDs. Bicyclononyne (BCN) was chosen due to i) its enhanced, compared to plain cyclooctyne, reactivity brought about by cyclopropane fusion,[121] and ii) its relatively high hydrophilicity in comparison to e.g., dibenzocyclooctynes.

To introduce the BCN functionality onto the surface of carboxyl-containing QD, a short bifunctional linker BCN-NH_2 (*Scheme 4.4*) was used. This enabled the carbodiimide-mediated formation of amide bonds with the surface carboxyl groups of the QD. The reaction between the QD-carboxyl and BCN-NH_2 proceeded very rapidly in borate buffer (pH 7.4). The purification of obtained conjugates (referred to as QD-BCN with subscripts designating four different conditions) was accomplished using a combination of size exclusion chromatography (SEC) and ultrafiltration. By changing the molar excess of BCN-NH_2, four conjugates with different BCN labeling densities were prepared and in a next step conjugated to LAPNA, thus permitting the fine-tuning of the number of PNA molecules on a nanoparticle.

SPPS of label acceptor PNA probes was accomplished according to Fmoc strategy, as presented in *Scheme 2.11* and described in detail in the experimental section for every LAPNA. However, some critical points are mentioned here since they were not trivial and were established experimentally within the course of this work.

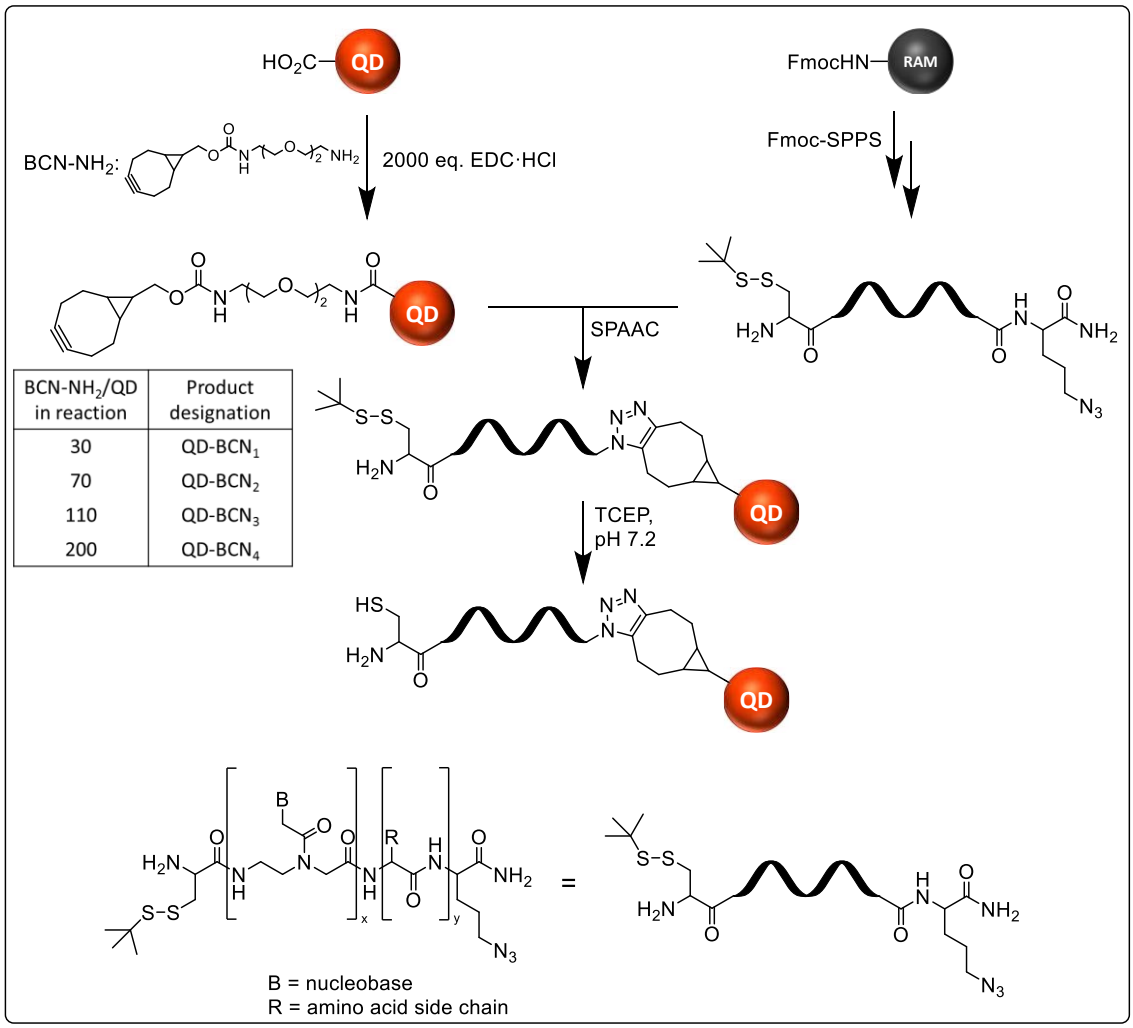

BCN-NH_2/QD in reaction	Product designation
30	QD-BCN_1
70	QD-BCN_2
110	QD-BCN_3
200	QD-BCN_4

Scheme 4.4. Two-step approach for immobilization of PNA on a nanoparticle. By varying the concentration of BCN-NH_2 during the EDC-mediated amide bond formation on the QD surface, four QD-BCN conjugates with varied BCN loading were prepared. These couplings were performed in 20 mM borate buffer (pH 7.4), using 2000 eq. of EDC·HCl, and a specified molar excess of BCN-NH_2 (as detailed in the scheme). Strain-promoted azide-alkyne cycloaddition (SPAAC) was performed in MOPS buffer (50 mM, pH 7.2). Deprotection of StBu group was performed using the solution of 15 mM TCEP in MOPS buffer (50 mM, pH 7.2). Adopted with permission from[101]. Copyright 2018 American Chemical Society.

Originally, LAPNA was synthesized using a Trt-protected cysteine side chain (*Figure 4.8*a). This protecting group is acid labile and is removed during the total cleavage of PNA with TFA. It is generally recommended to perform the TFA-mediated cleavage of thiol-containing peptides in the presence of thiol scavengers, such as ethanedithiol (EDT) or dithiothreitol (DTT)[122] which quench the reactive carbocations released during the deprotection of amino acid side chains and exocyclic amino groups of the PNA nucleobases. However, such scavengers have been shown to reduce azides to amines,[123] and should be, thus, avoided. Therefore, I decided to use a thiol-free cleavage cocktail that consisted of TFA/TIS/H_2O. This was envisioned to scavenge the carbocations while keeping the azido moieties preserved. This mixture was used for the cleavage of the PNA probe with Trt-protected Cys residue (PNAd0). Unfortunately, the scavenging of carbocations by water and TIS was not efficient. This exposed the deprotected thiol groups of PNA to the reaction with benzhydryl cations, released during the deprotection of exocyclic amino groups of PNA nucleobases, thereby

producing a substantial quantity of undesired benzhydryl adduct, as is illustrated in *Figure 4.8*b. Furthermore, the UPLC retention time of PNAd0 was very similar to those of truncated and deletion sequences. This was envisioned to complicate the HPLC purification.

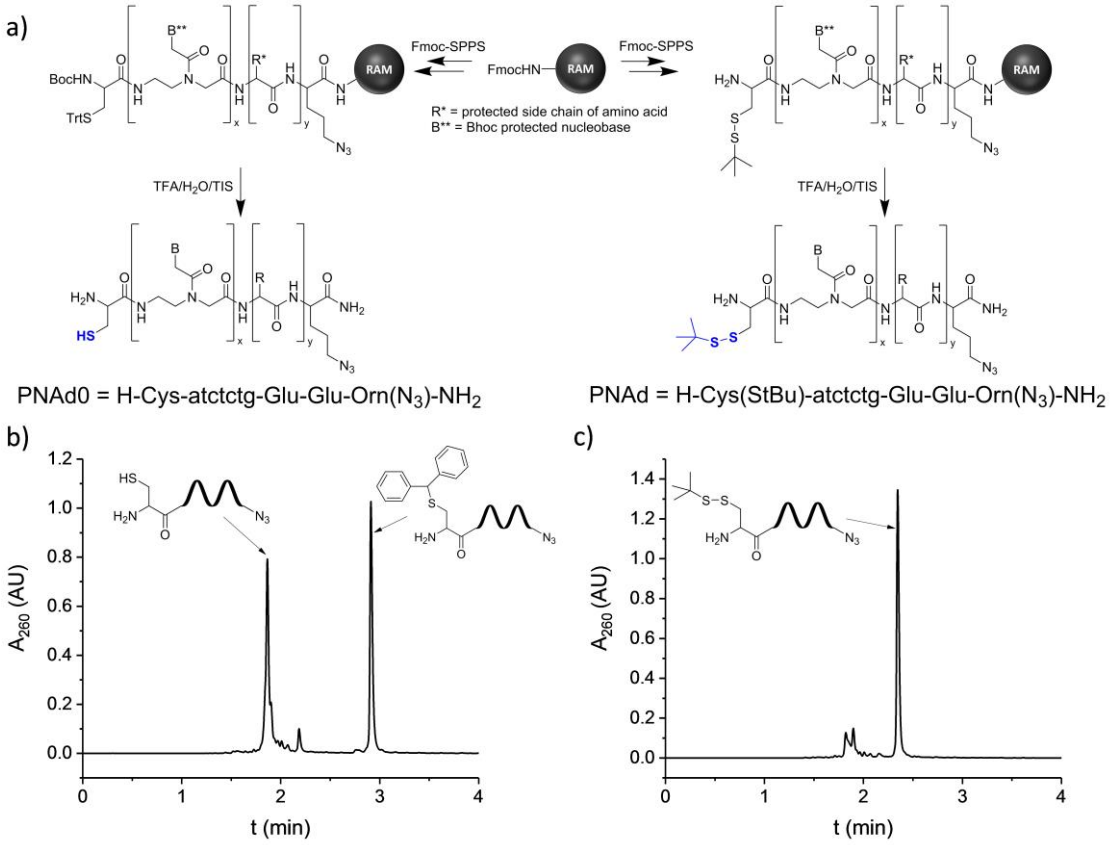

Figure 4.8. (a) Schematic presentation of two LAPNA synthetic routes. Left: synthesis of LAPNA using the Boc-Cys(Trt)-OH building block. Right: synthesis of LAPNA using Fmoc-Cys(StBu)-OH building block. (b) UPLC trace of the crude product of PNAd0 synthesis. UPLC gradient: 3 to 40 % of solvent B in 4 min. t_R(PNAd0) = 1.87 min. (c) UPLC trace of the crude product of PNAd synthesis. UPLC gradient: 3 to 40 % of solvent B in 4 min. t_R(PNAd) = 2.35 min. ESI-MS analysis of the crude products is provided in the appendix (Figure 9.18 for PNAd0, and Figure 9.19 for PNAd). Following the HPLC purification, PNAd was obtained in an 11 % yield. Incorporation of Cys with TFA-stable StBu-protecting group allows for the cleavage of the resulting PNA conjugate using non-toxic thiol-free cleavage cocktail. Additionally, the presence of StBu increases the hydrophobicity of the PNA molecule and simplifies its HPLC purification.

I assumed that the introduction of an N-terminal cysteine using Fmoc-Cys(StBu)-OH building block, which contains a TFA-resistant side chain protecting group, would enable a successful cleavage of PNA from the solid support even in the presence of low concentrations of non-toxic scavengers (TIS and H_2O). Protection of thiol functionality in the form of a disulfide prevents its nucleophilic attack of carbocations in the total cleavage/deprotection. The crude product of such synthesis (*Figure 4.8*c) contains low amounts of side products and illustrates the efficiency of the selected protocol. Additionally, the introduction of cysteine functionality with the StBu-protecting group enhanced the hydrophobicity of the product compared to the truncates and deletion sequences, thereby simplifying the HPLC purification.

The UPLC trace and ESI-MS spectrum of HPLC-purified PNAd is shown in *Figure 9.7* and confirms the high purity of the obtained product. The synthetic strategy was subsequently used for the SPPS of other LAPNAs affording them in 4 – 11 % yields, depending on the PNA sequence. These low yields were likely due to the losses of products during the purification via HPLC, rather than to the synthesis conditions. For example, the SPPS of PNAd produced relatively low amounts of side products, as illustrated in *Figure 4.8*c, yet the reaction yield was merely 11 % following the chromatographic purification. Nevertheless, the produced quantities were sufficient for the synthesis of QD-LAPNA conjugates.

In terms of azide-alkyne cycloaddition, coupling of LAPNA with an StBu-protected Cys residue is beneficial, since it helps to avoid the possible thiol-yne addition, which has been reported to be a major side reaction during SPAAC couplings.[124] Following the conjugation of LAPNA to the QD, which proceeds through the formation of a triazole (*Scheme 4.4*), and subsequent purification via SEC, the StBu group can be elegantly removed by the reduction with TCEP in aqueous buffer, and used for downstream applications.

4.2.2 Quantification of QD-bound functionalities *via* UV-Vis and fluorescence spectroscopy

4.2.2.1 Quantification of BCN/QD labeling density

Estimation of the labeling densities of four QD-BCN conjugates was performed by incubating the functional nanoparticles with a high excess of azide-labeled Cy5 (*Figure 4.9*a), followed by purification and spectroscopic characterization (*Figure 4.9*b and c). Absorption spectra (*Figure 4.9*b) of QD-BCN-Cy5 conjugates corroborated the reactivity of nanoparticle-immobilized BCN groups. The increase in the intensity of the vibrionic shoulder in the absorption spectrum of Cy5 indicated the formation of H-aggregates among surface-bound Cy5 molecules for all systems except QD-BCN$_1$-Cy5, which had the lowest Cy5 labeling density. In order not to underestimate the number of QD-bound Cy5 molecules, integral absorbance coefficients were used for the calculations of Cy5 labeling densities of QD-BCN-Cy5 conjugates (except QD-BCN$_1$-Cy5) according to the procedure described below. The results of these calculations are presented in *Table 4.4*.

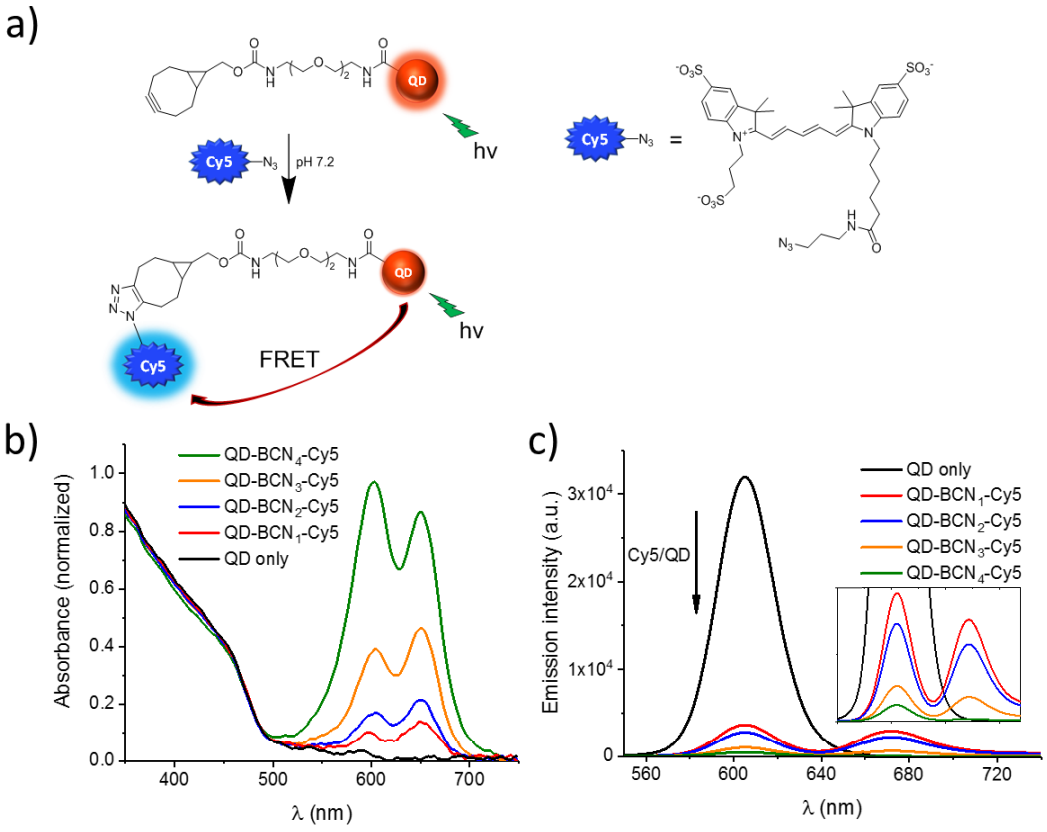

Figure 4.9. Quantification of QD-immobilized bicyclononyne (BCN) groups obtained after immobilization reactions at varied amine/carboxylic acid ratios. a) Principle of quantification of BCN labeling density using conjugation with Cy5-azide. After the completion of SPAAC between the QD-BCN and Cy5-azide all conjugates were purified by SEC, as described in experimental section to ensure that the excess dye is removed after the completion of reaction. Normalized UV-Vis (b) and raw photoluminescence (c) spectra of QD-BCN-Cy5 conjugates with 4 different labeling densities. The formation of H-type dimers with increasing Cy5 labeling density results in the quenching of Cy5 emission despite enhanced FRET. Adopted with permission from[101]. Copyright 2018 American Chemical Society.

Based on the procedure previously derived for the optical determination of dye labeling density,[125] the number of QD-bound Cy5 molecules was calculated using the Equations 3-7 (eqs. 3-7). The ratio between Cy5 and QD was calculated according to equation 3:

$$Cy5/QD = C_{Cy5}/C_{QD} \quad \text{(eq. 3)}$$

where C_{Cy5} and C_{QD} are the concentrations of Cy5 and QD, respectively. The concentration of QD was calculated according to equation 4 (eq. 4):

$$C_{QD} = \frac{A_{349}}{\varepsilon_{349} \cdot l} \quad \text{(eq. 4)}$$

Here, A_{349} is the absorbance at 349 nm, ε_{349} the molar extinction coefficient at 349 nm, based on the information obtained from QD manufacturer ($1.14 \cdot 10^7$ $M^{-1}cm^{-1}$), and l the optical pathway, respectively. The integral absorbance of Cy5 was calculated according to equation 5 (eq. 5):

$$F_{Cy5} = \int_{499}^{700} A(\lambda)\, d\lambda \quad \text{(eq. 5)}$$

Here, $A(\lambda)$ is the absorbance of Cy5, corrected for the absorbance of the QD. To correlate the absorbance of Cy5 at its absorption maximum with the integral absorbance, the coefficient K was introduced (eq. 6).

$$K = C_{Cy5mon.} \cdot \varepsilon_{Cy5}(\lambda_{max}) \cdot l / F_{Cy5mon.} \quad \text{(eq. 6)}$$

Here, C_{Cy5mon} is the concentration of monomeric Cy5, $\varepsilon_{Cy5}(\lambda_{max})$ is the molar absorption coefficient at the absorption maximum ($2.51 \cdot 10^5$ $M^{-1}cm^{-1}$), and $F_{Cy5mon.}$ the integral absorbance of monomeric Cy5 calculated according to eq. 5. Finally, the concentration of Cy5 was calculated using equation 7:

$$C_{Cy5} = K \cdot \frac{F_{Cy5}}{\varepsilon_{Cy5}(\lambda_{max}) \cdot l} \quad \text{(eq. 7)}$$

The calculations of Cy5/QD labeling densities revealed that four conjugates with the Cy5/QD ratios in the range of 7 to 90 were obtained by reacting the Cy5-azide with the QD-BCN nanoconjugates (*Table 4.4*). Of note, the conditions used for the preparation of conjugate QD-BCN_4 allow the conversion of most of the available surface carboxyl groups into the respective amides. This stems from the fact that the original content of carboxyl groups on the surface of ITK605 QDs is in the range of 80-100 (according to the information provided by the manufacturer: Thermo Fischer Scientific).

Table 4.4. Photometric characterization of four QD-BCN-Cy5 conjugates with different labeling densities. Overlap integrals ($J(\lambda)$) and Förster radii (R_0) were calculated based on UV-Vis spectra of the purified conjugates; FRET efficiencies ($E(FRET)$) were calculated based on luminescence spectra according to equation 8 (eq. 8); radii of QD-BCN-Cy5 (r_{QD}) were calculated according to eq. 10.

Conjugate	Cy5/QD (UV-Vis)	$J(\lambda)$, $M^{-1}cm^{-1}nm^4$	R_0, Å	E(FRET)	r_{QD}, Å*
QD-BCN$_1$-Cy5	7	$1.16 \cdot 10^{16}$	74.7	0.89	73
QD-BCN$_2$-Cy5	15	$1.25 \cdot 10^{16}$	75.7	0.91	81
QD-BCN$_3$-Cy5	37	$1.40 \cdot 10^{16}$	77.2	0.97	79
QD-BCN$_4$-Cy5	90	$1.49 \cdot 10^{16}$	77.9	0.99	77

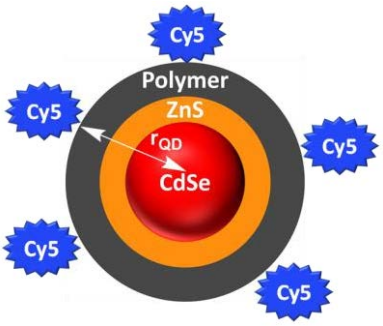

Scheme 4.5. Schematic presentation of the calculation of QD radius using the spectroscopic data listed in Table 4.4. The QD radius (r_{QD}) is assumed to be equal to the average distance between the center of the QD and surface immobilized Cy5 dyes. The objects are drawn not to scale and are only used for illustrative purposes.

Photoluminescence spectra of QD-BCN-Cy5 conjugates illustrated the strong quenching of QD emission due to the energy transfer to surface-bound acceptor dyes, as was expected (*Figure 4.9*c). The sensitized emission of Cy5, however, did not rise with increased FRET, which was caused by the formation of non-emissive H-aggregates on the QD surface. It is reasonable to assume that at high Cy5/QD ratios the diminution of sensitized Cy5 emission is also affected by homo-FRET between the surface-immobilized dye molecules. This photoluminescence data was subsequently utilized to evaluate the average separation distance between the center of the QD and Cy5. This was accomplished by using the FRET efficiency calculated according to eq. 8:[107]

$$E(FRET) = 1 - \frac{F_{DA}}{F_D} \qquad \text{(eq. 8)}$$

where $E(FRET)$ is FRET efficiency, F_{DA} is QD luminescence in the presence of Cy5, and F_D is QD emission in the absence of Cy5. Then, based upon the formula for FRET efficiency in the presence of multiple acceptors (eq. 9):

$$E(FRET) = \frac{nR_0^6}{nR_0^6 + r^6} \qquad \text{(eq. 9)}$$

the formula for the calculation of the average distance separating the center of the QD and Cy5 molecules was derived (eq. 10):

$$r = R_0 \sqrt[6]{\frac{n(1-E)}{E}} \qquad \text{(eq. 10)}$$

Here, *n* is the number of FRET acceptors and *r* the separation distance between the center of the QD and the FRET acceptor. The number of acceptors was estimated from absorption measurements and the FRET efficiencies were calculated from the fluorescence spectra of the conjugates (*Table 4.4*) according to eq. 8. Based on these parameters, the separation distance between the center of the QD and surface-bound Cy5 was calculated for QD-BCN-Cy5 conjugates and averaged to estimate the radius of the QD. QD-BCN$_1$-Cy5 was excluded from the calculation of the average since the respective *r* value was significantly different from the other three measurements and affected the precision of the averaging procedure. The obtained value $r_{av.}$ = 78.8 Å was used for the calculations described below.

4.2.2.2 Quantification of PNA/QD ratio.

To assess the availability of the QD-immobilized PNA probes for hybridization with RNA the QD-conjugate was incubated with complementary Cy5-labeled RNA (RNA-Cy5c). It was envisioned that formation of PNA/RNA duplexes on the nanoparticle surface would lead to proximity-induced FRET between the QD and Cy5. To verify the Watson-Crick nature of interactions between the PNA and RNA, control experiments with noncomplementary Cy5-modified RNA were performed (RNA-Cy5nc). RNA-Cy5nc was expected to not interact with the QD-PNA and to not induce FRET.

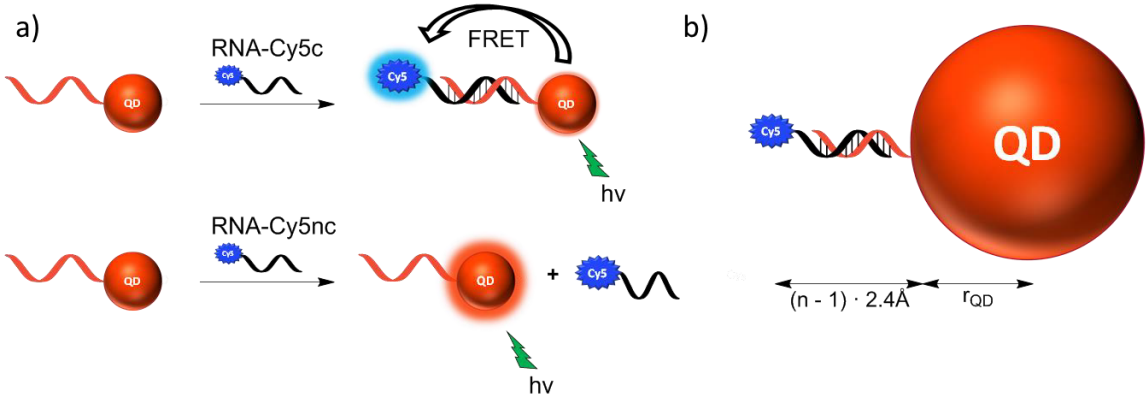

Scheme 4.6. Principle of quantifying the PNA labeling density via FRET. a) Confirmation of specific Watson-Crick base pairing between the QD-bound PNA and complementary RNA using RNA-Cy5c (complementary strand) and RNA-Cy5nc (noncomplementary strand used as positive control); b) calculation of the distance between the center of a nanoparticle and Cy5 for a PNA/RNA-Cy5c duplex formed on the QD; n designates the number of nucleobases in the PNA; the rise per base pair of 2.4 Å is a value taken from the literature.[126] The as-calculated distance was used to quantify the PNA/QD ratio using eq. 11. Adopted with permission from[101]. Copyright 2018 American Chemical Society.

The number of FRET acceptors was calculated from luminescence measurements according to equation 11 (eq. 11).

$$n = \frac{Er^6}{R_0^6(1-E)} \qquad \text{(eq. 11)}$$

The distance between the center of the QD and Cy5 was calculated as a sum of the QD radius (the calculation of which was described above) and the contribution of PNA/RNA-Cy5c duplex to the overall size of the conjugate (*Scheme 4.6*). It has been shown via NMR experiments that PNA/RNA duplexes adopt a conformation similar to that of an A-RNA duplex,[127] with a very low rise per base pair value of 2.4 Å.[126] The latter parameter was used to estimate the length of the PNA/RNA duplex and subsequently used to calculate the number of PNA per QD according to eq. 11. The R_0 for the pair ITK605/RNA-Cy5c was calculated to be 76.6 Å (*Figure 9.20* and *Table 9.1*).

Table 4.5. PNA sequences used for the preparation of QD-PNA conjugates, and Cy5-labeled RNA sequences used for the surface group analysis of nanobioconjugates. PNA/QD designates the labeling density of PNA acceptor probes on the QD. *Due to the high degree of nonspecific interactions between the QD-immobilized PNAa and Cy5-labeled RNA, the calculated value of 9 PNA/QD may not accurately reflect the true labeling density and should be treated as an estimate.

LAPNA sequences (N→C terminus)	**Designation**	**PNA/QD**
H-Cys-atctctg-Gly-Orn(N_3)-NH_2	PNAa	9*
H-Cys(StBu)-atctctg-Glu-Glu-Orn(N_3)-NH_2	PNAd	3, 16
H-Cys(StBu)-ggatctct-Glu-Glu-Orn(N_3)-NH_2	PNAg	5
H-Cys(StBu)-tctctggtctt-Glu-Glu-Orn(N_3)-NH_2	PNAj	4, 11, 33, 59
RNA sequences (5'→3')		
GGAAAGACCAGAGAUC – Cyanine 5	RNA-Cy5c	
GACACAAUAGGCGAAG – Cyanine 5	RNA-Cy5nc	

Within the course of this work, a series of QD-PNA conjugates (*Table 4.5*) was prepared to optimize the performance of OTR, as will be described in detail in the following sections. These nanobioconjugates contained LAPNA with varied nucleobase and amino acid composition and had different labeling densities. The kinetics of hybridization between the QD-PNA conjugates and RNA-Cy5c as well as the time course of nonspecific adsorption of RNA-Cy5nc on the nanoparticle surface are shown in *Figure 4.10* for conjugates that contained 7- and 8-mer PNA probes.

The collected data corroborated the presence of LAPNA on the nanoparticle as was signaled by the substantial quenching of QD emission upon incubation of QD-PNA conjugates with RNA-Cy5c. Noteworthy, the presence of RNA-Cy5nc also led to the quenching of QD emission. This was ascribed to nonspecific interactions between the nanobioconjugates and RNA-Cy5nc. As illustrated in *Figure 4.10*a-d, the hybridization between the short PNA probes and RNA-Cy5c on the QD surface is very slow and reaches completion within the course of several days. The adsorption of RNA-Cy5nc on the QD is similarly sluggish and is strongest for conjugate QD-$(PNAa)_9$. This could be caused by the lack of glutamic acid residues within the PNAa that makes the respective nanoconjugate more hydrophobic, compared to other systems.

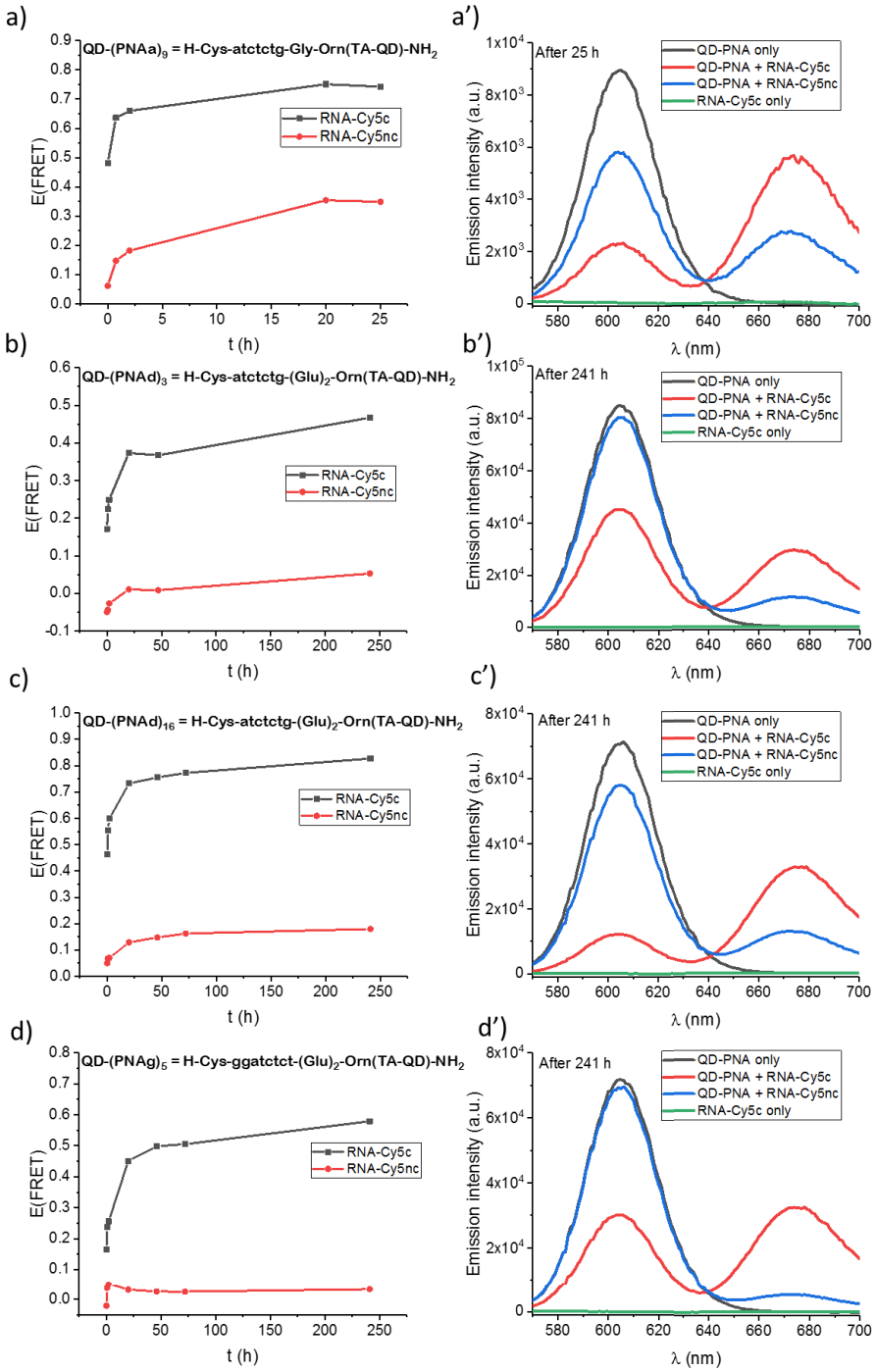

Figure 4.10. Quantification of the labeling density of QD-PNA conjugates containing 7- or 8-mer PNA sequences. a-d) Time course of binding between the QD-PNA conjugates and complementary RNA-Cy5 (RNA-Cy5c) or noncomplementary RNA-Cy5 (RNA-Cy5nc). a'-d') Photoluminescence spectra recorded after the specified time in the absence of RNA (grey), in the presence of RNA-Cy5c (red) and RNA-Cy5nc (blue). PNA and RNA sequences and their designations are provided in Table 4.5. The subscripts designate the PNA/QD labeling ratio. Photoluminescence spectra were recorded after the FRET efficiency reached saturation. $\lambda_{ex} = 435$ nm.

Next, the loadings of four QD-PNAj conjugates with different labeling densities were estimated (*Figure 4.11*). As shown in *Figure 4.11*a, the hybridization between the surface-bound PNAj (an 11-mer) and RNA-Cy5c proceeds efficiently for all conjugates and is completed within the course of a day. The nonspecific adsorption of noncomplementary RNA on the nanoparticle surface is negligible

when conjugate QD-$(PNAj)_4$ is used, however, is noticeable for the other three conjugates, which have higher PNA content. Apparently, these interactions correlate with the PNA labeling density, and nanoparticles with higher PNA/QD accommodate higher quantities of noncomplementary RNA.

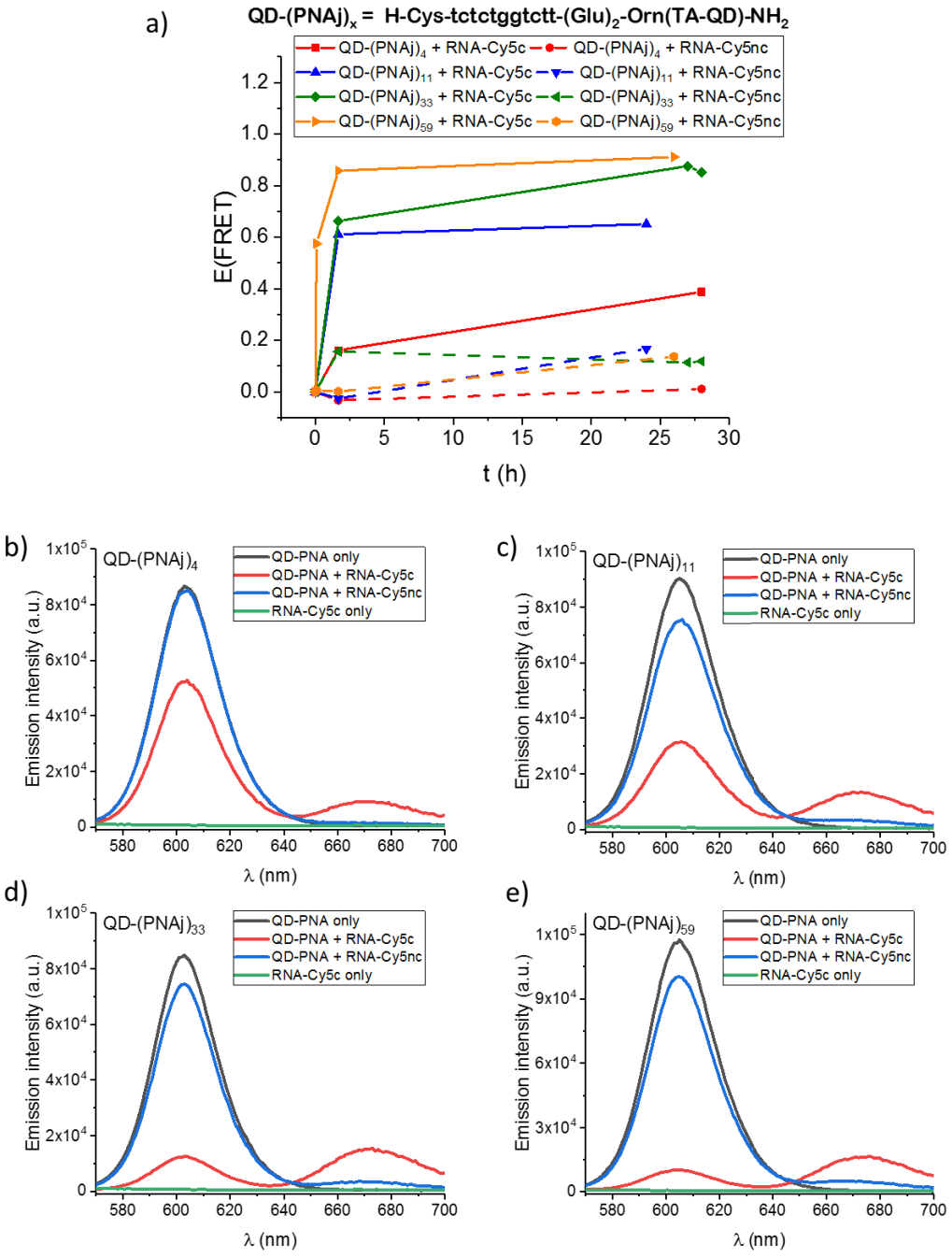

Figure 4.11. Quantification of the labeling densities of four QD-PNAj conjugates. a) Time course of hybridization between the QD-PNA and RNA-Cy5c (solid lines), and of the adsorption of RNA-Cy5nc on the QD surface (hashed lines). b-e) Luminescence spectra of QD-$(PNAj)_4$ (b), QD-$(PNAj)_{11}$ (c), QD-$(PNAj)_{33}$ (d) and QD-$(PNAj)_{59}$ (e) in the presence of RNA-Cy5c (red) or RNA-Cy5nc (blue), and in the absence of RNA (grey). λ_{ex} = 435 nm. The shown photoluminescence spectra were recorded after the FRET efficiency stopped to increase. The purpose of these experiments was to estimate the PNA labeling density, rather than to study the kinetics in detail, therefore only a few kinetic points were measured. To corroborate that the energy transfer proceeds via FRET, time-resolved measurements were carried out for QD-$(PNAj)_{59}$ conjugate (Figure 9.21).

Experiments described in subchapter 4.2.2.2 provided some important insights into the properties of QD-PNA conjugates. Firstly, QD-bound PNA probes are available for hybridization with the complementary RNA regardless of the PNA labeling density. Secondly, the kinetics of PNA/RNA hybridization on the nanoparticle surface is relatively slow, especially in the case of 7- and 8-mer probes, implying that the utilization of such conjugates for OTR-based detection schemes may require long incubation times. Finally, noncomplementary RNA adsorbs on the QD-PNA surface nonspecifically and induces low FRET signal, the degree of which was sequence- and labeling density dependent. It remained to be tested whether these interactions would interfere with the discrimination between the target and non-target RNA in an OTR format.

4.2.3 Synthesis of label donor PNA (LDPNA) probes

Initially, synthesis of LDPNA was attempted on the solid phase (*Scheme 4.7*). This approach was unsuccessful and resulted in extremely poor yields. This was attributed to the crowding of bulky and hydrophobic PNA molecules on the surface of the solid support that interfered with the formation of thioester at the C-terminus of the assembled PNA oligomer. Similar complications have been reported by Grossmann et al.[47] for the formation of dabcyl thioester at the PNA C-terminus. Therefore, an alternative strategy for the synthesis of a thioester was needed.

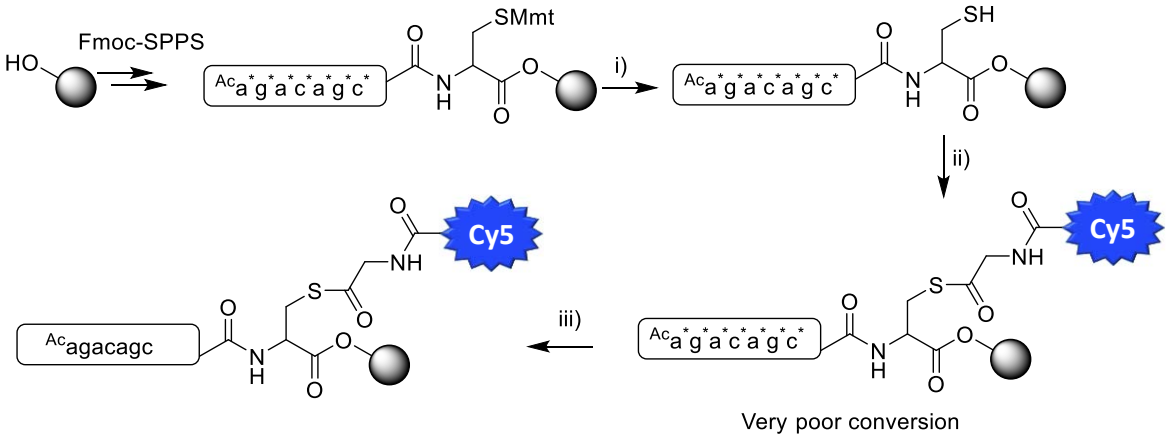

Scheme 4.7. Schematic presentation of the synthesis of LDPNA attempted on the solid phase. The formation of a thioester at the C-terminus of the assembled PNA oligomer produced very poor yields. i) TFA/TIS/DCM = 1/5/94; ii) 1. Fmoc-Gly-OH, PyBOP, NMM, DMF; 2. DBU/DMF = 5/95; 3. Cy5-CO_2H, PyBOP, NMM, DMF; iii) TFA/TIS/water/m-cresol = 85/5/5/5. Cy5 = FEWCy5. * = Bhoc protecting group.

A reasonable alternative to the formation of thioester on the solid phase is to perform a thiol exchange in solution which has been reported by Michaelis et al.[108] The strategy was adopted for the reaction between a thioester of sulfonated Cy5 dye (Cy5-Gly-MESNa) and a thiol-containing PNA, which successfully proceeded in aqueous buffer (*Figure 4.12*a).

First, a thioester of Cy5 was produced. This involved the solid phase assembly of thioester of the dye and its subsequent liberation from the solid support by using an excess of thiol reagent (MESNa) under basic conditions. The purification of Cy5-Gly-MESNa was accomplished via size-exclusion chromatography by using PD MiniTrap G-10 column. This rapid purification technique allowed to separate the excess of thiol reagent (MESNa) and base (DIPEA) from the product of reaction due to a significant difference in their molecular weights. In a separate step, a PNA oligomer with a C-terminal cysteine functionality was synthesized by using Fmoc-based SPPS and purified via RP-HPLC.

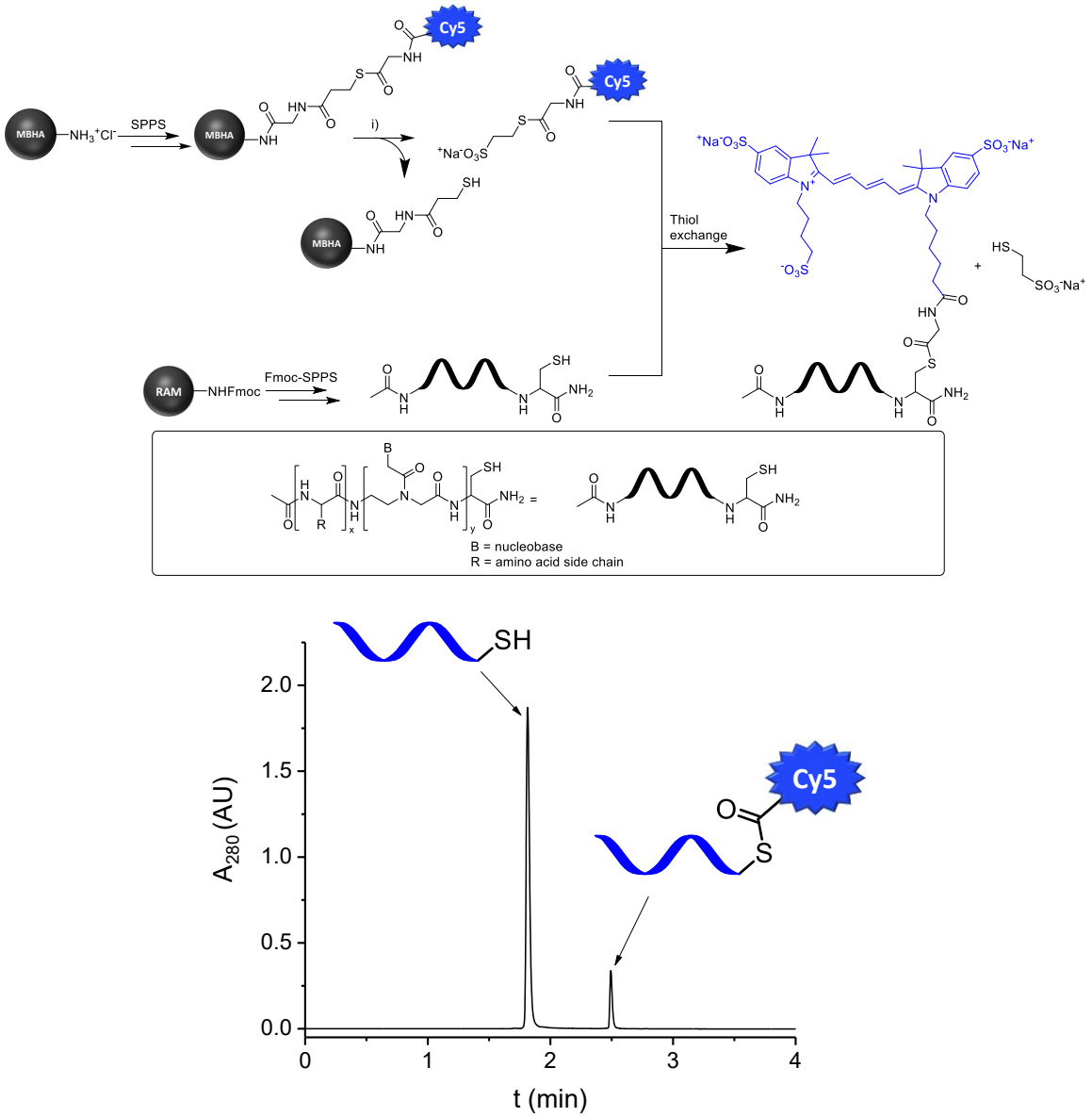

Figure 4.12. Top: Synthesis of LDPNA using the thiol exchange approach in solution. Details on the synthesis of thiol-containing PNA and Cy5-Gly-MESNa are described in the experimental section. i) 15 eq. MESNa, 7.5 eq. DIPEA, DMF/H_2O = 5/1. Bottom: UPLC trace of the crude product of thioester synthesis (PNAc) following the separation of Cy5-Gly-MESNa by precipitation. ESI-MS analysis of the components of reaction is provided in the appendix (Figure 9.23). Conditions of UPLC run: 3 to 40 % of solvent B in 4 min.

Finally, the transthioesterification reaction was carried out to produce the LDPNA probe (*Figure 4.12*, top panel). The reaction was performed in a borate buffer in the presence of TCEP to keep the thiol groups of PNA in a reduced form. The yields of this reaction were typically low (< 4 %) due to the significant losses of product during the purification steps, reversibility of thiol exchange process and hydrolysis of thioester under the reaction conditions.

The bottleneck of the purification strategy was the separation of the product of reaction (LDPNA) from the unreacted Cy5-Gly-MESNa. This was accomplished by the precipitation of the PNA-thioester either by the addition of TFA solution in water and subsequent centrifugation or by the

centrifugation of the chilled reaction mixture. The choice of protocol depended on the solubility of a specific LDPNA. This procedure permits the precipitation of LDPNA, while keeping the Cy5-Gly-MESNa in solution, thereby allowing the separation of the dye prior to HPLC purification. Such step is essential due to the very significant tailing of the peak of Cy5-Gly-MESNa in the HPLC run even when sharp gradients are used (*Figure 9.22*), making it very difficult to separate if from the product of reaction (LDPNA) chromatographically. Preparative RP-HPLC was, however, performed at a later stage to separate the thiol-PNA oligomer from the LDPNA, which had substantially different retention times (*Figure 4.12*, bottom panel). This step brings about additional losses of product due to the HPLC-related limitations. Despite the poor yields, the quantities of synthesized LDPNA probes were sufficient for the intended experiments, and further optimizations of the thioester synthesis were not carried out at this stage. More details on the synthesis of PNA and Cy5-Gly-MESNa are provided in the experimental section for every prepared LDPNA. The sequences of synthesized LDPNA probes are given in *Table 4.6*.

Table 4.6. Label donor PNA probes used in the study.

LDPNA sequences (N→C terminus)	**Designation**
Ac-agacagc-Cys(Cy5-Gly)-NH_2	PNAc
Ac-Glu-Glu-gacagc-Cys(Cy5-Gly)-NH_2	PNAf
Ac-Glu-Glu-Glu-agacagc-Cys(Cy5-Gly)-NH_2	PNAi
Ac-Glu-Glu-Glu-Gly-gagacagca-Cys(Cy5-Gly)-NH_2	PNAl

4.3 Optimization of QD-based OTRs

4.3.1 Design of PNA probes

Sensitive and selective OTRs require careful design of the reactive probes, particularly when using PNA instead of conventional DNA oligomers. As was described earlier, the ideal pair of probes should exhibit high affinity and specificity for the nucleic acid target, and low degree of nonspecific interactions in its absence. The binding affinity between the PNA and RNA increases with enhanced probe length, while the specificity follows the opposite trend. Therefore, the probes need to be as short as possible to ensure the discrimination between the matched and mismatched target sequences, and long enough to bind the NAT with high affinity under the assay-relevant conditions (considering concentrations of probes, ionic strength, temperature). The hydrophobicity of PNA oligomers, and hence, the tendency to aggregate is determined by the length and purine content, and long and purine rich (particularly G) PNAs are poorly water soluble. To find the optimal balance between the abovementioned features several PNA with different compositions were synthesized and tested as candidates for QD-based OTR.

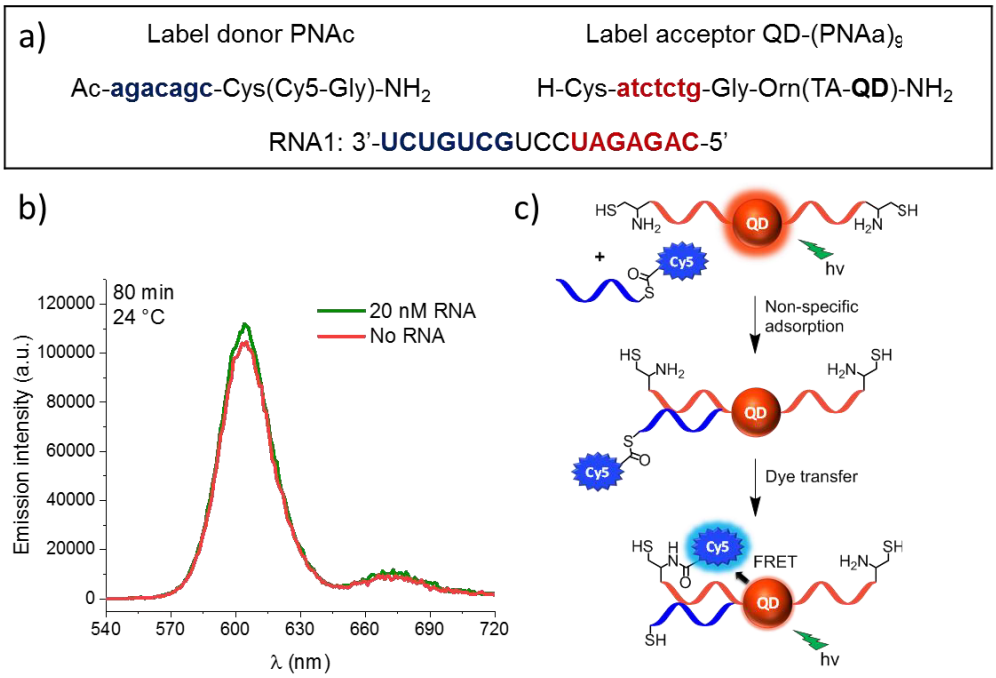

Figure 4.13 RNA detection with the probes PNAc and QD-(PNAa)$_9$. a) PNA probes and RNA target sequences. b) Photoluminescence spectra recorded 80 min after the incubation of QD-(PNAa)$_9$ and PNAc with and without RNA target. Conditions: C(QD-(PNAa)$_9$) = 2 nM, C(PNAc) = 30 nM, C(RNA1) = 20 nM. Buffer: borate buffer (50 mM borate, 20 mM NaCl, 5 mM TCEP, pH 7.3). T = 24 °C. λ_{ex} = 435 nm. c) Schematic presentation of nonspecific interactions between the PNA probes in the absence of RNA target. Adopted with permission from[101]. Copyright 2018 American Chemical Society.

Preliminary experiments involved the use of two 7-mer PNA probes (*Figure 4.13*a). The probes were designed to adjacently hybridize with the target with three unpaired nucleotides between the reactive groups of the LAPNA and LDPNA. It has been shown by Grossmann et al.[48] that such

positioning of the reactive probes can result in higher rates of transfer due to the increased flexibility at the reaction site. Thus, the probes QD-$(PNAa)_9$ and PNAc were incubated with the target RNA for 80 min and the photoluminescence spectra were measured thereafter.

As can be seen in *Figure 4.13*b, the FRET efficiency in the presence and absence of RNA is almost identical, implying that LAPNA and LDPNA are brought into proximity not via the adjacent annealing with the RNA, but rather through nonspecific interactions, as schematically depicted in *Figure 4.13*c. This will result in a false-positive result during the assay. This effect was attributed to hydrophobic interactions between the LDPNA and LAPNA on the nanoparticle surface. Therefore, it was decided to introduce more negative charges into both LA- and LDPNA probes by incorporating glutamic acid residues at the C- and N-terminus respectively.

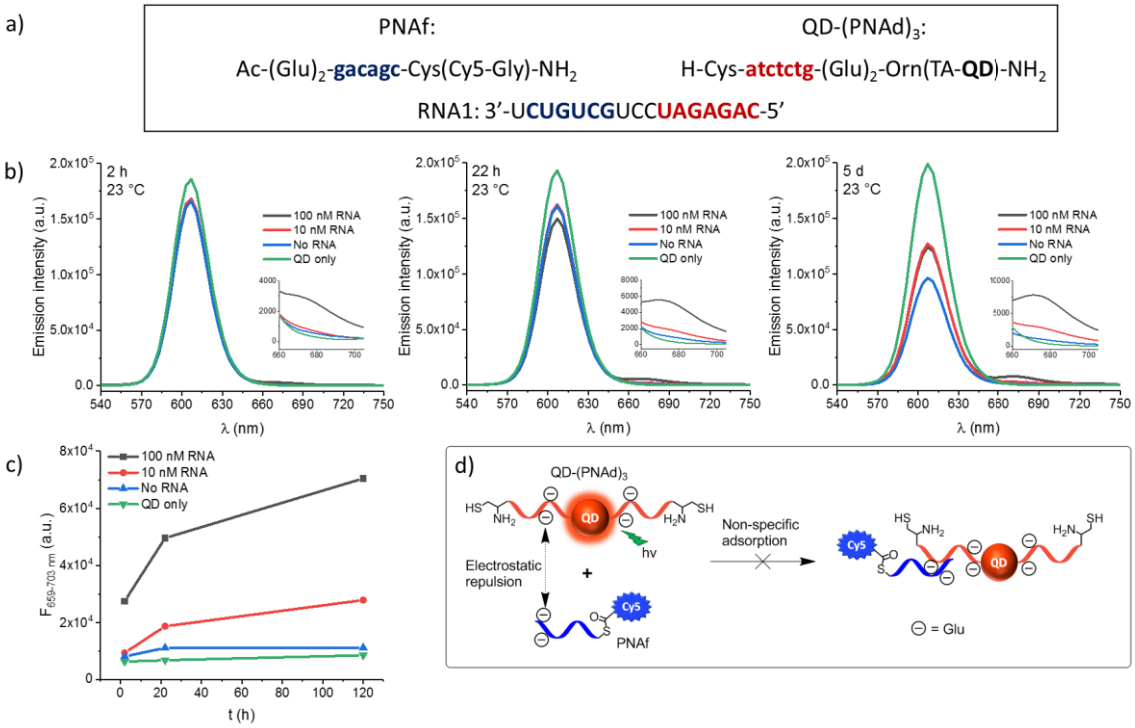

Figure 4.14 RNA detection with the probes QD-$(PNAd)_3$ and PNAf. a) PNA probes and RNA target sequences. b) Photoluminescence spectra recorded at different kinetic points of target-catalyzed dye transfer reaction at varied RNA concentrations. c) Time course of FRET-induced Cy5 emission in the presence of different concentrations of RNA target. Conditions: C(QD-$(PNAd)_3$) = 10 nM. C(PNAf) = 200 nM. Buffer: borate buffer (50 mM borate, 5 mM TCEP, 100 mM NaCl, pH 7.4). T = 23 °C. λ_{ex} = 435 nm. d) Schematic presentation of the impact of electrostatic repulsion between Glu-modified PNA probes on nonspecific interactions.

The first pair of Glu-containing probes consisted of a 7-mer LAPNA (QD-$(PNAd)_3$) and a 6-mer LDPNA (PNAf), each bearing two glutamic acid residues (*Figure 4.14*a). As illustrated in *Figure 4.14*b, these modifications substantially diminished the degree of nonspecific adsorption between the PNA probes even after prolonged incubation times, thereby decreasing the probability of false-positive results. The system was successfully used for the detection of 10 and 100 nM RNA after 1 day, as shown in *Figure 4.14*b and c.

While the detection of RNA using the probes QD-$(PNAd)_3$ and PNAf was successful, the rate of signaling kinetics was slow (*Figure 4.14*c). It was envisioned that an increase in temperature could facilitate the RNA exchange and, thus, improve the rate of the reaction. Furthermore, higher temperature enhances the diffusion rate, thereby accelerating the collision between the RNA and QD-bound PNA, which was expected to result in faster hybridization between the PNA and RNA target. To test these assumptions, detection of RNA in the concentration range of 4 to 100 nM was performed at 30 °C (*Figure 4.15*).

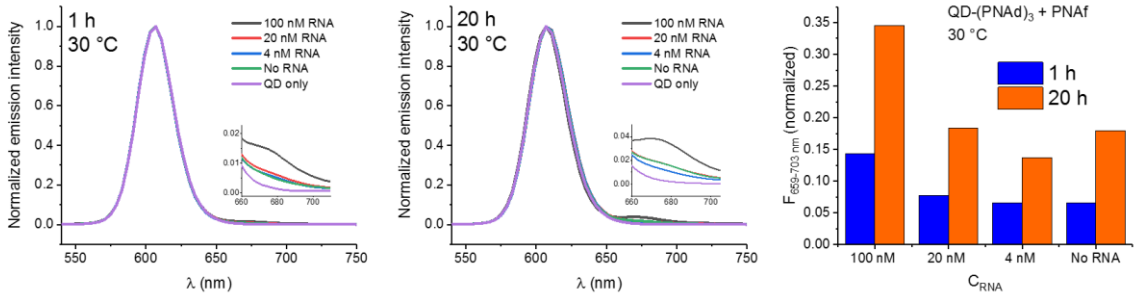

Figure 4.15 Detection of RNA in the range of 4 – 100 nM with the probes QD-$(PNAd)_3$ and PNAf at 30 °C. Normalized luminescence spectra recorded after 1 h (a) and 20 h (b). c) Emission intensity in Cy5 channel for different RNA concentrations. Conditions: C(QD-$(PNAd)_3$) = 10 nM, C(PNAf) = 200 nM. Buffer: borate buffer (50 mM borate, 5 mM TCEP, 100 mM NaCl, pH 7.4). T = 30 °C. λ_{ex} = 435 nm. Spectra were normalized to the maximum of QD emission.

As illustrated in *Figure 4.15*, only 100 nM RNA could be discriminated from the background when the OTR was performed at 30 °C. It is likely that higher temperature reduces the binding affinity between the PNA and RNA and hampers the detection of low nM RNA concentrations. Moreover, the sensitized emission of Cy5 was very moderate even after 20 h of incubation, which was attributed to an insufficient number of Cy5 molecules on the nanoparticle surface.

To enhance the binding affinity of the QD-LAPNA conjugate, an 8-mer probe (PNAg) (*Figure 4.16*a) was synthesized and coupled to the nanoparticle (QD-$(PNAg)_5$). Detection of RNA in a concentration range of 0.5 – 50 nM using this probe in conjunction with PNAf is illustrated in *Figure 4.16*, panels b and c. Even though 5 and 50 nM of target could be detected after a day, sub-nanomolar concentrations of RNA were clearly beyond the limit of detection. Furthermore, only a very low sensitization of Cy5 emission could be achieved with this pair of PNA probes.

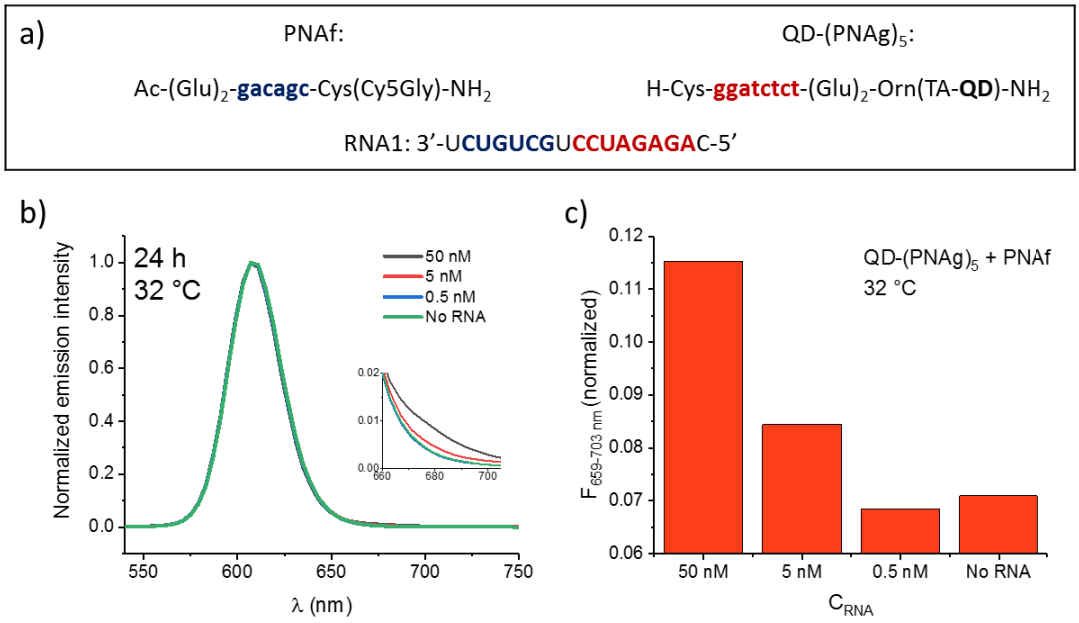

Figure 4.16 Detection of RNA in the range 0.5 – 50 nM with the probes QD-$(PNAg)_5$ and PNAf. a) PNA probes and RNA target sequences. b) Normalized luminescence spectra recorded after 24 h. c) Emission intensity in Cy5 channel after 24 h for different target concentrations. Conditions: C(QD-$(PNAg)_5$) = 10 nM, C(PNAf) = 75 nM. Buffer: borate buffer (50 mM borate, 5 mM TCEP, 100 mM NaCl, pH 7.4). T = 32 °C. λ_{ex} = 435 nm. Spectra were normalized to the maximum of QD emission.

To circumvent these encountered obstacles, it was decided to use a QD conjugate with higher PNA labeling density. This measure was expected to enhance the positive cooperativity effect, and to improve the affinity of binding between the QD-immobilized PNA and RNA target. The latter trend has been observed for DNA probes, immobilized on gold[128] and magnetic nanoparticles.[119] In addition, higher PNA content was expected to enhance the FRET efficiency by providing the means to bring more FRET acceptors onto the QD surface. Therefore, the loading of LAPNA was increased to 16 PNA/QD (QD-$(PNAd)_{16}$) and this conjugate was combined with a 7-mer LDPNA (PNAi) (PNA sequences are shown in *Figure 4.17*a).

As predicted, the use of QD-PNA conjugate with increased PNA labeling density substantially enhanced FRET efficiency, resulting in the notable boost of sensitized Cy5 emission in the presence of an RNA target. At the same time, the nonspecific interactions between the PNA probes remained relatively weak despite the high concentrations of both PNA probes used. Noteworthy, this pair of probes (QD-$(PNAd)_{16}$ and PNAi) features the same nucleobase composition as the nonmodified (without glutamic acid units) probes QD-$(PNAa)_9$ and PNAc (*Figure 4.13*), described at the beginning of this chapter. It could be assumed that the improved signal-to-noise ratio in the case of Glu-modified probes is achieved due to the strong electrostatic repulsion that counteracts the attractive forces between the probes, thereby alleviating the aggregation.

PNAi:	QD-$(PNAd)_{16}$:
Ac-$(Glu)_3$-**agacagc**-Cys(Cy5-Gly)-NH_2	H-Cys-**atctctg**-$(Glu)_2$-Orn(TA-**QD**)-NH_2
RNA1: 3'-**UCUGUCG**UCC**UAGAGAC**-5'	

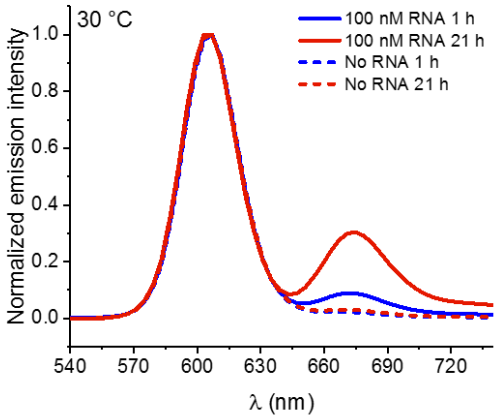

Figure 4.17 Detection of 100 nM RNA with the probes QD-$(PNAd)_{16}$ and PNAi. a) Sequences of PNA probes and RNA target. b) Normalized luminescence spectra recorded after 1 h and 21 h. Conditions: C((QD-$PNAd)_{16}$) = 10 nM, C(PNAi) = 200 nM. Buffer: borate buffer (50 mM borate, 5 mM TCEP, 100 mM NaCl, pH 7.4). T = 30 °C. λ_{ex} = 435 nm. Spectra were normalized to the maximum of QD emission.

To further explore the performance of the newly designed system, the detection of RNA using lower concentrations of probes was carried out (*Figure 4.18*). In these experiments the molar ratios between the components were kept at the same level as during the experiment described above, but the total concentration was decreased by a factor of 5. This was envisioned to provide a better understanding of the affinity of these short PNA probes for the RNA target and the concentration dependency of nonspecific interactions.

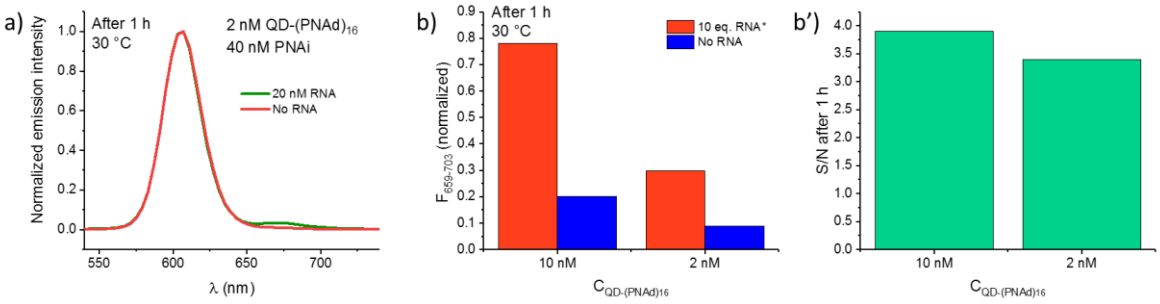

Figure 4.18 Testing of two different PNA probes concentrations for optimal signal amplification. a) Detection of 20 nM RNA with the probes QD-$(PNAd)_{16}$ and PNAi at low probe concentrations. The molar ratios between the probes and the RNA were kept at the same level as shown in Figure 4.17, but the total concentration was decreased by a factor of 5. Conditions: C((QD-$PNAd)_{16}$) = 2 nM, C(PNAi) = 40 nM, C(RNA1) = 20 nM. Buffer: borate buffer (50 mM borate, 5 mM TCEP, 100 mM NaCl, pH 7.4). T = 30 °C. λ_{ex} = 435 nm. Spectra were normalized to the maximum of QD emission. Comparison of sensitized emission intensity of Cy5 (b) and S/N (b') for different probe concentrations in the presence and in the absence of RNA target. *RNA equivalents relative to QD concentration.

As illustrated in *Figure 4.18*a, lowering the concentrations of PNA probes diminished both the signal and the background. The decrease in signal that is induced upon incubation with the RNA target probably is due to the reduction in the affinity of PNA/RNA binding at lower concentrations. The

decrease in the rate of nonspecific adsorption of PNAi on the QD-$(PNAd)_{16}$ very likely also is due to the penalization of multimolecular interactions under dilution conditions. Consequently, the signal-to-noise ratio remains almost unchanged when the concentration is decreased by a factor of 5. It was decided to carry out further experiments at 2 nM of QD-$(PNAd)_{16}$, aiming to slow down the nonspecific interactions. The higher labeling density, compared to the previously used, was expected to provide a sufficient affinity for the RNA target and permit the detection of low abundance RNA after prolonged incubation times. The successful detection of RNA in the nanomolar range using these probes is presented in *Figure 4.19*.

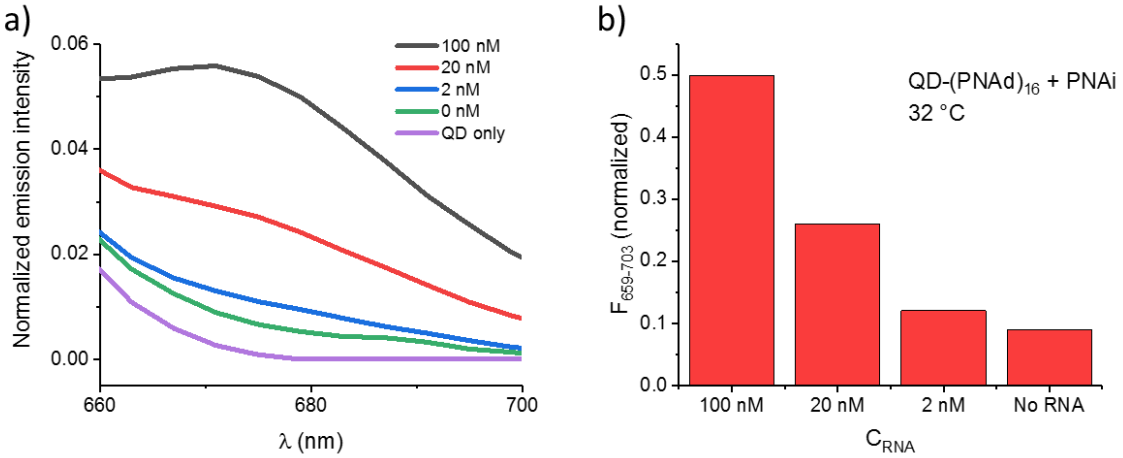

Figure 4.19 Detection of RNA in the range of 2 to 100 nM using the probes QD-$(PNAd)_{16}$ and PNAi. a) Normalized luminescence spectra recorded after 24 h. b) Normalized emission in Cy5 channel as a function of target concentration. Conditions: C(QD-$(PNAd)_{16}$) = 2 nM, C(PNAi) = 40 nM, C(RNA1) = 2 - 100 nM. Buffer: borate buffer (50 mM borate, 5 mM TCEP, 50 mM NaCl, pH 7.4). The reaction was performed at 27°C for 40 min, and then at 32°C for 24 h. λ_{ex} = 435 nm. Spectra were normalized to the maximum of QD emission.

As shown in *Figure 4.19*, detection of RNA in the nM range could be accomplished within a day, however, detection of lower quantities of RNA called for further optimization. An extension of PNA probes was envisioned to be the most straightforward way to improve the binding affinity between the PNA and RNA, thus enabling the use of QDs at pM concentrations and detection of low RNA concentrations. To that end, an 11-mer LAPNA (PNAj) and a 9-mer LDPNA (PNAl) (PNA sequences are given in *Figure 4.20*) were synthesized. To compare the performance of QD-PNAj with different labeling densities, four conjugates with the PNAj/QD ratios in the range of 4-59 were prepared and subsequently tested.

Preliminary experiments were carried out by using a QD with intermediate PNA load (11 PNA/QD). First, OTR in the presence of 10 nM of complementary RNA (RNAc) and noncomplementary RNA (RNAnc) (sequences are given in *Figure 4.20*a) was studied. The RNA target (RNAc) contained 28-nucleotides, in contrast to RNA1 used for the previous experiments (a 17-mer). It was expected that RNAc could fold and form a thermodynamically stable secondary structure. Indeed, the melting

temperature of an RNAc hairpin was calculated to be 62 °C (at C_{NaCl} = 50 mM) using free online OligoAnalyzer 3.1 Software. To facilitate unfolding, experiments were performed at 47 °C.

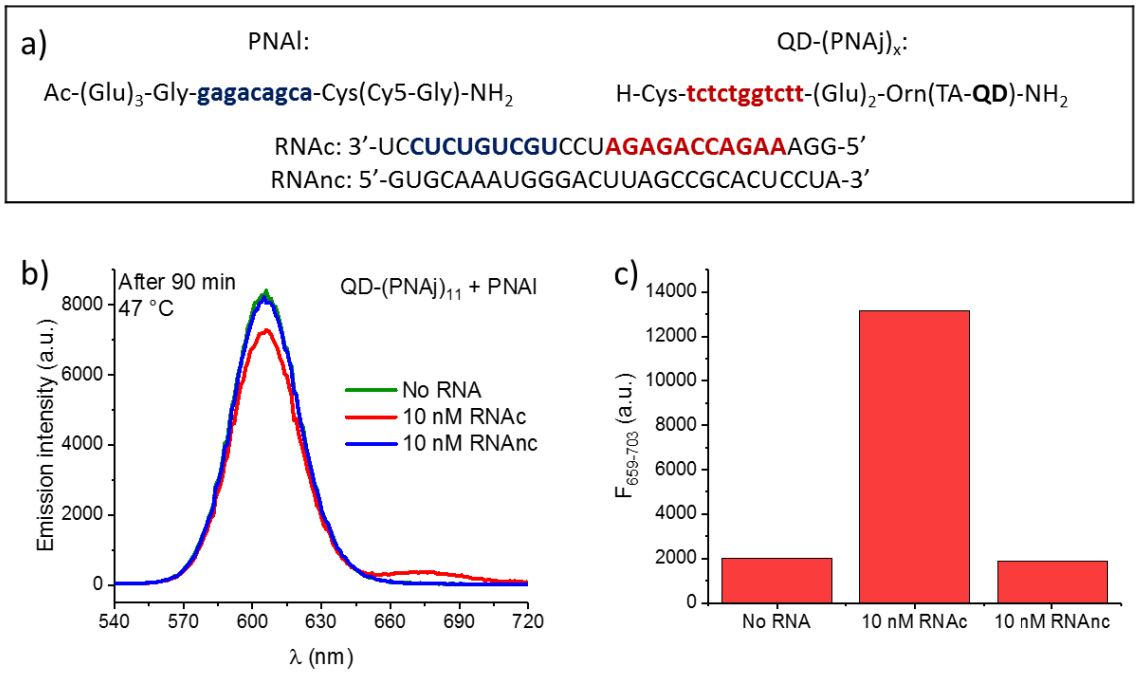

Figure 4.20 a) Sequences of PNA probes with high affinity (x = 4, 11, 33, or 59), complementary RNA target (RNAc) and noncomplementary RNA (RNAnc) sequences used in the study. Luminescence spectra (b) and sensitized emission of Cy5 (c) recorded after 90 min of reaction between QD-$(PNAj)_{11}$ and PNAl in the presence of RNAc, RNAnc, and in the absence of RNA. Conditions: C(QD-$(PNAj)_{11}$) = 400 pM, C(PNAl) = 4 nM; Buffer: citrate buffer (40 mM citrate, 2 mM TCEP, 50 mM NaCl, 0.05% (w/v) TWEEN20, pH 7.0). T = 47°C. λ_{ex} = 435 nm.

As illustrated in *Figure 4.20*, panels b and c, 10 nM RNAc can be detected already after 90 min even though the experiments were performed at an elevated temperature and QD-$(PNAj)_{11}$ was uses at a pM concentration, emphasizing the advantages of using longer PNA probes over the shorter ones. In addition, RNAnc did not provide any signal enhancement, thereby confirming target specificity of the detection system.

To assess the sensitivity of RNA detection and to evaluate the impact of different concentrations of RNAnc on the background, experiments with a broader range of RNA concentrations were performed (*Figure 4.21*). While RNAc in the nanomolar range could be detected within 1 h, detection in sub-nanomolar range was not achieved. Importantly, the concentration of RNAnc (in the tested range of 1 to 100 nM) did not provide any signal enhancement in the Cy5 channel. Furthermore, the background signal in the presence of RNAnc seemed to be lower than in the absence of any RNA.

In an effort to improve the kinetics of hybridization and strand exchange, the concentration of QD-$(PNAj)_{11}$ was reduced to 250 pM and the temperature increased to 52 °C. This did not, however, result in improved signal-to-noise ratios (S/N) (*Figure 9.24*).

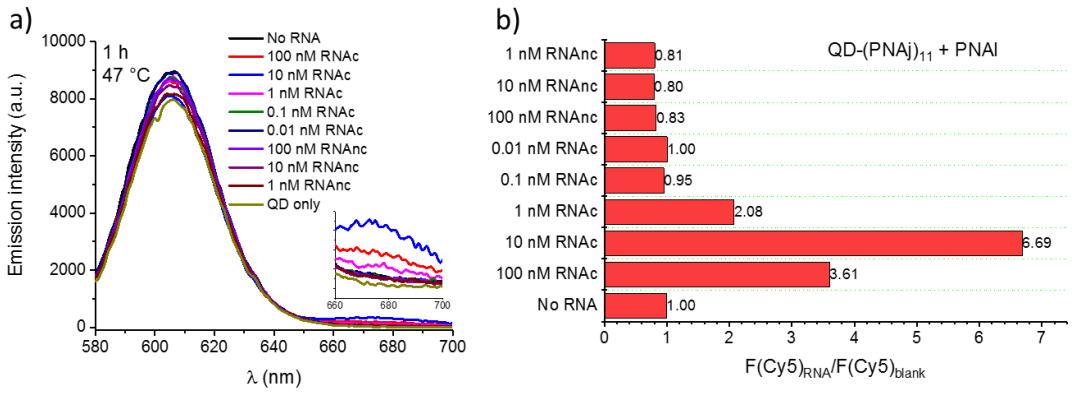

Figure 4.21 Detection of RNAc in the range of 0.01 – 100 nM with the probes QD-$(PNAj)_{11}$ and PNAl. Luminescence spectra (a) and sensitized emission of Cy5 plotted as a signal-to-noise ratio (b) for different concentrations of RNAc and RNAnc. Conditions: C(QD-$(PNAj)_{11}$) = 400 pM, C(PNAl) = 4 nM; Buffer: citrate buffer (40 mM citrate, 2 mM TCEP, 50 mM NaCl, 0.05% (w/v) TWEEN20, pH 7.0). Spectra were measured after 1 h of incubation at T = 47 °C. λ_{ex} = 435 nm. Fluorescence intensities in Cy5 channel were corrected for the signal induced by QD only.

The rather low signal-to-noise ratio at low target concentration could be due to inefficient strand exchange or high background. It was assumed that lower PNAj loading of QD-PNAj would result in reduced background signal due to the diminished hydrophobicity of the nanobioconjugate, hence giving way to lower FRET in the absence of RNA target. Kinetics of RNA detection using QD-$(PNAj)_4$–a conjugate with lowest PNA labeling density–are presented in *Figure 4.22*. As evident from the emission spectra, nanomolar concentrations of target could be clearly distinguished from the background already after 1 h, and the target-induced signal amplification did not decrease after 3 h, in contrast to conjugate QD-$(PNAj)_{11}$ (*Figure 9.24*). The S/N did not, however, substantially increase after longer reaction times (*Figure 4.22*d), which indicates that lower PNA labeling density does not eliminate the nonspecific interactions between the PNA probes, yet only weakens them.

The results demonstrate that conjugates QD-$(PNAj)_4$ and QD-$(PNA)_{11}$ can be used to successfully detect RNA in the range of 1 to 100 nM within 1 hour. I inferred that longer PNA probes allow for significantly faster kinetics of detection compared to the short ones, described at the beginning of the chapter. Additionally, detection could be performed at elevated temperatures, which makes the folded RNA sequences accessible for binding of PNA probes.

Realizing that optimization of temperature regime for QD-based OTR is not trivial and depends on multiple factors (RNA folding, affinity of PNA/RNA binding, thioester hydrolysis, PNA-PNA aggregation, etc.), screening experiments covering a broad range of temperatures in small steps were required to optimize the conditions for efficient OTR. For these experiments four QD-PNAj conjugates with labeling densities in the range of 4-59 were used.

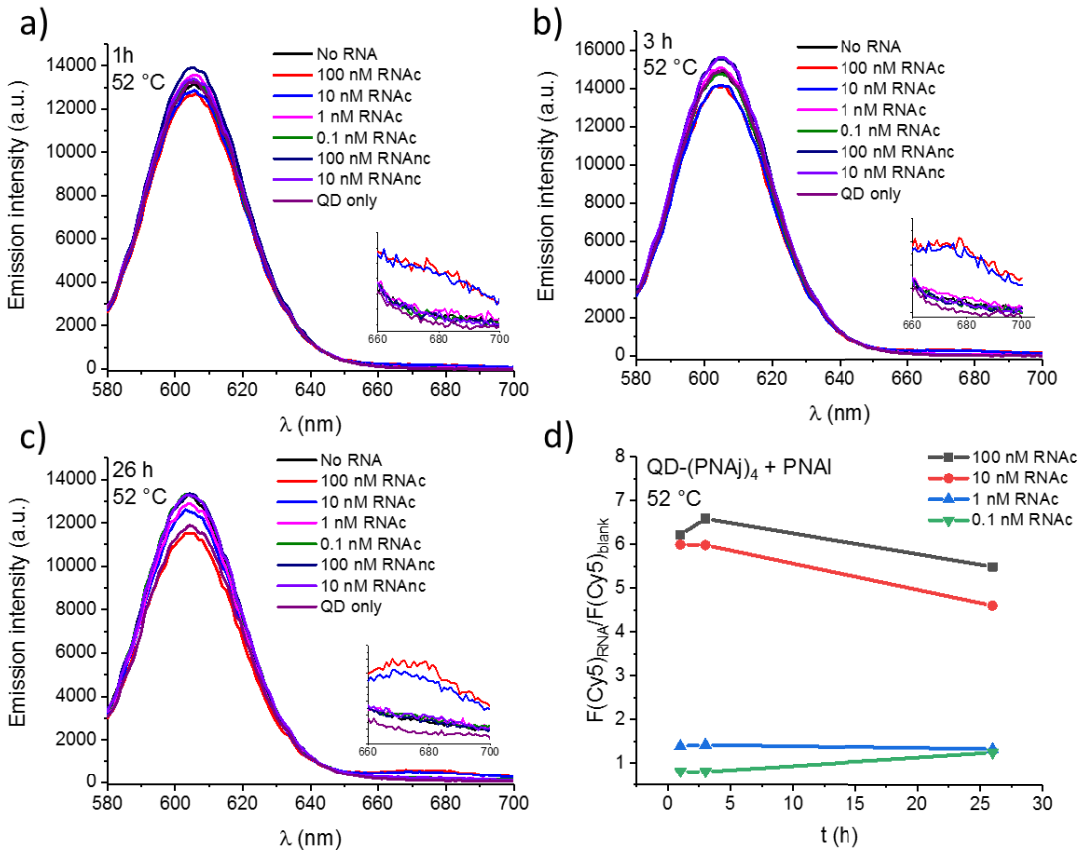

Figure 4.22. Detection of RNAc in the range of 0.1 – 100 nM with the probes QD-(PNAj)$_4$ and PNAl. a-c) Emission spectra recorded after 1h, 3 h, and 26 h of reaction. d) Time course of OTR plotted as S/N in the Cy5 channel (emission was corrected for the signal of QD only). Conditions: C(QD-(PNAj)$_4$) = 500 pM, C(PNAl) = 4 nM. Citrate buffer (40 mM citrate, 2 mM TCEP, 50 mM NaCl, 0.05% (w/v) TWEEN20, pH 7.0). T = 52°C. λ_{ex} = 435 nm.

To evaluate the impact of temperature on OTR, 100 pM and 10 nM of RNA target were utilized to catalyze the dye transfer. The best QD-PNAj conjugate was expected to provide considerable signal enhancement for both concentrations applied. Four QD-PNAj conjugates were used at different concentrations (expressed in QD), to maintain the concentrations of PNA molecules in a narrow range. For these experiments, the solution that contained the QD-PNA probe and the RNA target was heated to a defined temperature for 25 min, after which point the LDPNA was added, and the reaction was incubated for additional 2.5 h. FRET-induced emission of Cy5 was used as a readout of the OTR. The ratio between the background-corrected fluorescence in Cy5 channel in the presence and absence of RNA target was plotted as a function of temperature (*Figure 4.23*).

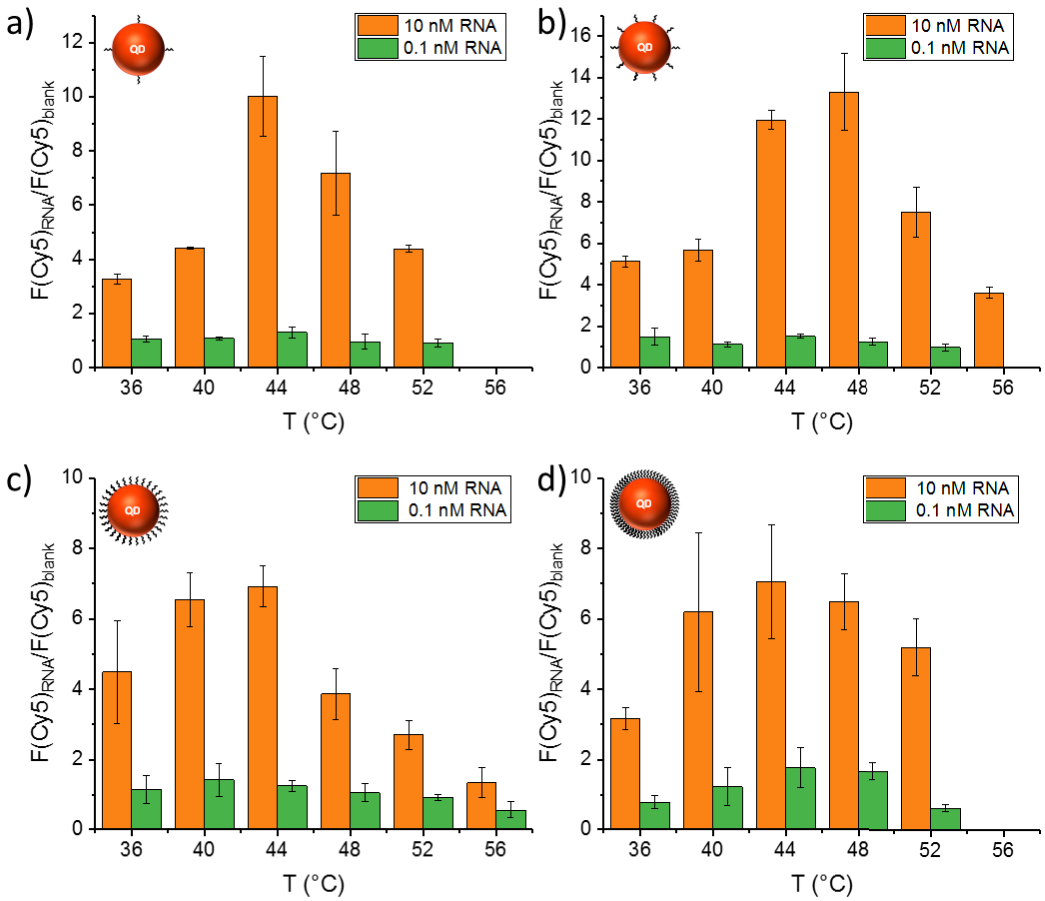

Figure 4.23 RNA-catalyzed dye transfer in the presence of 10 nM and 0.1 nM of RNAc at different temperatures for four QD-PNAj conjugates; the measurements were performed 2.5 h after PNAl addition. The blank is buffer that only contains QD-PNAj and PNAl. Conditions: Citrate buffer (40 mM citrate, 2 mM TCEP, 50 mM NaCl, 0.05% (w/v) TWEEN20, pH 7.0). a) C(QD-$(PNAj)_4$) = 350 pM, C(PNAl) = 3.5 nM, b) C(QD-$(PNAj)_{11}$) = 250 pM, C(PNAl) = 3.5 nM, c) C(QD-$(PNAj)_{33}$) = 50 pM, C(PNAl) = 1 nM, d) C(QD-$(PNAj)_{59}$) = 25 pM, C(PNAl) = 1 nM. λ_{ex} = 435 nm. All experiments were performed in duplicate; error bars represent standard deviations. The experiments were performed for screening purposes to select the temperature range for optimal signal enhancement.

The temperature screen revealed a notable increase in the OTR efficiency for each QD-PNA conjugate with elevated temperature, with the highest S/N ratio observed at temperatures in the range of 44 - 48 °C and 40 - 44 °C for 10 nM RNA and 100 pM RNA, respectively. A similar tendency has been reported before for solution-based OTR.[15] The improved efficiency of OTR with higher temperatures results from the diminished affinity of PNA probes for RNA and concomitant acceleration of strand exchange reactions. Moreover, the RNA secondary structure becomes more unstable at higher temperatures, which improves its availability for PNA binding. However, temperatures ≥ 52 °C significantly decrease the binding affinity between the probes and RNA, and accelerate the hydrolysis of the thioester, thereby resulting in lower signal-to-background ratios.

Interestingly, the QD surface load affects the temperature dependence of the dye transfer efficiency. With QD-$(PNAj)_4$ and QD-$(PNAj)_{11}$ the temperature dependence of dye transfer efficiency was more pronounced compared to QD-$(PNAj)_{33}$ and QD-$(PNAj)_{59}$. As of now, there is no definitive

explanation for this behavior. Regardless of the mechanistic rationale, the temperature screening studies indicated that for 10 nM RNA, the best S/N ratio was obtained with the system QD-$(PNAj)_{11}$, while in the case of 100 pM RNA, the most sensitive response was achieved with QD-$(PNAj)_{59}$. Therefore, these two systems were used for assessing the assay capabilities.

4.3.2 Kinetics and sensitivity of RNA detection

The systems QD-$(PNAj)_{11}$ and QD-$(PNAj)_{59}$ were assessed in greater detail. The time course of signaling was assessed by performing the reactions in a buffer containing 100 nM of RNAnc to evaluate the impact of foreign RNA on the detection efficiency. As illustrated in *Figure 4.24* (panels a and b), RNAc in the concentration range of 0.1 nM to 100 nM can be detected using QD-$(PNAj)_{11}$ and QD-$(PNAj)_{59}$ already within 80 min and 30 min, despite the high concentration of RNAnc in the matrix, respectively. These findings corroborate the formation of specific PNA/RNA duplexes on the QD surface and minimal interferences from RNAnc.

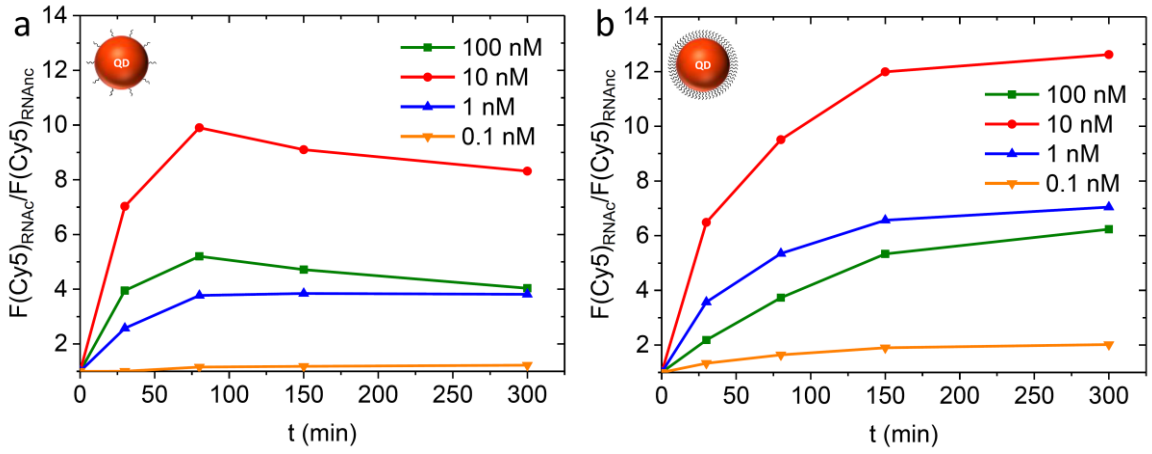

Figure 4.24. Kinetics of RNA detection for different concentrations of RNAc obtained using QD-$(PNAj)_{11}$ (a) and QD-$(PNAj)_{59}$ (b) in the presence of 100 nM RNAnc. Conditions: a) C(QD-$(PNAj)_{11}$) = 250 pM, C(PNAl) = 3.5 nM; b) C(QD-$(PNAj)_{59}$) = 25 pM, C(PNAl) = 1 nM. Matrix: 100 nM RNAnc in citrate buffer (40 mM citrate, 2 mM TCEP, 50 mM NaCl, 0.05% (w/v) TWEEN20, pH 7.0). T = 44°C. λ_{ex} = 465 (35) nm, λ_{em} = 670 (25) nm. Cy5 emission was corrected for the emission of QD only and divided by the signal induced by RNAnc. Adopted with permission from[101]. Copyright 2018 American Chemical Society.

As shown in *Figure 4.24*, for all RNA concentrations used, the S/N reaches a saturation after 2.5 h, yet even for a relatively high concentration of RNA (1 nM) the reaction is not quantitative (the completion is not reached). This may be due to the hydrolysis of the thioester (*Figure 4.25*)−a competitive reaction that renders the LDPNA unreactive by cleaving off the Cy5.

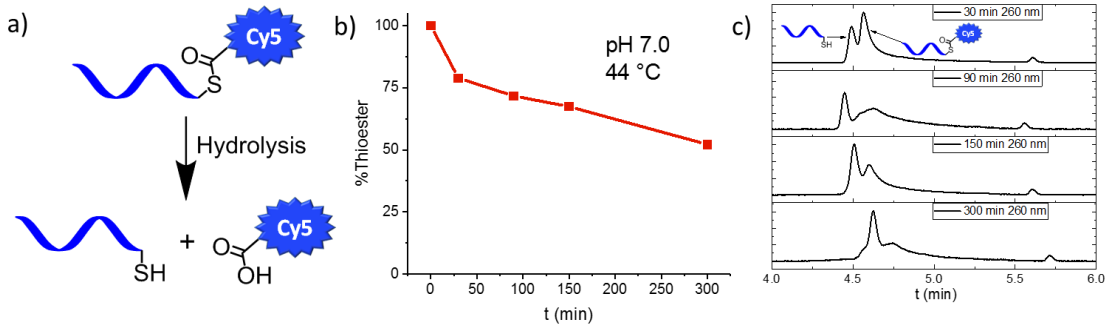

Figure 4.25. Kinetics of PNAl hydrolysis. a) Schematic presentation of thioester hydrolysis. b) Kinetics of PNAl hydrolysis at pH 7.0. c) UPLC data used to calculate the stability of PNAl. Conditions: C(PNAl) = 9.4 µM; Citrate buffer (40 mM citrate, 2 mM TCEP, 50 mM NaCl, 0.05% (w/v) TWEEN20, pH 7.0), T = 44 °C. Hydrolysis was monitored via UPLC-MS using the gradient: 2 to 25 % of solvent B in 6 min. Due to the presence of TWEEN20 in the reaction mixture the starting material (thioester) and the product of hydrolysis (thiol) are difficult to separate using UPLC and their peaks overlap. Therefore, the integration of the peak of thioester was corrected for the peak of free thiol to correctly evaluate the fraction of thioester at different time points. Adopted with permission from[101]. Copyright 2018 American Chemical Society.

While the S/N starts to drop (QD-(PNAj)$_{11}$ (*Figure 4.24*a)), or remains unchanged (QD-(PNAj)$_{59}$ (*Figure 4.24*b)) after 150 min, for both systems, the intensity of Cy5 emission continuously rises even after longer reaction times as shown in *Figure 9.28*. The decreased signal enhancement at longer incubation times results from the increased background signal, induced by nonspecific interactions between the LAPNA and LDPNA. This background signal does not reach a plateau, rather increases linearly. This was noticed to have a more pronounced effect on the S/N ratio for the detection of high concentrations of RNA (10 and 100 nM) compared to lower ones (1 and 0.1 nM). The subsequent assay experiments were performed for a period of 5 h to achieve the broadest possible detection range, since after this time point all tested RNA concentrations induced a signal enhancement that exceeded that of the matrix and were well distinguishable from the latter.

Next, experiments with a broader range of RNA concentrations were performed. By using the conjugate QD-(PNAj)$_{11}$, 40 pM RNA is clearly distinguishable from the matrix after 5 h, however only concentrations higher than 100 pM were above the LOD. The latter was defined as the sum of the signal induced by the matrix (buffer containing 100 nM of RNAnc) and three times its standard deviation (*Figure 4.26*a). In contrast, the conjugate QD-(PNAj)$_{59}$ offered a wider detection range of 10 pM to 100 nM (*Figure 4.26*b), which renders this system the best candidate for RNA detection.

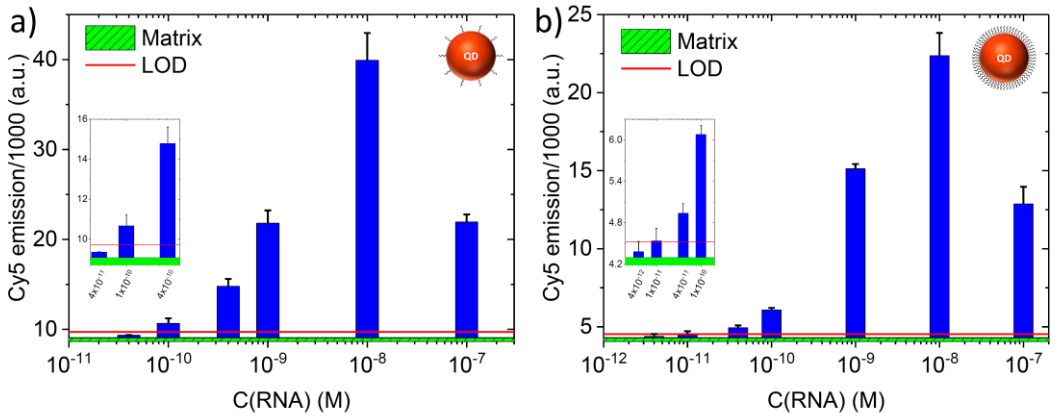

Figure 4.26. Detection of RNAc in the range of concentrations in the presence of 100 nM RNAnc. Cy5 emission was measured after 5 h and plotted without correction. Conditions: a) C(QD-$(PNAj)_{11}$) = 250 pM, C(PNAl) = 3.5 nM. Experiments were performed in duplicate; the error bars represent the standard deviations. b) C(QD-$(PNAj)_{59}$) = 25 pM, C(PNAl) = 1 nM. The average values of three or four measurements are plotted; the error bars represent the standard deviations. Statistical test for outliers is shown in Figure 9.26. Matrix: 100 nM RNAnc in citrate buffer (40 mM citrate, 2 mM TCEP, 50 mM NaCl, 0.05% (w/v) TWEEN20, pH 7.0). T = 44°C. λ_{ex} = 465 (35) nm, λ_{em} = 670 (25) nm. LOD was calculated as: matrix signal + 3*standard deviation. To illustrate that the fluctuations in temperature did not affect the precision of the fluorescence measurements in the wells, experiments shown in Figure 9.27 were performed. Adopted with permission from[101]. Copyright 2018 American Chemical Society.

An interesting observation is that 100 nM of target produced less signal than 10 nM. The rationale for this phenomenon is that at 100 nM the concentration of RNA is 100-fold higher than the concentration of PNA probes (*Figure 4.26*b). As a result, the probability that both QD-LAPNA and LDPNA hybridize with the same RNA strand is low. Without an OTR, the FRET efficiency would remain insignificant and it would be impossible to detect RNA at the concentrations this high. However, under the conditions of dynamic strand exchange–that is when probes are in an equilibrium between the unbound and bound states–the OTR leads to the product formation and concomitant FRET-induced signaling.

To corroborate that the FRET-induced Cy5 emission was indicative of a chemical reaction between the LAPNA and LDPNA, rather than adjacent annealing with the target without dye transfer, as shown in *Scheme 4.8*, control experiments were performed. These involved the quenching of the OTR with a base (*Scheme 4.8*) that was expected to induce the cleavage of thioester and effectively clear the QD surface from Cy5 unless it is bound via a hydrolytically stable amide bond.

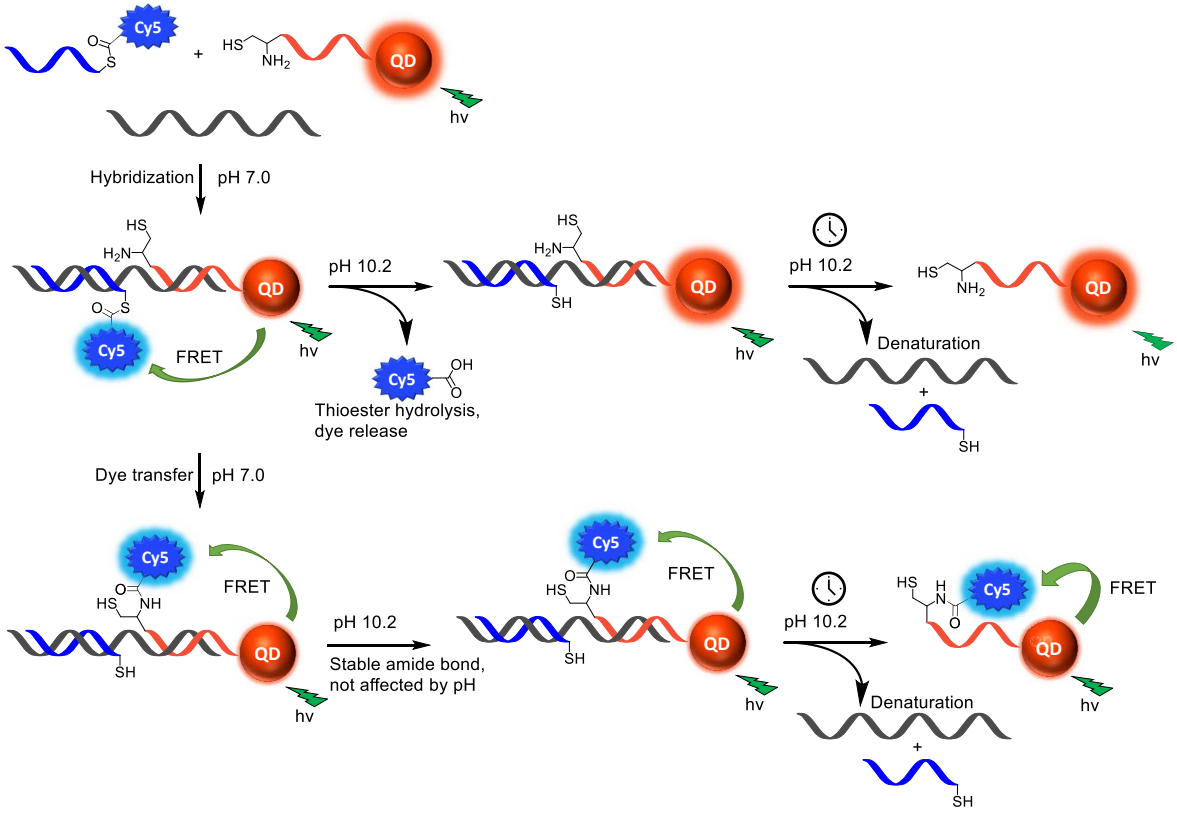

Scheme 4.8 Schematic presentation of the hydrolysis of thioester and its impact on FRET. Following the hydrolysis of LDPNA, the FRET between the QD and Cy5 can only be indicative of an amide bond formation on the nanoparticle surface, thereby excluding the possibility of proximity-induced FRET. Additionally, high pH is expected to cause the denaturation of PNA/RNA, thus promoting the transition from rigid duplex conformation to a flexible single strand conformation of QD-immobilized PNA.

The on-QD transfer reaction was quenched after 110 min by increasing the pH to 10.2. Under these conditions, the LDPNA probes are subject to hydrolysis of the thioester, thereby cleaving off the fluorophore (*Figure 9.34*). Without the occurrence of dye transfer, this treatment would lead to a decrease of the intensity of the QD-induced Cy5 emission. As illustrated in *Figure 4.27*, FRET-induced Cy5 signal obtained within the course of the templated reaction between the LAPNA and LDPNA resists base treatment, which is indicative of the formation of a stable covalent bond. Moreover, a substantial increase in Cy5 emission following the increase in pH was observed (*Figure 4.27*). It is reasonable to assume that high pH induces the denaturation of PNA/RNA duplexes. Single-stranded PNA is highly flexible and brings the Cy5 closer to the QD surface thereby enhancing the efficiency of energy transfer, since FRET efficiency sharply depends on the distance between the luminophores with shorter distances leading to higher FRET.

A very interesting observation is the decrease in FRET signaling observed when the matrix was subjected to an increase in pH (*Figure 4.27*a). It appears likely that within the first 110 min (at pH 7.0) PNAl nonspecifically adsorbs on the QD surface, thereby inducing low FRET signal. However not all thioester molecules would react with the cysteine functionalities of LAPNA within this time frame. Consequently, following the increase in pH, the unreacted QD-adsorbed thioesters hydrolyze,

releasing the Cy5 into the solution, thereby depriving the QD of FRET acceptors and effectively diminishing the background.

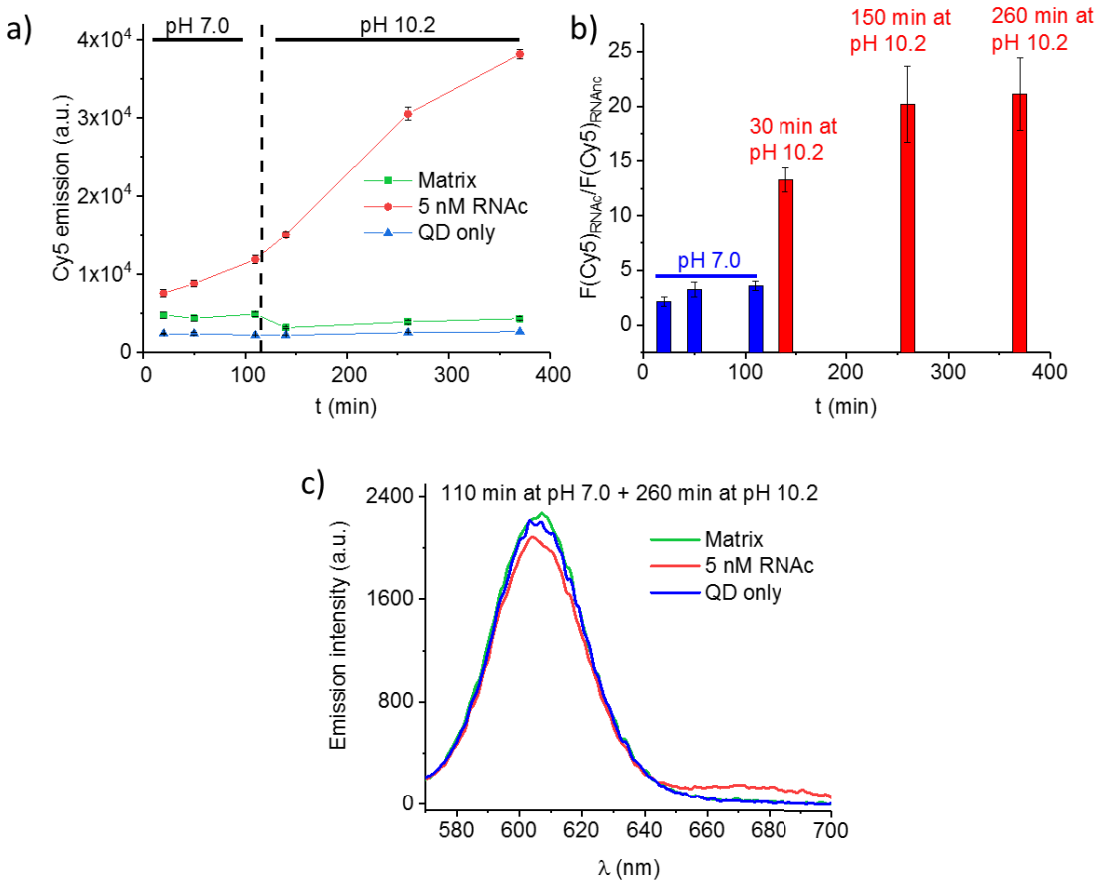

Figure 4.27 Confirmation of covalent bond formation using thioester hydrolysis. a,b) Time course of FRET-induced signaling for reactions performed at pH 7.0 and after the increase of pH to 10.2. Emission intensity in Cy5 channel (a) and signal-to-noise ratio (b) under different conditions. λ_{ex} = 465 (35) nm, λ_{em} = 670 (25). c) Emission spectra recorded 260 min after the increase of pH to 10.2. λ_{ex} = 435 nm. The reaction was performed in citrate buffer (40 mM citrate, 2 mM TCEP, 50 mM NaCl, 0.05% (w/v) TWEEN20, 100 nM of RNAnc, pH 7.0) for 110 min at 44 °C. Afterwards, the pH was adjusted to 10.2 by the addition of borate buffer (220 mM, pH 10.6) at a ratio of 1 to 5 (V/V) relative to the reaction mixture, and the solution was left shaking at 44 °C to facilitate the hydrolysis. C(QD-$(PNAj)_{11}$) = 250 pM, C(PNAl) = 3.5 nM, C(RNAc) = 5 nM. "Matrix" designates the buffer that contains 100 nM of RNAnc. Experiments were performed in duplicate, error bars represent the standard deviations.

Despite the detection limit in the pM range, only a low turnover in template was achieved even after 5 h using QD-PNAj conjugates. This was ascribed to the very slow rate at which the RNA as well as LDPNA dissociate from the ternary complex, thereby hampering the turnover in template. To test whether the temperature gradient can overcome this drawback, the cycling between the 44 °C and 58 °C was tested. This treatment was expected to first facilitate the hybridization between the PNA probes and RNA target resulting in dye transfer (44 °C) and then to induce the dissociation of RNA (58 °C) from a ternary complex. This approach was not successful due to the accelerated hydrolysis of thioester at elevated temperature and to the very sluggish hybridization between the probes and RNA target (*Figure 9.29*).

4.3.3 Optimization of assay conditions for the "mix and measure" approach. New and potent strategies for suppressing the nonspecific interactions

4.3.3.1 Influence of surfactants on the performance of OTR

The results described in the last two subchapters illustrated that the performance of QD-based OTR strongly depends on the PNA/QD density, with high PNA content being beneficial for faster signal enhancement. This permitted the use of QD-$(PNAj)_{59}$ at extremely low concentration (25 pM) while still generating significant fluorescent output. The optimization of temperature regime revealed that the OTR proceeds most effectively in a narrow temperature range. The major constraint of the QD-based OTR system remains the nonnegligible background signal brought about by nonspecific interactions between the QD-LAPNA and LDPNA as was illustrated in *Figure 9.28*. The experiments described in the following sections will show how the use of various surfactants and combinations thereof can help alleviate the degree of PNA-PNA aggregation and simplify the detection scheme.

The attempts to detect RNA directly from lysed serum revealed that such approach is impractical (*Figure 9.30*). Experimentally it was established that the buffer solution (AVL buffer) typically used for the lysis of viral particles precludes the hybridization between the PNA and RNA (*Figure 9.31*). This was attributed to guanidinium thiocyanate – a strong denaturant that is present in buffer at a very high concentration (50-70 %(w/w)). Additionally, the components of serum seem to have a negative impact on the hybridization and induce strong scattering that interferes with the detection by the means of fluorescence at the applied probe concentrations (*Figure 9.30*).

It was presumed that only the RNA target that has been previously extracted from the biological sample could be effectively detected using the developed OTR approach. To make the detection of low abundance RNA target feasible, it would be necessary to decrease the LOD. One way to achieve this is by further suppressing the NSI between the LDPNA and LAPNA, which occur to a noticeable degree despite the use of charged PNA probes and make it difficult to discriminate between the "low abundance target" and "no target" states. The latest solution to prevent the NSI involved the preheating of sample that contained QD-LDPNA and RNA target for 25 min prior to the addition of LDPNA. This approach combined with the use of TWEEN20 allowed to alleviate the nonspecific interactions, yet it did not fully eliminate them. Moreover, such an approach is applicable if the reaction is carried out in a reasonably big volume of buffer (e.g. 280 µl) so that evaporation is not significant within the reaction time.

If RNA detection is to be performed from RNA extract, the use of small reaction volumes is very advantageous, since this allows to preconcentrate the target. For example, if RNA is obtained from

10 ml of serum, it is beneficial to dissolve the obtained RNA extract in an as small volume as possible (e.g., 20 µl) to achieve effective pre-concentration of the target (in this example – 500-fold) in a tested sample. Clearly, preheating the solution for 25 min prior to LDPNA addition is impractical using such small volumes, requiring alternative means that would allow the mixing of all components (RNA target and PNA probes) without prior heating. To achieve this goal, more potent ways to limit the degree of nonspecific interactions are needed. These must permit the mixing all components in a microtiter plate at room temperature. Such approach would also exclude the need for additional equipment (thermoshaker) and minimize the quantity of required consumables such as plastic tubes.

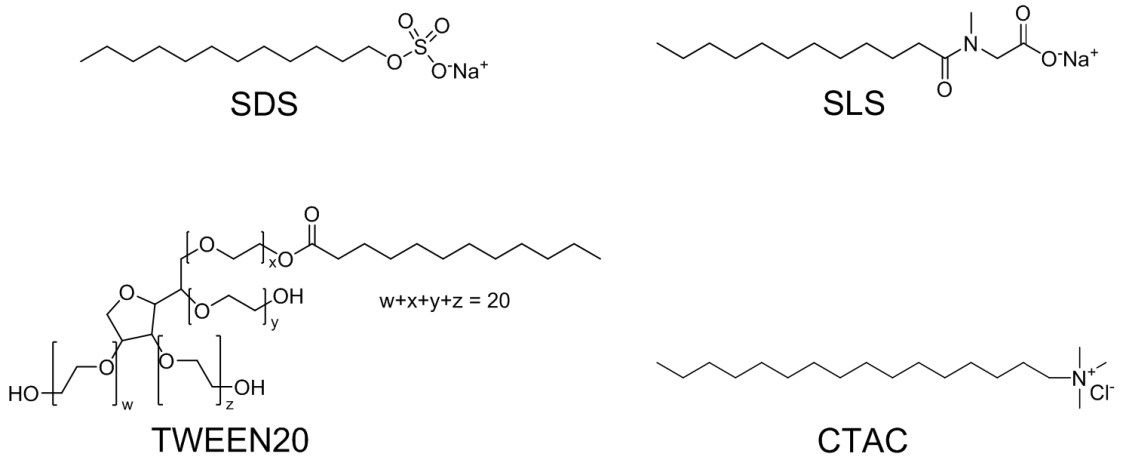

Scheme 4.9 Structures of surfactants that were used in the screening experiments aimed to decrease the background. SDS = sodium dodecyl sulfate, SLS = sodium lauroyl sarcosinate, TWEEN20 = polyoxyethylene (20) sorbitan monolaurate, CTAC = cetyltrimethylammonium chloride.

Table 4.7. Properties of surfactants used to optimize the content of buffer for RNA detection.

Surfactant	CMC, mM	CMC, % (w/v)	Charge at pH 7.0
SDS	8.2[129]	0.24	Negative
SLS	9.6[130]	0.28	Negative
TWEEN20	0.06[131]	0.0074	Non-ionic
CTAC	1.58[132]	0.051	Positive

An attractive strategy for the suppression of nonspecific interactions between the PNA probes is the use of surfactants; amphiphilic compounds, capable of disrupting the nonspecific interactions between the hydrophobic molecules. Generally, the surfactants are categorized according to the hydrophilic segment, which may be either ionic (anionic, cationic, zwitterionic) or non-ionic. To evaluate the effects of surfactants of different classes, screening experiments were performed. These involved the OTR reactions in buffers containing cationic (CTAC), non-ionic (TWEEN20) or anionic (SDS or SLS) surfactant (chemical structures are presented in *Scheme 4.9*). The critical micelle concentrations (CMC) and main properties of the selected surfactants are listed in *Table 4.7*.

The first set of experiments involved the use of surfactants at concentrations exceeding their CMC, as is usually recommended to achieve a reduction in the degree of NSI. The concentrations of both probes were increased by a factor of 3 relative to the optimal concentrations to boost the rate of NSI and to better illustrate the different behavior of probes under varied conditions. No preheating of the samples was carried out prior to the addition of LDPNA. Following the mixing of all components, the microtiter plate was covered with the transparent film for spectrophotometric measurements and inserted into the fluorescence reader. Temperature within the reader was kept at 40 °C, instead of optimal 44 °C due to the technical limitations of the reader's heating block.

As evident from the obtained data (*Figure 4.28*a-e), the studied surfactants affect both the NSI between the PNA probes and their hybridization with the RNA target. SDS significantly diminishes the degree of NSI between the PNA probes by disrupting the hydrophobic interactions between them. Unfortunately, it also affected the achievable signal-to-noise ratios. Probably, hybridization did not proceed well under the denaturing conditions imposed by 0.5 % SDS. Interestingly, another anionic surfactant, SLS, permitted the hybridization between the PNA and RNA, albeit it did not decrease the NSI between the probes to the extent as SDS did. This remarkable difference between the two surfactants of the same group (anionic) emphasizes the impact of surfactant's charged group on the performance of QD-based OTR. The effect of non-ionic surfactant (TWEEN20) on the hybridization was similar to SLS, however, the nonspecific adsorption occurs faster when TWEEN20 is used. It is reasonable to assume that the nonpolar tails of the studied anionic and non-ionic surfactants interact with the hydrophobic domains of PNA and prevent the PNA-PNA interactions.

The cationic detergent (CTAC) dramatically accelerates the NSI between the probes. In fact, the PNA-PNA interactions are stronger in the presence of CTAC than in the absence of any additives. It is likely that the positive charge of the polar group of this surfactant cancels out the negative charges of PNA probes, thereby decreasing electrostatic repulsion between them and enhancing the background. Therefore, CTAC was excluded from further studies.

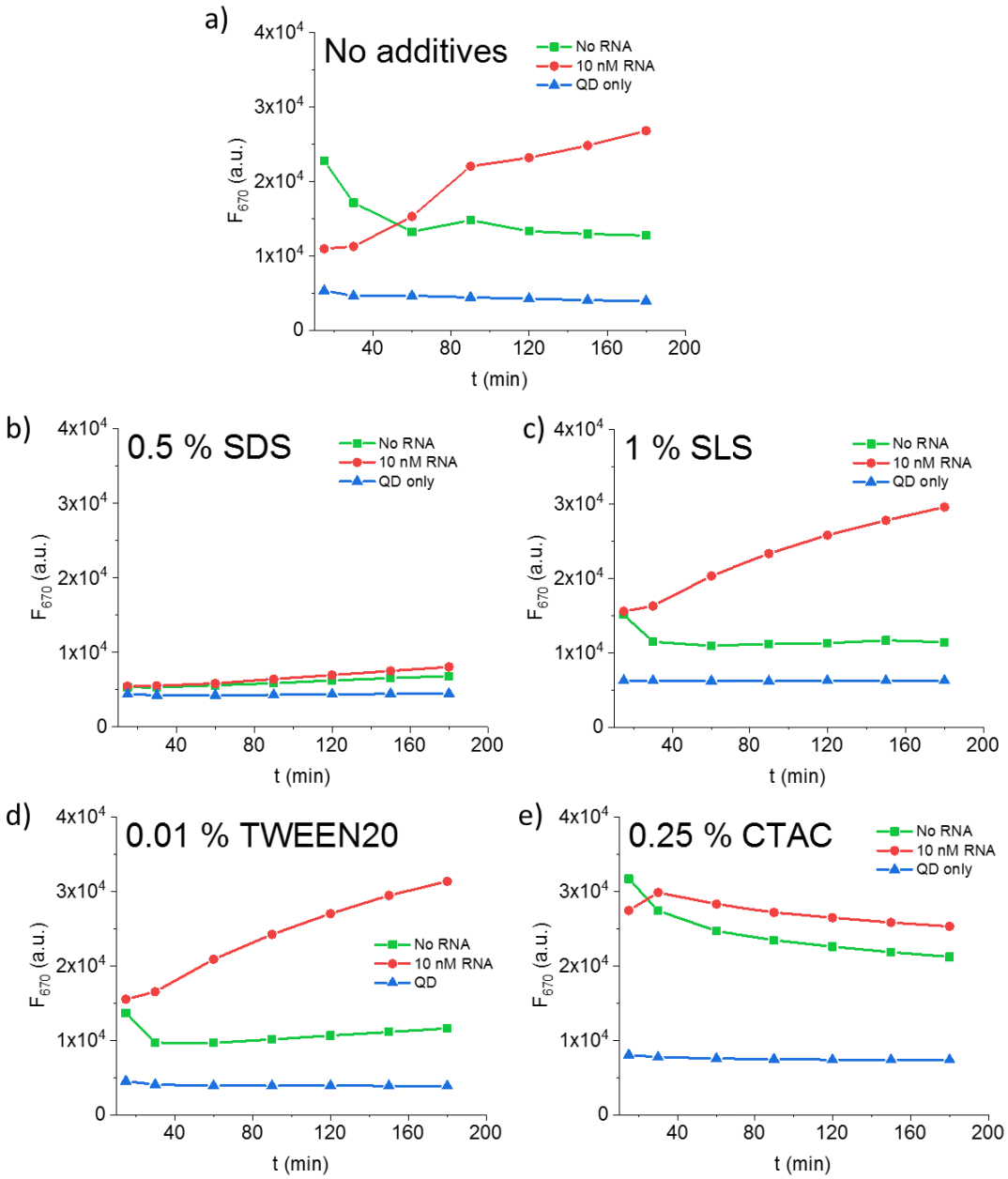

Figure 4.28. Impact of surfactants of different classes used at C > CMC on the degree of nonspecific interactions (NSIs) between the QD-$(PNAj)_{59}$ and PNAl. Detection of 10 nM RNAc in the absence of additives (a), in the presence of 0.5 % SDS (b), 1 % SLS (c), 0.01 % TWEEN20 (d), and 0.25 % CTAC (e). Conditions: C(QD-$(PNAj)_{59}$) = 75 pM, C(PNAl) = 2.5 nM, C(RNAc) = 10 nM. Citrate buffer: 40 mM citrate, 2 mM TCEP, 50 mM NaCl, specified content of surfactant (w/v), pH 7.0. T = 40 °C. λ_{ex} = 465 (35) nm, λ_{em} = 670 (25) nm. The concentrations of probes were 3 times higher than the optimal concentrations, thereby increasing the rate of NSI. All components were mixed at room temperature in a 96-well microtiter plate, covered with the transparent film and the kinetics were measured using Infinite F200pro (Tecan) reader.

Subsequently, the screening of the surfactants at different concentrations was performed. The aim of these experiments was to select the concentration that would diminish the degree of NSI between the probes, while not hampering the hybridization with the target. Anionic detergents were tested first because they provided the most notable reduction in background at concentrations exceeding their CMC. As illustrated in *Figure 4.29*, SDS remains a strong denaturant even at concentrations significantly below its CMC. However, among the concentrations studied only 0.02 % SDS provided

S/N higher than the additive-free buffer (*Figure 4.30*a). Lower concentration of SDS (0.004 %) was insufficient to prevent nonspecific interactions between the PNA probes. The concentration of SLS has a less pronounced influence on the performance of the system, as is illustrated in *Figure 4.29*b and all concentrations tested–either higher or lower than CMC–improved the S/N compared to the additive-free buffer (*Figure 4.30*b).

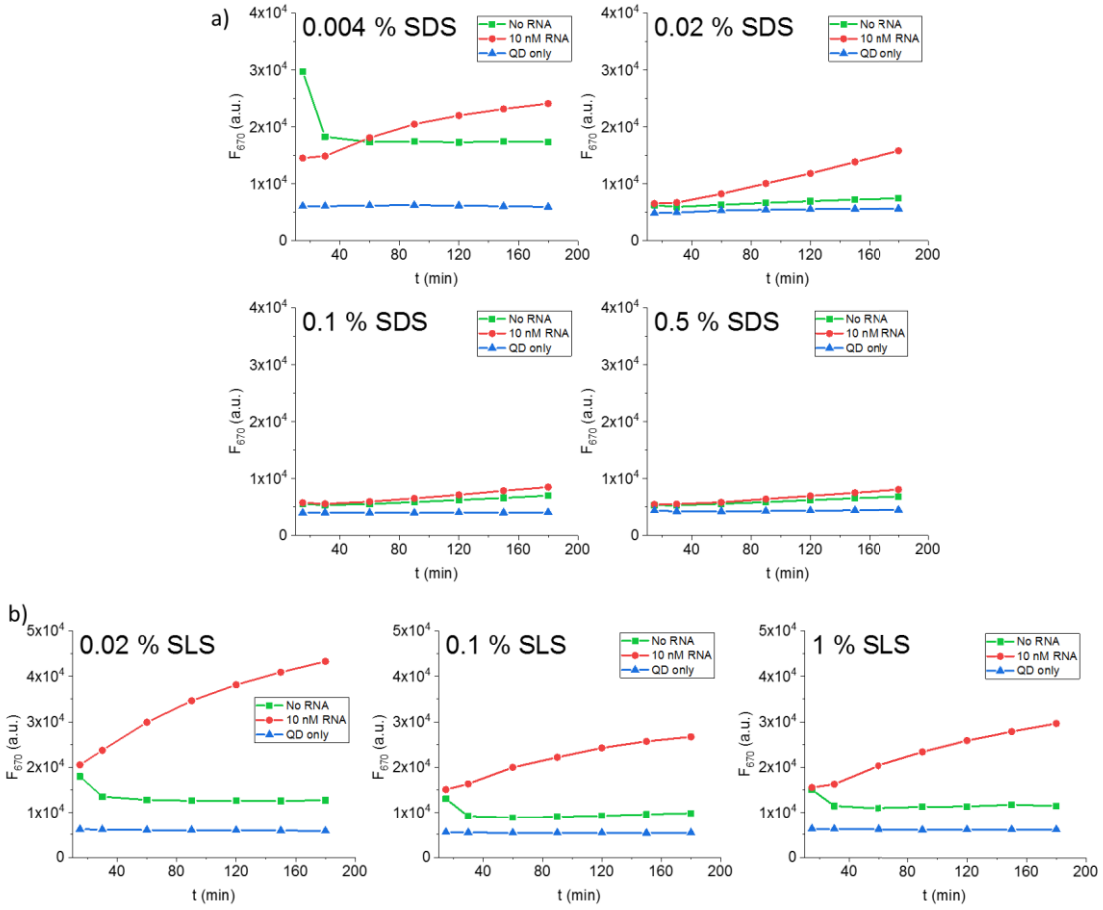

Figure 4.29. Impact of different concentrations of SDS (a) and SLS (b) on the efficiency of PNA/RNA hybridization and nonspecific interactions (NSIs) between PNA probes during the OTR. Conditions: C(QD-(PNAj)$_{59}$) = 75 pM, C(PNAl) = 2.5 nM, C(RNAc) = 10 nM. Buffer: 40 mM citrate, 2 mM TCEP, 50 mM NaCl, specified content of SDS (a) or SLS (b) (w/v), pH 7.0. T = 40 °C. λ_{ex} = 465 (35) nm, λ_{em} = 670 (25) nm.

An interesting aspect of the signaling in the absence of RNA is a spike after 15 min of reaction time and subsequent decline in the background after 30 min. This behavior is particularly pronounced when very low concentrations of surfactants or no additives are used. The reason for such an increased signal in the absence of RNA is the initial adsorption of LDPNA onto the nanoparticle surface at room temperature and subsequent desorption induced by heating the sample to 40 °C. This effect plays a smaller role when lower concentrations of QD-PNA are used and/or the heating of the sample that contains QD-PNA and RNA is performed prior to the addition of LDPNA probe.

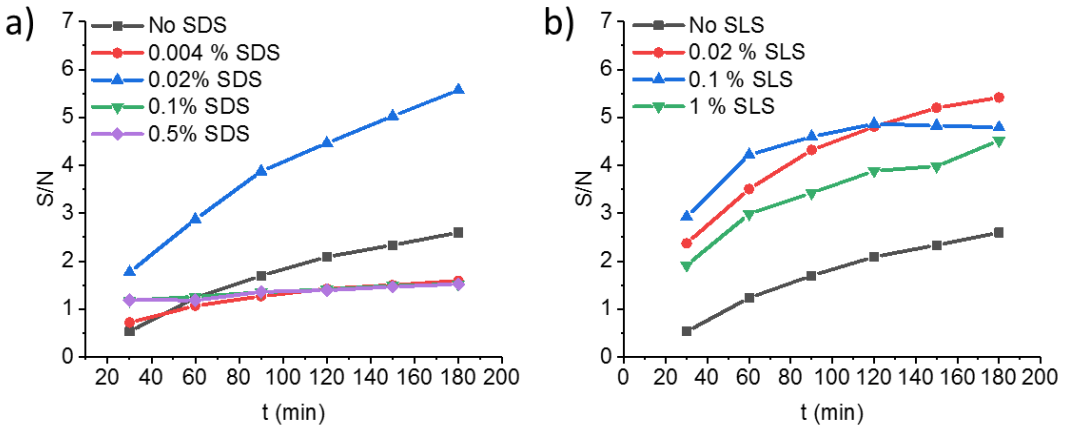

Figure 4.30. Impact of different buffer concentrations of SDS (a) and SLS (b) on the signal amplification obtained during the OTR between QD-$(PNAj)_{59}$ and PNAl. Conditions: C(QD-$(PNAj)_{59}$) = 75 pM, C(PNAl) = 2.5 nM, C(RNAc) = 10 nM. Buffer: 40 mM citrate, 2 mM TCEP, 50 mM NaCl, specified content of surfactant (w/v), pH 7.0. T = 40 °C. λ_{ex} = 465 (35) nm, λ_{em} = 670 (25) nm. The signal was corrected for the emission of QD only.

Having established the general trends for the surfactants it was decided to also test a combination of different surfactants as this could potentially result in the formation of a more efficient denaturation mixture. Subsequently, the combinations of different surfactant pairs were prepared. It was envisioned that the mixture of an anionic (SDS or SLS) and a non-ionic (TWEEN20) detergent could result in the formation of mixed micelles, i.e., micelles composed of two different kinds of surfactants. Such an approach was expected to provide the means to fine tune the composition of hybridization buffer by combining the benefits of detergents of different classes. First, different ratios of SDS/TWEEN20 were studied (*Figure 9.32*). As shown in *Figure 9.33* and *Table 4.8*, the S/N is strongly affected by the concentrations of SDS and TWEEN20. As anticipated, the synergetic effect leads to an improved S/N, with the best combination (0.02% SDS + 0.05 % TWEEN20) providing better results than each surfactant alone at the respective concentration (*Table 4.8*).

Table 4.8. Signal-to-noise ratios after 3 h of target-templated reaction using the studied surfactants and combinations thereof. Conditions: C(QD-$(PNAj)_{59}$) = 75 pM, C(PNAl) = 2.5 nM, C(RNAc) = 10 nM. Buffer: 40 mM citrate, 2 mM TCEP, 50 mM NaCl, specified content of surfactants (w/v), pH 7.0. T = 40 °C. For these experiments the concentrations of both PNA probes were increased by a factor of 3 relative to the optimum to accelerate the NSIs between them.

Additive	S/N after 3 h	Combination of additives	S/N after 3 h
No additives	2.60	0.02 % SDS/0.01 % TWEEN20	3.86
0.25 % CTAC	1.30	0.04 % SDS/0.01 % TWEEN20	3.66
0.004 % SDS	1.59	0.004 % SDS/0.05 % TWEEN20	4.78
0.02 % SDS	5.57	0.02 % SDS/0.05 % TWEEN20	**6.81**
0.1 % SDS	1.52	0.04 % SDS/0.05 % TWEEN20	4.29
0.5 % SDS	1.52	0.1 % SDS/0.04 % TWEEN20	4.32
0.02 % SLS	5.41	0.2 % SDS/0.03 % TWEEN20	1.93
0.1 % SLS	4.79	0.1 % SLS/0.05 % TWEEN20	**5.81**
1 % SLS	4.52		
0.01 % TWEEN20	3.56		
0.05 % TWEEN20	3.53		

The compilation of all experiments with surfactants, including those that combined SLS and TWEEN20 are presented in *Table 4.8*. The best signal amplification was obtained when either SDS or SLS was used at C < CMC in a combination with 0.05 % TWEEN20. Subsequently, these two buffer compositions were utilized to assess the OTR in the presence of pM concentrations of RNA target.

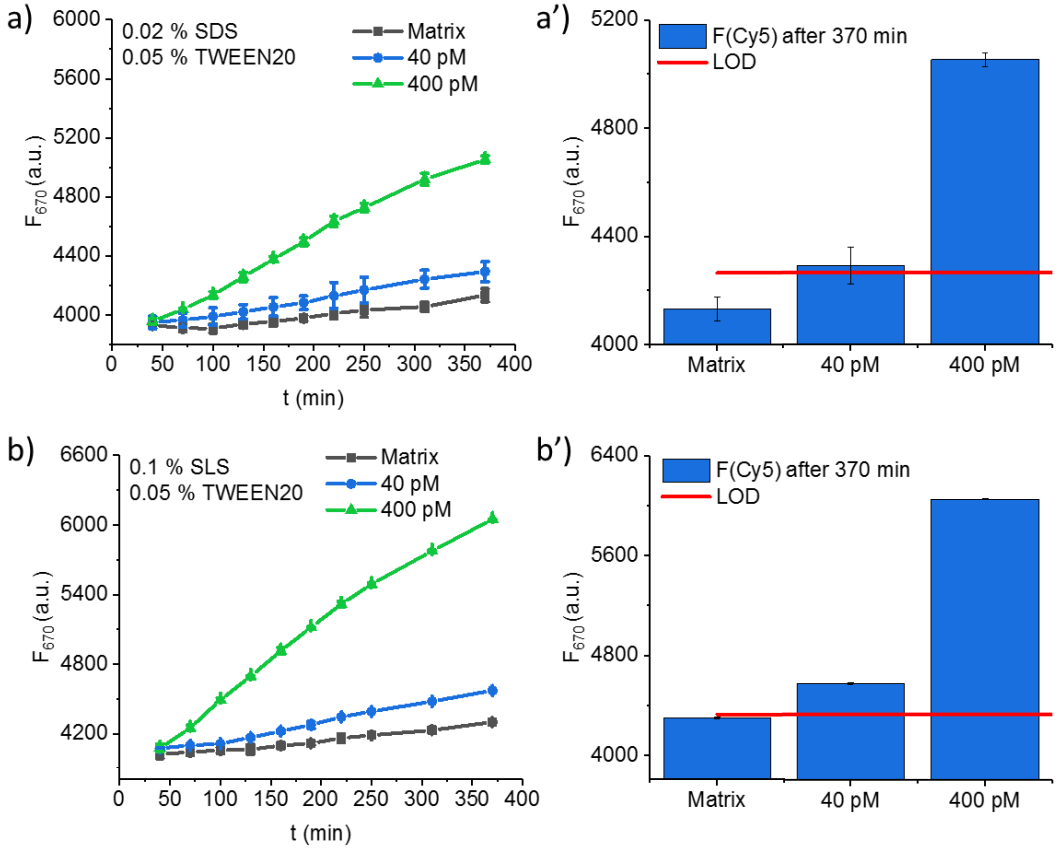

Figure 4.31. RNA-catalyzed dye transfer at different concentrations of RNA template in buffers with different contents of surfactants. Kinetics of RNA detection (a,b), and FRET-induced Cy5 emission after 370 min of templated reaction at different RNAc concentrations (a',b'). Conditions: C(QD-(PNAj)$_{59}$) = 25 pM, C(PNAl) = 600 pM, 40 or 400 pM of RNAc. Matrix: 100 nM RNAnc in citrate buffer (40 mM citrate, 2 mM TCEP, 50 mM NaCl, 0.05 % (w/v) TWEEN20, 0.02 % SDS (a) or 0.1 % SLS (b), pH 7.0). T = 40 °C. λ_{ex} = 465 (35) nm, λ_{em} = 670 (25) nm. Experiments were performed in a duplicate, error bars represent the standard deviations.

As illustrated in *Figure 4.31*, both buffers afforded the detection of 40 and 400 pM of RNAc despite the mixing of components at room temperature. Interestingly, the buffer that contained 0.1 % SLS and 0.05 % TWEEN20 provided stronger signal enhancement in the presence of both tested concentrations of RNA (*Figure 4.31*b') than the combination of 0.02 % SDS and 0.05 % TWEEN20 (*Figure 4.31*a'). This may result from the faster hybridization kinetics when the former buffer was used. Indeed, the increase in background signal is very similar for both buffers tested, however, the rate of templated reaction is accelerated if SLS, instead of SDS, is used in combination with TWEEN20 (*Table 4.9*). These results suggest that SDS has a more profound effect on the

hybridization efficiency between the probes and the target. Therefore, the buffer that contained SLS and TWEEN20 was used for all further experiments.

Table 4.9. Comparison of the initial signal enhancements of RNA-catalyzed dye transfer in buffers that contained different combinations of surfactants. Slope was calculated using the linear regression of Cy5 signal in the time range of 70 to 220 min.

	0.02 % SDS + 0.05 % TWEEN20			**0.1 % SLS + 0.05 % TWEEN20**		
	Slope (Fluor./min)	R^2	$Slope_i/Slope_{matrix}$	Slope (Fluor./min)	R^2	$Slope_i/Slope_{matrix}$
Matrix	0.65 ± 0.07	0.96	1.0 ± 0.1	0.70 ± 0.07	0.96	1.0 ± 0.1
40 pM RNA	1.03 ± 0.05	0.992	**1.6 ± 0.2**	1.91 ± 0.04	0.9986	**2.7 ± 0.3**
400 pM RNA	3.83 ± 0.07	0.9987	**5.9 ± 0.6**	7.05 ± 0.07	0.9996	**10 ± 1**

4.3.3.2 Impact of base-induced OTR quenching on the sensitivity of RNA detection

Having established the buffer composition that substantially suppressed the NSIs between the PNA probes, additional measures that could boost the S/N of RNA detection, were sought. As shown in *Figure 4.27*, the addition of a base after a certain incubation time can substantially improve the S/N of RNA detection. This advancement was made possible by the cleavage of QD-adsorbed thioesters that were responsible for FRET in the absence of target. It was envisioned that such treatment could in principle improve the detection of low concentrations of RNA target and to help discriminate between the "no target" and "low abundance RNA" states (*Figure 4.32*). To that end, the transfer reaction was carried out for 200 min and subsequently quenched by the addition of a base.

As illustrated in *Figure 4.32*, the addition of base after 200 min leads to a sharp decrease in Cy5 signaling after 15 min for all concentrations tested. Interestingly, following the initial drop after 200 min (after quenching with base) the emission of Cy5 starts to rapidly increase in the presence of 200 pM of target, remains at the same level (20 pM target) or continues to slowly decrease and reaches a plateau at 2 pM or if no target is present. I speculate that the initial drop in signal is due to the hydrolysis of thioesters (LDPNAs) that have formed ternary complexes with LAPNA and RNA but not yet reacted with the cysteine moieties of the LAPNA. The subsequent increase in signal for 200 pM RNA is probably induced by the transition of Cy5-linked LAPNA from rigid duplex into a flexible single strand following the base exposure. This can be expected to increase FRET efficiency and concomitant signal increase in the Cy5 channel.

The improved S/N during the detection of 20 pM and 200 pM of RNAc 30 min after the addition of base (*Figure 4.32*c), indicates that such treatment is very advantageous for signal enhancement at low RNA concentrations. For the detection of lower concentrations of RNA, further optimization is necessary, namely, faster hybridization kinetics is needed to achieve low and sub-picomolar LODs.

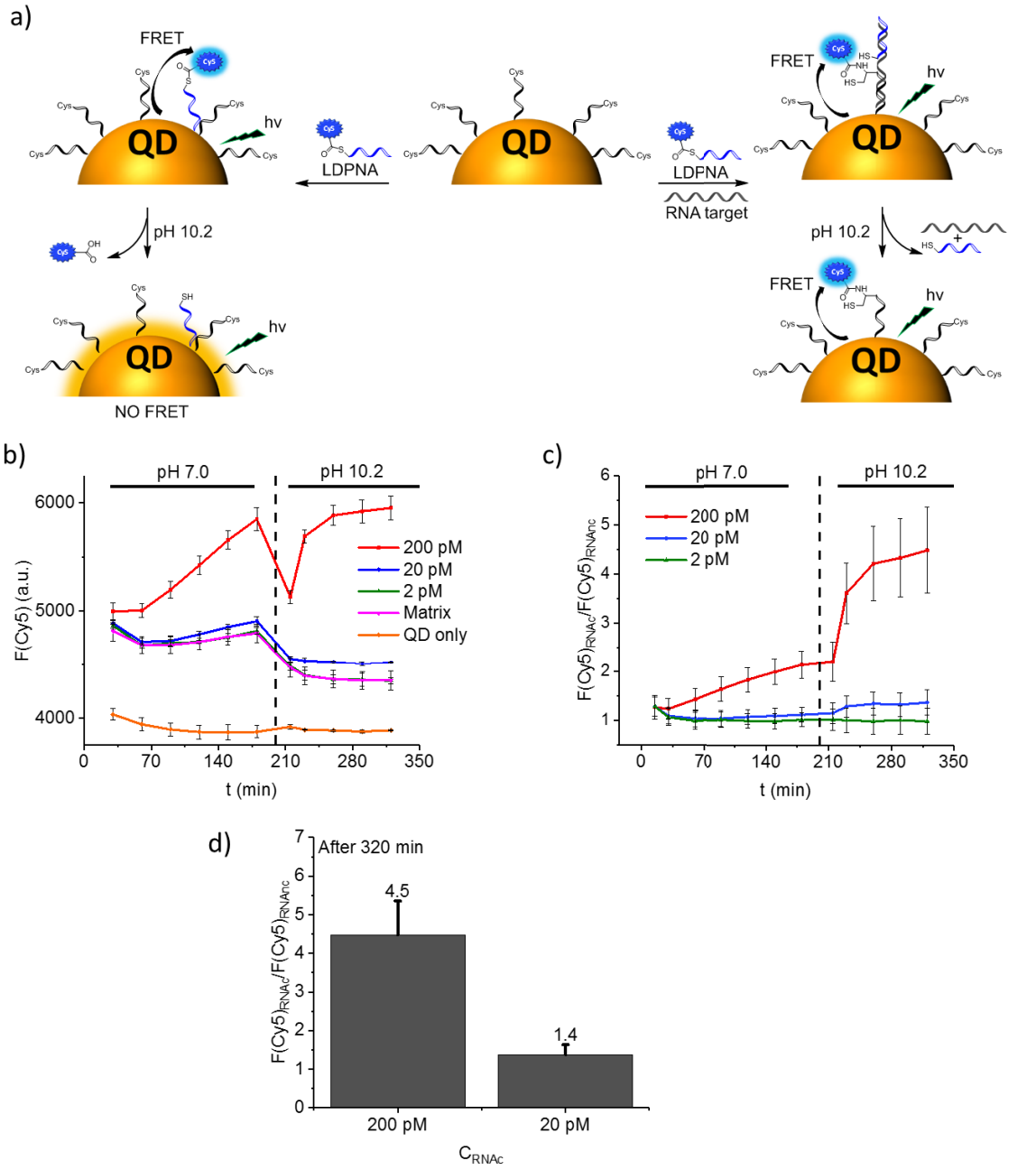

Figure 4.32. Thioester hydrolysis as a tool to improve the S/N of RNA detection. a) Schematic presentation of the impact of basic pH on the LDPNA, nonspecifically adsorbed on the QD-LAPNA (left) and on the dye transfer in the presence of RNA target (right). b,c) Time-course of FRET-induced Cy5 signaling for reactions performed at different concentrations of RNA target. Emission intensity in Cy5 channel (b) and S/N ratio (c) at pH 7.0 (the first 200 min) and after the increase of pH to 10.2 (200 min-320 min). d) S/N 120 min after the increase of pH to 10.2. Conditions: C(QD-$(PNAj)_{59}$) = 25 pM, C(PNAl) = 600 pM. Matrix: 100 nM RNAnc in citrate buffer (40 mM citrate, 2 mM TCEP, 50 mM NaCl, 0.05 % (w/v) TWEEN20, 0.1 % (w/v) SLS, pH 7.0). pH was adjusted to 10.2 by the addition of borate buffer (220 mM, pH 10.6) at a ratio of 1 to 5 (v/v) relative to the reaction mixture. T = 40 °C. λ_{ex} = 465 (35) nm, λ_{em} = 670 (25) nm. All experiments were performed in a triplicate, except matrix (6 times); error bars represent the standard deviations.

4.3.3.3 Influence of formamide on the OTR

The experiments described above were performed at elevated temperature to destabilize the secondary structure of RNA and to reduce the degree of NSI between the PNA probes. It is advantageous, however, to perform the detection at room temperature. Firstly, under such conditions the hydrolysis of the thioester is slower. This can allow to increase the reaction time without losing the reactive LDPNA. Secondly, measurements at room temperature produce a higher fluorescent signal due to the higher QY of Cy5 at room temperature (*Figure 9.25*).

To perform such experiments, it is necessary to use denaturating agents that destabilize the RNA secondary structure. Anticipating that formamide could accomplish this task, different concentrations of this compound were tested to optimize the buffer composition for RNA detection at 26 °C.

As illustrated in *Figure 4.33* the content of formamide has a profound effect on the efficiency of RNA-templated transfer reaction. Without or at 1 % formamide, the background signal exceeds the signal induced by 2 nM RNA target, implying that under such conditions RNA folding precludes the formation of PNA/RNA duplexes. Additionally, the nonspecific interactions are very strong at room temperature, making it impossible to distinguish the target from the background. At 4 % formamide, the signal induced by the RNA target can already be distinguished from the background (*Figure 4.33*c), albeit the enhancement is very weak with S/N = 1.4 after 3 h. In contrast, 20 % formamide allows for the detection of 2 nM RNA already after 15 min of incubation, with S/N reaching 6.6 after 3 h.

Increasing the pH to 10.2 after 180 min improved the S/N ratios for all buffer compositions used (*Figure 4.33*e). This treatment revealed that at 0 % or 1 % of formamide in buffer (*Figure 4.33*a and b) only a negligible fraction of FRET is caused by the hybridization between the PNA probes and the target, and most signal in Cy5 channel is produced by the nonspecifically adsorbed LDPNA, regardless of whether the RNA is present or not. Otherwise, the Cy5 emission in the presence of target would not decrease so sharply following the hydrolysis. On the other hand, 20 % of formamide both effectively disrupt the RNA secondary structure and prevents the nonspecific interactions between the probes, thereby inducing notable signal enhancement (*Figure 4.33*d).

These results demonstrate that the use of formamide is clearly advantageous if the detection is to be performed at room temperature. This allows to perform the assay using simpler equipment and to boost the fluorescence output due to the enhanced Cy5 QY at lower temperatures.

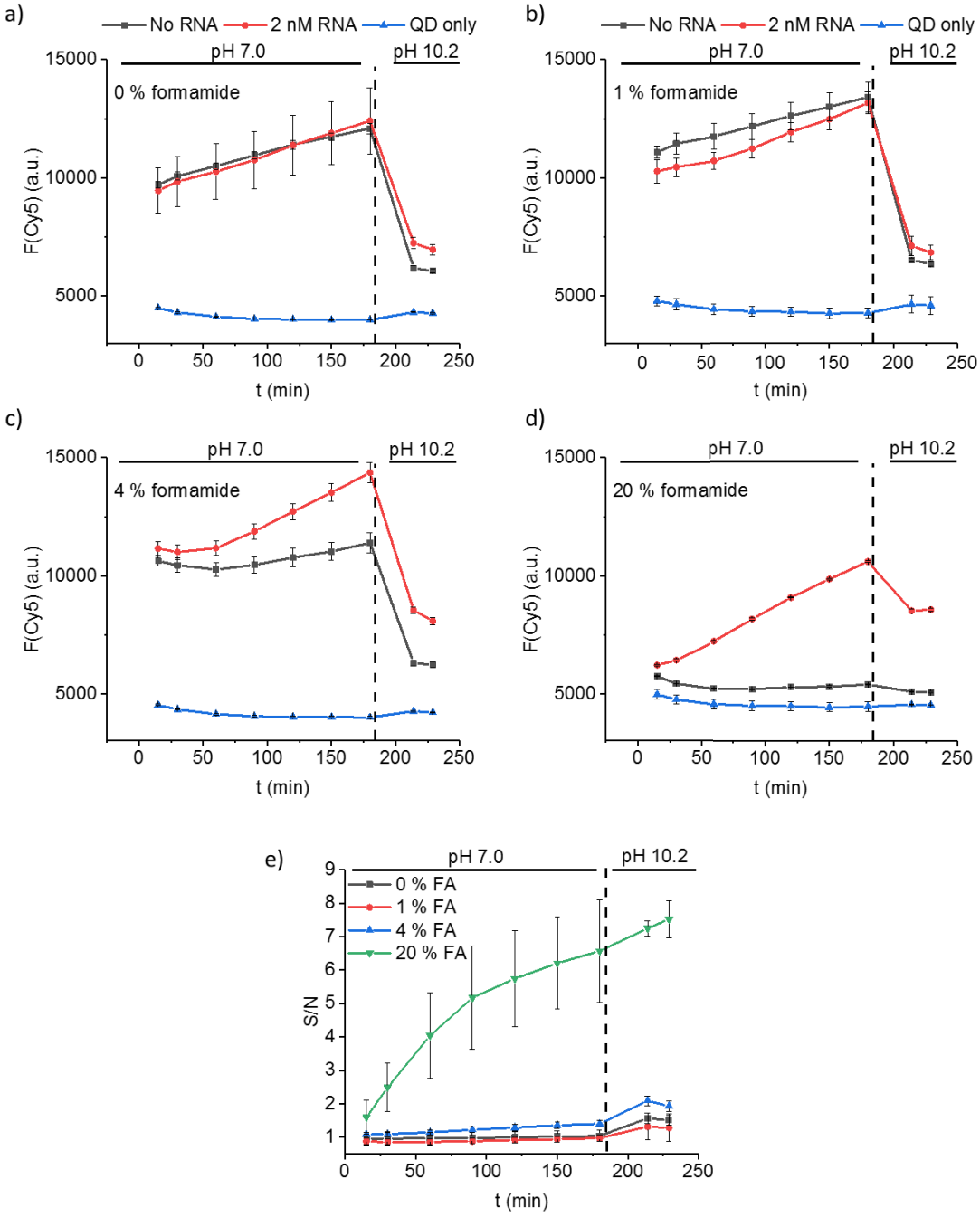

Figure 4.33 Optimization of formamide (FA) concentration for the detection of RNA at room temperature. Time course of RNA templated reaction between the QD-$(PNAj)_{59}$ and PNAl in the absence of formamide (a), in the presence of 1 % formamide (b), 4 % formamide (c), and 20 % formamide (d). e) Comparison of S/N for different buffer compositions during the detection of 2 nM of RNA target. Conditions: C(QD-$(PNAj)_{59}$) = 25 pM, C(PNAl) = 1 nM, C(RNAc) = 2 nM. Reaction was performed in a total volume of 200 µl. Initial buffer composition (0-180 min): a-c) 40 mM citrate, 50 mM NaCl, 2 mM TCEP, 0.05 % (w/v) TWEEN20, 0.1 % (w/v) SLS, specified content of formamide, pH 7.0; d) 32 mM citrate, 40 mM NaCl, 2 mM TCEP, 0.035 (w/v) TWEEN20, 0.1 % (w/v) SLS, 20 % formamide, pH 7.0. Reaction was performed at pH 7.0 for 180 min. Afterward the pH was adjusted to 10.2 by the addition of 40 µl of borate buffer (220 mM borate, pH 10.6) to hydrolyze all unreacted thioesters. T = 26 °C. λ_{ex} = 465 (35) nm, λ_{em} = 670 (25) nm. All experiments were performed in duplicate. This data indicates that the formamide content in buffer should exceed 20 % to permit RNA detection at room temperature.

4.3.4 Comparison of QD-based OTR to other methods in the field

The assay described in this work enables the detection of as little as 20 pM (4 fmol) of RNA target in a microtiter plate by using a conventional fluorescence reader. The optimized approach involves two steps: i) the mixing of PNA probes and RNA target, followed by incubation at 40 °C in a fluorescence reader; and ii) exposure of the reaction mixture to basic conditions, that improves the signal amplification by reducing the background signal. The assay requires very low concentrations of PNA probes (25 pM of QD-LAPNA, and 600 pM of LDPNA), can be performed isothermally and tolerates the presence of high concentration (100 nM) of noncomplementary RNA. In this sub-chapter the critical comparison of the developed system to other methods in the field is provided.

The recently reported one-step reverse transcription PCR assay allowed very sensitive detection of dengue genomic RNA with LOD in the range of 0.8 to 3 aM, depending on the serotype. This was accomplished by reverse transcribing the viral RNA into the complementary DNA, enzymatic pre-amplification of the latter, and subsequent detection of amplicons with fluorescent binders.[133] Another enzyme-based technique–reverse transcription loop-mediated isothermal amplification–has been used for the detection of dengue RNA with the LOD of 7 aM.[134] The method permitted isothermal detection of RNA and provided the sensitivity similar to PCR approaches. As of now, enzymatic methods for nucleic acid diagnostics are considerably more sensitive than the assay developed by me.

Compared to most QD-based systems that do not exploit the templated chemistry, the QD-based OTR offers a better sensitivity.[78, 135-138] This was achieved by using extremely bright polymer-coated QDs at very low concentration in conjunction with target-catalyzed signal amplification. It should be noted, however, that a few QD-based systems performed better than the system described in this thesis. For example, femtomolar LOD was achieved by using the FRET system that relied on energy transfer from the QD to a non-emissive quencher.[80] The approach utilizes the quenching of QD photoluminescence as a read-out, which can be prone to target analyte-independent quenching effects. This may impact the reliability and precision of the assay. A different FRET assay, which exploits single particle florescence measurements in a continuous flow, permitted the detection of DNA in the low femtomolar range.[81] Despite the very high sensitivity, the approach required complex instrumentation−a custom-made setup for confocal fluorescence measurements. In contrast, the assay developed by me can be performed using standard laboratory equipment, readily available in any laboratory that deals with fluorescent assays.

The developed system is significantly more sensitive compared to the gold nanoparticle-based Sticky-flares, reported by Briley et al.[139] This approach relied on the release of fluorescently labeled reporter probe from the nanoconjugate into solution upon binding with the complementary RNA and

permitted the LODs in nanomolar range. Gold nanoparticle loaded split DNAzyme probe permitted the LOD of 10 pM RNA.[140] This was achieved through the activation of nanoparticle-bound DNAzyme by the RNA target and subsequent cleavage of the fluorescently labeled substrate strand. This assay provided slightly higher sensitivity than the one described in this thesis.

The QD-based OTR compares favorably to the graphene oxide-DNA platform used for the multiplexed fluorescent detection of RNA reported by Yu et al.[141] The latter assay provided the LODs in the range of 136 to 210 pM, depending on the target.

A very interesting microarray assay that uses gold nanoparticle probes for the simultaneous detection of RNA and proteins was recently reported by the Mirkin group.[142] The strategy involved the capture of biotinylated RNA on the microarray slide, followed by the labeling with gold nanoparticles. The read-out was accomplished by using the light scattering of the conjugated gold nanoparticles. The approach offered an impressive LOD of 50 fM of RNA and a possibility to carry out the analyses of different classes of biomolecules simultaneously. On the other hand, the approach requires biotinylation of the nucleic acid target prior to its detection and involves multiple steps (e.g., washing of the slides, gold deposition). These features render the approach more cumbersome, yet significantly more sensitive than the assay developed by me.

Rhodamine-loaded polymeric nanoparticles were recently used for the construction of a FRET platform, which enabled the detection of sub-picomolar concentrations of nucleic acid target.[143] Such sensitivity was brought about by the very high molar absorptivity of the polymeric nanoparticles ($\varepsilon_{550} = 3.8 \cdot 10^8$ $M^{-1}cm^{-1}$) and the phenomenon of light-harvesting that permitted the energy transfer from thousands of donor dyes of nanoparticle to only 23 FRET acceptors. As of now, this system is more sensitive compared to the one developed by me. This is likely due to the outstanding brightness of the dye-loaded nanoparticles and the use of DNA probes, which are less prone to nonspecific interactions, compared to PNA oligomers.

It would also be instructive to compare the QD-based OTR to organic dye-based systems that exploit nucleic acid target for signal amplification. The previously developed transfer reactions, which utilize native chemical ligation principle, offered similar detection sensitivity in the low picomolar range,[15, 47] however were less cost-efficient, since the use of moderate-to-high nanomolar concentrations of probes was required. Very rapid templated reactions described by Shibata et al.[144] and Sadhu et al.[13] provided lower LODs of 0.5 pM and 5 pM, respectively, however were more time-consuming than the assay developed by me, which can be performed within a 3- and 5 times shorter time period. Furthermore, I defined the LOD based on the signal provided by the high concentration of noncomplementary RNA, as opposed to the abovementioned organic dye-based

systems for which the LODs were calculated based on the signal induced by the probes in the absence of any nucleic acids.

The developed QD-based OTR compares favorably to the dually labeled PNA FIT probes, that were reported to provide a LOD of 40 pM.[89] The achieved LOD is also lower compared to the ones provided by molecular beacons labeled with organic dyes (LOD = 500 pM),[145] or label-free multifunctional molecular beacons (LOD = 250 pM).[146]

5 Conclusions & Outlook

Conclusions

Within the course of this work, a nanoparticle-based approach for target-templated RNA detection was developed. The system consisted of two reactive peptide nucleic acid (PNA)-based probes. Label acceptor (LAPNA) probe was immobilized on a semiconductor quantum dot (QD) nanoparticle and contained a cysteine residue at the N-terminus (*Scheme 5.1*). Label donor (LDPNA) probe was functionalized with a cyanine dye, attached as a thioester. These recognition elements were designed to hybridize adjacently to the complementary RNA. The presence of RNA target in the sample triggered the reaction between the functional groups of PNA, which proceeded in a native chemical ligation manner and resulted in the transfer of cyanine dye onto the QD, as shown in *Scheme 5.1*. This could be monitored via fluorescence spectroscopy by measuring the energy transfer from the QD to the cyanine dye.

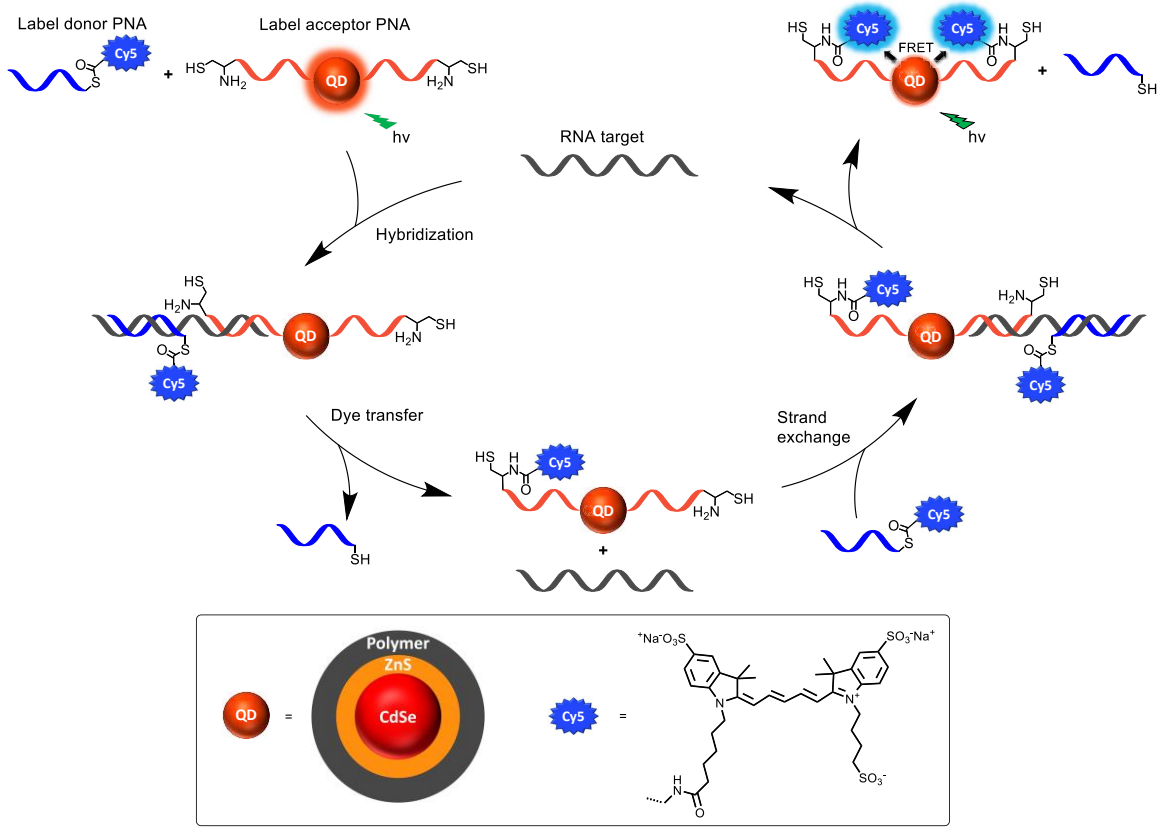

Scheme 5.1 Target-catalyzed RNA detection using QD as FRET donor and Cy5 as FRET acceptor (top). Polymer-encapsulated semiconductor QD and asymmetric Cy5 selected for assay development (bottom).

Polymer-encapsulated QDs were chosen to act as a FRET donor due to their exceptional brightness and good colloidal stability, and subsequently used as a carrier of label acceptor PNA probes. Highly

hydrophilic and bright asymmetric tri-sulfo-Cy5 was selected for the role of FRET acceptor and subsequently used for the synthesis of label donor PNA probes.

To immobilize the LAPNA on the surface of the QD, a two-step strain-promoted azide-alkyne cycloaddition-based strategy was developed (*Scheme 5.2*). This approach permitted bioorthogonal immobilization of cysteine functionalized PNA on a QD and adjustment of PNA labeling density. Experimentally it was established that incorporation of negatively charged glutamic acid residues into both PNA probes during the solid phase PNA synthesis was vital to prevent the LDPNA from nonspecifically adsorbing on the surface of QD-LAPNA.

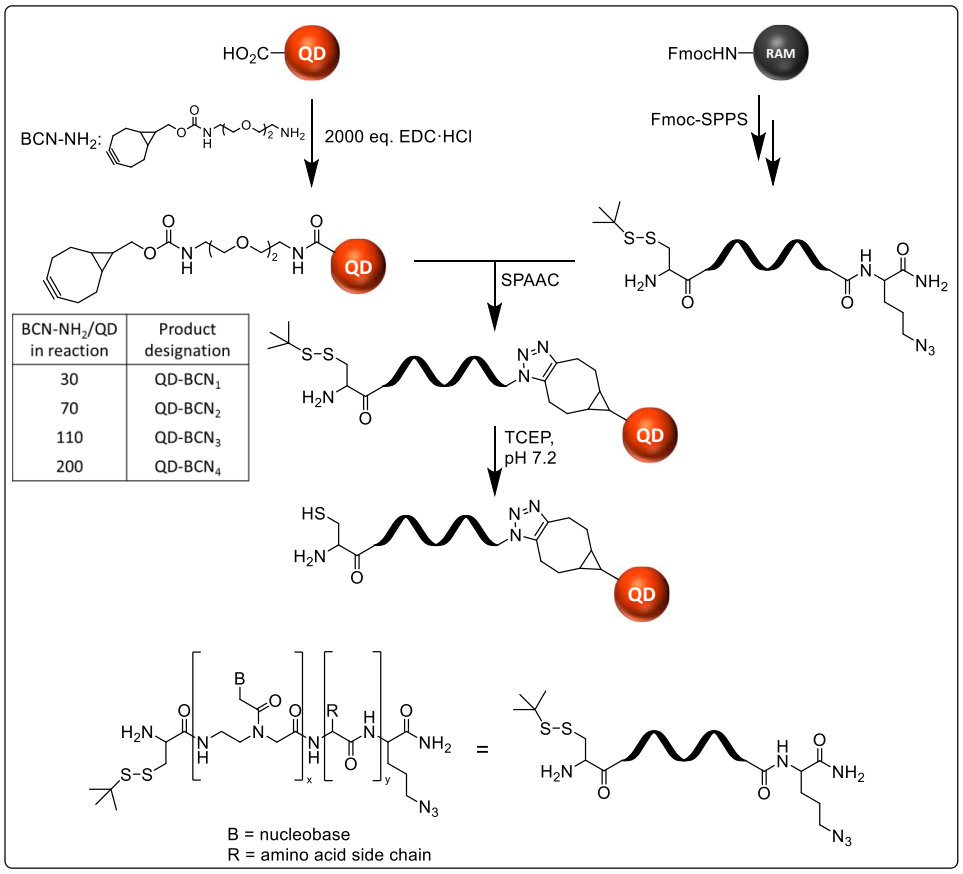

Scheme 5.2. Strategy for the immobilization of LAPNA on a QD using strain-promoted azide-alkyne cycloaddition (SPAAC).

The RNA-templated reactions between short PNA probes (combinations of 6-8-mers) were monitored by measurement of Cy5 emission upon excitation of the QD at 435 nm. These systems allowed the detection of nanomolar concentrations of RNA target within one day. The rather high LOD is probably due to sluggish kinetics of PNA-RNA hybridization on the QD surface. An extension of the PNA probes to a 9-mer (LDPNA) and an 11-mer (LAPNA) (*Figure 5.1*, top panel) decreased the LOD to the picomolar range, as shown in *Figure 5.1*, bottom panel. Detection of an RNA target was accomplished despite the presence of high excess (100 nM) of noncomplementary RNA in buffer. This outcome was made possible by i) using QD-PNAj conjugate with a high PNA

labeling density that provided high affinity binding to RNA target, ii) elevating temperature to destabilize the secondary structure of RNA and accelerate strand exchange reactions, and iii) the use of a combination of surfactants – polyoxyethylene (20) sorbitan monolaurate (TWEEN20) and sodium lauroyl sarcosinate (SLS) to suppress nonspecific interactions between the PNA probes. With these conditions, combined with the use of bandpass filter-based fluorescence read-out, the assay was performed using only a microtiter plate and conventional fluorescence reader, despite the probes being used at extremely low (pM) concentrations.

PNAl: Ac-$(Glu)_3$-Gly-**gagacagca**-Cys(Cy5-Gly)-NH_2

QD-$(PNAj)_{59}$: H-Cys-**tctctggtctt**-$(Glu)_2$-Orn(TA-**QD**)-NH_2

RNAc: 3′-UC**CUCUGUCGU**CCU**AGAGACCAGAA**AGG-5′

RNAnc: 5′-GUGCAAAUGGGACUUAGCCGCACUCCUA-3′

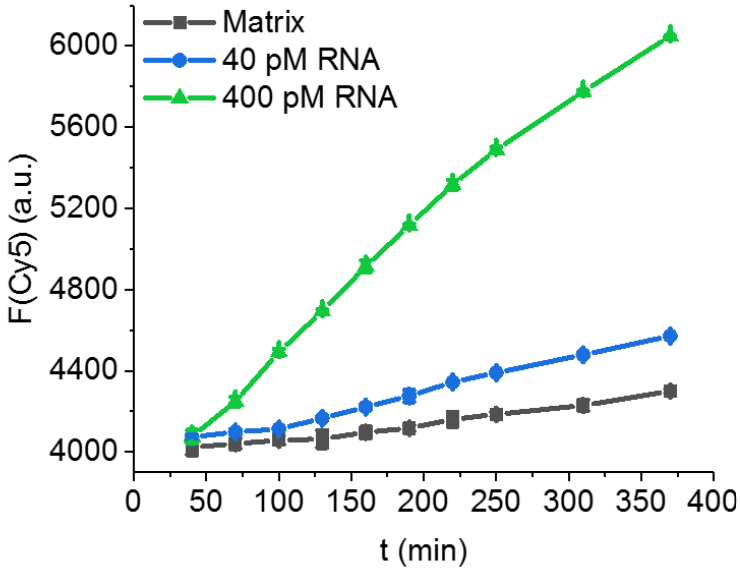

Figure 5.1. Top: PNA probes (QD-$(PNAj)_{59}$ and PNAl) of optimized nucleobase- and amino acid composition that were used for the detection of RNA; complementary (RNAc) and noncomplementary (RNAnc) RNA sequences used in the study. Bottom: Time course of RNA-catalyzed dye transfer monitored via FRET-induced emission of Cy5. Conditions: C(QD-$(PNAj)_{59}$) = 25 pM, C(PNAl) = 600 pM, 40 or 400 pM of RNAc. Matrix: 100 nM RNAnc in citrate buffer (40 mM citrate, 2 mM TCEP, 50 mM NaCl, 0.05 % TWEEN20 (w/v), 0.1 % SLS (w/v), pH 7.0). T = 40 °C. λ_{ex} = 465 (35) nm, λ_{em} = 670 (25) nm. Experiments were performed in a duplicate, error bars represent the standard deviations.

A further increase in sensitivity of the method was obtained when base (pH 10.2) was added after the OTR (*Figure 5.2*a). Under these conditions, the thioester bond in LDPNA undergoes hydrolysis. As a result, nonspecifically adsorbed LDPNA probes will release Cy5. The resulting decrease of the background signal is illustrated in *Figure 5.2*b. The strategy was found to significantly improve the signal enhancement in the presence of low concentrations of RNA target (*Figure 5.2*c) and confirmed that the detection of RNA proceeded through the formation of a hydrolytically stable amide bond. This approach allows to carry out the assay using the conventional microtiter plate reader and permits the detection of as low as 20 pM RNA within 320 min.

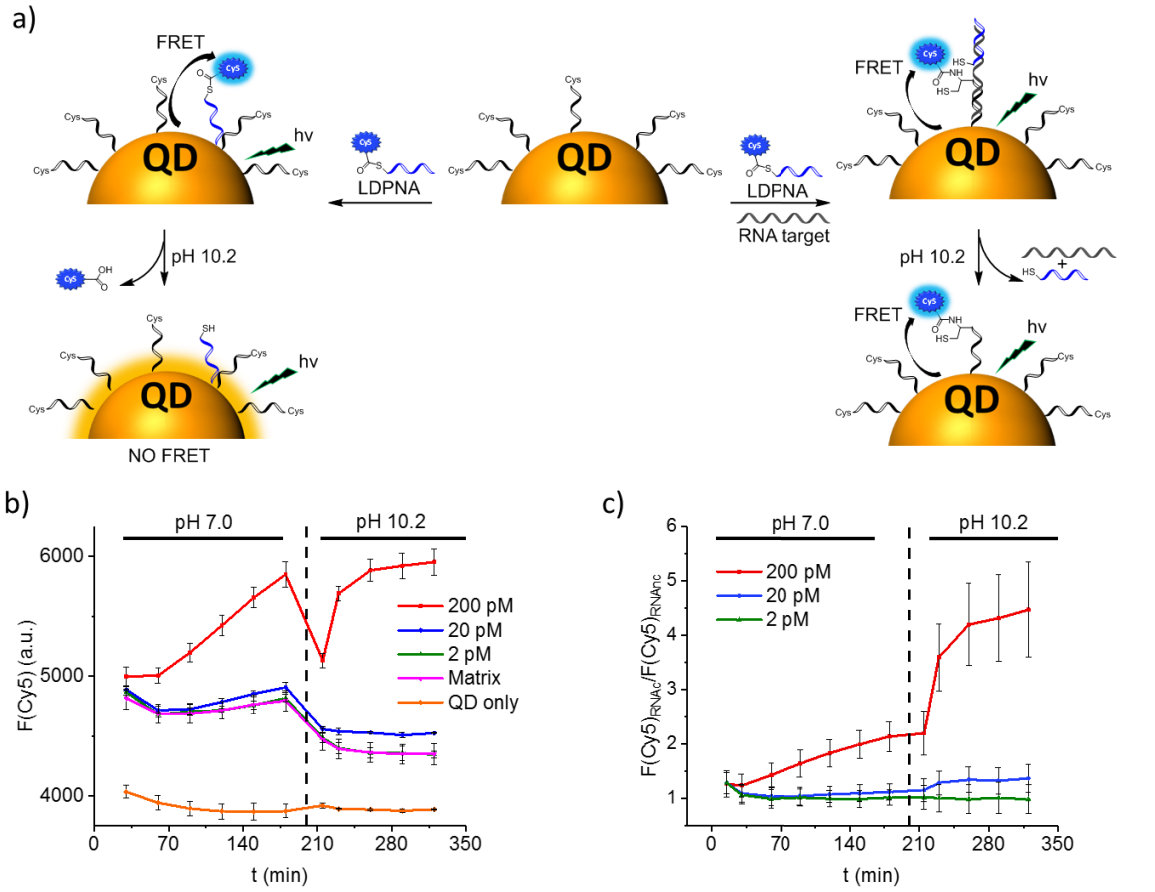

Figure 5.2. Thioester hydrolysis as a tool to improve the S/N of RNA detection. a) Schematic presentation of the impact of basic pH on the LDPNA nonspecifically adsorbed on the QD-LAPNA (left) and on the dye transfer in the presence of RNA target (right). b,c) Time-course of FRET-induced Cy5 signaling for reactions performed at different concentrations of RNA target before and after the addition of base. All experiments were performed in a triplicate, except matrix (6 times); error bars represent the standard deviations.

Quantum dot-based oligonucleotide-templated reactions are a new and powerful tool for RNA detection owing to the economic and performance benefits. The unprecedented brightness of quantum dots combined with the signal enhancement by target-templated reaction allows the acquisition of optical (fluorescent) signals at very low probe concentrations, making the strategy an attractive cost-efficient alternative to other enzyme-free RNA/DNA detection schemes. This stems from the fact that the amount of reactive antisense probes can be considerably reduced, without sacrificing sensitivity.

Outlook

This work has illustrated that QD-based OTR systems can be successfully used for the detection of RNA using target-templated transfer of an organic dye onto the QD. While the approach offered several important advantages over organic dye-based strategies, the sensitivity must be further improved to detect lower RNA concentrations. Firstly, the kinetics of PNA/RNA binding on the surface of a nanoparticle could be accelerated by using longer probes, thereby decreasing the assay duration. Furthermore, the ability to perform the reaction within a shorter time frame would minimize the impact of thioester hydrolysis on the detection scheme, since it would have less time to compete with the target-catalyzed acyl transfer. Secondly, despite the successful efforts to decrease the degree/rate of nonspecific adsorption of LDPNA on the QD-LAPNA, this process was not eliminated and led to non-negligible FRET signal in the absence of RNA target. One way to tackle this issue would be to use PNA probes with a higher content of glutamic acid residues, and/or probes with lower purine content, although the latter strategy is less straightforward and depends on the conserved regions of the viral genome. Alternatively, enhanced probes with a charged backbone (e.g., locked nucleic acid (LNA)) could be used instead of PNA in order to increase the electrostatic repulsion between the recognition elements, thus diminishing the background. To eliminate the need to carry out the OTR on the nanoparticle surface altogether, the target-templated reaction could be in principle performed in solution and its product subsequently separated using the QD to achieve the read-out. For example, instead of immobilizing the label acceptor probe on the QD, it could be equipped with a biotin functionality and used for the OTR in solution. The OTR product could be then separated using the streptavidin-functionalized QDs thereby enabling FRET-based read-out. Such a detection scheme is envisioned to offer faster kinetics of hybridization and higher turnover in this QD-based FRET read-out system.

Furthermore, the assay strategy should be in principle applicable to other kinds of polymer-coated nanoparticles, such as Cd-free QDs, and gold nanoparticles or nanoclusters which could ultimately be used for production of environmentally friendly assay kits. The developed approach is potentially useful for identification of biomarkers in biological samples of affected individuals, or for routine screening of donated blood for the presence of undesirable viral or bacterial species.

6 Experimental Section

6.1 Materials & Methods

6.1.1 Chemicals

Quantum dots Qdot® 605 VIVID carboxyl were purchased from Thermo Fischer Scientific. TOP/TOPO passivated core/shell CdSe/CdS QDs were purchased from CAN GmbH. CdTe QDs passivated with mercaptosuccinic acid (MSA) were purchased from PlasmaChem GmbH. RNA oligonucleotides were obtained from Biomers.net. Resins for SPPS were purchased from Rapp polymer and Novabiochem, protected amino acids from Novabiochem, Iris Biotech, and Bachem, respectively. PNA monomers were purchased from Link technologies. Cy5-carboxylic acid (product number S 2405) was purchased from FEW chemicals and Cy5-N_3 (sulfo-Cy5-azide) from Jena Bioscience. Illustra MicroSpin G-50, PD MiniTrap G-10 and G-25 columns were obtained from GE Healthcare, Amicon Ultra-0.5 centrifugal filter devices with NMWL 10 kDa from Merck Millipore, and ultrapure DNase/RNase free water, used for the preparation of buffer solutions, from Thermo Fischer Scientific, respectively. Chemicals used for the preparation of buffer solutions were of molecular biology grade (RNase-free) and purchased from Sigma-Aldrich. Other chemicals were purchased from Roth, Sigma-Aldrich, Carbolution Chemicals and TCI.

6.1.2 Analytical methods

Analytical UPLC-MS.

UPLC-MS spectra were recorded with an "Acquity UPLC" (Waters) system using the column: ACQUITY UPLC® Peptide BEH C18, 130 Å, 1.7 µm, 2.1 x 50 mm. A binary mixture of **solvent A: 98.9% H_2O, 1% MeCN, 0.1% TFA**, and **solvent B: 98.9% MeCN, 1 % H_2O, 0.1% TFA** was used for the preparation of a mobile phase. A linear gradient with a flow rate of 0.5 ml/min and a column temperature 50 °C were used for all samples. Optical signal detection was performed at 260 nm unless otherwise noted. ESI-MS spectra were recorded in a positive mode.

Preparative HPLC.

PNA probes were purified on an Agilent 1100 series instrument with the semi-preparative column (VP 250/10, Nucleodur C18 Gravity, 5 µm). Purifications were performed at room temperature using the flow rate of 6 ml/min. The solvents used for the binary eluent mixture were: **Solvent A: 98.9% H_2O, 1% MeCN, 0.1% TFA**, and **Solvent B: 98.9% MeCN, 1 % H_2O, 0.1% TFA**. Optical monitoring of signals was performed at 260 nm, 280 nm, and/or 650 nm. The combined fractions of purified products were lyophilized and stored at -20°C prior to further use.

MALDI-TOF MS.

MALDI-TOF mass spectra were recorded with "*AXIMA Confidence*" instrument (Shimadzu Biotechnology) in a positive mode using α-Cyano-4-hydroxycinnamic acid (CHCA) as matrix. For the measurements, 1 µl of sample was mixed with 1 µl of the matrix, the mixture was dried on air and subsequently analyzed using MALDI-TOF mass spectrometry.

UV-Vis spectroscopy.

Absorption measurements used for the calculation of quantum yields were performed on a *Specord 210 Plus* (Analytik Jena) spectrometer using the cuvettes with 1 cm pathway. Absorption spectra of QD conjugates, concentrations of RNA and PNA oligos, were recorded on a *NanoDrop ND-1000* spectrometer. The molar extinction coefficients of the PNA probes were calculated based on a base composition model using the ATDBio.com online software.

Fluorescence spectroscopy.

QYs of QDs were measured absolutely with a *Quantaurus Spectrometer C11347* (Hamamatsu). QYs of organic dyes were measured relative to quantum yield standards using a calibrated *FLS920* (Edinburgh Instruments) fluorescence spectrometer. Other luminescence spectra were recorded either on a *NanoDrop ND-3300* fluorometer (FL1) or *FluoroMax®-4* (Horiba scientific) fluorescence spectrometer.

Fluorescence spectroscopy measurements using microplate readers.

Fluorescence measurements in 96- or 384-well plates were performed using the *Infinite® M200pro* (Tecan) reader or *Infinite® F200pro* (Tecan) microplate reader. Fluorescence measurements were performed in a top mode. Black polypropylene 96-well plates and 384-well non-binding well plates were purchased from Greiner Bio-One GmbH.

For OTRs performed in a thermoshaker: the samples were heated using the thermoshaker and then transferred to the microtiter plate for fluorescence measurements, with the temperature in the reader adjusted to 31 °C or 32 °C.

For OTRs performed in a microtiter plate: following the mixing of all components, the microtiter plate was sealed with film (Greiner ViewSeal, transparent), inserted into the reader and the fluorescence was measured at the incubation temperature.

NMR spectroscopy.

^{1}H and ^{13}C NMR spectra were recorded using the Bruker nuclear spectrometers Avance II 300 MHz and Avance II 500 MHz. The deuterated solvent (DMSO-d6) for NMR spectroscopy was purchased from Deutero GmbH. Chemical shifts (δ) are given in parts-per-million (ppm). The coupling constants (*J*) are given in Hertz (Hz). The obtained NMR spectra were calibrated using the ^{1}H and ^{13}C signals of the solvent (DMSO-d6) (^{1}H δ = 2.50 ppm; ^{13}C δ = 39.52 ppm). ^{13}C NMR experiments were carried out by using attached proton test (APT) to distinguish between the quaternary carbon and CH_2 signals (negative) from CH and CH_3 signals (positive). NMR spectra were analyzed using the MNova NMR software. To designate the multiplicity of recorded signals the following abbreviations were used: s = singlet, d = doublet, t = triplet, q = quartet, quint = quintet, dt = doublet of triplets, m = multiplet.

6.2 Synthesis of Cyanine Dyes

6.2.1 Synthesis of symmetric di-sulfo Cy5

Synthesis of 2,3,3-trimethyl-1-(4-sulfobutyl) indolium, inner salt (1)

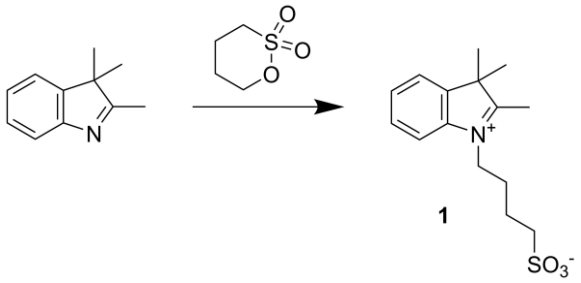

Synthesis of compound **1** was based on the reported procedure with some modifications.[109] In brief, 1.875 g (11.8 mmol) of 2,3,3-trimethylindolenine was mixed with 1.7 ml (16.5 mmol) of 1,4-butane sultone. Then the mixture was stirred at 120 °C for 165 min. Next, the solidified pink substance was washed with hexane, dissolved in 3.5 ml of ethanol, and precipitated by the addition of 5 ml of cold diethyl ether, and acetone until most of the solid crystallized. Finally, the product was filtered and dried under high vacuum to afford 1.362 g of pink solid (yield 39 %). The NMR spectral data was in agreement with the published data.[109]

$C_{15}H_{21}NO_3S$. MW = 295.40 g/mol. ^{1}H NMR (500 MHz, DMSO-d6) δ 8.06 – 8.00 (m, 1H, C**H**$_{Ar}$), 7.86 – 7.80 (m, 1H, C**H**$_{Ar}$), 7.64 – 7.58 (m, 2H, C**H**$_{Ar}$, C**H**$_{Ar}$), 4.54 – 4.44 (m, 2H, C**H**$_2$), 2.85 (s, 3H, C**H**$_3$), 2.03 – 1.89 (m, 2H, C**H**$_2$), 1.81 – 1.66 (m, 2H, C**H**$_2$), 1.53 (s, 6H, 2 x C**H**$_3$). Note: Methylene group with the chemical shift at δ 2.50 (2H, 2 x C**H**$_2$-SO_3^-) overlaps with the peak of the solvent and was resolved via ^{1}H-^{1}H COSY NMR (Appendix).

Synthesis of 2-bromomalonodianile (2).

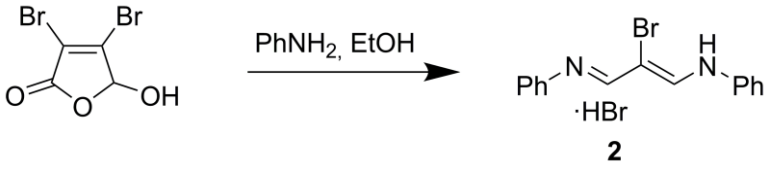

The protocol was based on the known procedure.[110] A solution of 1.0 ml (11.1 mmol) of freshly distilled aniline in 4.65 ml of dry ethanol was added to a solution of 1.43 g (5.55 mmol) of mucobromic acid in 6.6 ml of dry ethanol under stirring. The addition of aniline was accomplished within 9 min at 22 °C. Then the mixture was heated to 40 °C for 15 min. Next, the solution was cooled down in an ice bath that resulted in the formation of yellow precipitate that was subsequently

removed by filtration and washed with cold diethyl ether. Afterwards, the crude was dissolved by the addition of 20 ml of dry ethanol and heating to 90 °C. Following the cooling, the product was precipitated with 50 ml of cold diethyl ether, isolated via filtration and washed with cold diethyl ether. Finally, the solid was dried under high vacuum affording 605 mg (yield 29 %) of deep yellow crystals. NMR spectral data was in agreement with the published data.[110]

$C_{15}H_{14}Br_2N_2$. MW = 382.10 g/mol. ^{1}H NMR (300 MHz, DMSO-d6) δ 11.56 (s, 2H, 2 x N**H**), 9.49 (s, 2H, 2 x C**H**), 7.68 (d, *J* = 8.1 Hz, 4H, 4 x C$\mathbf{H}_{Ar}$), 7.50 (t, *J* = 7.8 Hz, 4H, 4 x C$\mathbf{H}_{Ar}$), 7.33 (t, *J* = 7.3 Hz, 2H, 2 x C$\mathbf{H}_{Ar}$). ^{13}C NMR APT (75 MHz, DMSO-d6) δ 157.60 (2 x **C**H), 138.58 (2 x $\mathbf{C}_{aryl}$), 129.74 (4 x **C**H_{aryl}), 127.02 (2 x **C**H_{aryl}), 119.55 (4 x **C**H_{aryl}), 89.25 (**C**-Br).

Synthesis of symmetric disulfo-Cy5-Br (3).

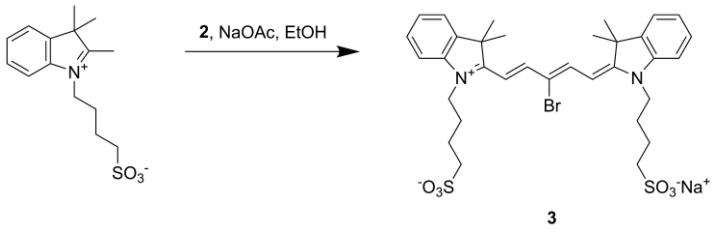

3

The procedure was based on the reported synthesis of asymmetric cyanine and was subsequently optimized for the synthesis of a symmetric cyanine.[147] 0.389 g (1.3 mmol) of **1** were mixed with 0.278 g (0.73 mmol) of **2** and 0.123 g (1.5 mmol) of sodium acetate in 21 ml of dry ethanol under Ar atmosphere and stirred at 85 °C for 3 h. Afterwards, the mixture was cooled to room temperature and cold diethyl ether was slowly added to a solution that resulted in the formation of blue crystals that were subsequently separated by filtration. The product was purified with flash chromatography using MeOH/DCM (20:80) as an eluent. The collected fraction was concentrated using rotary evaporator and dried under high vacuum. This afforded 208 mg (43 % yield) of **3** as blue powder.

$C_{33}H_{40}BrN_2NaO_6S_2$. MW = 727.70 g/mol. ^{1}H NMR (300 MHz, DMSO-d6) δ 8.51 (d, *J* = 13.4 Hz, 2H, 2 x C**H** (methine bridge)), 7.68 (d, *J* = 7.2 Hz, 2H, 2 x C$\mathbf{H}_{Ar}$), 7.56 (d, *J* = 8.0 Hz, 2H, 2 x C$\mathbf{H}_{Ar}$), 7.44 (t, *J* = 7.7 Hz, 2H, 2 x C$\mathbf{H}_{Ar}$), 7.31 (t, *J* = 7.4 Hz, 2H, 2 x C$\mathbf{H}_{Ar}$), 6.34 (d, *J* = 13.4 Hz, 2H, 2 x C**H** (methine bridge)), 4.19 (t, *J* = 6.9 Hz, 4H, 2 x C$\mathbf{H}_2$), 1.96 – 1.76 (m, 4H, 2 x C$\mathbf{H}_2$), 1.72 (s, 14H, 2 x C$\mathbf{H}_2$*, 4 x C$\mathbf{H}_3$). *Resolved via 1H-1H COSY NMR. Note: Methylene group with the chemical shift at δ 2.50 (4 H, 2 x C$\mathbf{H}_2$-SO_3^-) overlaps with the peak of the solvent and was resolved via ^{1}H-^{1}H COSY NMR (Appendix).

Synthesis of symmetric disulfo-Cy5-carboxyl (Cy5(4))

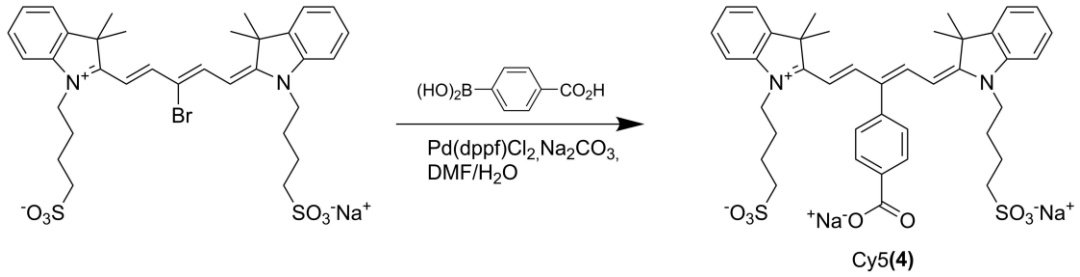

Cy5(**4**)

The introduction of carboxyl functionality into the polymethine chain of Cy5 was performed via a Suzuki coupling. The synthetic procedure was based on that, described by Wycisk et al.,[111] however several modifications were introduced. Most importantly, the introduction of Na_2CO_3 into the reaction mixture was performed to facilitate the successful coupling. For the synthesis, 131.4 mg (0.18 mmol) of **3** were mixed with 33.4 mg (0.20 mmol) of 4-carboxyphenylboronic acid, 19.4 mg (0.027 mmol) of Pd(dppf)Cl_2 (II), and 38.8 mg (0.37 mmol) of Na_2CO_3 in 6 ml of Ar-saturated DMF/water (1.7/1, v/v) mixture and stirred at 70 °C for 155 min. Purification was accomplished via flash chromatography using the mixture of MeOH/DCM (70:30) as an eluent. The product-containing fraction was subsequently collected, solvent removed on a rotary evaporator and the product dried under high vacuum. The reaction afforded 40 mg of blue crystals (yield 28 %). Molar extinction coefficient of the dye was estimated experimentally (ε_{642} = 101 000 $M^{-1}cm^{-1}$).

$C_{40}H_{44}N_2Na_2O_8S_2$. MW = 790.90 g/mol. UPLC: t_R = 2.92 min (3 to 80 % of Solvent B in 4 min). ESI-MS: m/z = 747.6 ($[M+H]^+$, calculated: 747.9-acid). ^{1}H NMR (500 MHz, DMSO-d6) δ 8.48 (d, *J* = 14.1 Hz, 2H, 2 x C**H** (methine bridge)), 8.21 (d, *J* = 7.6 Hz, 2H, 2 x C$\mathbf{H}_{Ar}$, (phenyl substituent)), 7.64 (d, *J* = 7.4 Hz, 2H, 2 x C$\mathbf{H}_{Ar}$ (indolenine ring)), 7.45 – 7.35 (m, 4H, 2 x C$\mathbf{H}_{Ar}$, 2 x C$\mathbf{H}_{Ar}$ (indolenine ring), 7.30 (d, *J* = 7.9 Hz, 2H, 2 x C$\mathbf{H}_{Ar}$ (phenyl substituent), 7.25 (t, *J* = 7.5 Hz, 2H, 2 x C$\mathbf{H}_{Ar}$ (indolenine ring)), 5.71 (d, *J* = 14.2 Hz, 2H, 2 x C**H** (methine bridge)), 3.73 (t, *J* = 6.4 Hz, 4H, 2 x C$\mathbf{H}_2$), 2.44 – 2.39 (m, 4H, 2 x C$\mathbf{H}_2$), 1.75 (s, 12H, 4 x C$\mathbf{H}_3$), 1.66 – 1.55 (m, 4H, 2 x C$\mathbf{H}_2$), 1.55 – 1.45 (m, 4H, 2 x C$\mathbf{H}_2$).

6.2.2 Synthesis of symmetric di-sulfo Cy7

Synthesis of Cl-substituted methine bridge (5).

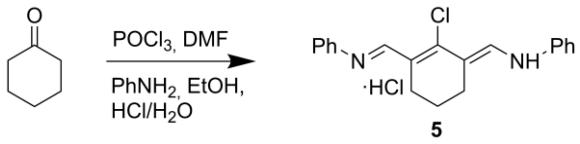

5

Synthesis of **5** was performed similarly to the procedure described by Flanagan et al.[114] with some modifications. First, 11 ml of $POCl_3$ were dropwise added to 13 ml of dry, Ar-saturated DMF in an ice bath within the course of 20 min under Ar atmosphere. The mixture was then stirred for additional 30 min. Next, the ice bath was removed, and 5.5 ml of cyclohexanone were added dropwise within the course of 16 min at room temperature and the stirring was continued for 30 min. Color of the mixture changed from pink to yellow and then to amber. Next, the solution was heated to 130 °C and left reacting for additional 100 min. Then a mixture containing 9.2 ml of freshly distilled aniline and 9.5 ml of dry ethanol was added to the flask within the course of 13 min and stirring was continued for additional 30 min at room temperature. Afterward, the mixture was poured into 110 ml of cold H_2O/HCl (10:1) solution on an ice bath to precipitate the hydrochloride salt of the formed product. The supernatant was discarded, the solid was washed with acetone and diethyl ether and separated by filtration. The crystals were then washed with cold ether and cold water and finally with the mixture Et_2O/acetone (4:1). Finally, the product was re-crystallized from 320 ml of ethanol, filtrated and dried under high vacuum to afford 4.57 g (yield 24 %) of dark purple solid. The ^{1}H NMR spectral data was in agreement with published data[114], except the signal of N**H** protons, that was observed by me at δ 11.52 (see Appendix) but was not listed by the authors.

$C_{20}H_{20}Cl_2N_2$. MW = 359.29 g/mol. ^{1}H NMR (300 MHz, DMSO-d6) δ 11.52 (s, 2H, 2 x N**H**), 8.47 (s, 2H, C**H** (methine bridge)), 7.64 (d, *J* = 7.8 Hz, 4H, 4 x C$\mathbf{H}_{Ar}$), 7.43 (t, *J* = 7.9 Hz, 4H, 4 x C$\mathbf{H}_{Ar}$), 7.23 (t, *J* = 7.4 Hz, 2H, 2 x C$\mathbf{H}_{Ar}$), 2.76 (t, *J* = 5.7 Hz, 4H, 2 x C$\mathbf{H}_2$), 1.89 – 1.70 (m, 2H, C$\mathbf{H}_2$). ^{13}C NMR APT (75 MHz, DMSO-d6) δ 155.53 (**C**-Cl), 148.64 (2 x **C**H (methine bridge)), 139.61 (2 x $\mathbf{C}_{Ar}$), 129.68 (4 x **C**H_{Ar}), 126.29 (2 x **C**H_{Ar}), 119.00 (4 x **C**H_{Ar}), 115.05 ($\mathbf{C}_q$ (methine bridge)), 24.95 (2 x **C**H_2), 19.47 (**C**H_2).

Synthesis of disulfo-Cy7-Cl (6).

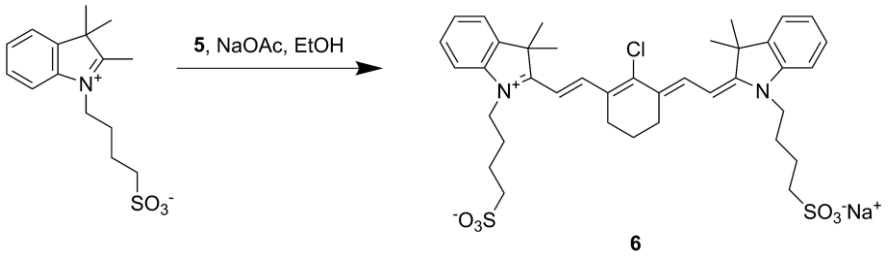

6

Disulfo-Cy7-Cl (Compound **6**) was synthesized similarly to the compound **3**. In short, 0.926 g (3.1 mmol) of **1** were mixed with 0.735 g (2.0 mmol) of **5,** and 0.322 g (3.9 mmol) of sodium acetate in 50 ml of dry ethanol. The mixture was stirred under Ar atmosphere at 85 °C for 200 min. Following the cooling to room temperature, the crude was precipitated with cold Et_2O, filtered and washed with cold Et_2O. Purification was accomplished by flash chromatography using the mixture of DCM/MeOH (4:1). The combined fractions of the product were dried using the rotary evaporator and additionally under high vacuum to afford 275 mg of green solid (yield: 23 %). The NMR spectra data was in agreement with published data, except the peak at δ 2.50 that was resolved by me using ^{1}H-^{1}H COSY NMR, which was not listed by the authors.[148]

$C_{38}H_{46}ClN_2NaO_6S_2$. MW = 749.35 g/mol. ^{1}H NMR (300 MHz, DMSO-d6) δ 8.25 (d, *J* = 14.1 Hz, 2H, 2 x C**H** (methine bridge)), 7.62 (d, *J* = 7.3 Hz, 2H, 2 x C$\mathbf{H}_{Ar}$), 7.55 – 7.35 (m, 4H, 4 x C$\mathbf{H}_{Ar}$), 7.27 (t, *J* = 7.4 Hz, 2H, 2 x C$\mathbf{H}_{Ar}$), 6.37 (d, *J* = 14.2 Hz, 2H, 2 x C**H** (methine bridge)), 4.22 (t, *J* = 6.3 Hz, 4H, 2 x C$\mathbf{H}_2$ (sulfobutyl chain)), 2.72 (t, *J* = 4.8 Hz, 4H, 2 x C$\mathbf{H}_2$ (chlorocyclohexenyl ring)), 1.90 – 1.70 (m, 10H, 2 x C$\mathbf{H}_2$, 2 x C$\mathbf{H}_2$ (sulfobutyl chain), C$\mathbf{H}_2$ (chlorocyclohexenyl ring)), 1.67 (s, 12H, 4 x C$\mathbf{H}_3$). Note: Methylene group with the chemical shift at δ 2.50 (4 H, 2 x C$\mathbf{H}_2$-SO_3^-) overlaps with the peak of the solvent and was resolved via ^{1}H-^{1}H COSY NMR (Appendix).

Synthesis of disulfo-Cy7-NH-PEG-NHBoc (7).

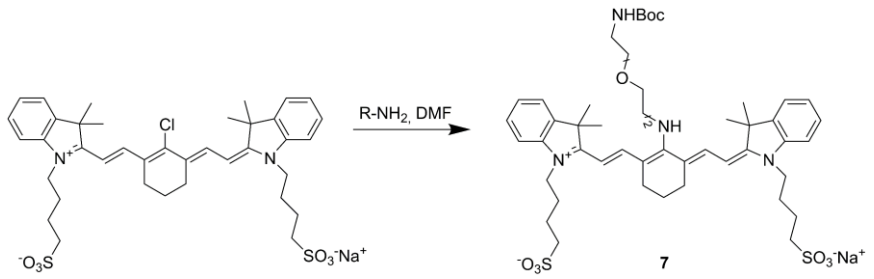

7

Synthesis of compound **7** was performed based on the published procedure with some modifications. 75 mg (0.1 mmol) of **6** were mixed with 2 eq. of bifunctional linker and 1.6 eq. of DIPEA in 4.3 ml of dry, Ar-saturated DMF and stirred under Ar atmosphere at 80 °C for 9 h. The color of solution

changed from dark green to dark blue. Finally, the product was purified via RP-C18 chromatography using MeOH/H_2O (60:40) as an eluent and dried under vacuum. R_f (H_2O/MeOH = 30/70) = 0.48 (RP-C18). $C_{49}H_{69}N_4NaO_{10}S_2$. MW = 961.22 g/mol. The yield of the reaction was not estimated due to the fast degradation of the product.

6.2.3 Synthesis of Cy5-Gly-MESNa (**8**) on the solid phase

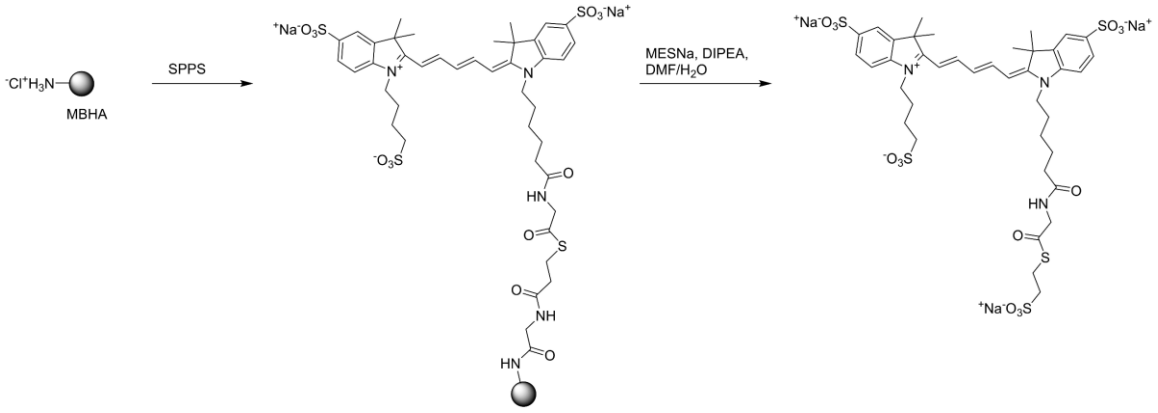

The synthesis was performed according to the procedure reported by Michaelis et al.[49] with some modifications. MBHA·LL resin (0.67 mmol/g) was used as a solid support. After the swelling with 2 ml of DMF (30 min), the resin was treated with 1.5 ml of DIPEA/DMF (10:90) (2 x 4 min). Wash: DMF (10 x 1 ml). Afterwards, a mixture of 1 eq. of Fmoc-Gly-OH, 1 eq. PyBOP, and 2 eq. NMM in DMF was added to the resin after a brief pre-activation and left reacting for 90 min. C(AA) = 0.09 M. Wash: DMF (10 x 1 ml). Capping of the residual amino groups was performed with 1.5 ml of DMF/acetic anhydride/2,6-lutidine (89:5:6) (2 x 5 min). Wash: DMF (10 x 1 ml). Next, the Fmoc deprotection was done with 1 ml of DMF/piperidine (4:1) mixture (2 x 5 min) and the loading of resin was estimated to be 0.08 mmol/g by spectrophotometric Fmoc monitoring. This was accomplished by measuring the absorbance of the deprotection solution at 301 nm and using the Beer-Lambert law ($A = \varepsilon \cdot l \cdot C$) to convert the optical density into the respective concentration; the molar extinction coefficient of the piperidine-dibenzofulvene adduct ($\varepsilon_{301} = 7800\ M^{-1}cm^{-1}$) was used for the calculations. The subsequent synthesis scale was 4.8 µmol. Next, a mixture of 8 eq. Trt-MPA-OH, 8 eq. PyBOP and 12 eq. NMM in DMF was briefly pre-activated and added to the resin (2 x 30 min). C(Trt-MPA-OH) = 0.1 M. Capping was performed for 3 min once. Afterward, the resin was washed with DMF (10 x 1 ml) and DCM (10 x 1 ml). Then, part of the resin was separated and the synthesis was continued on a 2.9 µmol scale. The resin was swollen in 1 ml DCM for 40 min and Trt group was removed by the treatment with 1 ml of TFA/TIS (90:10) (20 min + 40 min). Wash: DCM (10 x 1 ml) and DMF (10 x 1 ml). Then, Boc-Gly-OH was coupled: 6 eq. Boc-Gly-OH, 6 eq. PyBOP, 12 eq. NMM in DMF (2 x 30 min). C(AA) = 0.1 M. Wash: DMF (10 x 1 ml) and DCM (10 x 1 ml). Afterwards, the Boc group was removed by treatment with 1 ml of TFA/DCM/m-cresol (50:45:5) (1 x 60 min), washed with DCM (10 x 1 ml) and DMF (10 x 1 ml) and swollen in 1 ml of DMF (20 min). Subsequently, the syringe was loaded with a mixture of 2.6 eq. Cy5-CO_2H, 2.6 eq. PyBOP and 5.2 eq. DIPEA in DMF. C(Cy5-CO_2H) = 0.04 M. Coupling was carried out for 90 min once. Then, the resin was washed with DMF (15 x 1 ml), DCM (10 x 1 ml) and additionally with 1 ml DMF (5 x 30 min). To liberate a thioester into solution, 15 eq. MESNA and 7.5 eq. DIPEA

in a mixture of DMF/H_2O (5:1) were added to the resin (2 x 60 min). C(MESNa) = 0.24 M. The resin was washed with 0.2 ml DMF twice and thioester-containing fractions were combined. The solvent was removed under high vacuum and the remainder dissolved in TFA/H_2O (0.01:99.99) and purified via SEC, using PD MiniTrap G-10 column (eluent: TFA/H2O (0.01:99.99)). The purified fraction was aliquoted, lyophilized and stored at – 20 °C. A blue solid was obtained in a 45 % yield (1.3 µmol, 1.3 mg).

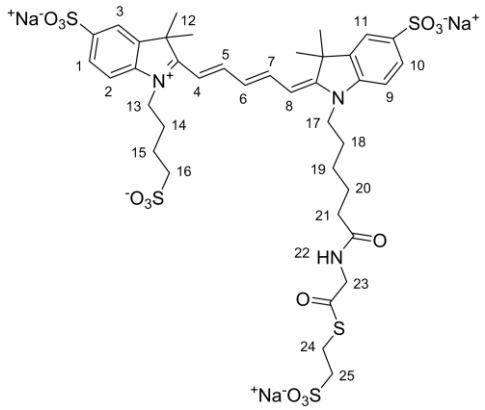

$C_{39}H_{48}N_3Na_3O_{14}S_5$. MW = 1012.09. ε = 251 000 $M^{-1}cm^{-1}$. MALDI-TOF: m/z = 947.22 ($[M+H]^+/1$], calc. 947.15 - acid). UPLC: t_R = 1.59 min (3 to 90 % of Solvent B in 4 min). Note: during the UPLC analysis very strong tailing of the product peak was observed. ESI-MS: m/z = 946 ($[M+H]^+/1$], calc. 947 – acid), 473 ($(M+2H)^{2+}/2$, calc. 474 – acid). ^{1}H NMR (500 MHz, DMSO-d6) δ 8.52 (t, J = 6.1 Hz, 1H, 22-NH), 8.40 – 8.30 (m, 2H, 5-CH, 7-CH), 7.81 – 7.77 (m, 2H, 3-CH, 11-CH), 7.62 (dt, J = 8.2, 1.6 Hz, 2H, 1-CH, 10-CH), 7.37 – 7.30 (m, 2H, 2-CH, 9-CH), 6.61 (t, J = 12.3 Hz, 1H, 6-CH), 6.43 – 6.27 (m, 2H, 4-CH, 8-CH), 4.11 – 4.06 (m, 4H, 13-CH_2, 17-CH_2), 3.94 (d, J = 6.1 Hz, 2H, 23-CH_2), 3.05 – 2.99 (m, 2H, 24-CH_2), 2.59 – 2.56 (m, 2H, 25-CH_2), 2.16 (t, J = 7.3 Hz, 2H, 21-CH_2), 1.78 – 1.72 (m, 4H, 15-CH_2, 18-CH_2), 1.68 (s, 12H, 12-CH_3), 1.68 (2H, 14-CH_2, overlapped), 1.58 (quint, J = 7.4 Hz, 2H, 20-CH_2), 1.41 – 1.35 (m, 2H, 19-CH_2). Note: Peak (2H, 16-CH_2) overlaps with the solvent peak and was identified using ^{1}H-^{1}H COSY NMR.

6.3 Synthesis of PNA Probes

6.3.1 General procedures

Manual Fmoc-based solid phase PNA synthesis.

Manual SPPS was performed in 2 ml polyethylene syringe reactors equipped with the frit disc. Syntheses were performed on a Tentagel RRam resin with the original loading of 0.18 - 0.2 mmol/g, unless otherwise noted.

Swelling: Prior to each synthesis, the resin was swollen in 1 ml DMF for 30 min, and subsequently washed with DMF (10 x 1 ml).

Deprotection: for the removal of Fmoc-protecting group, the resin was treated with DMF/piperidine (4:1) ("deprotection solution") for a defined time. After each deprotection step, the resin was washed with DMF (10 x 1 ml).

Coupling: Details on the specific conditions used for each probe are provided below. After each coupling step, the resin was washed with DMF (5 x 1 ml).

Capping: A mixture of DMF/acetic anhydride/2,6-lutidine (89:5:6) ("capping solution") was added to the resin for a specific time. Afterward, the resin was washed with DMF (10 x 1 ml). After the last capping step, the resin was washed with DMF (10 x 1 ml) and DCM (10 x 1 ml) and dried under high vacuum prior to the cleavage.

Automated Fmoc-based solid phase PNA synthesis.

Automated solid phase PNA synthesis was carried out on a linear synthesizer "Intavis ResPep" according to an Fmoc-strategy. All syntheses were performed on a Tentagel RRam resin with the original loading of 0.18 - 0.2 mmol/g, unless otherwise noted.

Swelling: Swelling of the resin with DMF was performed for 5 min (6 x 0.4 ml).

Deprotection: For Fmoc-deprotection, the resin was treated with a "deprotection solution" (DMF/piperidine (4:1)). For the synthesis at 2 µmol scale, the first deprotection step was carried out with **200 µl of the deprotection solution for 5 min (x 2)**, and subsequent deprotections were carried out with **200 µl of deprotection solution for 2 min (x 2)**, unless otherwise noted. Deprotection was followed by the wash step with DMF (7 x 0.35 ml).

Coupling: For the coupling of PNA monomers, a mixture of Fmoc-protected PNA monomer, HCTU and NMM was pre-activated for 2 min and subsequently added to the resin. For the coupling of amino acids, Fmoc-protected AA, HCTU, Oxyma and NMM was pre-activated for 2 min, then added to the resin and left to react for a specified amount of time. Stock solutions of PNA and AA monomers were prepared in NMP, stock solutions of NMM were prepared in DMF. Coupling was always followed by washing with DMF (3 x 0.2 ml).

Capping: For the acetylation of residual amino groups a "capping solution" (DMF/acetic anhydride/2,6-lutidine (89:5:6)) was used. For the synthesis at 2 μmol scale the capping step was carried out with **200 μl of capping solution for 2 min (x 2)**, unless otherwise noted. After the capping, the resin was washed with DMF (4 x 0.3 ml). After the last capping step, the resin was washed with DMF (5 x 0.23 ml) and dry ethanol (7 x 0.23 ml) and dried under high vacuum prior to the cleavage.

Cleavage and work-up.

Cleavage of PNA from the solid support and removal of TFA-labile protecting groups was performed with a cocktail that contained TFA and a specified content of scavengers. Following the cleavage, the TFA fraction was collected and the resin washed with pure TFA (2 x 0.2 ml) to extract the residual product. The combined fractions were concentrated on a rotary evaporator. Next, 2 ml of cold, Ar-saturated diethyl ether were added to precipitate the product. At this step the mixture may be left in the freezer (- 20 °C) for 20 min to facilitate the precipitation. The crude was subsequently separated by centrifugation and the supernatant discarded. The washing step was repeated 3 more times. Finally, the pellet was dried with Ar, dissolved in a binary mixture: TFA/H_2O (0.1:99.9), and purified using preparative HPLC. Whenever the solubility of the crude in TFA/H_2O (0.1:99.9) mixture was incomplete, a small volume of MeCN was added to the mixture, however its content did not exceed the initial content of MeCN in the HPLC gradient.

6.3.2 Synthesis and analytical data of PNA probes

Synthesis of PNAa.

Synthesis was performed manually according to an Fmoc strategy at 7 µmole scale. *Deprotection*: Cycle 1: 1.5 ml of deprotection solution (2 x 8 min). Cycle 2-10: 1.5 ml of deprotection solution (2 x 5 min). *Coupling:* 4 eq. of Fmoc-protected PNA monomer or AA (Fmoc-Orn(N_3)-OH or Fmoc-Cys(Trt)-OH), 4 eq. PyBOP, 8 eq. NMM. C(monomer) = 0.09 M. Couplings were performed for 1 h. *Capping:* 1.5 ml of capping solution (1 x 3 min). Following the synthesis, the resin was dried under high vacuum, 71% of the resin was used for the cleavage of the probe. *Cleavage:* 0.9 ml of TFA/H_2O/m-cresol/TIS (85:5:5:5) mixture for 90 min. *Preparative HPLC gradient:* 1 - 30 % of solvent B in 45 min.

PNAa: H-Cys-atctctg-Gly-Orn(N_3)-NH_2.
$C_{85}H_{113}N_{43}O_{26}S$. MW = 2185.17 g/mol.
UPLC gradient: 2 to 20 % of solvent B in 4 min. t_R = 2.73 min.
ESI-MS: m/z = 1093.1 ($[M+2H]^{2+}/2$, calc. 1093.6), 729.3 ($[M+3H]^{3+}/3$, calc. 729.4).
ε_{260} = 61 020 $M^{-1}cm^{-1}$. OD_{260} = 44.6. Yield: 15 % (0.73 µmol).

Synthesis of Cy5(4)-Gly-PNAa.

Synthesis was performed at 0.8 µmol scale using the resin with previously assembled PNAa, (described above) as a starting material. *Coupling:* 8 eq. of Fmoc-Gly-OH, 8 eq PyBOP, and 16 eq NMM in 100 ul DMF. Coupling was performed for 70 min twice. *Capping:* 1.2 ml of "capping solution" for 3 min. In a separate step, Cy5(**4**) was converted into its carboxylic acid by mixing 2.8 mg of Cy5(**4**) (3.64 µmol) with 300 µl TFA and subsequently dried using rotary evaporator and then high vacuum. The obtained acid of Cy5(**4**) was then coupled to the PNA on the solid phase. *Coupling:* 4.6 eq. Cy5(**4**) (acid), 4.6 eq. PyBOP, and 9.2 eq. NMM in DMF. Coupling was performed for 1 h. *Cleavage:* 0.7 ml of TFA/H_2O/m-cresol/TIS (85:5:5:5) for 2 h. Note: Solution turns *yellow* during the cleavage, however following the evaporation of TFA the compound gains its original blue color. *Preparative HPLC gradient:* 10 to 70 % of solvent B in 30 min.

Cy5(4)-Gly-PNAa: Cy5(**4**)-Gly-Cys-atctctg-Gly-Orn(N_3)-NH_2.
$C_{127}H_{160}N_{46}O_{34}S_3$. MW = 2971.15 g/mol.
UPLC gradient: 3 to 60 % solvent B in 4 min. t_R = 3.18 min.
ESI-MS: m/z = 991.1 ($[M+3H]^{3+}/3$, calc. 991.4).
ε_{642} = 101 000 $M^{-1}cm^{-1}$. OD_{642} = 0.21. Yield: 0.3 % (2 nmol).

Synthesis of Cy5(4)-AEEA-Gly-PNAa.

Synthesis was performed at 0.3 μmol scale similarly to the procedure used for Cy5(**4**)-Gly-PNAa. For the coupling of AEEA unit the following conditions were used: 14 eq. Fmoc-AEEA-OH, 12 eq. PyBOP, and 12 eq. NMM were mixed in 100 ul DMF and added to the resin after the brief pre-activation. C(monomer) = 0.04 M. The coupling was performed for 110 min in a duplicate. *Capping:* 1.2 ml of capping solution (3 min). *Deprotection:* 1.2 ml of deprotection solution (5 min + 7 min). Prior to coupling the Cy5(**4**) was converted into its carboxylic acid according to the procedure described above, using 6.9 mg of Cy5(**4**) and 0.5 ml TFA. Coupling of Cy5(**4**): 15 eq. Cy5(**4**) (acid), 18 eq. PyBOP and 30 eq. NMM were mixed in 75 μl DMF and added to the resin. Coupling was performed for 100 min. Second coupling was performed for 140 min, using the same conditions, except higher excess of PyBOP (23 eq.). Then the resin was washed with DMF (20 x 1 ml), ethanol (10 x 1 ml) and DCM (10 x 1 ml). Finally, the resin was washed with 2 ml of DMF several times until the "wash" fraction changed its color from dark blue to very pale blue. Note: Cy5 nonspecifically adsorbs on the surface of the solid support and its removal from the resin can only be accomplished by frequent and prolonged washing steps that result in the desorption of the dye and its release into solution. *Cleavage:* 0.5 ml of TFA/H_2O/m-cresol/TIS (85:5:5:5) for 2 h. *Preparative HPLC gradient:* 25 to 70 % of solvent B in 30 min.

Cy5(4)-AEEA-Gly-PNAa: Cy5(**4**)-AEEA-Gly-Cys-atctctg-Gly-Orn(N_3)-NH_2.
$C_{133}H_{171}N_{47}O_{37}S_3$. MW = 3116.30 g/mol.
UPLC gradient: 3 to 60 % of solvent B in 4 min. t_R = 3.16 min.
ESI-MS: m/z = 1039.6 ($[M+3H]^{3+}/3$, calc. 1039.8).
ε_{642} = 101 000 $M^{-1}cm^{-1}$. OD_{642} = 15.5. Yield: 51 % (153 nmol).

Synthesis of FEWCy5-Gly-PNAa.

Synthesis was performed at 0.2 umole scale similarly to the synthesis of Cy5(**4**)-Gly-PNAa. The last step was performed using the NHS-ester of FEWCy5 (6 eq.), C(Dye) = 0.014 M. The coupling was performed for 4 h. *Cleavage*: 0.4 ml of TFA/H_2O/m-cresol/TIS (85:5:5:5) for 160 min. *Preparative HPLC gradient:* 15 to 50 % of solvent B in 30 min.

FEWCy5-Gly-PNAa: FEWCy5-Gly-Cys-atctctg-Gly-Orn(N_3)-NH_2.
$C_{122}H_{158}N_{46}O_{37}S_4$. MW = 2989.13 g/mol.
UPLC gradient: 3 to 60 % of solvent B in 4 min. t_R = 1.94 min.
ESI-MS: m/z = 996.9 ($[M+3H]^{3+}/3$, calc. 997.4).
ε_{648} = 251 000 $M^{-1}cm^{-1}$. OD_{648} = 0.16. Yield: 0.3 % (0.6 nmol).

Synthesis of PNAb.

Synthesis was carried out according to an Fmoc strategy at 2 μmol scale. Synthesis was performed using the automated synthesizer. *Coupling:* Cycle 1: 6 eq. Fmoc-Cys(Mmt)-OH, 5.4 eq. HCTU, 6 eq. Oxyma Pure, 14 eq. NMM in DMF. C(AA) = 0.15 M. (20 min x 2). Cycle 2-end: 4 eq. Fmoc-protected PNA monomer, 3.6 eq. HCTU, 8 eq. NMM. C(PNA) = 0.12 M. (15 min x 2). *Cleavage:* 1 ml of TFA/TIS/H_2O (95:2.5:2.5) for 90 min. *Preparative HPLC gradient:* 5 to 25 % of solvent B in 30 min.

PNAb: Ac-agacagc-Cys-NH_2.
$C_{80}H_{101}N_{47}O_{20}S$. MW = 2073.06 g/mol.
UPLC gradient: 3 to 40 % of solvent B in 4 min. t_R = 1.69 min.
ESI-MS: m/z = 1037.4 ($[M+2H]^{2+}/2$, calc. 1037.5), 691.9 ($[M+3H]^{3+}/3$, calc. 692.0).
MALDI-TOF: m/z = 2076 ($[M+H]^{+}/1$], calc. 2074).
ε_{260} = 75 600 $M^{-1}cm^{-1}$. OD_{260} = 12.4. Yield: 7 %. (165 nmol).

Synthesis of PNAc.

17 nmol of Cy5-Gly-MESNa (**8**) was mixed with 2 eq. of PNAb in a borate buffer (50 mM borate, 20 mM NaCl, 5 mM TCEP, pH 7.4) and left shaking at 25 °C for 16 h. The concentration of Cy5-Gly-MESNa in a reaction mixture was kept at 0.17 mM. Afterwards, the mixture was cooled down to +4 °C, centrifuged for 2 min, and the supernatant was discarded. The remainder was dissolved and subsequently purified via preparative HPLC using a gradient: 10 to 30 % of solvent B in 35 min.

PNAc: Ac-agacagc-Cys(Cy5-Gly)-NH_2.
$C_{117}H_{146}N_{50}O_{31}S_4$. MW = 2877.01 g/mol.
UPLC gradient: 3 to 40 % of solvent B in 4 min. t_R = 3.04 min.
ESI-MS: m/z = 960.1 ($[M+3H]^{3+}/3$, calc. 960.0).
MALDI-TOF: m/z = 2879 ($[M+H]^{+}/1$], calc. 2878).
ε_{648} = 251 000 $M^{-1}cm^{-1}$. OD_{648} = 0.03. Yield: 1 % (0.12 nmol).

Synthesis of PNAd0 and PNAd.

Synthesis was carried out according to an Fmoc strategy at 2 μmol scale. The coupling of the first three amino acids and all PNA monomers was accomplished using the automated synthesizer. *AA coupling*: 5 eq. Fmoc-protected AA, 5 eq. Oxyma Pure, 4.5 eq. HCTU, 12.5 eq. NMM, C(AA) = 0.15 M (25 min x 2); *PNA coupling*: 4 eq. Fmoc-protected PNA monomer, 3.6 eq. HCTU, 8 eq. NMM, C(PNA) = 0.12 M (20 min x 2). *Capping:* 0.2 ml of capping solution (2 min x 2). Then the resin was dried and its fractions used for the synthesis of PNAd0 and PNAd using the methods described below.

PNAd0: Coupling of Boc-Cys(Trt)-OH was performed manually at 0.55 μmol scale. *Coupling*: 10 eq. Boc-Cys(Trt)-OH, 10 eq. HOBt, 10 eq. PyBOP, 25 eq. 2,4,6-collidine, C(AA) = 0.06 M. (40 min x 2). *Capping*: 1 ml of capping solution (3 min x 1). *Cleavage*: 0.5 ml of TFA/TIS/H_2O (94:3.5:2.5) for 100 min.

PNAd: Coupling of Fmoc-Cys(StBu)-OH was performed manually at 0.55 μmol scale. *Coupling:* 10 eq. Fmoc-Cys(StBu)-OH, 10 eq. HOBt, 10 eq. PyBOP, 25 eq. 2,4,6-collidine, C(AA) = 0.06 M (40 min x 2). *Capping:* 1 ml of capping solution (3 min x 1). *Deprotection* of terminal Fmoc-group: 0.5 ml of deprotection solution (2 x 2 min). *Cleavage:* 0.5 ml of TFA/TIS/H_2O (94:3.5:2.5) for 110 min. *Preparative HPLC gradient:* 10 to 30 % of solvent B in 30 min.

PNAd: H-Cys(StBu)-atctctg-Glu-Glu-Orn(N_3)-NH_2.
$C_{97}H_{132}N_{44}O_{31}S_2$. MW = 2474.49 g/mol.
UPLC gradient: 3 to 40 % of solvent B in 4 min. t_R = 2.20 min.
ESI-MS: m/z = 1238.0 ($[M+2H]^{2+}$/2, calc. 1238.3), 825.7 ($[M+3H]^{3+}$/3, calc. 825.8).
ε_{260} = 61 020 $M^{-1}cm^{-1}$. OD_{260} = 3.8. Yield: 11 % (63 nmol).

Synthesis of PNAe.

Synthesis was carried out according to an Fmoc strategy at 2 μmol scale. The first amino acid was coupled manually: 4 eq. Fmoc-Cys(Mmt)-OH, 4 eq. HOBt, 4 eq. PyBOP, 10 eq. 2,4,6,-collidine, C(AA) = 0.08 M (30 min x 2). *Capping:* 1 ml of capping solution (3 min x 1). The following synthesis was performed using an automated synthesizer. *Deprotection:* before PNA couplings: 200 μl of deprotection solution (2 min x 2); before AA couplings: 200 μl of deprotection solution (5 min x 2). *Coupling:* PNA coupling: 4 eq. PNA monomer, 3.6 eq. HCTU, 8 eq. NMM, C(PNA) = 0.12 M (15 min x 2). AA coupling: 5 eq. AA, 5 eq. Oxyma Pure, 4.5 eq. HCTU, 12.5 eq. NMM, C(AA) = 0.15 M (25 min x 2). *Capping:* 0.2 ml of capping solution (2 min x 2).

Deprotection of terminal Fmoc-group was performed manually using 1 ml of deprotection solution: 3 min + 5 min. The acetylation of terminal amino group was accomplished by the treatment with 1 ml of capping solution (3 min + 5 min). *Cleavage:* 0.5 ml of TFA/TIS/H_2O/m-cresol (87.5/5/2.5/5) for 100 min (half of the resin). *Preparative HPLC gradient:* 5 to 25 % of solvent B in 30 min.

PNAe: Ac-Glu-Glu-gacagc-Cys-NH_2.
$C_{79}H_{102}N_{42}O_{24}S$. MW = 2055.99 g/mol.
UPLC gradient: 3 to 40 % of solvent B in 4 min. t_R = 1.49 min.
ESI-MS: m/z = 1028.8 ($[M+2H]^{2+}$/2, calc. 1029.0), 686.33 ($[M+3H]^{3+}$/3, calc. 686.34).
ε_{260} = 61 740 $M^{-1}cm^{-1}$. OD_{260} = 13.3. Yield: 21 % (215 nmol).

Synthesis of PNAf.

5.6 nmol of Cy5-Gly-MESNa (**8**) were mixed with 4 eq. of PNAe in a borate buffer (50 mM borate, 15 mM TCEP, pH 7.2) and left reacting for 2 days at room temperature. C(Cy5-Gly-MESNa) = 80 µM. Then, the solvent was removed under high vacuum, the residue washed with 50 µl of 0.1% TFA solution in water and subsequently purified using preparative HPLC. *Preparative HPLC gradient:* 10 to 35 % of solvent B in 35 min.

PNAf: Ac-Glu-Glu-gacagc-Cys(Cy5-Gly)-NH_2.
$C_{116}H_{147}N_{45}O_{35}S_4$. MW = 2859.95 g/mol.
UPLC gradient: 3 to 60 % of solvent B in 4 min. t_R = 1.94 min.
ESI-MS: m/z = 954.4 ($[M+3H]^{3+}$/3, calc. 954.3).
MALDI-TOF: m/z = 2860 ($[M+H]^{+}$/1], calc. 2861).
ε_{648} = 251 000 $M^{-1}cm^{-1}$. OD_{648} = 0.016. Yield: 1 % (64 pmol).

Synthesis of PNAg.

Synthesis was performed similarly to the synthesis of PNAd using the automated synthesizer at 2 µmol scale. Coupling of Fmoc-Cys(StBu)-OH was performed at 0.7 µmol scale in analogy to the synthesis of PNAd using double couplings (60 min + 30 min). *Cleavage:* 0.5 ml of TFA/TIS/H_2O (92.5:5:2.5) for 30 min. *Preparative HPLC gradient:* 10 to 30 % of solvent B in 30 min.

PNAg: H-Cys(StBu)-ggatctct-Glu-Glu-Orn(N_3)-NH_2.
$C_{108}H_{145}N_{51}O_{34}S_2$. MW = 2765.79 g/mol.
UPLC gradient: 3 to 40 % of solvent B in 4 min. t_R = 2.33 min.
ESI-MS: m/z = 923.1 ($[M+3H]^{3+}$/3 calc. 922.9).
ε_{260} = 71 370 $M^{-1}cm^{-1}$. OD_{260} = 1.9. Yield: 4 % (27 nmol).

Synthesis of PNAh.

The first amino acid was coupled manually to Tentagel RRam resin (2 μmol). Subsequent synthesis was performed analogously to the assembly of PNAe. *Cleavage:* 0.5 ml of TFA/TIS/H_2O/m-cresol (87.5:5:2.5:5) for 100 min (45 % of the resin). *Preparative HPLC gradient:* 10 to 30 % of solvent B in 30 min.

PNAh: Ac-Glu-Glu-Glu-agacagc-Cys-NH_2.
$C_{95}H_{122}N_{50}O_{29}S$. MW = 2460.40 g/mol.
UPLC gradient: 3 to 40% of solvent B in 4 min. t_R = 1.61 min.
ESI-MS: m/z = 1231.0 ($[M+2H]^{2+}$/2, calc. 1231.2), 821.2 ($[M+3H]^{3+}$/3, calc. 821.1).
ε_{260} = 75 600 $M^{-1}cm^{-1}$. OD_{260} = 21.8. Yield: 32 % (288 nmol).

Synthesis of PNAi.

Synthesis was performed similarly to PNAf, except the reaction time was extended to 5 days. Prior to preparative HPLC, the crude was purified with SEC (PD MiniTrap G-10) using the mixture of TFA/MeCN/H_2O (0.1:10:89.9) as a mobile phase. *Preparative HPLC gradient*: 10 to 30 % of solvent B in 35 min.

PNAi: Ac-Glu-Glu-Glu-agacagc-Cys(Cy5-Gly)-NH_2.
$C_{132}H_{167}N_{53}O_{40}S_4$. MW = 3264.3590 g/mol
MALDI-TOF: m/z = 3262 ($[M+H]^+$/1], calc. 3265).
ε_{648} = 251 000 $M^{-1}cm^{-1}$, OD_{648} = 0.014. Yield: 1 % (54 pmol).

Synthesis of PNAj.

The synthesis was performed according to an Fmoc strategy using Tentagel RRam resin (0.2 mmol/g). Coupling of the first three amino acids was performed manually at 10 μmol scale. For the first Fmoc deprotection step, the resin was treated with 1 ml of deprotection solution (2 x 5 min). Then, the resin was preloaded with first AA: 4 eq. Fmoc-Orn(N_3)-OH, 4 eq. PyBOP, 4 eq. HOBt, and 10 eq. 2,4,6-collidine were mixed in DMF and pre-activated for 1 min. C(AA) = 0.1 M. Next, the solution was added to the resin and left to couple (20 min x 2). *Capping:* 1 ml of capping solution (1 x 3 min). The couplings of Fmoc-Glu(OtBu)-OH building blocks were performed in the same manner, but the deprotection step was carried out for 2 min twice. Finally, the resin was washed with DMF (10 x 1 ml) and DCM (10 x 1 ml) and dried under high vacuum.

Part of the resin was separated and used for the coupling of the PNA monomers on an automated synthesizer at 3 μmol scale. Coupling of PNA monomers on an automated synthesizer: *Deprotection:* Cycle 1-7: 0.3 ml of deprotection solution (2 x 2 min). Cycle 8-11: (2 x 4 min). *Coupling:* Cycle 1-7: 4 eq. Fmoc-protected PNA monomer, 3.6 eq. HCTU and 8 eq. NMM. C(PNA) = 0.12 M. The reaction was performed for 15 min in a duplicate. Cycle 8-11: Coupling time was extended to 25 min. *Capping:* 0.2 ml of capping solution (2 x 2 min). Finally, the resin was dried under high vacuum overnight and used for the incorporation of N-terminal Cysteine manually (using one third of the resin). Coupling of Fmoc-Cys(tBu)-OH: Fmoc deprotection was performed by treating the resin with 0.3 ml of deprotection solution (2 x 4 min). Following the washing step, a mixture of 8 eq. Fmoc-Cys(StBu)-OH, 8 eq. PyBOP, 8 eq. HOBt, 20 eq. 2,4,6,-colidine in DMF was briefly pre-activated and added to the resin. C(AA) = 0.1 M. Coupling was performed for 40 min in duplicate. Deprotection of the terminal Fmoc group: 0.3 ml of deprotection solution (2 x 2 min).

Cleavage: Cleavage of PNA probe from the resin was performed with 0.5 ml of TFA/TIS/H_2O (92.5:5:2.5) mixture for 90 min. *Preparative HPLC gradient:* 10 - 30 % of solvent B in 30 min.

PNAj: H-Cys(StBu)-tctctggtctt-Glu-Glu-Orn(N_3)-NH_2.
$C_{140}H_{187}N_{61}O_{47}S_2$. MW = 3538.36 g/mol.
UPLC gradient: 3 to 40% of solvent B in 4 min. t_R = 2.61 min.
ESI-MS: m/z = 1181.1 ($[M+3H]^{3+}$/3, calc. 1180.5), 886.2 ($[M+4H]^{4+}$/4, calc. 885.6).
MALDI-TOF: m/z = 3541 ($[M+H]^{+}$/1], calc. 3539).
ε_{260} = 87 660 $M^{-1}cm^{-1}$. OD_{260}= 7.9. Yield: 9 % (90 nmol).

Synthesis of PNAk.

The synthesis was performed according to an Fmoc strategy. The first AA was coupled manually at 10.3 μmol scale. First Fmoc-deprotection step: 1 ml of deprotection solution (2 x 5 min). Then, the resin was preloaded with the first amino acid. To that end, 4 eq. Fmoc-Cys(Mmt)-OH, 4 eq. PyBOP, 4 eq. HOBt, and 10 eq. 2,4,6-collidine were mixed in DMF and pre-activated for 1 min. C(AA) = 0.1 M. Then the solution was added to the resin and left to couple for 20 min under vigorous shaking. The procedure was performed twice. Capping: 1 ml of capping solution (1 x 3 min). Following thee washing step: DMF (10 x 1 ml) and DCM (10 x 1 ml) the resin was dried under high vacuum. Part of the resin was separated and used for the coupling of PNA monomers on an automated synthesizer at 5 μmol scale (see below).

Coupling of PNA monomers and AA using the automated synthesizer: *Deprotection:* Cycle 1: 0.3 ml of deprotection solution (2 x 4 min). Cycle 2-9: 0.25 ml of deprotection solution (1 x 2 min) + 0.3 ml of deprotection solution (1 x 2 min). Cycle 10-13: 0.25 ml of deprotection solution (1 x 3

min) + 0.3 ml of deprotection solution (1 x 3 min). Cycle 14: 0.3 ml of deprotection solution (2 x 4 min). *Coupling:* Cycle 1-9 (coupling of PNA monomers): 4 eq. Fmoc-protected PNA monomer, 3.6 eq. HCTU, and 6 eq. NMM. C(PNA) = 0.13 M. The reactions were performed for 15 min in duplicate. Cycle 10 (coupling of Fmoc-Gly-OH): 4 eq. AA, 3.6 eq. HCTU and 6 eq. NMM. C(AA) = 0.13 M. The reaction was performed for 20 min twice. Cycle 11-13 (coupling of Fmoc-Glu(OtBu)-OH): 4 eq. AA, 3.6 eq. HCTU, 4 eq. Oxyma Pure and 10 eq. NMM. C(AA) = 0.13 M. The reactions were performed for 20 min twice. *Capping:* Cycle 1-13: 0.3 ml of capping solution (2 x 2 min). Cycle 14: 0.3 ml of capping solution (2 x 4 min).

Cleavage: 1.2 ml of TFA/TIS/H_2O/m-cresol/EDT (88:5:2:3:2) for 90 min. *Preparative HPLC gradient:* 7 - 25 % of solvent B in 30 min.

PNAk: Ac-$(Glu)_3$-Gly-gagacagca-Cys-NH_2.

$C_{119}H_{151}N_{65}O_{35}S$. MW = 3083.95 g/mol.

UPLC gradient: 3 to 60 % of solvent B in 4 min. t_R = 1.71 min.

ESI-MS: m/z = 1028.95 ($[M+3H]^{3+}$/3, calc. 1028.99), 772.3 ($[M+4H]^{4+}$/4, calc. 772.0), 617.7 ($[M+5H]^{5+}$/5, calc. 617.8).

MALDI-TOF: m/z = 3080 ($[M+H]^{+}$/1], calc. 3085).

ε_{260} = 99 810 $M^{-1}cm^{-1}$. OD_{260} = 36.8. Yield: 7 % (368 nmol).

Synthesis of PNAl.

93 nmol of PNAk were mixed with a 3-fold molar excess of Cy5-Gly-MESNa in a borate buffer (50 mM borate, 50 mM NaCl, 5 mM TCEP, pH 8.0) and shaken for 3 h at 25 ˚C in the dark. C(PNAk) = 0.37 mM. Afterwards, 1 ml of cold 0.1% TFA solution in water was added to the reaction solution and mixture was centrifuged for 2 min. The supernatant was discarded, the precipitation step was repeated with 0.2 ml of the same solution. Then, a mixture of TFA/MeCN/H_2O/DMF (0.1:7:89.9:3) was added and the centrifugation step was repeated. The remainder was dissolved in 75 ul DMSO, followed by the addition of 500 ul of TFA/MeCN/H_2O (0.1:7:92.9) and purified via HPLC using the gradient 10 – 30 % of solvent B in 30 min.

PNAl: Ac-$(Glu)_3$-Gly-gagacagca-Cys(Cy5-Gly)-NH_2.

$C_{156}H_{196}N_{68}O_{46}S_4$. MW = 3887.95 g/mol.

UPLC gradient: 3 to 40 % of solvent B in 4 min. t_R = 2.29 min.

ESI-MS: m/z = 972 ($[M+4H]^{4+}$/4, calc. 973).

MALDI-TOF: m/z = 3892 ($[M+H]^{+}$/1], calc. 3889).

ε_{648} = 251 000 $M^{-1}cm^{-1}$. OD_{648} = 0.92. Yield: 4 % (4 nmol).

6.4 Functionalization of QDs

6.4.1 Phase transfer of hydrophobic QDs into water

The procedure for the transfer of hydrophobic QDs into water from hexane was based on the reported by Dai et al.[106] First, 30 µl of stock solution of 2.1 nmol TOP/TOPO coated CdSe/CdS QDs in hexane was diluted with 80 µl of hexane, mixed with 1 ml ethanol and the QDs were collected by centrifugation at 10,000 rpm for 10 min. The supernatant was discarded, and procedure repeated once. Next, the QDs were resuspended in 0.6 ml of chloroform, mixed with 70 µl of ethylenediamine and shaken for 40 min. Afterwards, 0.5 ml of Ar-saturated water solution with the specified content of MPA was added and the mixture was shaken for 80 min. Absorbance and emission spectra were recorded prior to the purification step to illustrate the impact of ligand exchange on the spectroscopic features of QD.

6.4.2 Functionalization of polymer-coated QDs with cycloalkyne groups

Prior to the reactions the original storage buffer of carboxyl ITK605 QDs was exchanged to borate buffer (20 mM, pH 7.4) to avoid the possible influence of the components of the original solution on the reaction. This was accomplished by performing four cycles of ultrafiltration (AmiconUltra-0.5, 10 kDa). For the functionalization with BCN groups, carboxyl QDs were mixed with 30 (QD-BCN_1), 70 (QD-BCN_2), 110 (QD-BCN_3) or 200 (QD-BCN_4) equivalents of bifunctional linker (BCN-NH_2), and 2000 equivalents of EDC·HCl in a borate buffer (20 mM, pH 7.4). Immediately after the mixing of components, the mixture was thoroughly vortexed for 3 min and left shaking for 40 min at 25 ˚C (300 rpm). Concentration of QDs during the reaction was always maintained at 1.2 µM. Afterwards, a 3.5-fold (v/v) excess of borate buffer (50 mM, pH 8.5) was added to the solution and the mixture was left in the dark for additional 40 min to hydrolyze any residual O-acylisourea intermediates. Next, the nanoconjugate was purified using PD MiniTrap G-25 column according to the gravity protocol, eluent: borate buffer (50 mM, pH 8.5). Finally, the mixture was preconcentrated and buffer exchanged into MOPS (50 mM, pH 7.2) via ultrafiltration (AmiconUltra-0.5, 10 kDa). A total of three buffer exchange cycles were carried out. The retained solution was down-spun by centrifugation at 1000 G for 2 min at 20 ˚C and stored in the fridge (+4 ˚C).

6.4.3 Immobilization of label acceptor PNA on a QD

QD-(PNAa)$_9$: QD-BCN_1 was mixed with 100 eq. of PNAa in Ar-saturated MOPS buffer (50 mM, pH 7.2). The mixture was vortexed for 2 min and left shaking at 125 rpm for 3 days in the dark. The concentration of QD during the reaction was kept at 0.65 µM. Next, a solution of TCEP in borate buffer (50 mM borate, 10 mM TCEP, pH 7.2) was added to the reaction mixture (20 000 eq. TCEP relative to QD concentration) and the mixture was left shaking for 4 h. This was done to reduce any

disulfide bonds that may have formed during the reaction. Finally, the nanoconjugate was purified using Illustra MicroSpin G50 column. The recovery of the conjugate was carried out at 735 G for 2 min (20 °C).

QD-(PNAd)$_3$: QD-BCN$_1$ was mixed with 100 eq. of PNAd in MOPS buffer (50 mM MOPS, pH 7.2), vortexed for 3 min and left shaking in the dark for 24 h at 23 °C (300 rpm). The concentration of QD in the reaction mixture was kept at 0.65 μM. Next, an aliquote of concentrated NaCl solution was added to adjust the C(NaCl) to 50 mM and the reaction was left to proceed for 3 days. Afterward, the residual BCN groups were capped by the addition of 1200 eq. of 2-azidoacetic acid (2-AAA) (1 day). Finally, the conjugate was purified using Illustra MicroSpin G50 column.

QD-(PNAg)$_5$: QD-BCN$_1$ was mixed with 100 eq. of PNAg in MOPS buffer (50 mM MOPS, pH 7.2). The following steps were carried out according to the protocol described for the synthesis of QD-(PNAd)$_3$.

QD-(PNAd)$_{16}$: QD-BCN$_3$ was mixed with 220 eq. of PNAd in MOPS buffer (50 mM MOPS, pH 7.2), vortexed for 2 min, and left shaking for 1 day at 25 °C (300 rpm), the concentration of QD in the reaction mixture was kept at 0.52 μM. Then, the C(NaCl) was adjusted to 50 mM and the mixture was left shaking for 3 days. Next, the residual BCN groups were capped using 2200 eq. of 2-AAA (1 day). Purification was performed using Illustra MicroSpin G50 column.

QD-(PNAj)$_x$: QD-BCN$_1$ was used for the preparation of QD-(PNAj)$_4$, QD-BCN$_2$ for QD-(PNAj)$_{11}$, QD-BCN$_3$ for QD-(PNAj)$_{33}$, and QD-BCN$_4$ for QD-(PNAj)$_{59}$. In a typical procedure, QD-BCN conjugate was mixed with a 100-fold (QD-(PNAj)$_4$) or 150-fold (QD-PNAj)$_{11, 33, 59}$) molar excess of PNAj in MOPS buffer (50 mM MOPS, pH 7.2), vortexed for 2 min and left to react for 3 days at 25°C (300 rpm). Concentration of QD was kept at 1 μM for all conjugates except QD-(PNAj)$_{11}$ (0.6 μM). Afterward, a 3500-fold excess of 2-azidoacetic acid was added to cap any residual BCN groups. QD-PNA conjugates were purified using Illustra MicroSpin G50 column. The recovery of conjugate was performed at 500 G for 2 min (20°C).

Dithiol bonds can be either reduced prior to the transfer reaction by treatment with a 100-fold (v/v) excess of TCEP-containing MOPS buffer (50 mM MOPS, 15 mM TCEP, pH 7.2) for 5 min or reduced in a separate step, purified *via* SEC G50 and stored in a deprotected form in Ar-saturated buffer. Within the course of this work it was noticed that QD-(PNAj)$_{59}$ stored in a protected form (StBu “ON”) at +4 °C retained its colloidal stability for at least 9 months.

6.5 Surface Group Analysis of Functionalized QDs

6.5.1 Quantification of the labeling density of QD-BCN conjugates

To estimate the number of BCN groups per nanoparticle, each QD-BCN conjugate was reacted with a 100-500-fold molar excess of Cy5-N_3 (depending on the conjugate) at a C(QD) in the range of 0.5-1.0 µM in MOPS buffer (50 mM, pH 7.2) for 7 days at 25 °C. The completion of reaction was monitored *via* FRET. The prepared QD-BCN-Cy5 conjugates were then purified via SEC (G50). The removal of excess Cy5-N_3 was performed at 735 G for 2 min (20°C). In order to confirm the removal of Cy5 upon purification and to assess the potential for non-specific absorption of Cy5 on the nanoparticle surface, QD-carboxyl was mixed with the Cy5-N_3 and purified in the same fashion as QD-BCN-Cy5 conjugates. Absorption spectra were recorded on a NanoDrop ND-1000 spectrometer. Luminescence spectra were recorded on a NanoDrop ND-3300 fluorometer. $\lambda_{ex.}$ = 435 nm. For luminescence measurements, the concentration of each conjugate was adjusted to 10 nM with 50 mM borate buffer, pH 8.5.

6.5.2 Quantification of the labeling density of QD-PNA conjugates

To confirm that QD-immobilized PNA are available for hybridization, QD-PNA conjugates were incubated with an excess of complementary Cy5-labeled RNA (RNA-Cy5c). Noncomplementary Cy5-labeled RNA (RNA-Cy5nc) was used as a negative control. Completion of hybridization was monitored via FRET and photoluminescence spectra were recorded after the emission of FRET donor ceased to decrease. All experiments were carried out by using borate buffer (50 mM borate, 5 mM TCEP, 50 mM NaCl, pH 8.8 or 8.9).

QD-$(PNAa)_9$ was diluted to the concentration of 1.9 nM, and incubated with 160 eq. of either RNA-Cy5c or RNA-Cy5nc for 25 h. The concentrations of QD-$(PNAd)_3$, QD-$(PNAd)_{16}$ and QD-$(PNAg)_5$ were adjusted to 10 nM and they were incubated with a 100-fold excess of either RNA-Cy5c or RNA-Cy5nc for 241 h. Photoluminescence spectra were recorded using Infinite M200pro (Tecan) fluorescence reader. λ_{ex} = 435 nm. The concentration of QD-PNAj conjugates was adjusted to 20 pM and they were mixed with a 150-fold excess of either RNA-Cy5c or RNA-Cy5nc. Emission spectra were recorded on a Fluoromax 4 (Horiba scientific) fluorescence spectrometer.

7 Abbreviations

2-AAA, 2-azidoacetic acid;

Å, angstrom;

AA, amino acid;

Ac_2O, acetic anhydride;

a.u., arbitrary units;

BCN, bicyclononyne;

Bhoc, benzhydryloxycarbonyl;

Boc, *tert*-butyloxycarbonyl;

CHCA, α-Cyano-4-hydroxycinnamic acid;

CMC, critical micelle concentration;

CO, cyclooctyne;

CTAC, cetyltrimethylammonium chloride;

Cy5, cyanine 5;

DABCYL, 4-(4-dimethylaminophenylazo)benzoyl;

DABSYL, 4-(4-Dimethylaminophenylazo)benzenesulfonyl;

DBU, 1,8-Diazabicyclo[5.4.0]undec-7-ene;

DCM, dichloromethane;

DIPEA, N,N-Diisopropylethylamine;

DMF, dimethylformamide;

DTT, dithiothreitol;

EDA, ethylenediamine;

EDANS, (5-((2-Aminoethyl)amino)naphthalene-1-sulfonic acid);

EDC·HCl, N-Ethyl-N′-(3-dimethylaminopropyl)carbodiimide hydrochloride;

EDT, 1,2-Ethanedithiol;

ESI, electrospray ionization;

Et_2O, diethyl ether;

FA, formamide;

FAM, fluorescein;

FIT, forced intercalation;

Fmoc, fluorenylmethyloxycarbonyl;

Fmoc-AEEA-OH, (2-(2-(Fmoc-amino)ethoxy)ethoxy)acetic acid;

HCTU, O-(1H-6-Chlorobenzotriazole-1-yl)-1,1,3,3-tetramethyluronium hexafluorophosphate;

HOBt, 1-Hydroxybenzotriazole;

HPLC, high-performance liquid chromatography;

LOD, limit of detection;

MALDI-TOF, matrix-assisted laser desorption/ionization coupled with time-of-flight MS;

MeCN, acetonitrile;

MeOH, methanol;

MESNa, 2-Mercaptoethanesulfonic acid sodium salt;

MOPS, 3-(*N*-morpholino)propanesulfonic acid;

MS, mass spectrometry;

MWCO, molecular weight cut-off;

NAT, nucleic acid target;

NIR, near-inrfared;

nm, nanometer;

NMM, N-Methylmorpholine;

NMP, N-Methyl-2-pyrrolidone;

ONT, oligonucleotide template;

OTR, oligonucleotide-templated reaction;

$Pd(dppf)Cl_2$, (1,1′-Bis(diphenylphosphino)ferrocene)dichloropalladium(II);

PNA, peptide nucleic acid;

PyBOP, (Benzotriazol-1-yloxy)tripyrrolidinophosphonium hexafluorophosphate;

QD, quantum dot;

QY, quantum yield;

R_0, Förster radius;

SDS, sodium dodecyl sulfate;

SEC, size exclusion chromatography;

SLS, sodium lauroyl sarcosinate;

S/N, signal-to-noise ratio;

SNP, single nucleotide polymorphism;

SPPS, solid phase peptide synthesis;

StBu, *tert*-butylthio;

TA, triazole;

TAMRA, 5-carboxytetramethylrhodamine;

TCEP, tris(2-carboxyethyl)phosphine hydrochloride;

TFA, trifluoroacetic acid;

TIS, triisopropylsilane;

Trt-MPA-OH, S-Trityl-3-mercaptopropionic acid;

TWEEN20, polyoxyethylene (20) sorbitan monolaurate;

UPLC, ultra-performance liquid chromatography.

8 List of Literature

[1] S. A. Byron, K. R. Van Keuren-Jensen, D. M. Engelthaler, J. D. Carpten, D. W. Craig, *Nat Rev Genet* **2016**, *17*, 257-271.

[2] I. M. Mackay, K. E. Arden, A. Nitsche, *Nucleic Acids Res.* **2002**, *30*, 1292–1305.

[3] J. Kuypers, K. R. Jerome, *J Clin Microbiol* **2017**, *55*, 1621-1628.

[4] H. D. VanGuilder, K. E. Vrana, W. M. Freeman, *Biotechniques* **2008**, *44*, 619-626.

[5] C. A. Heid, J. Stevens, K. J. Livak, P. M. Williams, *Genome Res.* **1996**, *6*, 986-994.

[6] P. N. Rys, D. H. Persing, *J. Clin. Microbiol.* **1993**, *31*, 2356–2360.

[7] M. Vaneechoutte, J. V. Eldere, *J Med Microbiol* **1997**, *46*, 188–194.

[8] J. Michaelis, A. Roloff, O. Seitz, *Org Biomol Chem* **2014**, *12*, 2821-2833.

[9] T. N. Grossmann, A. Strohbach, O. Seitz, *Chembiochem* **2008**, *9*, 2185-2192.

[10] C. Dose, O. Seitz, *Bioorg Med Chem* **2008**, *16*, 65-77.

[11] W. R. Algar, K. Susumu, J. B. Delehanty, I. L. Medintz, *Anal Chem* **2011**, *83*, 8826-8837.

[12] N. Hildebrandt, C. M. Spillmann, W. R. Algar, T. Pons, M. H. Stewart, E. Oh, K. Susumu, S. A. Diaz, J. B. Delehanty, I. L. Medintz, *Chem Rev* **2017**, *117*, 536-711.

[13] K. K. Sadhu, N. Winssinger, *Chemistry* **2013**, *19*, 8182-8189.

[14] D. Chang, K. T. Kim, E. Lindberg, N. Winssinger, *Bioconjug Chem* **2018**, *29*, 158-163.

[15] T. N. Grossmann, O. Seitz, *Chemistry* **2009**, *15*, 6723-6730.

[16] H. Zhang, F. Li, B. Dever, X. F. Li, X. C. Le, *Chem Rev* **2013**, *113*, 2812-2841.

[17] S. Tyagi, F. R. Kramer, *Nature Biotechnology* **1996**, *14*, 303-308.

[18] S. Jockusch, A. A. Marti, N. J. Turro, Z. Li, X. Li, J. Ju, N. Stevens, D. L. Akins, *Photochem Photobiol Sci* **2006**, *5*, 493-498.

[19] O. Adegoke, T. Kato, E. Y. Park, *Biosens Bioelectron* **2016**, *80*, 483-490.

[20] B. Dubertret, M. Calame, A. J. Libchaber, *Nature Biotechnology* **2001**, *19*, 365-370.

[21] S. Su, X. Wei, Y. Zhong, Y. Guo, Y. Su, Q. Huang, S.-T. Lee, C. Fan, Y. He, *ACS Nano* **2012**, *6*, 2582–2590.

[22] R. Yang, J. Jin, Y. Chen, N. Shao, H. Kang, Z. Xiao, Z. Tang, Y. Wu, Z. Zhu, W. Tan, *J Am Chem Soc* **2008** *130*, 8351-8358.

[23] J. Zheng, R. Yang, M. Shi, C. Wu, X. Fang, Y. Li, J. Li, W. Tan, *Chem Soc Rev* **2015**, *44*, 3036-3055.

[24] A. V. Hadjinicolaou, V. L. Demetriou, M. A. Emmanuel, C. K. Kakoyiannis, L. G. Kostrikis, *BMC Microbiol* **2009**, *9*, 97.

[25] O. Seitz, F. Bergman, D. Heindl, *Angew. Chem. Int. Ed.* **1999**, *38*, 2203-2206.

[26] F. Hovelmann, I. Gaspar, S. Loibl, E. A. Ermilov, B. Roder, J. Wengel, A. Ephrussi, O. Seitz, *Angew Chem Int Ed Engl* **2014**, *53*, 11370-11375.

[27] F. Hovelmann, O. Seitz, *Acc Chem Res* **2016**, *49*, 714-723.

[28] F. Hovelmann, I. Gaspar, J. Chamiolo, M. Kasper, J. Steffen, A. Ephrussi, O. Seitz, *Chem Sci* **2016**, *7*, 128-135.

[29] S. Kummer, A. Knoll, E. Socher, L. Bethge, A. Herrmann, O. Seitz, *Bioconjug Chem* **2012**, *23*, 2051-2060.

[30] D. M. Kolpashchikov, *Chem. Rev.* **2010**, *110*, 4709–4723.

[31] G. M. Fang, J. Chamiolo, S. Kankowski, F. Hovelmann, D. Friedrich, A. Lower, J. C. Meier, O. Seitz, *Chem Sci* **2018**, *9*, 4794-4800.

[32] R. Naylor, P. T. Gilham, *Biochemistry* **1966**, *5*, 2722–2728.

[33] M. Di Pisa, O. Seitz, *ChemMedChem* **2017**, *12*, 872 – 882.

[34] J. Saarbach, E. Lindberg, N. Winssinger, *Chimia (Aarau)* **2018**, *72*, 207-211.

[35] K. Gorska, N. Winssinger, *Angew Chem Int Ed Engl* **2013**, *52*, 6820-6843.

[36] A. P. Silverman, E. T. Kool, *Chem. Rev.* **2006**, *106*, 3775-3789.

[37] C. Dose, S. Ficht, O. Seitz, *Angew Chem Int Ed Engl* **2006**, *45*, 5369-5373.

[38] J. Sayers, R. J. Payne, N. Winssinger, *Chemical Science* **2018**, *9*, 896-903.

[39] S. Sando, E. T. Kool, *J. Am. Chem. Soc.* **2002**, *124*, 2096-2097.

[40] S. Sando, E. T. Kool, *J. Am. Chem. Soc.* **2002**, *124*, 9686-9687.

[41] H. Abe, E. T. Kool, *PNAS* **2006**, *103*, 263–268.

[42] H. Maruyama, R. Oikawa, M. Hayakawa, S. Takamori, Y. Kimura, N. Abe, G. Tsuji, A. Matsuda, S. Shuto, Y. Ito, H. Abe, *Nucleic Acids Res* **2017**, *45*, 7042-7048.

[43] P. Werther, J. S. Mohler, R. Wombacher, *Chemistry* **2017**, *23*, 18216-18224.

[44] J. Seckute, J. Yang, N. K. Devaraj, *Nucleic Acids Res* **2013**, *41*, e148.

[45] H. Abe, E. T. Kool, *J Am Chem Soc* **2004**, *126*, 13980-13986.

[46] W. A. Velema, E. T. Kool, *J Am Chem Soc* **2017**, *139*, 5405-5411.

[47] T. N. Grossmann, O. Seitz, *J Am Chem Soc* **2006**, *128*, 15596-15597.

[48] T. N. Grossmann, L. Roglin, O. Seitz, *Angew Chem Int Ed Engl* **2008**, *47*, 7119-7122.

[49] J. Michaelis, G. J. van der Heden van Noort, O. Seitz, *Bioconjug Chem* **2014**, *25*, 18-23.

[50] R. M. Franzini, E. T. Kool, *J. Am. Chem. Soc.* **2009**, *131*, 16021–16023.

[51] M. Röthlingshöfer, K. Gorska, N. Winssinger, *Org. Lett.* **2012**, *14*, 482-485.

[52] H. Wu, S. C. Alexander, S. Jin, N. K. Devaraj, *J Am Chem Soc* **2016**, *138*, 11429-11432.

[53] D. K. Prusty, M. Kwak, J. Wildeman, A. Herrmann, *Angew Chem Int Ed Engl* **2012**, *51*, 11894-11898.

[54] R. Rossetti, S. Nakahara, L. E. Brus, *The Journal of Chemical Physics* **1983**, *79*, 1086-1088.

[55] M. L. Steigerwald, A. P. Alivisatos, J. M. Gibson, T. D. Harris, R. Kortan, A. J. Muller, A. M. Thayer, T. M. Duncan, D. C. Douglass, L. E. Brus, *J. Am. Chem. Soc.* **1988**, *110*, 3046–3050.

[56] C. B. Murray, D. J. Norris, M. G. Bawendi, *J Am Chem Soc* **1993**, *115*, 8706-8715.

[57] C. B. Murray, C. R. Kagan, M. G. Bawendi, *Annu. Rev. Mater. Sci.* **2000**, *30*, 545–610.

[58] M. A. Hines, P. Guyot-Sionnest, *J. Phys. Chem.* **1996**, *100*, 468-471.

[59] S. V. Kershaw, A. S. Susha, A. L. Rogach, *Chem Soc Rev* **2013**, *42*, 3033-3087.

[60] J. Hühn, C. Carrillo-Carrion, M. G. Soliman, C. Pfeiffer, D. Valdeperez, A. Masood, I. Chakraborty, L. Zhu, M. Gallego, Z. Yue, M. Carril, N. Feliu, A. Escudero, A. M. Alkilany, B. Pelaz, P. del Pino, W. J. Parak, *Chemistry of Materials* **2016**, *29*, 399-461.

[61] J. Owen, L. Brus, *J Am Chem Soc* **2017**, *139*, 10939-10943.

[62] C. Bullen, P. Mulvaney, *Langmuir* **2006**, *22*, 3007-3013.

[63] P. Reiss, M. Protiere, L. Li, *Small* **2009**, *5*, 154-168.

[64] B. O. Dabbousi, J. Rodriguez-Viejo, F. V. Mikulec, J. R. Heine, H. Mattoussi, R. Ober, K. F. Jensen, M. G. Bawendi, *J. Phys. Chem. B* **1997**, *101*, 9463-9475.

[65] S. J. Rosenthal, J. McBride, S. J. Pennycook, L. C. Feldman, *Surf Sci Rep* **2007**, *62*, 111-157.

[66] G. Palui, F. Aldeek, W. Wang, H. Mattoussi, *Chem Soc Rev* **2015**, *44*, 193-227.

[67] E. Cai, P. Ge, S. H. Lee, O. Jeyifous, Y. Wang, Y. Liu, K. M. Wilson, S. J. Lim, M. A. Baird, J. E. Stone, K. Y. Lee, M. W. Davidson, H. J. Chung, K. Schulten, A. M. Smith, W. N. Green, P. R. Selvin, *Angew Chem Int Ed Engl* **2014**, *53*, 12484-12488.

[68] S. Tamang, G. Beaune, I. Texier, P. Reiss, *ACS Nano* **2011**, *5*, 9392–9402.

[69] G. P. Mitchell, C. A. Mirkin, R. L. Letsinger, *J. Am. Chem. Soc.* **1999**, *121*, 8122–8123.

[70] A. R. Clapp, E. R. Goldman, H. Mattoussi, *Nat Protoc* **2006**, *1*, 1258-1266.

[71] N. Zhan, G. Palui, H. Mattoussi, *Nat Protoc* **2015**, *10*, 859-874.

[72] E. Petryayeva, W. R. Algar, *Anal Chem* **2014**, *86*, 3195-3202.

[73] E. E. Lees, T.-L. Nguyen, A. H. A. Clayton, P. Mulvaney, *ACS Nano* **2009**, *3*, 1121–1128.

[74] C. Luccardini., C. Tribet., F. Vial., V. Marchi-Artzner., M. Dahan, *Langmuir* **2006**, *22*, 2304-2310.

[75] T. Pellegrino, L. Manna, S. Kudera, T. Liedl, D. Koktysh, A. L. Rogach', S. Keller, J. Radler, G. Natile, W. J. Parak, *Nano Lett* **2004**, *4*, 703-707.

[76] W. W. Yu, E. Chang, J. C. Falkner, Z. Junyan;, A. M. Al-Somali, C. M. Sayes, J. Johns, R. Drezek, C. V. L., *J Am Chem Soc* **2007**, *129*, 2871-2879.

[77] E. L. Bentzen, I. D. Tomlinson, J. Mason, P. Gresch, M. R. Warnement, D. Wright, E. Sanders-Bush, R. Blakely, S. J. Rosenthal, *Bioconjug Chem* **2005**, *16*, 1488-1494.

[78] W. R. Algar, U. J. Krull, *Sensors* **2011**, *11*, 6214-6236.

[79] W. R. Algar , U. J. Krull, *Anal. Chem.* **2009**, *81*, 4113–4120.

[80] S. Su, J. Fan, B. Xue, L. Yuwen, X. Liu, D. Pan, C. Fan, L. Wang, *ACS Appl Mater Interfaces* **2014**, *6*, 1152-1157.

[81] C.-Y. Zhang, H.-C. Yeh, M. T. Kuroki, T.-H. Wang, *Nature Materials* **2005**, *4*, 826-831.

[82] C.-y. Zhang, J. Hu, *Anal. Chem.* **2010**, *82*, 1921–1927.

[83] C.-y. Zhang, L. W. Johnson, *Anal. Chem.* **2006**, *78*, 5532-5537.

[84] P. Nielsen, M. Egholm, R. Berg, O. Buchardt, *Science* **1991**, *254*, 1497–1500.

[85] E. Uhlmann, A. Peyman, G. Breipohl, D. W. Will, *Angew. Chemie - Int. Ed.* **1998**, *37*, 2796–2823.

[86] J. C. Wu, Q. C. Meng, H. M. Ren, H. T. Wang, J. Wu, Q. Wang, *Acta Pharmacol Sin* **2017**, *38*, 798-805.

[87] P. E. Nielsen, M. Egholm, *Curr. Issues Mol. Biol.* **1999**, *1*, 89–104.

[88] K. Kilså Jensen, H. Ørum, P. E. Nielsen, B. Nordén, *Biochemistry* **1997**, *36*, 5072–5077.

[89] E. Socher, A. Knoll, O. Seitz, *Org Biomol Chem* **2012**, *10*, 7363-7371.

[90] M. Di Pisa, A. Hauser, O. Seitz, *Chembiochem* **2017**, *18*, 872-879.

[91] K. Hashimoto, Y. Ishimori, *Lab Chip* **2001**, *1*, 61-63.

[92] P. Jolly, M. R. Batistuti, A. Miodek, P. Zhurauski, M. Mulato, M. A. Lindsay, P. Estrela, *Sci Rep* **2016**, *6*, 36719.

[93] P. E. Nielsen, *Chemistry & Biodiversity* **2010**, *7*, 786-804.

[94] L. Christensen, R. Fitzpatrick, B. Gildea, K. H. Petersen, H. F. Hansen, T. Koch, M. Egholm, O. Buchardt, P. E. Nielsen, J. Coull, R. Berg, *Journal of Peptide Science* **1995**, *3*, 175-183.

[95] S. A. Thomson, J. A. Josey, R. Cadilla, M. D. Gaul, C. F. Hassman, M. J. Luzzio, A. J. Pipe, K. L. Reed, D. J. Ricca, R. W. Wiethe, S. A. Noble, *Tetrahedron* **1995**, *51*, 6179-6194.

[96] Y. M. Angell, J. Alsina, F. Albericio, B. G., *J. Peptide Res.* **2002**, *60*, 292-299.

[97] R. Chakrabarti, A. M. Klibanov, *J. Am. Chem. Soc.* **2003,**, *125*, 12531–12540.

[98] Z. Pianowski;, K. Gorska;, L. Oswald;, C. A. Merten;, N. Winssinger, *J. Am. Chem. Soc.* **2009**, *131*, 6492–6497.

[99] D. Al Sulaiman, J. Y. H. Chang, S. Ladame, *Angew Chem Int Ed Engl* **2017**, *56*, 5247-5251.

[100] G. O. Menendez, M. E. Pichel, C. C. Spagnuolo, E. A. Jares-Erijman, *Photochem Photobiol Sci* **2013**, *12*, 236-240.

[101] O. Zavoiura, U. Resch-Genger, O. Seitz, *Bioconjug Chem* **2018**, *29*, 1690−1702.

[102] N. G. Iglesias, A. V. Gamarnik, *RNA Biology* **2011**, *8*, 249-257.

[103] I. L. Medintz, H. Mattoussi, *Phys Chem Chem Phys* **2009**, *11*, 17-45.

[104] W. R. Algar, A. J. Tavares, U. J. Krull, *Anal Chim Acta* **2010**, *673*, 1-25.

[105] C. Curutchet, A. Franceschetti, Z. Alex;, G. D. Scholes, *J. Phys. Chem. C* **2008**, *112*, 13336–13341.

[106] M.-Q. Dai, L.-Y. L. Yung, *Chemistry of Materials* **2013**, *25*, 2193-2201.

[107] J. R. Lakowicz, *Principles of Fluorescence Spectroscopy*, 3 ed., Springer, New York, **2006**.

[108] J. Michaelis, PhD thesis, Humboldt-Universität zu Berlin (Berlin), **2014**.

[109] M. V. Kvach, S. V. Gontarev, I. A. Prokhorenko, I. A. Stepanova, V. V. Shmanai, V. A. Korshunb, *Russian Chemical Bulletin* **2006**, *55*, 159—163.

[110] R. Nanjunda, E. A. Owens, L. Mickelson, S. Alyabyev, N. Kilpatrick, S. Wang, M. Henary, W. D. Wilson, *Bioorg Med Chem* **2012**, *20*, 7002-7011.

[111] V. Wycisk, J. Pauli, P. Welker, A. Justies, U. Resch-Genger, R. Haag, K. Licha, *Bioconjug Chem* **2015**, *26*, 773-781.

[112] X. Wu, S. Chang, X. Sun, Z. Guo, Y. Li, J. Tang, Y. Shen, J. Shi, H. Tian, W. Zhu, *Chemical Science* **2013**, *4*.

[113] C. N. Njiojob, E. A. Owens, L. Narayana, H. Hyun, H. S. Choi, M. Henary, *J Med Chem* **2015**, *58*, 2845-2854.

[114] J. J. H. Flanagan, S. H. Khan, S. Menchen, S. A. Soper, R. P. Hammer, *Bioconjugate Chem.* **1997**, *8*, 751-756.

[115] L. Linck, P. Kapusta, U. Resch-Genger, *Photochemistry and Photobiology,* **2012**, *88*, 867–875.

[116] J. Pauli, K. Licha, J. Berkemeyer, M. Grabolle, M. Spieles, N. Wegner, P. Welker, U. Resch-Genger, *Bioconjug Chem* **2013**, *24*, 1174-1185.

[117] C. Wurth, M. Grabolle, J. Pauli, M. Spieles, U. Resch-Genger, *Nat Protoc* **2013**, *8*, 1535-1550.

[118] M. Fischler, A. Sologubenko, J. Mayer, G. Clever, G. Burley, J. Gierlich, T. Carell, U. Simon, *Chem Commun* **2008**, 169-171.

[119] J. I. Cutler, D. Zheng, X. Xu, D. A. Giljohann, C. A. Mirkin, *Nano Lett* **2010**, *10*, 1477-1480.

[120] A. Bernardin, A. Cazet, L. Guyon, P. Delannoy, F. Vinet, D. Bonaffe, I. Texier, *Bioconjug Chem* **2010**, *21*, 583-588.

[121] J. Dommerholt, S. Schmidt, R. Temming, L. J. Hendriks, F. P. Rutjes, J. C. van Hest, D. J. Lefeber, P. Friedl, F. L. van Delft, *Angew Chem Int Ed Engl* **2010**, *49*, 9422-9425.

[122] *Solid Phase Peptide Synthesis, Bachem*, Global Marketing, Bachem Group, **2016**.

[123] P. E. Schneggenburger, B. Worbs, U. Diederichsen, *J Pept Sci* **2010**, *16*, 10-14.

[124] R. van Geel, G. J. Pruijn, F. L. van Delft, W. C. Boelens, *Bioconjug Chem* **2012**, *23*, 392-398.

[125] M. Grabolle, R. Brehm, J. Pauli, F. M. Dees, I. Hilger, U. Resch-Genger, *Bioconjug Chem* **2012**, *23*, 287-292.

[126] A. Kiliszek, K. Banaszak, Z. Dauter, W. Rypniewski, *Nucleic Acids Res* **2016**, *44*, 1937-1943.

[127] Stephen C. Brown, Stephen A. Thomson, James M. Veal, D. G. Davis, *Science* **1994**, *265*, 777-780.

[128] R. Jin, G. Wu, Z. Li, C. A. Mirkin, G. C. Schatz, *J Am Chem Soc* **2003**, *125*, 1643-1654.

[129] E. E. G. Anlansson, S. N. Wall, M. Almgren, H. Hoffmann, I. Kielmann, W. Ulbricht, R. Zana, J. Lang, C. Tondre, *J. Phys. Chem.* **1976**, *80*, 905-922.

[130] G. B. Ray, S. Ghosh, S. P. Moulik, *Journal of Surfactants and Detergents* **2008**, *12*, 131-143.

[131] S. M. Bhairi, *Detergents. A guide to the properties and uses of detergents in biological systems*, Calbiochem-Novabiochem Corporation, **2001**.

[132] C. H. Tan, Z. J. Huang, X. G. Huang, *Anal Biochem* **2010**, *401*, 144-147.

[133] E. Alm, G. Lindegren, K. I. Falk, N. Lagerqvist, *BMC Infect Dis* **2015**, *15*, 493.

[134] B. T. Teoh, S. S. Sam, K. K. Tan, J. Johari, M. B. Danlami, P. S. Hooi, R. Md-Esa, S. AbuBakar, *BMC Infect Dis* **2013**, *13*, 387.

[135] X. Qiu, N. Hildebrandt, *ACS Nano* **2015**, *9*, 8449–8457.

[136] A. Shahmuradyan, U. J. Krull, *Anal Chem* **2016**, *88*, 3186-3193.

[137] W. R. Algar, U. J. Krull, *Anal Chim Acta* **2007**, *581*, 193-201.

[138] M. O. Noor, A. Shahmuradyan, U. J. Krull, *Anal Chem* **2013**, *85*, 1860-1867.

[139] W. E. Briley, M. H. Bondy, P. S. Randeria, T. J. Dupper, C. A. Mirkin, *Proc Natl Acad Sci U S A* **2015**, *112*, 9591-9595.

[140] Y. Wu, J. Huang, X. Yang, Y. Yang, K. Quan, N. Xie, J. Li, C. Ma, K. Wang, *Anal Chem* **2017**, *89*, 8377-8383.

[141] J. Yu, S. He, C. Shao, H. Zhao, J. Li, L. Tian, *Nanoscale* **2018**, *10*, 7067-7076.

[142] A. W. Scott, V. Garimella, C. M. Calabrese, C. A. Mirkin, *Bioconjug Chem* **2017**, *28*, 203-211.

[143] N. Melnychuk, A. S. Klymchenko, *J Am Chem Soc* **2018**, *140*, 10856-10865.

[144] A. Shibata, T. Uzawa, Y. Nakashima, M. Ito, Y. Nakano, S. Shuto, Y. Ito, H. Abe, *J Am Chem Soc* **2013**, *135*, 14172-14178.

[145] Y. W. Lin, H. T. Ho, C. C. Huang, H. T. Chang, *Nucleic Acids Res* **2008**, *36*, e123.

[146] H. Dong, J. Ma, J. Wang, Z. S. Wu, P. J. Sinko, L. Jia, *Mol Ther Nucleic Acids* **2016**, *5*, e302.

[147] M. E. Jung, W. J. Kim, *Bioorg Med Chem* **2006**, *14*, 92-97.

[148] N. Narayanan, G. Patonay, *J. Org. Chem.* **1995**, *60*, 2391-2395.

9 Appendix

NMR spectra

2,3,3-trimethyl-1-(4-sulfobutyl) indolium, inner salt (1)

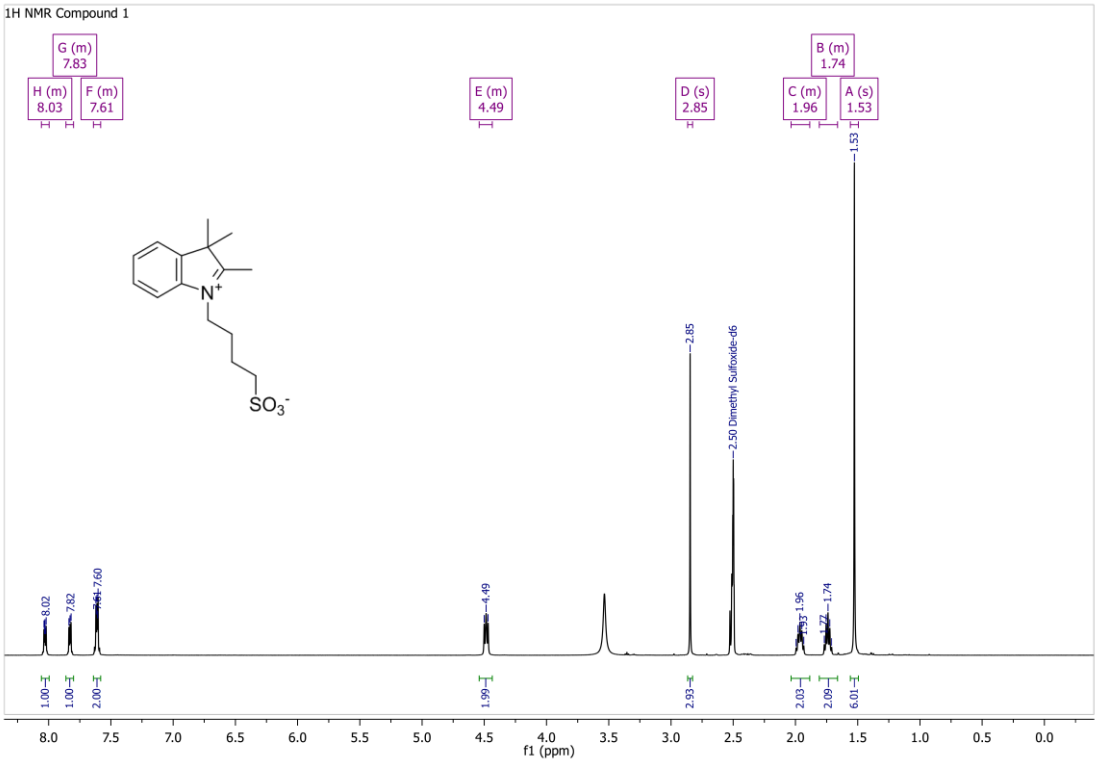

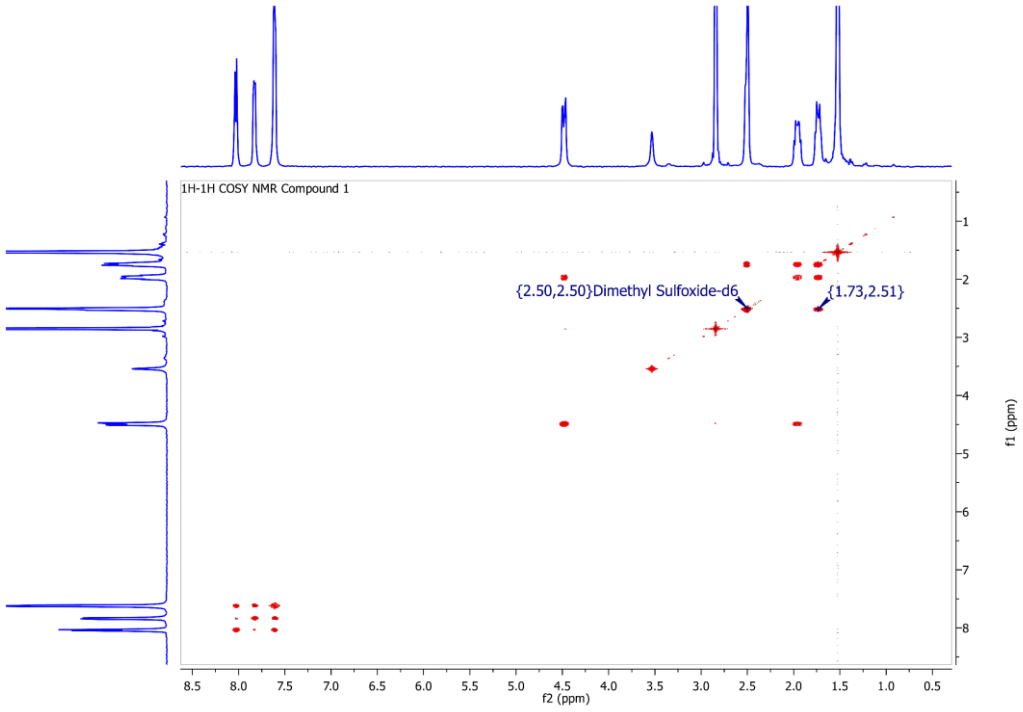

2-bromomalonodianile (2).

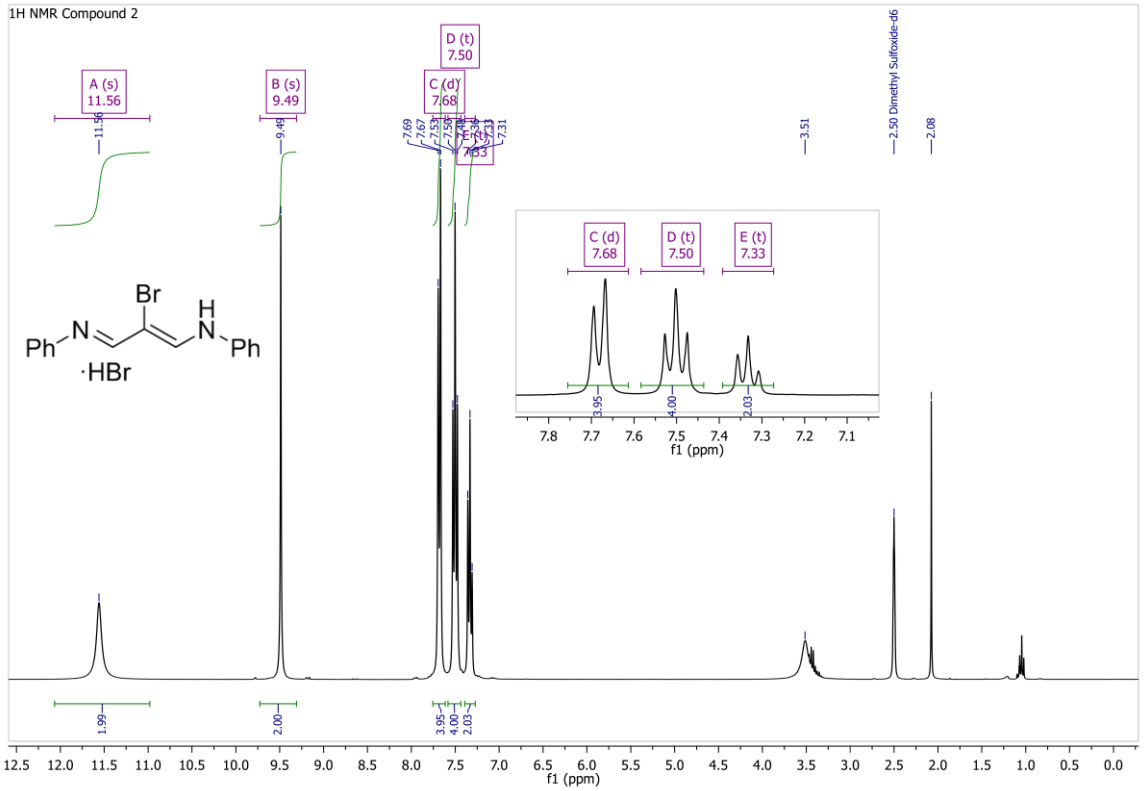

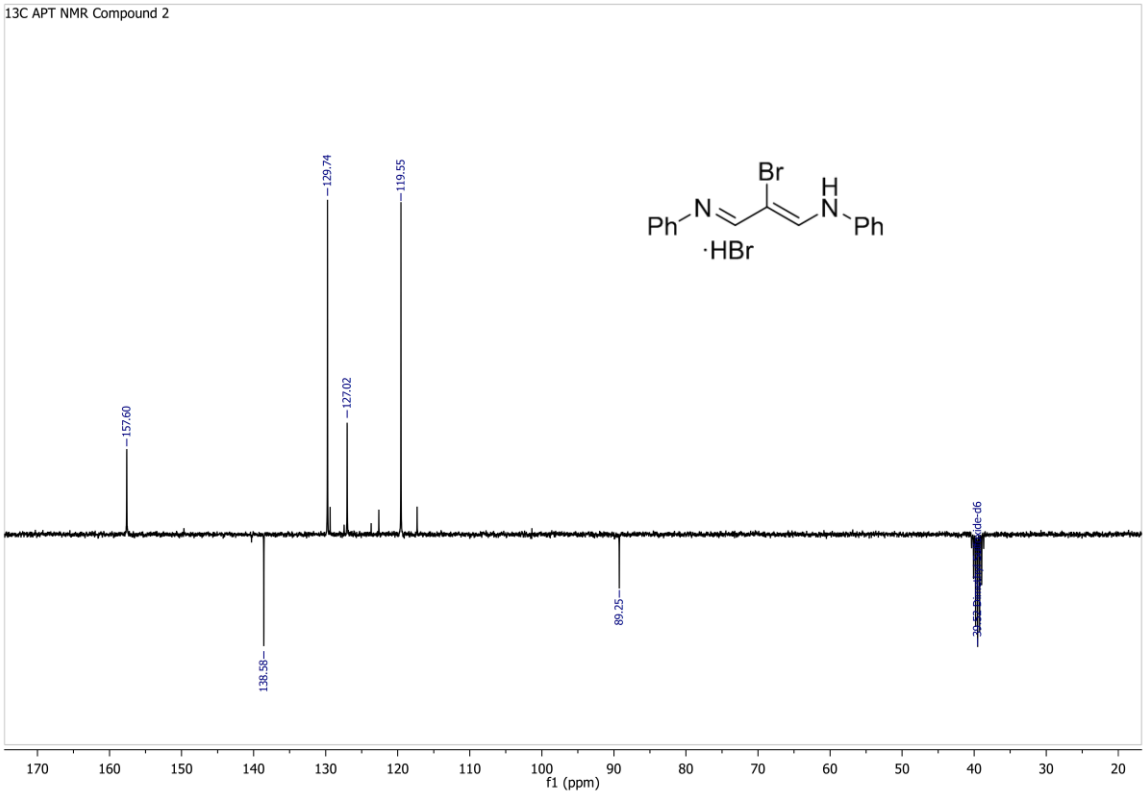

Symmetric disulfo-Cy5-Br (3).

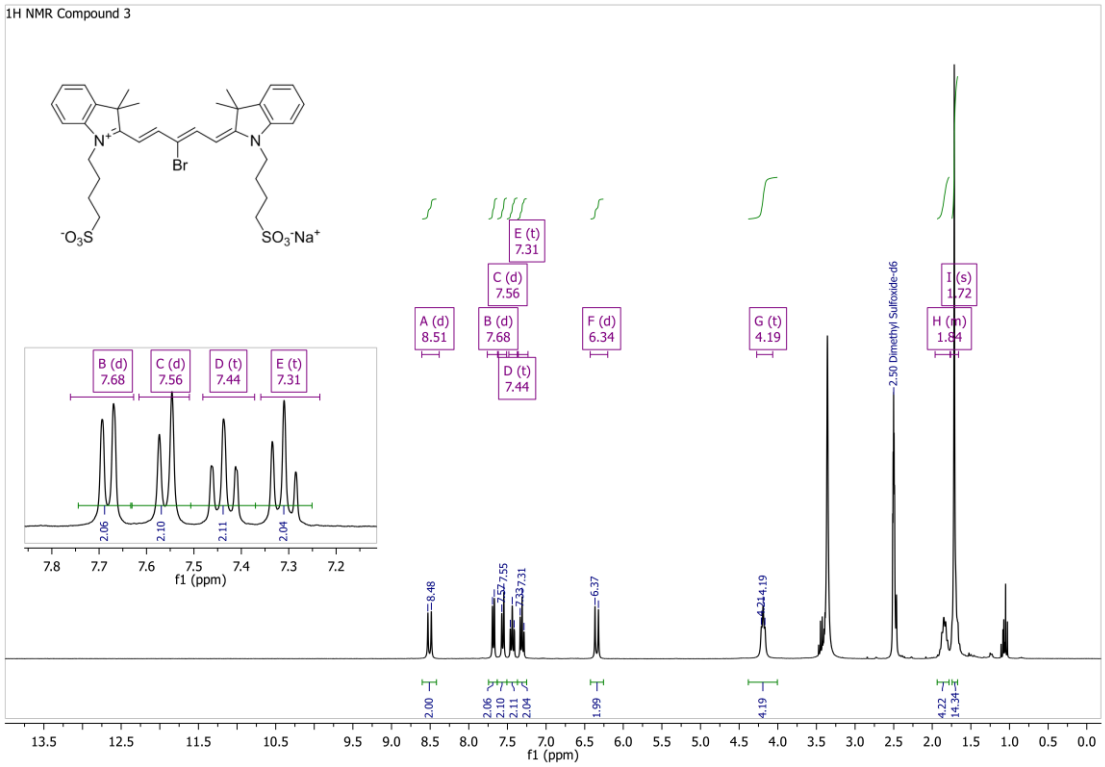

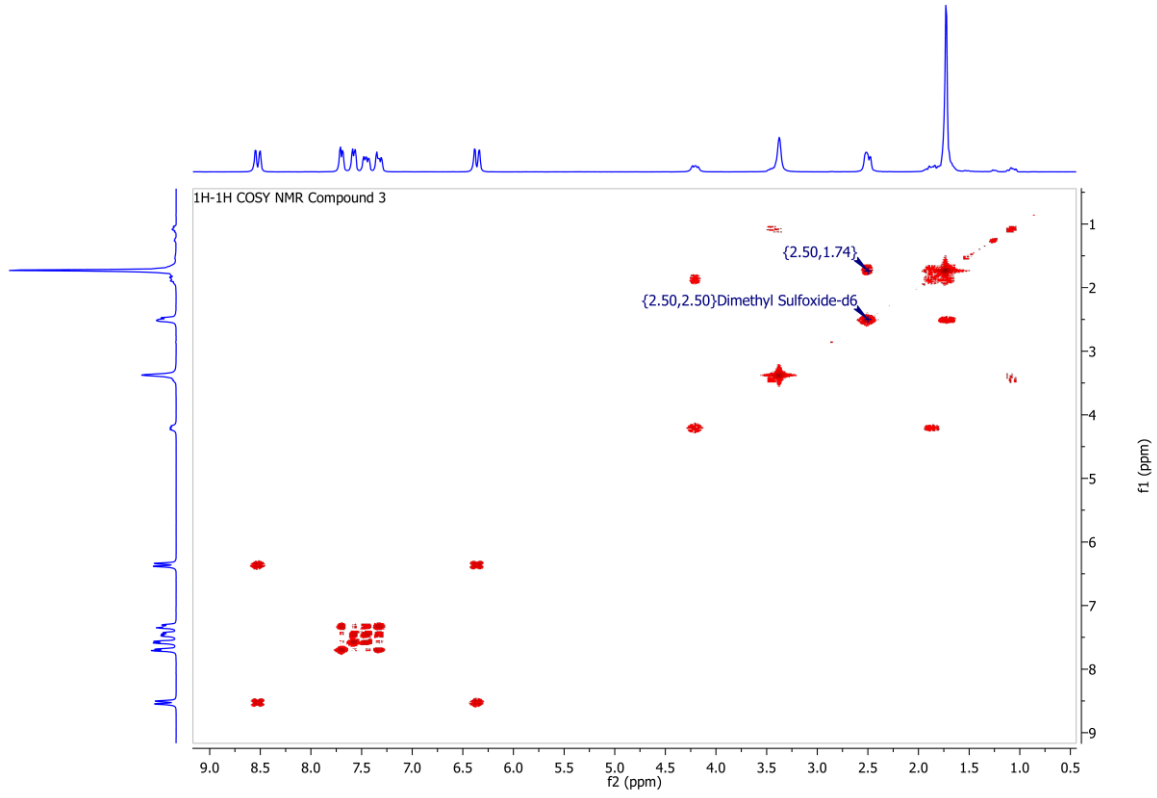

Symmetric disulfo-Cy5 carboxyl (Cy5(4)).

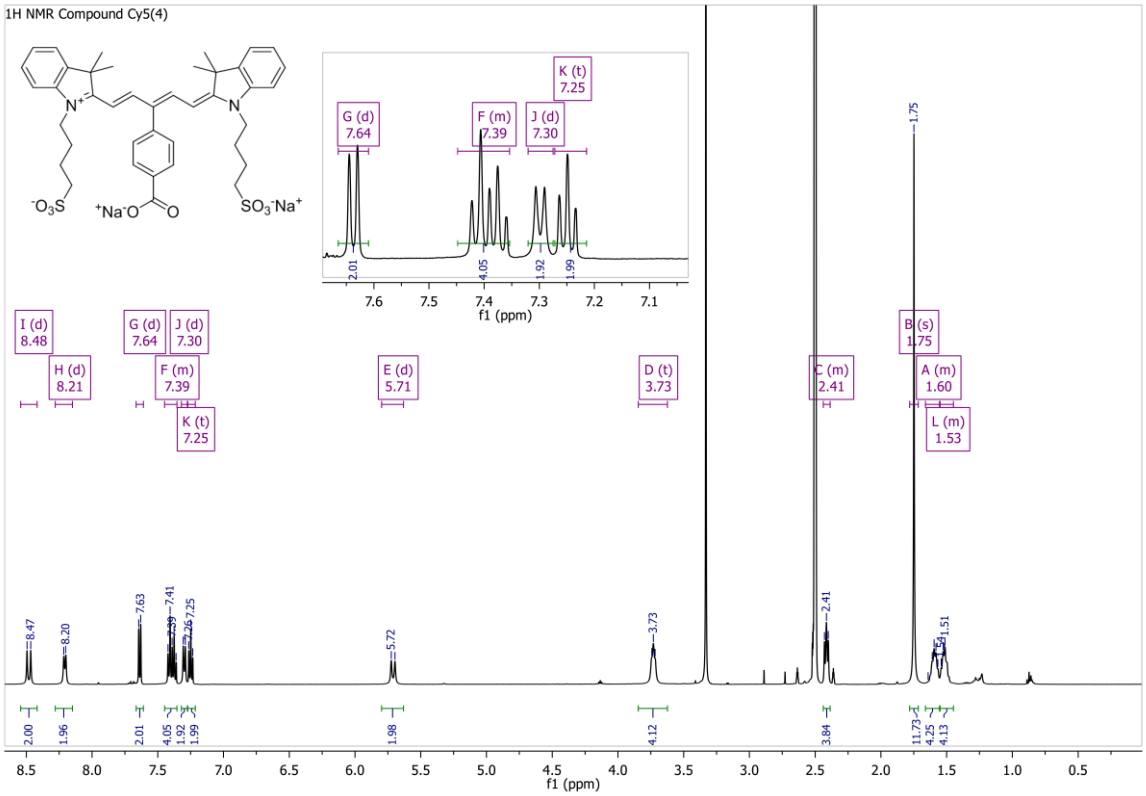

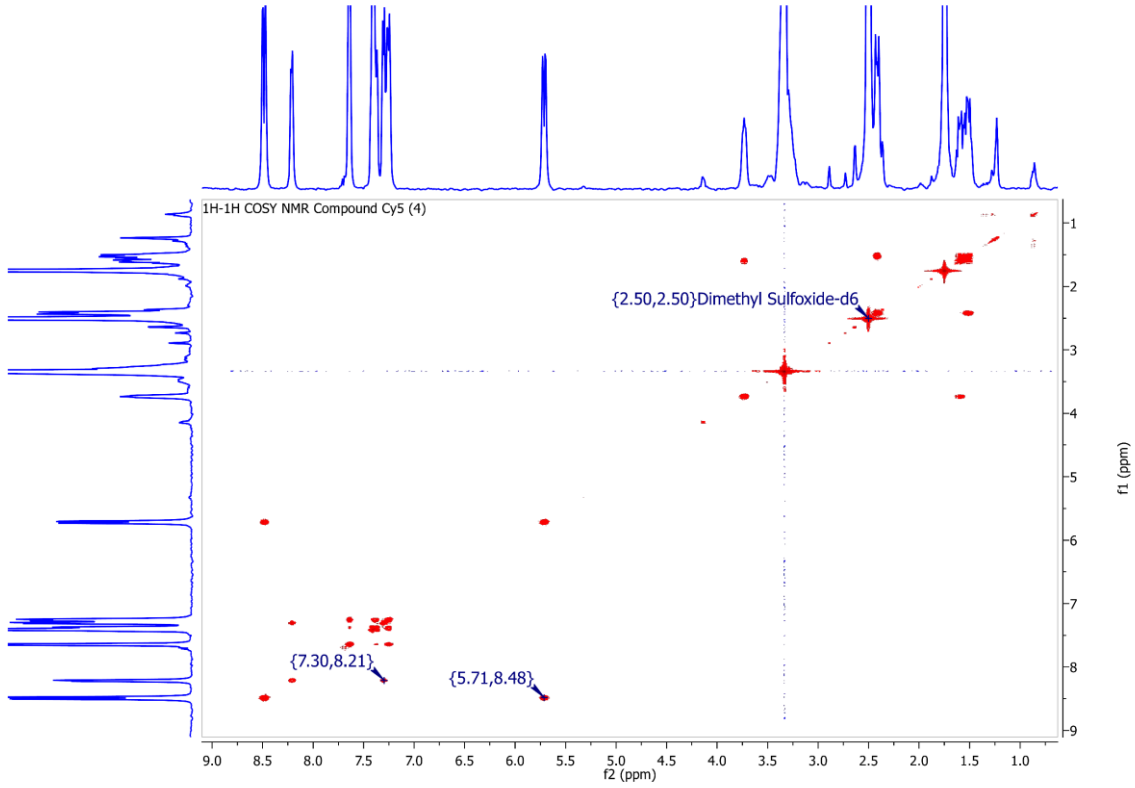

Cl-substituted methine bridge (5).

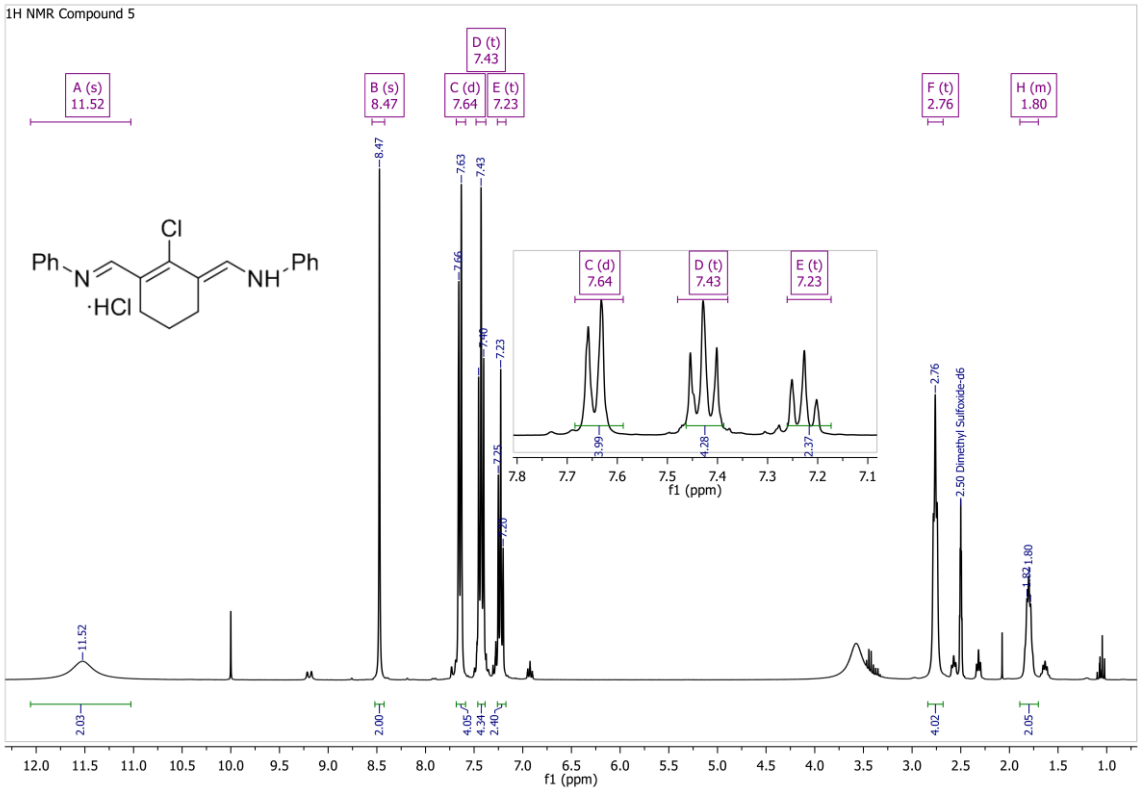

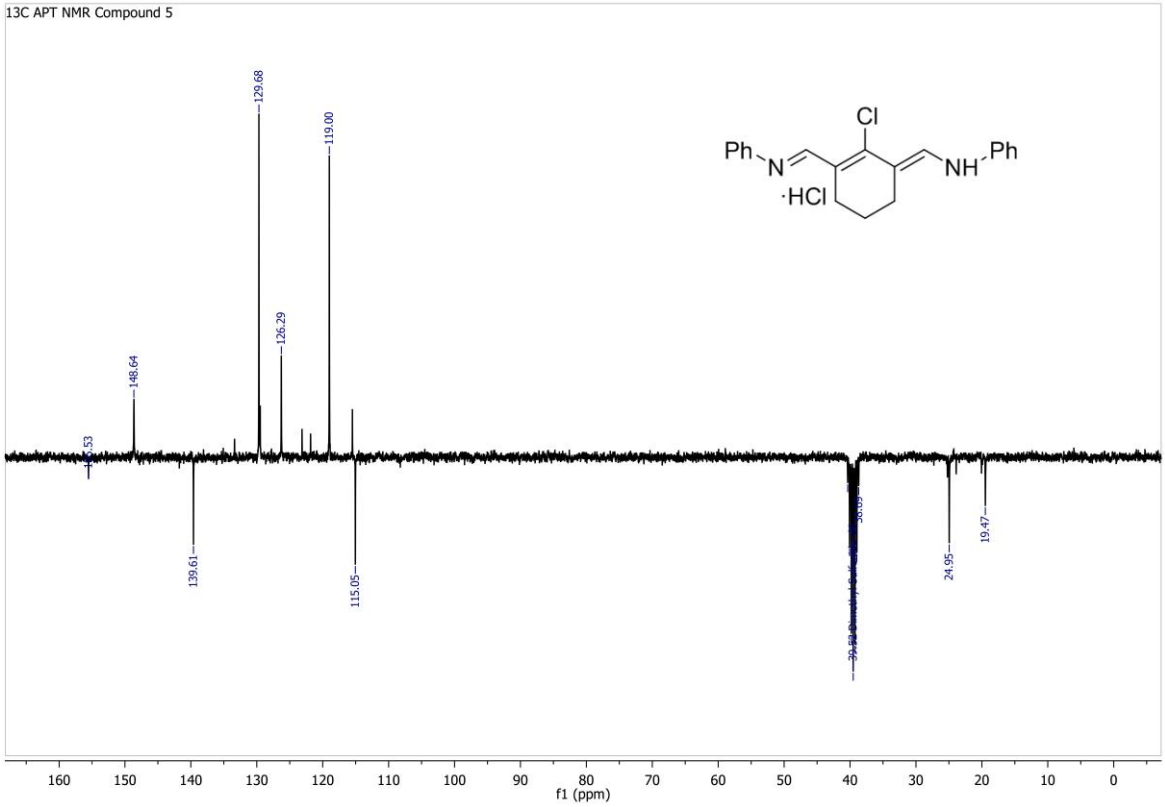

Symmetric dislufo-Cy7-Cl (6).

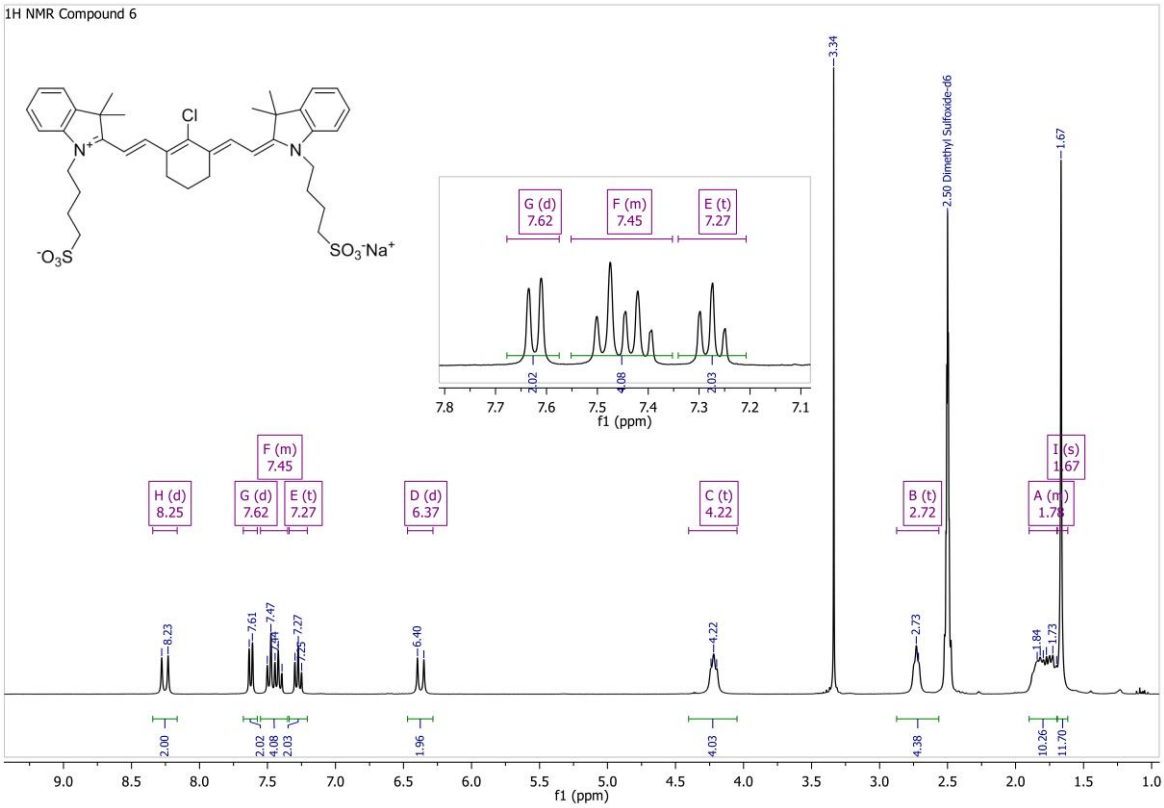

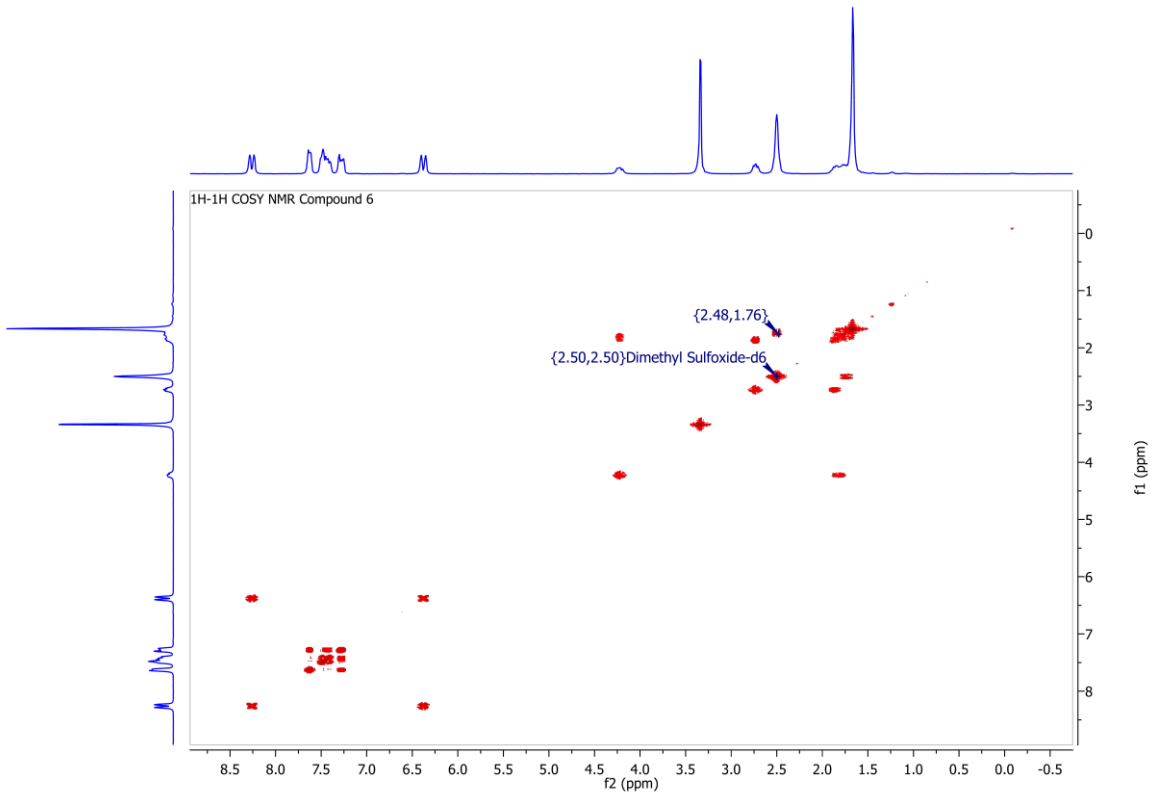

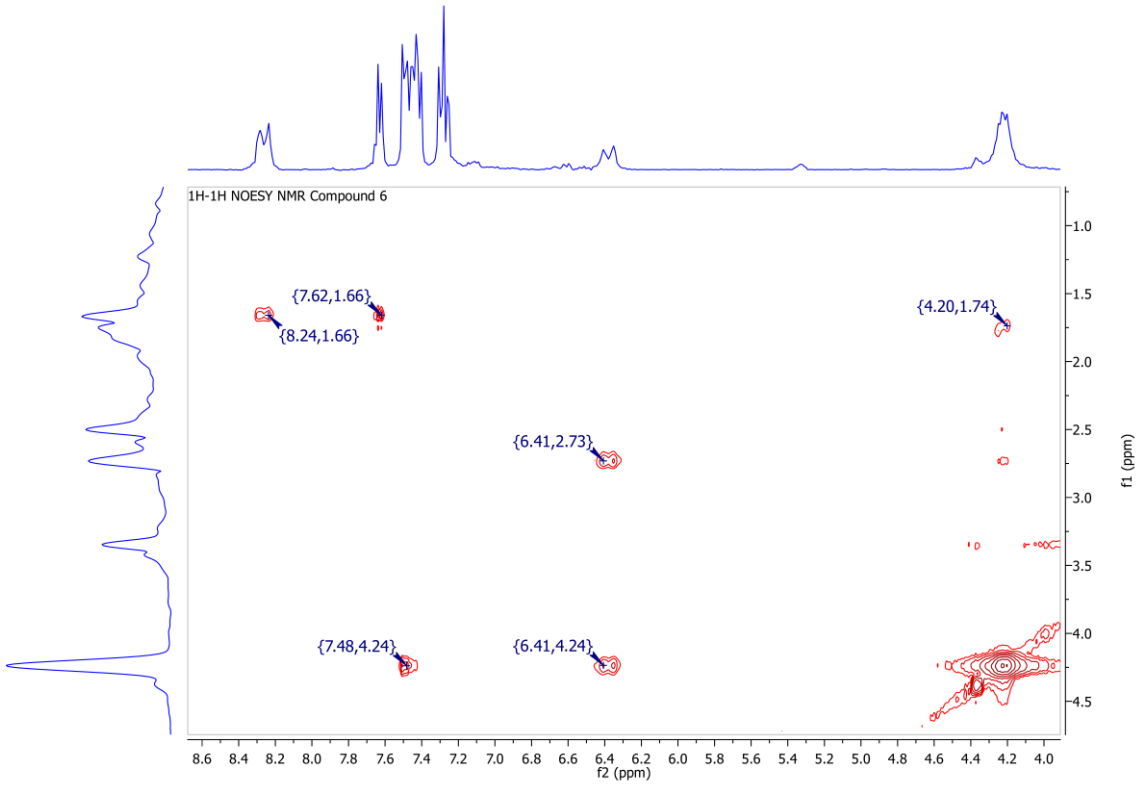
1H-1H NOESY NMR Compound 6
{7.62,1.66}
{8.24,1.66}
{4.20,1.74}
{6.41,2.73}
{7.48,4.24}
{6.41,4.24}
f2 (ppm)
f1 (ppm)

Cy5-Gly-MESNa (8).

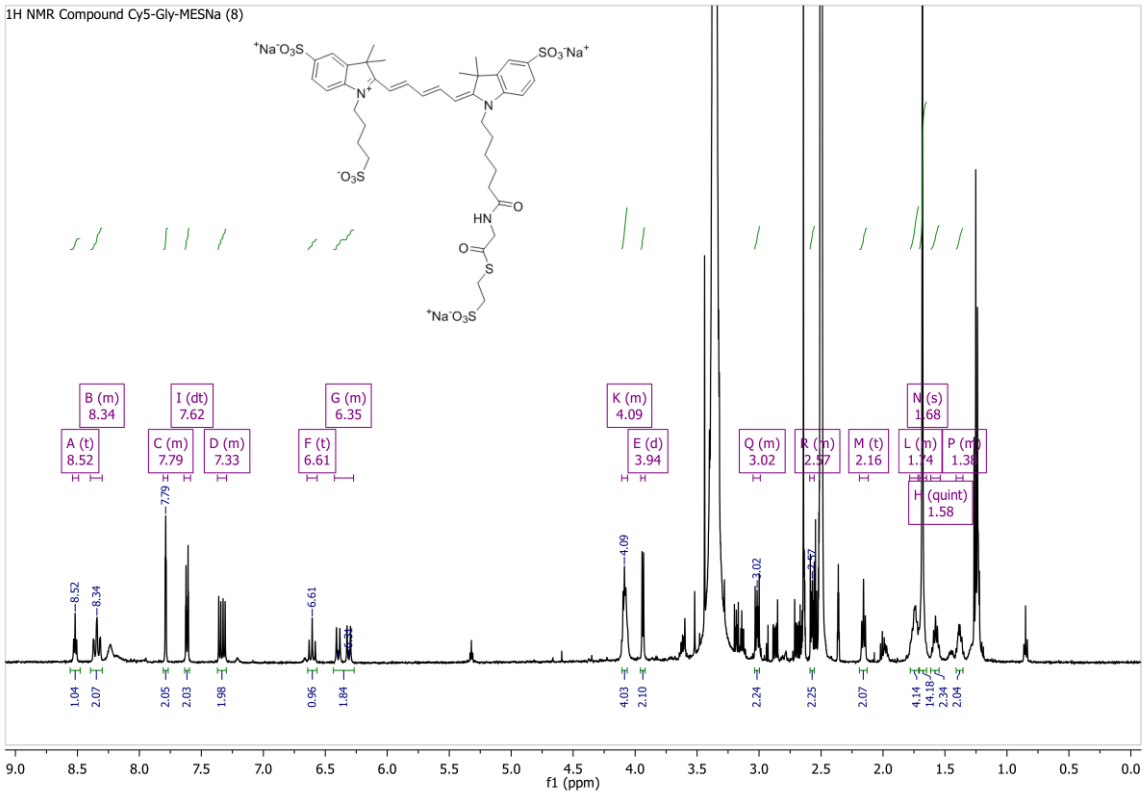

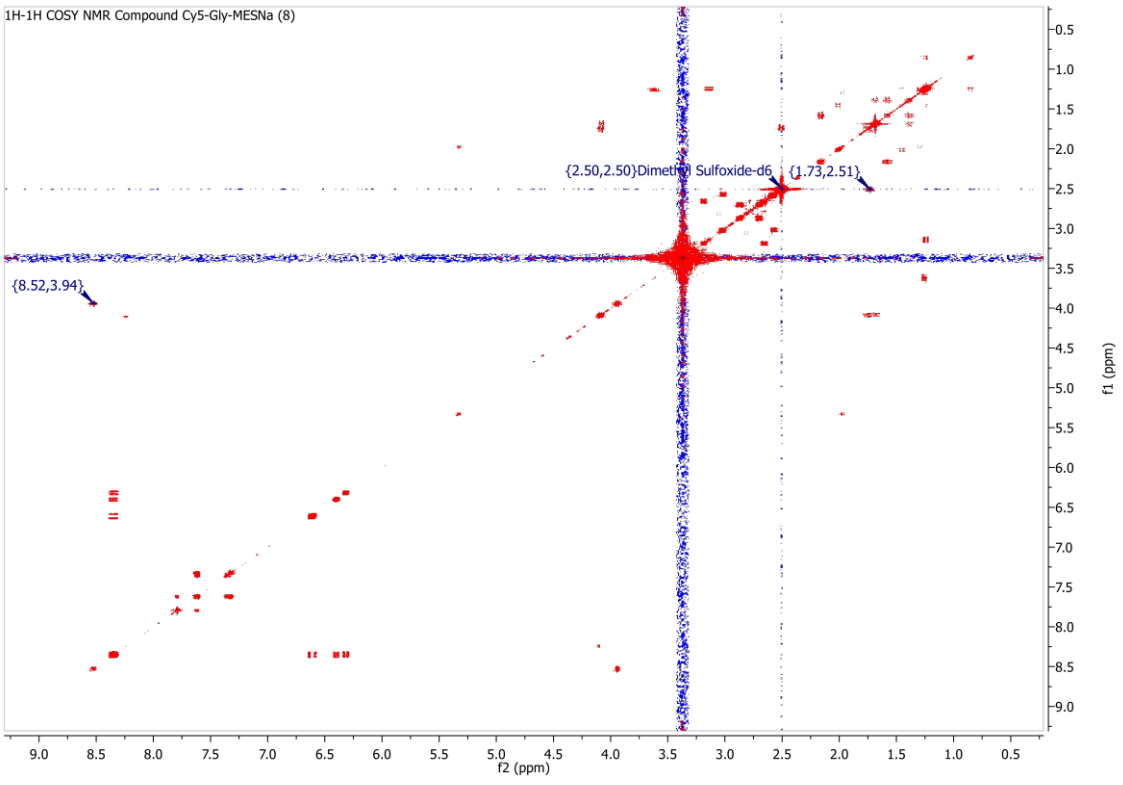

UPLC, ESI-MS and MALDI-TOF MS of PNA conjugates

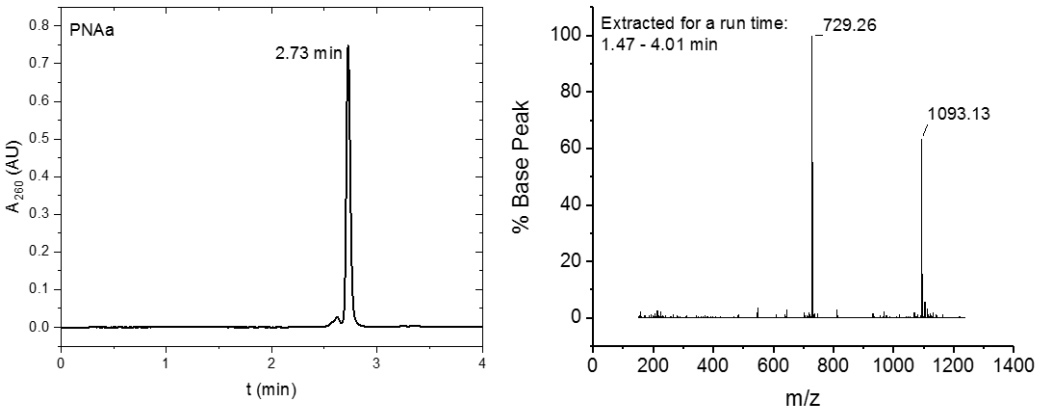

Figure 9.1 UPLC trace (left), and ESI-MS spectrum (right) of PNAa: H-Cys-atctctg-Gly-Orn(N_3)-NH_2. UPLC gradient: 2 to 20 % of solvent B in 4 min. Optical monitoring of signals was performed at 260 nm.

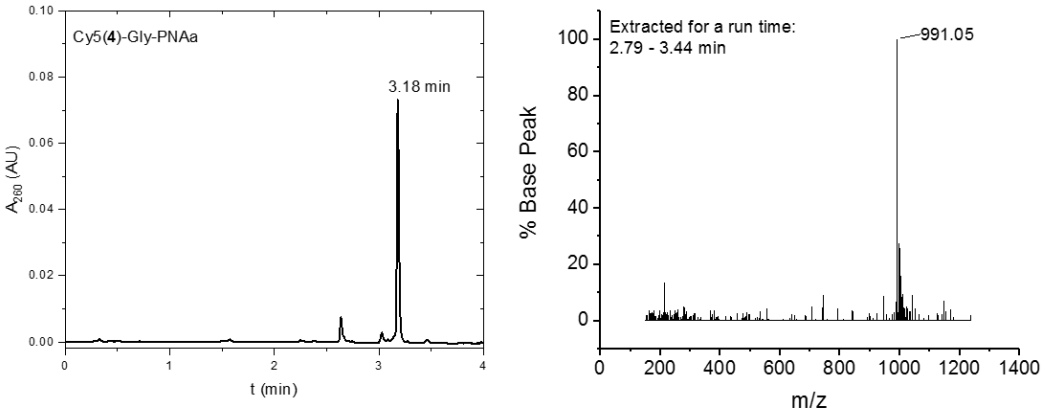

Figure 9.2 UPLC trace (left), and ESI-MS spectrum (right) of Cy5(**4**)-Gly-PNAa: Cy5**(4)**-Gly-Cys-atctctg-Gly-Orn(N_3)-NH_2. UPLC gradient: 3 to 60 % of Solvent B in 4 min. Optical monitoring of signals was performed at 260 nm.

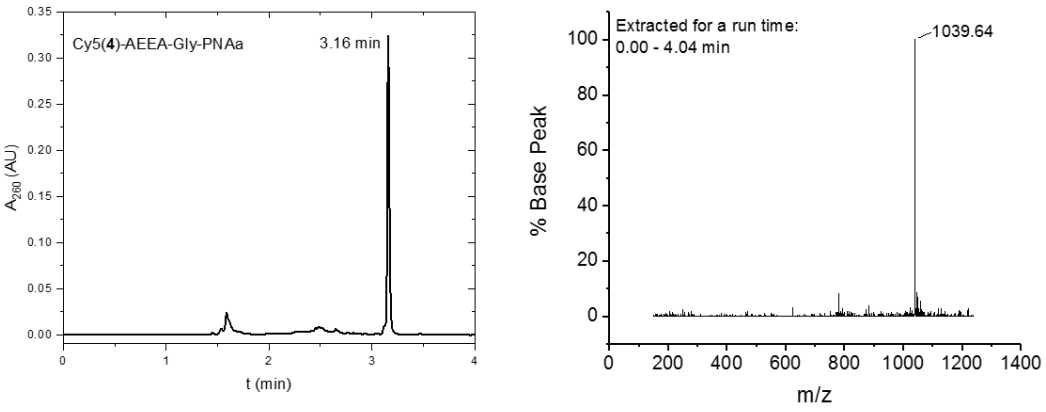

Figure 9.3 UPLC trace (left), and ESI-MS spectrum (right) of Cy5(**4**)-AEEA-Gly-PNAa: Cy5(**4**)-AEEA-Gly-Cys-atctctg-Gly-Orn(N_3)-NH_2. UPLC gradient: 3 to 60 % of Solvent B in 4 min. Optical monitoring of signals was performed at 260 nm.

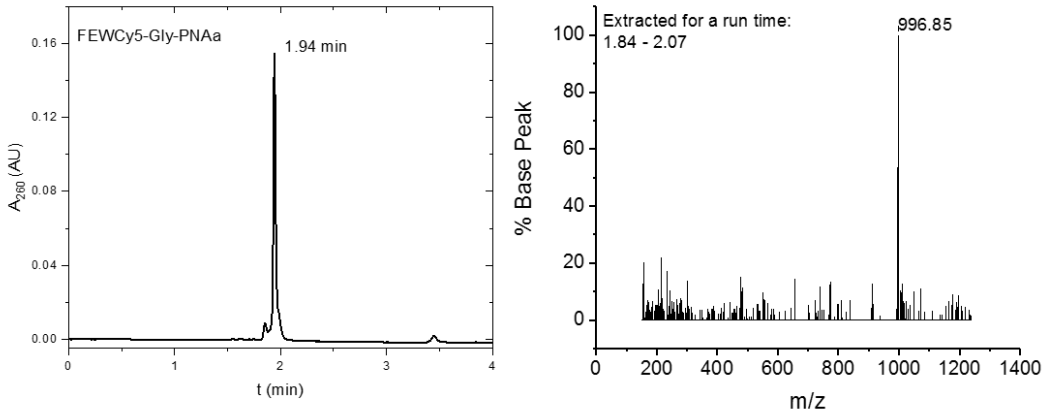

Figure 9.4 UPLC trace (left), and ESI-MS spectrum (right) of FEWCy5-Gly-PNAa: FEWCy5-Gly-Cys-atctctg-Gly-Orn(N_3)-NH_2. UPLC gradient: 3 to 60 % of Solvent B in 4 min. Optical monitoring of signals was performed at 260 nm.

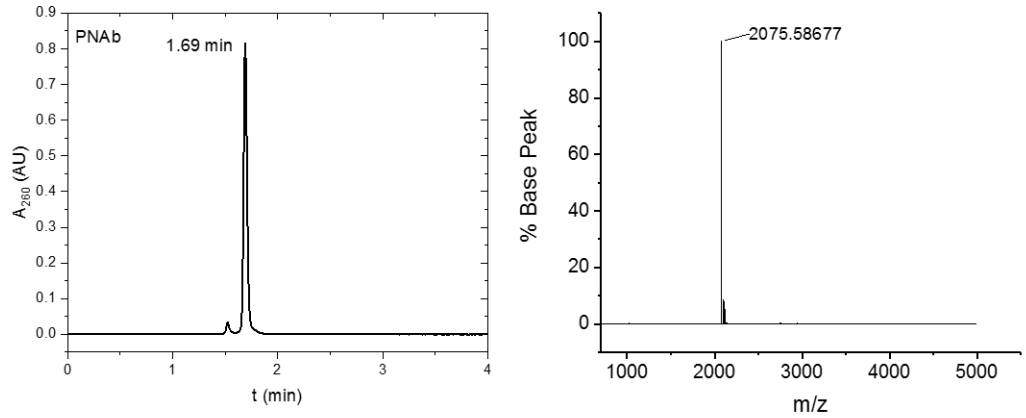

Figure 9.5 UPLC trace (a), and MALDI-TOF spectrum (b) of PNAb: Ac-agacagc-Cys-NH_2. UPLC gradient: 3 to 40 % Solvent B in 4 min. Optical monitoring of signals was performed at 260 nm.

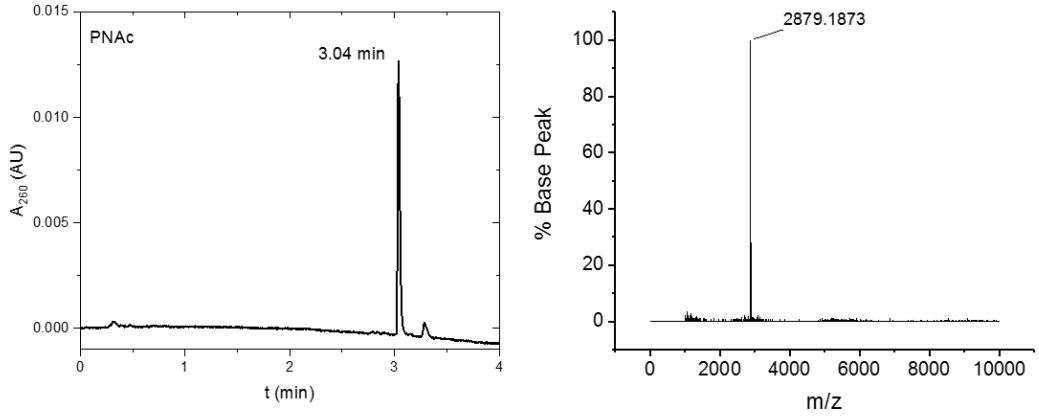

Figure 9.6 UPLC trace (left), and MALDI-TOF spectrum (right) of PNAc: Ac-agacagc-Cys(Cy5-Gly)-NH_2. UPLC gradient: 3 to 40 % Solvent B in 4 min. Optical monitoring of signals was performed at 260 nm.

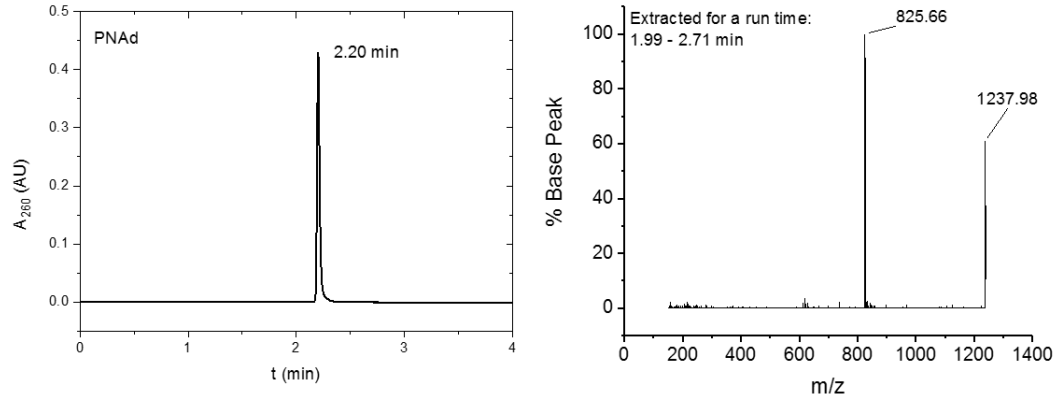

Figure 9.7 UPLC trace (left), and ESI-MS spectrum (right) of PNAd: H-Cys(StBu)-atctctg-Glu-Glu-Orn(N_3)-NH_2. UPLC gradient: 3 to 40 % Solvent B in 4 min. Optical monitoring of signals was performed at 260 nm.

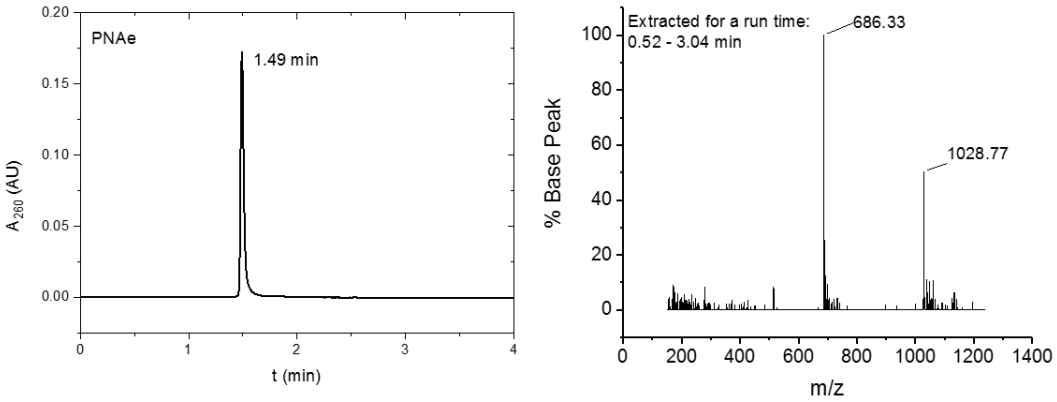

Figure 9.8 UPLC trace (left), and ESI-MS spectrum (right) of PNAe: Ac-Glu-Glu-gacagc-Cys-NH_2. UPLC gradient: 3 to 40 % Solvent B in 4 min. Optical monitoring of signals was performed at 260 nm.

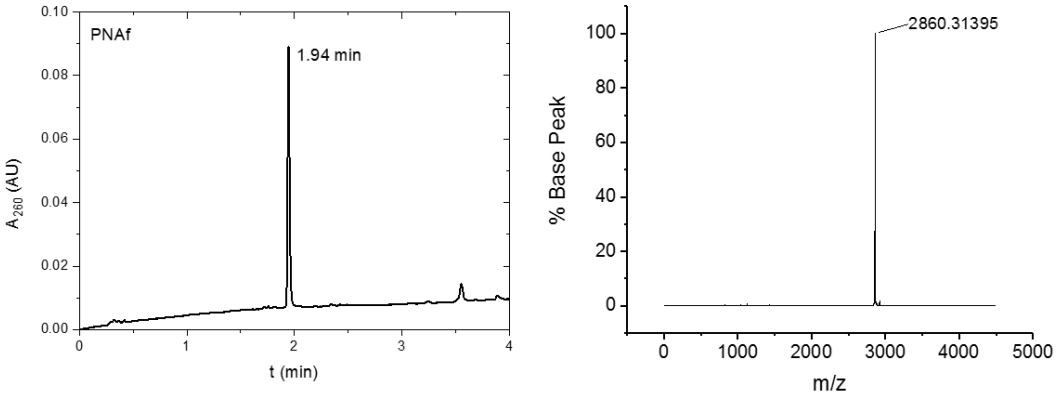

Figure 9.9 UPLC trace (left), and MALDI-TOF mass spectrum (right) of PNAf: Ac-Glu-Glu-gacagc-Cys(Cy5-Gly)-NH_2. UPLC gradient: 3 to 60 % of Solvent B in 4 min. Optical monitoring of signals was performed at 260 nm.

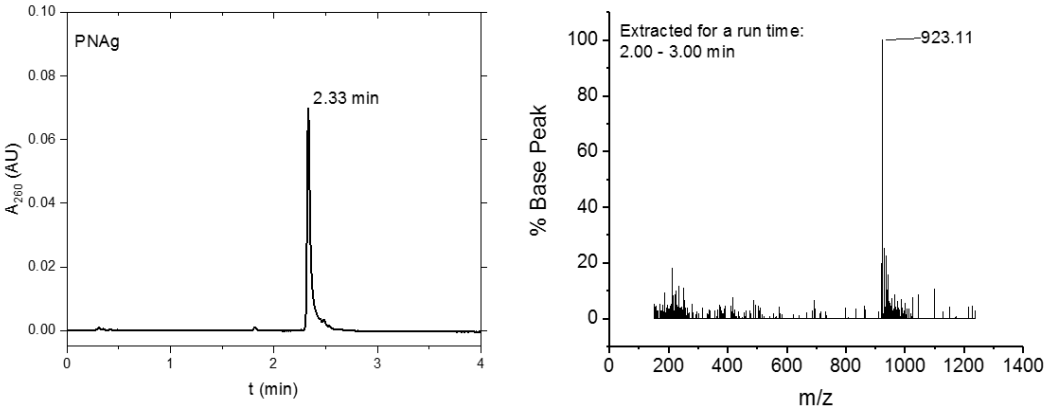

Figure 9.10 UPLC trace (left), and ESI-MS spectrum (right) of PNAg: H-Cys(StBu)-ggatctct-Glu-Glu-Orn(N_3)-NH_2. UPLC gradient: 3 to 40% of Solvent B in 4 min. Optical monitoring of signals was performed at 260 nm.

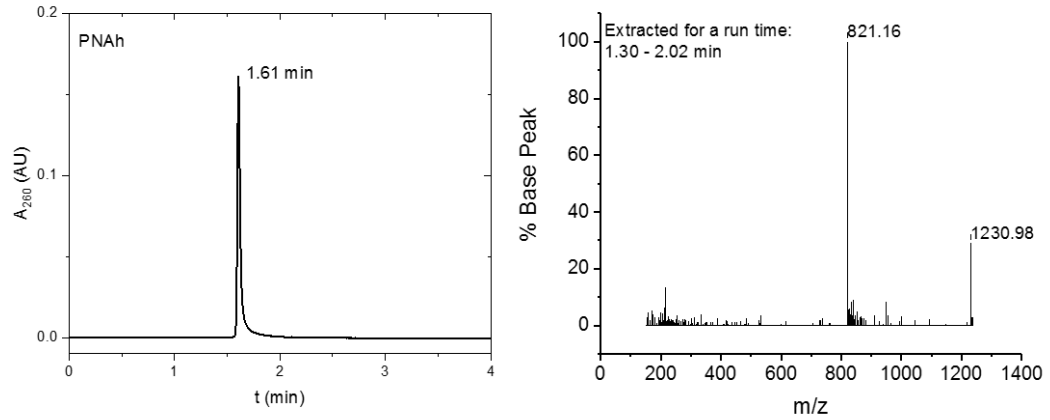

Figure 9.11 UPLC trace (left) and ESI-MS spectrum (right) of PNAh: Ac-Glu-Glu-Glu-agacagc-Cys-NH_2. UPLC gradient: 3 to 40% of Solvent B in 4 min. Optical monitoring of signals was performed at 260 nm.

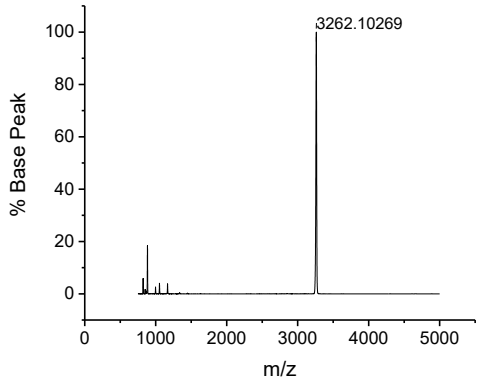

Figure 9.12. MALDI-TOF mass spectrum of PNAi. Ac-Glu-Glu-Glu-agacagc-Cys(Cy5-Gly)-NH_2.

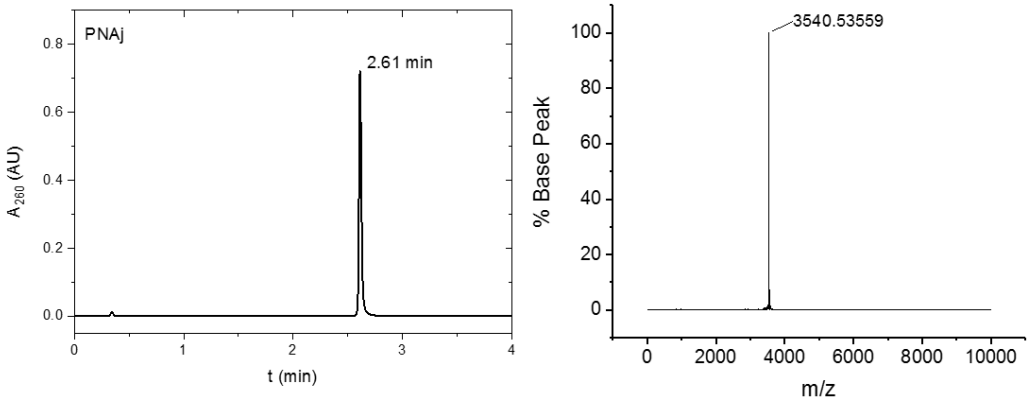

Figure 9.13 UPLC trace (left) and MALDI-TOF spectrum (right) of PNAj: H-Cys(StBu)-tctctggtctt-Glu-Glu-Orn(N_3)-NH_2. UPLC gradient: 3 to 40% of Solvent B in 4 min. Optical monitoring of signals was performed at 260 nm.

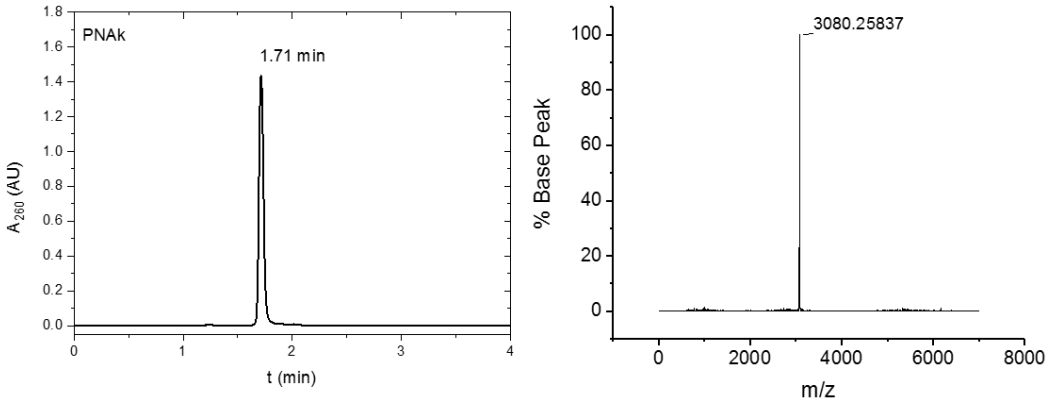

Figure 9.14 UPLC trace (left), and MALDI-TOF mass spectrum (right) of PNAk: Ac-$(Glu)_3$-Gly-gagacagca-Cys-NH_2. UPLC gradient: 3 to 60 % of Solvent B in 4 min. Optical monitoring of signals was performed at 260 nm.

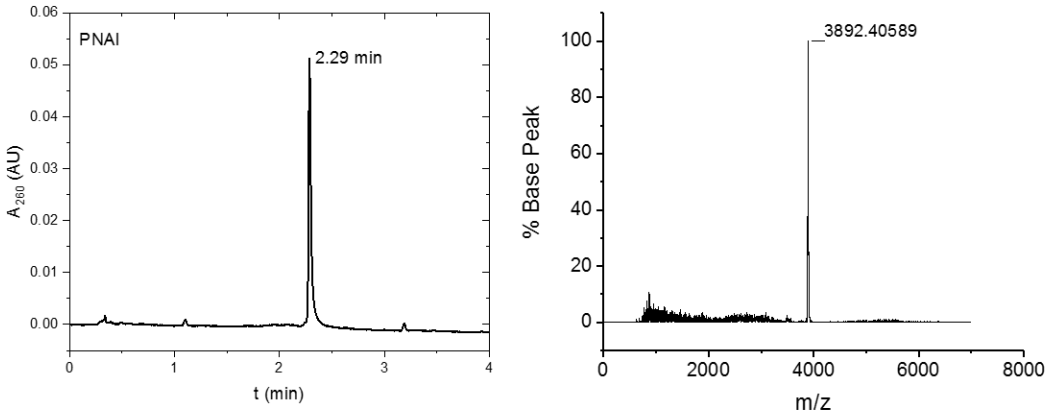

Figure 9.15 UPLC trace (left) and MALDI-TOF spectrum (right) of PNAl: Ac-$(Glu)_3$-Gly-gagacagca-Cys(Cy5-Gly)-NH_2. UPLC gradient: 3 to 40 % of Solvent B in 4 min. Optical monitoring of signals was performed at 260 nm.

Dissociation of mercaptosuccinic acid cap from the surface of CdTe core-only nanoparticles

To test the applicability of CdTe-MSA QDs for the envisioned application in OTR, preliminary experiments were performed to assess the extent of ligand dissociation under diluted conditions. To that end, CdTe QDs were modified with the Cy5 as shown in *Figure 9.16*. Prior to the conjugation step, the carboxyl-functionalized CdTe QDs were transferred into the reaction buffer (100 mM phosphate buffer, pH 7.1) via ultrafiltration, using the Amicon Ultra filter with 10 kDa MWCO, to remove any excess ligand and to adjust the pH to 7.1. The conjugation of Cy5 was carried out by using 10 eq. of amine-functionalized Cy5 and 500 eq. of EDC·HCl. The course of reaction was monitored by taking an aliquote of the reaction mixture, diluting it to the concentration of 22 nM and measuring the photoluminescence spectra upon excitation at 428 nm.

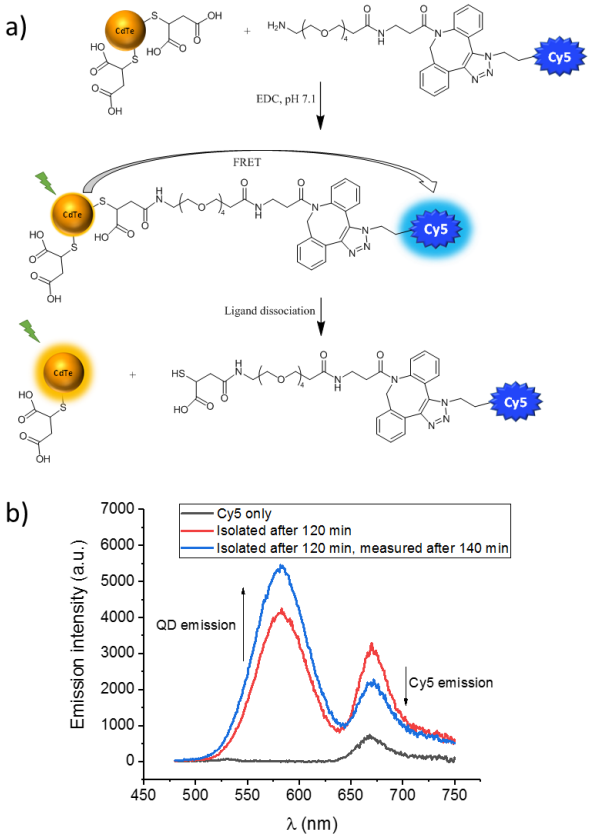

Figure 9.16. a) Illustration of the dissociation of mercaptosuccinic-based ligand following the conjugation of QD to the amine-functionalized Cy5. b) Emission spectra of QD-Cy5 conjugates recorded immediately after the separation of aliquote from the reaction mixture and after 140 min of incubation at C(QD) = 22 nM. Conditions: phosphate buffer (100 mM), pH 7.1, λ_{ex} = 428 nm. Presumably, the dissociation of thiol ligands from the nanoparticle surface under diluted conditions results in reduced FRET and increase in the emission of QD due to the decreased amount of Cy5 molecules on the QD.

Aggregation of PNA-Cy5 conjugates

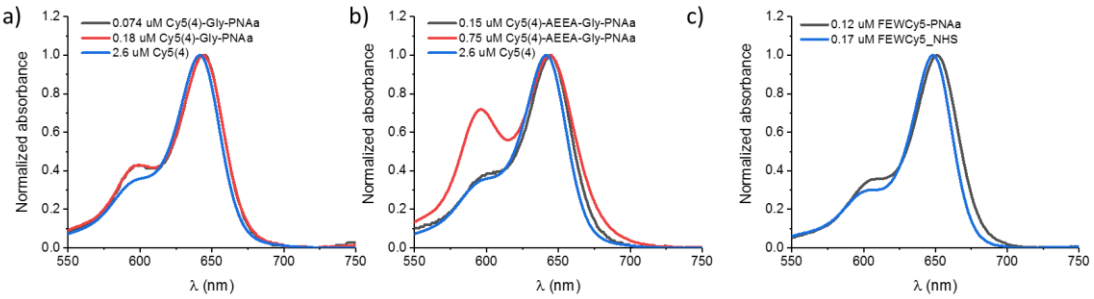

Figure 9.17. Absorbance spectra of Cy5-labeld PNAa conjugates. The formation of H-aggregates was evident by the increase in the intensity of the vibronic shoulder at 598 nm (a), 596 nm (b) and 606 nm (c).

ESI-MS data of the crude products of PNAd0 and PNAd synthesis

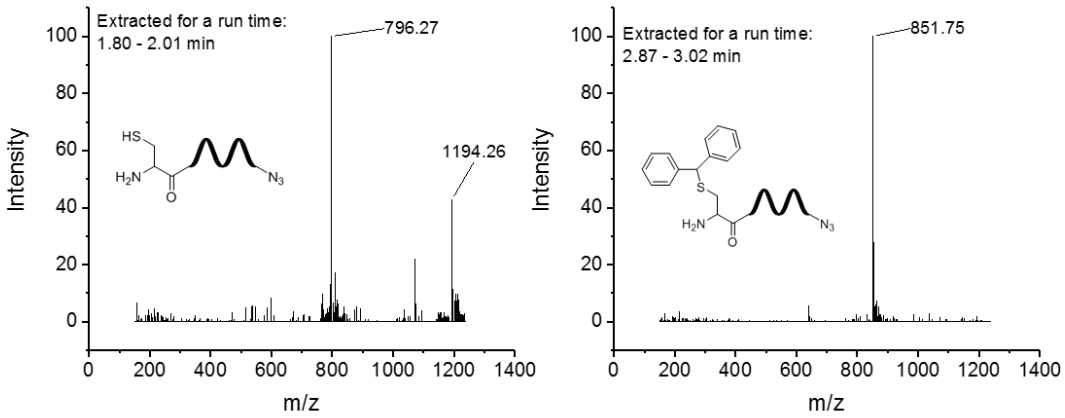

Figure 9.18. ESI-MS analysis of the crude product of PNAd0 synthesis. ESI-MS spectra were extracted for the peak of the PNAd0 (left) and for the peak of the benzhydryl adduct (right). ESI-MS$_{1.80\text{-}2.01\ min}$: 1194.3 ($[M+2H]^{2+}/2$, calc. 1194.2), 796.3 ($[M+3H]^{3+}/3$, calc. 796.5); ESI-MS$_{2.87\text{-}3.02\ min}$: 851.8 ($[M+3H]^{3+}/3$, calc. 851.9).

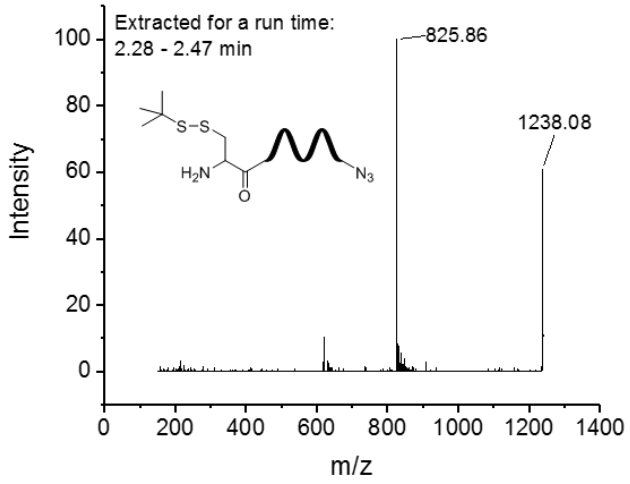

Figure 9.19. ESI-MS analysis of the crude product of PNAd synthesis. ESI-MS$_{2.28\text{-}2.47\ min}$: 1238.1 ($[M+2H]^{2+}/2$, calc. 1238.3), 825.9 ($[M+3H]^{3+}/3$, calc. 825.8).

Spectral overlap between the ITK605 emission and RNA-Cy5c absorbance.

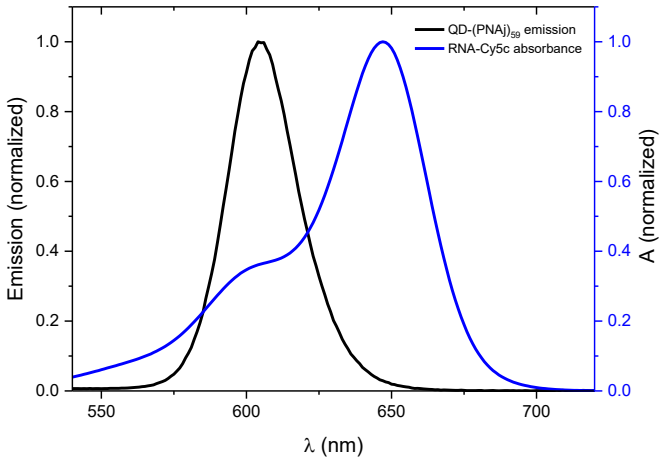

Figure 9.20. Spectral overlap between the emission of QD-$(PNAj)_{59}$ and absorbance of RNA-Cy5c.

Table 9.1. Overlap integral ($J(\lambda)$) and Förster radius (R_0) for ITK605 – RNA-Cy5c FRET pair.

FRET donor	FRET acceptor	$J(\lambda)$, $M^{-1}cm^{-1}nm^4$	R_0, Å
QD-$(PNAj)_{59}$	RNA-Cy5c	$1.35 \cdot 10^{16}$	76.6

Time-resolved measurements

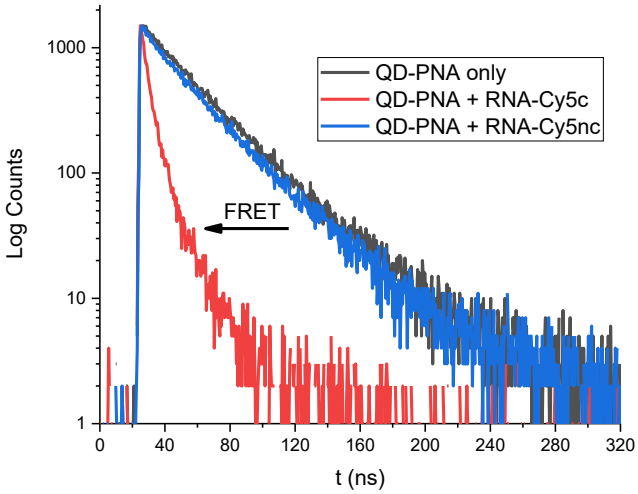

Figure 9.21. Luminescence decay curves of QD-$(PNAj)_{59}$ in the absence of RNA (grey), in the presence of RNA-Cy5c (red) and in the presence of RNA-Cy5nc (blue) after 26 h of incubation. λ_{ex} = 435 nm, λ_{em} = 605 nm. Luminescence decay measurements were performed using the FLS920 (Edinburgh Instruments) fluorometer that was equipped with a supercontinuum laser. Pulse repetition rate was set at 1 MHz. In the presence of RNA-Cy5c the lifetime of QD emission decreases, corroborating that the energy transfer occurs via FRET. Adopted with permission from[101]. Copyright 2018 American Chemical Society.

Attachment to the synthesis of LDPNA

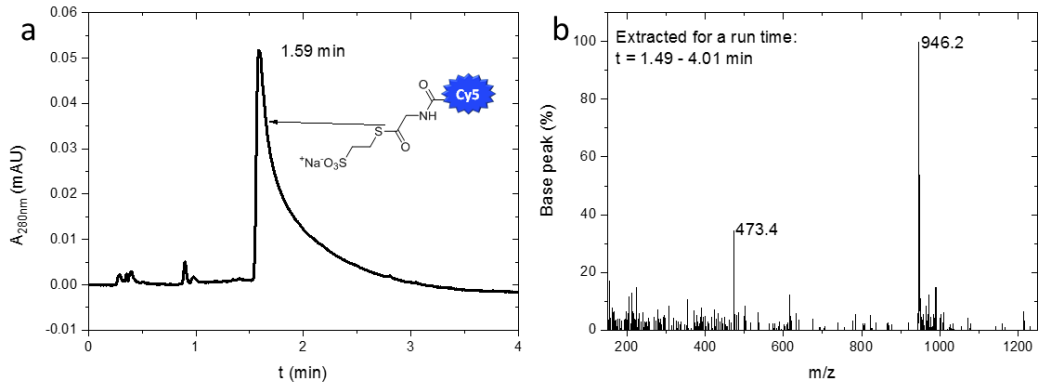

Figure 9.22. UPLC traces (a) and ESI-MS spectrum (b) of Cy5-Gly-MESNa. Conditions: 3 to 90 % of solvent B in 4 min. ESI-MS: m/z = 946 ($[M+1H]^{+}$, calc. 947), 473 ($[M+2H]^{2+}/2$, calc. 474).

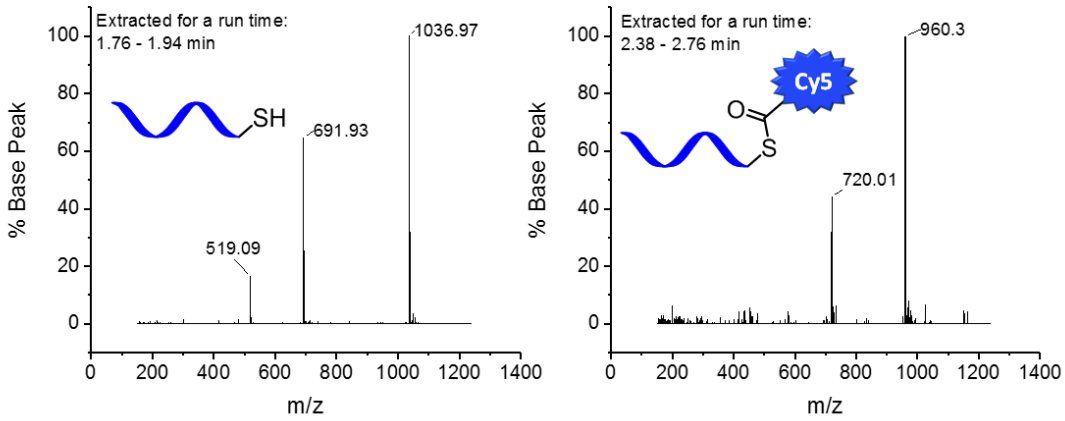

Figure 9.23. ESI-MS analysis of the crude product of PNAc synthesis via thiol exchange. ESI-MS spectra were extracted for the thiol component (PNAb) – left; and for the thioester (PNAc) – right. $ESI\text{-}MS_{1.76\text{-}1.94\ min}$ = 1037.0 ($[M+2H]^{2+}/2$, calc. 1037.5), 691.9 ($[M+3H]^{3+}/3$, calc. 692.0), 519.1 ($[M+4H]^{4+}/4$, calc. 519.3). $ESI\text{-}MS_{2.38\text{-}2.76\ min}$ = 960.3 ($[M+3H]^{3+}/3$, calc. 960.0), 720.0 ($[M+4H]^{4+}/4$, calc. 720.3).

Optimization of RNA detection conditions

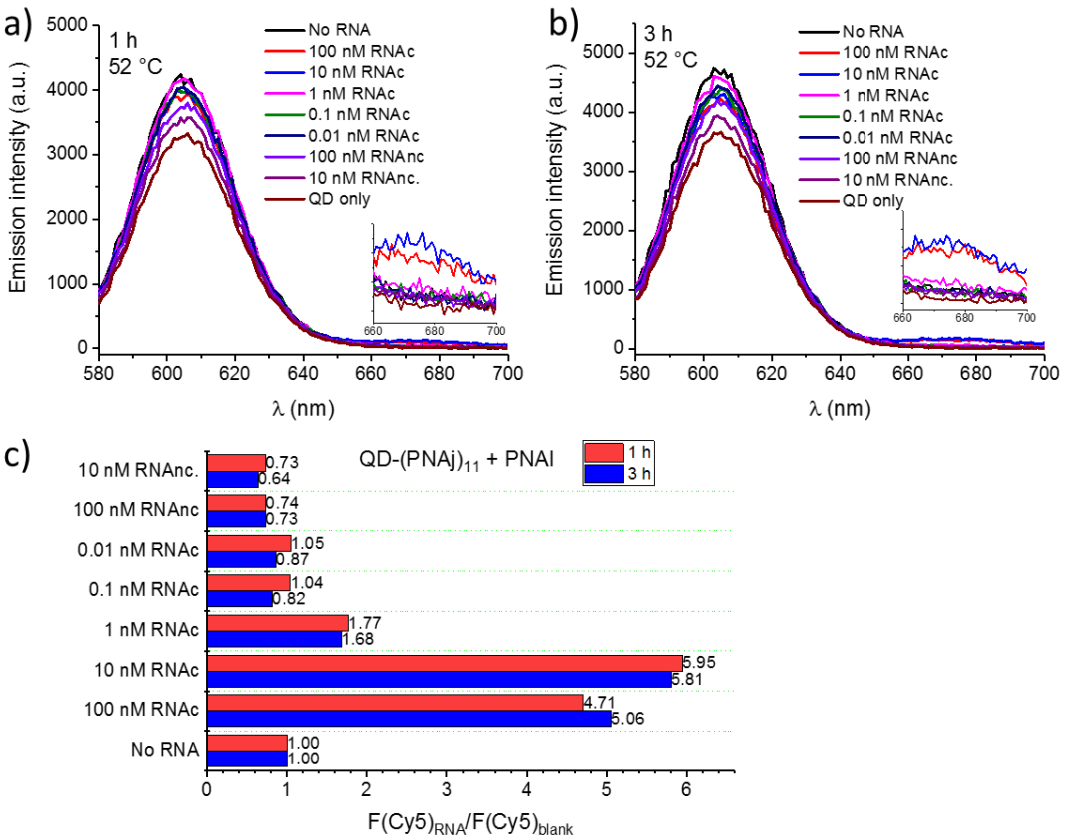

Figure 9.24. Detection of RNAc in the range of 0.01 – 100 nM with the probes QD-$(PNAj)_{11}$ and PNAl at 52 °C. Emission spectra after 1 h (a) and 3 h (b) of incubation. c) Signal-to-noise ratios for different concentrations of RNAc and RNAnc (emission was corrected for the signal of QD only). Conditions: C(QD-$(PNAj)_{11}$) = 250 pM, C(PNAl) = 3.5 nM. Citrate buffer (40 mM citrate, 2 mM TCEP, 50 mM NaCl, 0.05% (w/v) TWEEN20, pH 7.0). T = 52°C. λ_{ex} = 435 nm.

Impact of temperature on the fluorescence of QD and Cy5 and its effect on the spectral overlap and Förster radius of the respective FRET pair

Temperature affects the spectroscopic features of both the QD and Cy5 and needs to be considered to perform precise measurements. As shown in *Figure 9.25*a, the QYs of the QD and Cy5 drop with increasing temperature, seemingly favoring measurements at lower temperatures. Subsequently, based on the QD emission spectra measured at different temperatures, the impact of temperature on the spectral overlap integral and R_o (b) were assessed. This reveals a very weak dependence of the spectral overlap integral on temperatures and a more pronounced one on R_0, underlining that from the detection side, lower temperatures are obviously more favorable and strong fluctuations in temperature during assay readout should be avoided for very precise measurements as generally recommended for optical detection. Therefore, care was taken to perform all fluorescence measurements at a constant temperature to minimize its impact on the read-out.

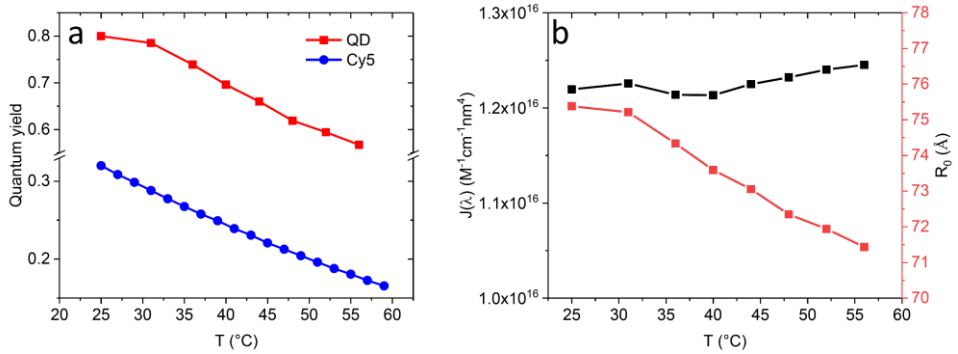

Figure 9.25. a) QY of QD (ITK605) and Cy5 (FEWCy5) as a function of temperature; b) Spectral overlap integral and Förster radius as a function of temperature.

Statistical test for outliers (to *Figure 4.26*)

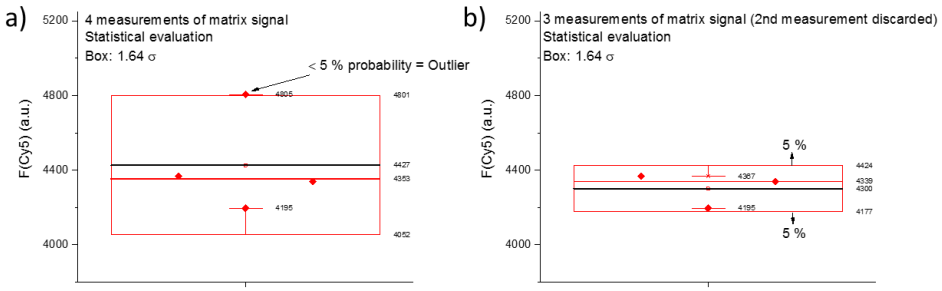

Figure 9.26. Statistical test for outliers using the 1.64σ stringency. The red box represents the range of μ ± 1.64σ. The signal of matrix was measured four times using four separately prepared samples (a) however the measurement of the second sample was discarded since it significantly affected the accuracy of the measurements by increasing the uncertainty that could lead to false-negative results in the assay. The uncertainty obtained from the three measurements (b) was significantly smaller, hence offering higher accuracy of the measurement.

Fluctuations of fluorescence measurements using 96-well plate and a fluorescence reader (to *Figure 4.26*)

To establish that the FRET-induced fluorescence of Cy5, measured with the fluorescence reader, does not fluctuate due to the changes in temperature and/or volume of the sample from well to well, the following experiment was performed. Ten solutions that contained LDPNA only (PNAl) were heated to 44 °C using a thermoshaker in low-binding Eppendorf tubes for 80 min, and then transferred into 10 wells of a 96-well plate. Next, the fluorescence of Cy5 was measured using the excitation at 590 nm. As is illustrated in *Figure 9.27*, the fluorescence measured out of 10 wells did not fluctuate significantly, neither followed any obvious pattern (increase or decrease), implying that the measurements using a series of RNA concentrations, shown in *Figure 4.26* are not affected by the instrument fluctuations or the change in temperature between the 44 and 32 °C that occurs after the transfer of samples to the microtiter plate.

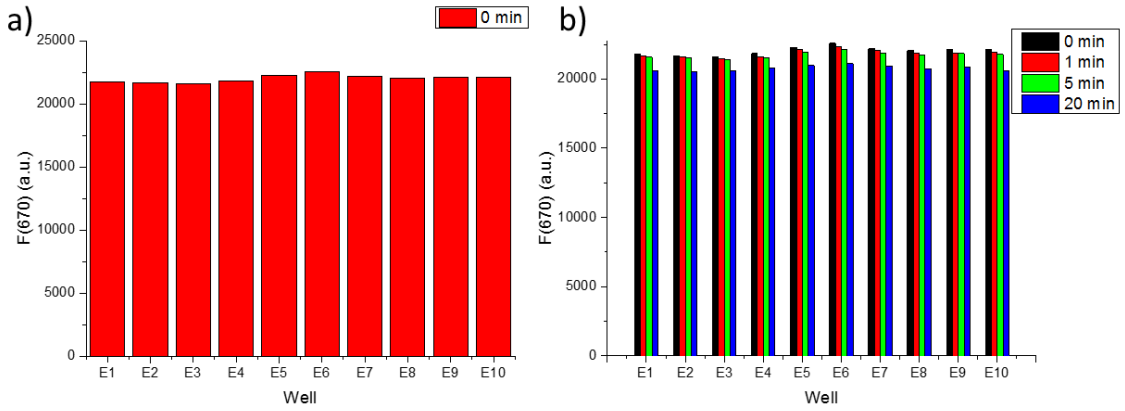

Figure 9.27. Fluctuations of fluorescence during the measurement of 10 samples with the same total volume and concentration of PNAl following the transfer of samples from the thermoshaker (44 °C) into the 96-well plate (32 °C). λ_{ex} = 590 (20) nm, λ_{em} = 670 (25) nm. T(fluorescence measurement) = 32 °C. t(measurement out of 1 well) = 2.9 sec.

Kinetics of FRET-induced Cy5 signaling for different concentrations of RNAc by using QD-(PNAj)$_{11}$ (left) or QD-(PNAj)$_{59}$ (right). Raw data.

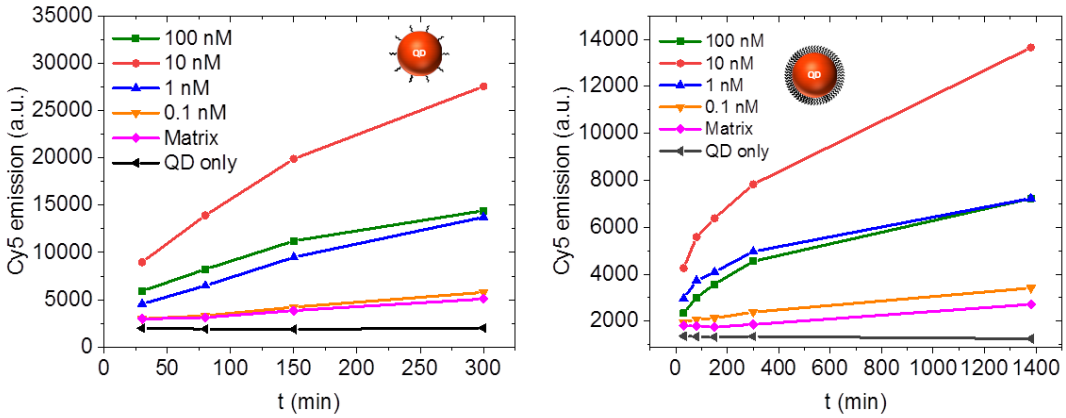

Figure 9.28. Kinetics of FRET-induced Cy5 signaling for different concentrations of RNAc by using QD-(PNAj)$_{11}$ (left) or QD-(PNAj)$_{59}$ (right) in the presence of 100 nM RNAnc. Conditions: left: C(QD-(PNAj)$_{11}$ = 250 pM, C(PNAl) = 3.5 nM; right: C(QD-(PNAj)$_{59}$ = 25 pM, C(PNAl) = 1 nM. Cy5 emission is plotted without correction. Matrix: 100 nM RNAnc in citrate buffer (40 mM citrate, 2 mM TCEP, 50 mM NaCl, 0.05% (w/v) TWEEN20, pH 7.0); T = 44°C.

Temperature gradient as the means to improve the turnover in template

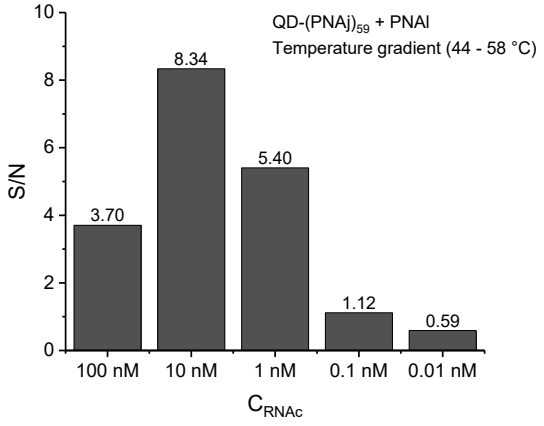

Figure 9.29. RNA detection using temperature gradient. Conditions: C(QD-(PNAj)$_{59}$ = 25 pM, C(PNAl) = 1 nM. Matrix: 100 nM of RNAnc in citrate buffer (40 mM citrate, 2 mM TCEP, 50 mM NaCl, 0.05% (w/v) TWEEN20, pH 7.0). Temperature cycle: 44 °C (20 min) + 58 °C (10 min). A total of 10 cycles was run (t_{tot} = 5h). It should be noted that the process of cooling down from 58 °C to 44 °C lasts for 5 min, therefore the reaction is exposed to a range of temperatures between the 44 and 58 °C for a notable time. Luminescence was recorded on Infinite F200pro (Tecan) reader using the bandpass filters: λ_{ex} = 465 (35) nm, λ_{em} = 670 (25) nm. The results obtained after 5 h of such treatment indicated that detection of low concentrations of RNA was significantly less efficient compared to isothermal temperature regime used previously.

Test experiments aimed at the detection of RNA directly from lysed serum sample

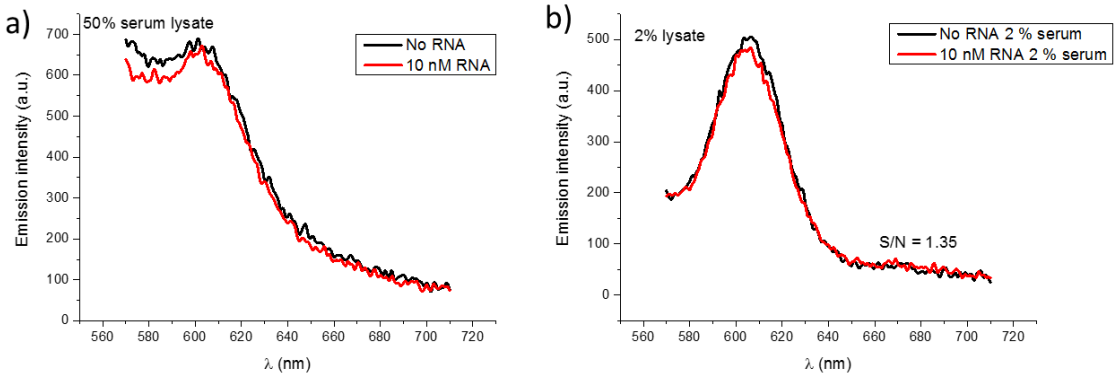

Figure 9.30. Detection of RNAc from lysed serum sample. For this experiments the lysed serum was spiked with the target RNA and added to the reaction buffer. Serum lysate was mixed with citrate buffer (200 mM citrate, 18 mM TCEP, 0.1 % (w/v) TWEEN20, 0 mM (a) or 70 mM (b) NaCl, pH 7.0) so that the final content of serum lysate was 50 % (a) or 2 % (b). $C(QD\text{-}PNAj)_{59}$ = 25 pM, C(PNAl) = 1 nM, C(RNAc) = 10 nM (final concentration). T = 41 °C. λ_{ex} = 435 nm. Luminescence spectra were recorded after 50 min of incubation at 41 °C. S/N for 2 % serum lysate was calculated from emission intensity in Cy5 channel. Reactions were performed in the reader, no pre-heating prior to donor addition was used. Serum lysis was performed according to the protocol of manufacturer (QIAGEN) using 140 µl of human serum. This data indicates that high concentration of serum induces strong scattering that bleeds through into the acceptor channel. However, reducing the content of serum lysate in buffer to 2 % did not significantly improve the detection sensitivity. To test whether the constraints were due to the components of the lysis buffer (AVL buffer) or to the components of the serum, experiments shown in Figure 9.31 were performed.

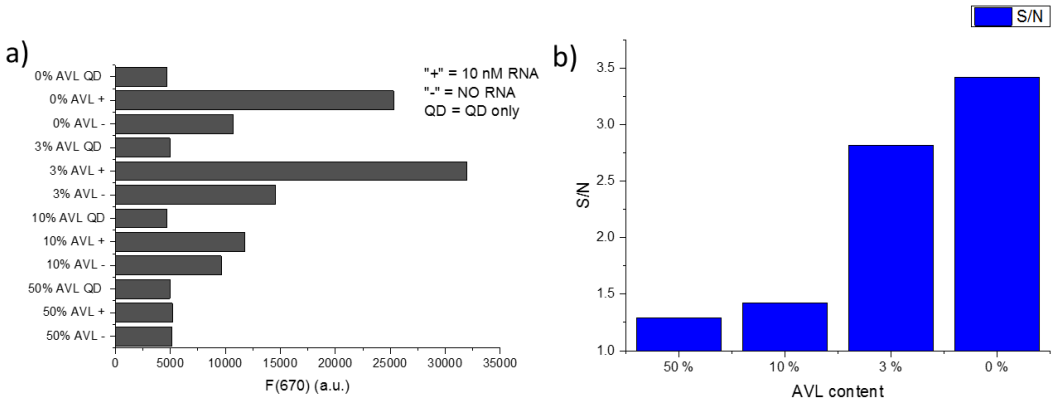

Figure 9.31. RNA detection in the presence of different amounts of lysis buffer (AVL). Fluorescence was recorded after 195 min of incubation at 41 °C. $C(QD\text{-}(PNAj)_{11})$ = 250 pM. C(PNAl) = 3.5 nM. C(RNAc) = 10 nM. Bandpass filters: λ_{ex} 465 (35) nm, λ_{em} 670 (25) nm. T= 41 °C. Incubation was performed in the reader, no pre-heating prior to donor addition was used. This data shows that AVL buffer has a strong impact on the OTR when used at high concentrations. This effect is weak if only 3 % of AVL buffer is used, however performing assays with such small concentration of lysed serum sample would greatly dilute the target RNA and is therefore disadvantageous.

Impact of additives on the nonspecific interactions netween the LAPNA and LDPNA

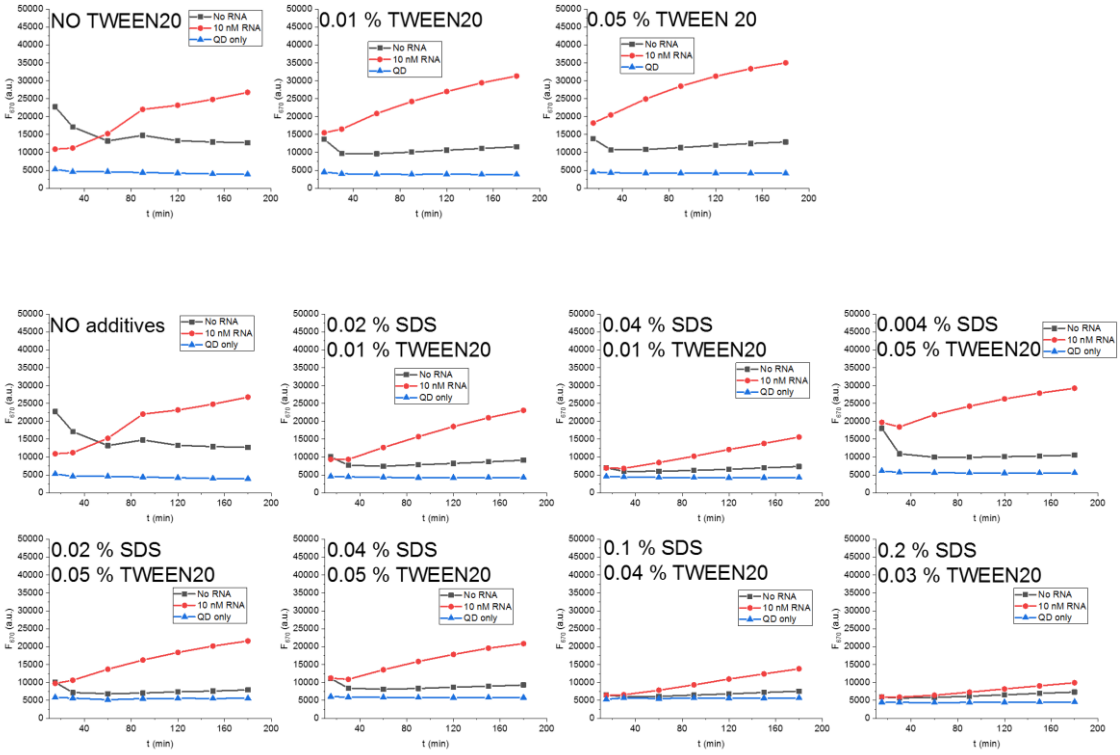

Figure 9.32. Screening experiments aimed at the identification of the best combination of additives for OTR-based RNA detection.

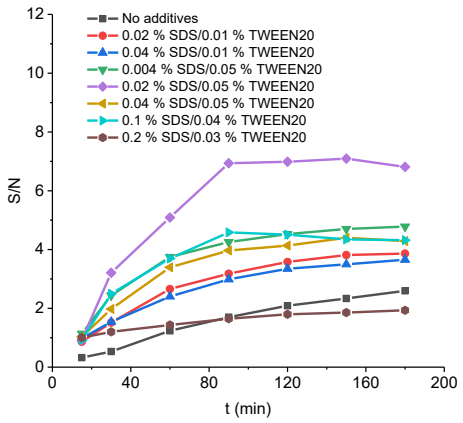

Figure 9.33. Optimization of buffer composition for target-catalyzed RNA detection. Conditions: C(QD-$(PNAj)_{59}$ = 75 pM, C(PNAl) = 2.5 nM, C(RNAc) = 10 nM. Buffer: 40 mM citrate, 2 mM TCEP, 50 mM NaCl, specified content of surfactants (w/v), pH 7.0. T = 40 °C. λ_{ex} = 465 (35) nm, λ_{em} = 670 (25) nm.

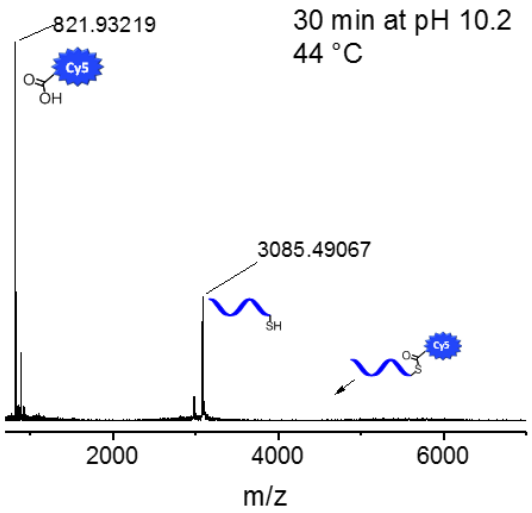

Figure 9.34. MALDI-TOF mass spectrum measured after 30 min of heating the PNAl at 44 °C and pH 10.2. pH was adjusted to 10.2 by mixing the citrate buffer (40 mM citrate, 2 mM TCEP, 50 mM NaCl, pH 7.0) and borate buffer (220 mM, pH 10.6) at a ratio of 5 to 1 (V/V). Reaction was quenched with the 2 % TFA solution in water, and subsequently MALDI-TOF mass spectrum was measured. The absence of residual thioester in the mass spectrum is indicative of its complete hydrolysis under the used conditions.

Acknowledgements

Firstly, I would like to thank my PhD supervisors: Dr. Ute Resch-Genger and Prof. Dr. Oliver Seitz for the very exciting PhD project, productive scientific discussions, substantial strategic advice and effective work on the publication and thesis. In addition, I would like to express my gratitude for the degree of scientific freedom I enjoyed during the PhD time, which allowed me to develop my own scientific approach and to carry out experiments in an independent manner.

I thank the School of Analytical Sciences Adlershof (SALSA) at Humboldt-Universität zu Berlin for the financial support of the first two years of my PhD and for the sponsorship of the scientific conferences and workshops I have attended. I am also thankful to all members of the SALSA organizing team for the support and input I received.

I am very grateful to Georgina Gavins, Tim Bilbrough, and Daniel Kage for the careful corrections of the first draft of my PhD thesis. Your input was very helpful, and I greatly appreciate the comments.

I would also like to thank my lab-mates at Humboldt-Universität zu Berlin: Tim Bilbrough, Georgina Gavins, Yannic Altrichter, Pablo Lores Lareo, and Ziv Harpaz, as well as the whole Seitz group for the excellent atmosphere at work and outside the lab.

I would like to thank the Division of Biophotonics at Bundesanstalt für Materialforschung und -prüfung (BAM) for the outstanding work together, as well as the free time we spent. I am also very grateful to my office-mates: Cui Wang, Daniel Kage, and Florian Weigert for the productive scientific discussions and for the friendly and fun atmosphere at the office.

Finally, I would like to thank my friends and family for the support during my PhD years.

Publikationsverzeichnis

Oleksandr Zavoiura, Ute Resch-Genger, and Oliver Seitz “Quantum Dot-PNA Conjugates for Target-Catalyzed RNA Detection” Bioconjugate Chem. 2018, 29, 1690−1702.

Vorträge auf wissenschaflichen Konferenzenzen

“Quantum dot-based FRET systems for RNA-catalyzed dengue virus detection” SPIE BiOS 2018, San Francisco, USA. 2018. (Vortrag).

“RNA detection by FRET systems based on Peptide Nucleic Acid-QD conjugates” 15th Conference on Methods and Applications in Fluorescence, Brügge, Belgien. 2017. (Poster).

Selbstständigkeitserklärung

Ich erkläre, dass ich die Dissertation selbständig und nur unter Verwendung der von mir gemäß § 7 Abs. 3 der Promotionsordnung der Mathematisch-Naturwissenschaftlichen Fakultät, veröffentlicht im Amtlichen Mitteilungsblatt der Humboldt-Universität zu Berlin Nr. 126/2014 am 18.11.2014 angegebenen Hilfsmittel angefertigt habe.

Berlin, den

Oleksandr Zavoiura